A STUDY OF THE EFFECTS OF INTERSTITIALS ON THE EMBRITTLEMENT OF TITANIUM AND ZIRCONIUM UNDER THE APPLICATION OF STATIC AND DYNAMIC LOADS

Thesis for the Degree of Ph. D.
MICHIGAN STATE UNIVERSITY
KARL JOSEPH PUTTLITZ
1971

LIBRARY
Michigan State
University

This is to certify that the

thesis entitled
A STUDY OF THE EFFECTS OF INTERSTITIALS ON THE EMBRITTLEMENT OF TITANIUM AND ZIRCONIUM UNDER THE APPLICATION OF STATIC AND DYNAMIC LOADS
presented by

Karl Joseph Puttlitz

has been accepted towards fulfillment
of the requirements for

Ph.D. degree in Metallurgy

Major professor

Date March 29, 1971

O-7639

BINDING BY
HOAG & SONS'
BOOK BINDERY INC.
LIBRARY BINDERS
PRINCPORT, MICHIGAN

ABSTRACT

A STUDY OF THE EFFECTS OF INTERSTITIALS ON THE
EMBRITTLEMENT OF TITANIUM AND ZIRCONIUM UNDER
THE APPLICATION OF STATIC AND DYNAMIC LOADS

Karl Joseph Kurz

The traditional [illegible] of interstitials on the mechanical [illegible] of both titanium and zirconium involving [illegible] making additions of [illegible] quantities of oxygen [illegible] drastically strengthen [illegible] at very modest levels. Although [illegible] it is the purpose of [illegible] that these materials will [illegible] fracture toughness after elevated temperature treatment in the atmospheres of these gases. Evidence is presented to show that both metals failed in a state of plane strain for all treatments of the test schedule for a 6.4 inch section plate. Additional evidence indicates that some losses in dynamic fracture toughness are due to changes in the phase morphology.

ABSTRACT

A STUDY OF THE EFFECTS OF INTERSTITIALS ON THE EMBRITTLEMENT OF TITANIUM AND ZIRCONIUM UNDER THE APPLICATION OF STATIC AND DYNAMIC LOADS

By

Karl Joseph Puttlitz

The traditional studies of the effects of interstitials on the mechanical properties of both titanium and zirconium involved the preparation of the alloys by making additions of these impurities to the melt. Small quantities of oxygen and nitrogen were found to drastically strengthen these metals and embrittle them at very modest levels. Although these facts are well documented, it is the purpose of this study to define the conditions that these materials will still possess good fracture toughness after elevated temperature treatment in the atmospheres of these gases. Evidence is presented to show that both metals failed in a state of plane stress for all treatments of the test schedule for a 0.4-inch section plate. Additional evidence indicates that some losses in dynamic fracture toughness are due to changes in the phase morphology.

Karl Joseph Puttlitz

Hydrogenated-pure and commercially-pure titanium, and reactor-grade zirconium are shown to fail under impulsive loading conditions. Fracture models constructed from the phase and fracture morphology are presented.

A STUDY OF THE EFFECTS OF INTERSTITIALS ON THE EMBRITTLEMENT OF TITANIUM AND ZIRCONIUM UNDER THE APPLICATION OF STATIC AND DYNAMIC LOADS

By

Karl Joseph Puttlitz

A THESIS

Submitted to
Michigan State University
in partial fulfillment of the requirements
for the degree of

DOCTOR OF PHILOSOPHY

Department of Metallurgy,
Mechanics, and Materials Science

College of Engineering

1971

G-70283

© Copyright by
KARL JOSEPH PUTTLITZ

1971

ACKNOWLEDGMENT

The author can only express gratitude and appreciation to Professor Auster [illegible] his thesis advisor, in a most inadequate way for his guidance during the experimental stages of the work and patience in reading the manuscript; even more for his encouragement as an educator in which capacity the author has gained the benefits over a ten year [illegible].

It is with pleasure that the author acknowledges his indebtedness to [illegible] Department of Metallurgy, Mechanics [illegible] are solely to be credited [illegible] thesis.

In completing his studies [illegible] the author wishes to thank:

The International Business Machines Corporation which has provided him with a Fellowship, [illegible] research funds, equipment, and any other [illegible] requested. The number of individuals within the organization to whom the author is indebted is [illegible] for singular mention.

The Reactive Metals Corporation [illegible] assistance in supplying some of the materials [illegible]

ACKNOWLEDGMENTS

The author can only express gratitude and appreciation to Professor Austen J. Smith, his thesis advisor, in a most inadequate way for his suggestions during the experimental stages of the work, and patience in reading the manuscript; even more for his contribution as an educator in which capacity the author has reaped the benefits over a ten year period.

It is with pleasure that the author acknowledges his indebtedness to the entire staff of the Department of Metallurgy, Mechanics, and Materials Science whom are solely to be credited for his formal professional training.

In completing his graduate studies the author wishes to thank:

The International Business Machines Corporation which has provided him with a Resident Study Fellowship, research funds, equipment, and any other aid that was requested. The number of individuals within the organization to whom the author is indebted is far too numerous for singular mention.

The Reactive Metals Corporation for their cooperation in supplying some of the materials used in this study.

Mr. Robert Walton for generating the computer programs used in the study, and aid with the impact instrumentation.

The Division of Engineering Research for financial support, and prompt services rendered by its departments: the machine shop, that prepared the samples; and the electronics shop.

The MSU glass blowing shop, who skillfully and painstakingly remade the delicate fixture used for the gas treatments several times due to design alterations.

The author wishes to express a special thanks to his family, especially his parents, who have been an endless source of love, kindness, encouragement and inspiration; and by their example engendered within him both a will and a desire to strive for excellence in all his endeavors, but never to abandon humility with success.

Lastly, but certainly not in importance, the author wishes to express his most sincere gratitude to his wife, Dianne. Without her unending devotion, understanding, confidence, and support this and previous educational pursuits could never have been a reality.

TABLE OF CONTENTS

Page

LIST OF TABLES xii

LIST OF FIGURES xiv

Chapter

I. INTERSTITIALS IN α-TITANIUM AND α-ZIRCONIUM . 1
1.1.0 General Background 1
1.2.1 Titanium 2
1.2.2 Zirconium 4
1.3.0 History of Brittleness Problems Due to Interstitials 5
1.4.0 Position and Distribution of Interstitials in Titanium and Zirconium 7
1.5.0 Constitution of Titanium and Zirconium with Interstitials: Theoretical and General Considerations 11
1.5.1 Effect of d-Electron Additions on α-β Transformation 12
1.6.0 Constitution of Titanium and Zirconium with Interstitials Diagrams and Features 14
1.6.1 Solubility Relationships of Titanium and Zirconium with Nitrogen 14
1.6.2 Constitution of Titanium and Zirconium with Oxygen 19
1.6.3 Constitution of Titanium and Zirconium with Hydrogen 21
1.7.0 Reaction Kinetics of Interstitial Gases with Titanium and Zirconium . . . 28
1.7.1 Metals Reaction with Oxygen 29
1.7.2 Metals Reaction with Nitrogen 30
1.7.3 Metals Reaction with Air 30

II. THE EFFECT OF INTERSTITIALS ON THE MECHANICAL PROPERTIES OF TITANIUM AND ZIRCONIUM 32
2.1.0 Strengthening Theories of Interstitial Oxygen and Nitrogen in Titanium and Zirconium 32
2.2.0 Effect of Interstitials on Cleavage Fracture and Plastic Deformation of Alpha Titanium and Zirconium 34

Chapter Page

2.2.1.0 Cleavage and the Effect of Interstitials 34
2.2.1.1 A Theory of Hydrogen Embrittlement in Titanium and Zirconium 35
2.2.2.0 Plastic Deformation and the Effect of Interstitials 38
2.2.2.1 Plastic Deformation in α-Titanium 39
2.2.2.2 Plastic Deformation in α-Zirconium 39
2.3.0 Effect of Interstitials on Strength and Ductility 42
2.3.1 Effect on Titanium 45
2.3.2 Effect on Zirconium 47
2.4.0 Impact Strength of Titanium and Zirconium 49
2.4.1 Effect of Hydrogen on Impact Strength of Titanium and Zirconium . . 50
2.4.2 Effect of Nitrogen on Impact Strength of Titanium and Zirconium . . 52
2.4.3 Effect of Oxygen and Oxygen Equivalents on Impact Strength of Titanium and Zirconium 53
2.4.4 Accumulative Effects of Interstitials on Impact Strength of Titanium and Zirconium 53
2.4.5 Combined Factors Affecting Impact Strength 54

III. METAL FRACTURE CHARACTERISTICS 56
3.1.0 State of Stress 56
3.2.0 State of Strength 57
3.3.0 Levels of Aggregation 58
3.4.0 Behavior 61
3.5.0 Fracture Modes 62
3.6.0 Crystallographic Classification 62
3.6.1 Cleavage 63
3.6.2 Shear 64
3.7.0 Appearance and the Effect of Aggregation 65

IV. HISTORICAL DEVELOPMENT OF FRACTURE THEORY . . 68
4.1.0 Misconceptions 68
4.2.0 The Classical Theory of Notch Brittleness 70
4.2.1 Ludwik's Postulations 70
4.2.2 Velocity Effects 75
4.2.3 Shear Lips 76

Chapter Page

4.3.0 Discrepancy Between Theoretical and Observed Strengths 77
4.3.1 Early Experiments 77
4.3.2 Theoretical Strength 78
4.4.0 Griffith Thermodynamic Crack Propagation Criteria and Fracture Stress Relationship 80
4.4.1 Griffith Concept Applied to Metals: Plastic Flow Required . . . 87
4.4.2 Plasticity in Brittle Fractures . . . 87
4.4.3 Ductile Fractures Not Covered by Griffith Equation 90

V. LINEAR ELASTIC FRACTURE MECHANICS 92
5.1.0 Introduction 92
5.2.0 Fracture Correlation Poor Between Ordinary Tension Testing and Service Failures 93
5.3.0 Fracture Modes 94
5.4.0 Arbitrary Parameters to Define Notch Toughness 94
5.5.0 Modern Fracture Mechanics 97
5.5.1 The Strain Energy Release Rate--Simple Elastic Model 98
5.5.1.1 Definition of G From Energy Considerations 100
5.5.2 The Relationship Between Strain Energy Release Rate and Elastic Compliance 101
5.5.3 Strain Energy Release Rate--Compliance Relationship is Completely General 105
5.5.4 The Stress Intensity Factor 107
5.5.4.1 The Stress Intensity Parameter as a Measure of Fracture Toughness 110
5.5.5 The Relationship Between the Strain Energy Release Rate and the Stress Intensity Factor 111
5.6.0 Plane Stress and Plane Strain Condition 116
5.6.1 Dependence of G and K on Thickness and Fracture Appearance 116
5.6.2 Plane Stress to Plane Strain Transition 118
5.6.3 Plasticity Effects 118
5.6.3.1 Size of the Plastic Zone . . 122
5.6.3.2 Effect of Plasticity on G and K Measurements and Calculations 124
5.6.3.3 Constraint Parameter 125

Chapter		Page
VI.	STATIC FRACTURE MECHANICS	128
	6.1.0 Pop-In Method for Determining G_{IC}	128
	6.2.0 Monitoring the Crack Opening	131
	6.3.0 Static Determination of G and K via Single-Edge-Notch Tension Specimen	133
	6.3.1.1 General Calibration Procedure	134
	6.3.1.2 Development of the Polynomial Form	135
VII.	DYNAMIC FRACTURE MECHANICS	137
	7.1.0 Instrumented Impact-Initial Studies	137
	7.1.1 Static Calibration of Load Transducers.	139
	7.2.0 Charpy Impact Test Accuracy and Repeatability: Conventional and Instrumented	141
	7.3.0 Crack Formation and Progression of Charpy Specimens During Loading	143
	7.3.1 Interpretation of Charpy Impact Load-Displacement Curves	144
	7.4.0 Background on Charpy Impact Techniques Used in Dynamic Fracture Mechanics	148
	7.4.1 Strain Rate Effects on Fracture Mechanics Parameters	150
	7.4.2 Problems Due to Oscillations in the Load-Time Record	151
	7.5.0 Controversy Over the Use of the Charpy Impact Test for the Determination of Fracture Mechanics Parameters	154
VIII.	EXPERIMENTAL METHODS	157
	8.1.0 Material	157
	8.1.1 Titanium--High Purity (Electrorefined).	157
	8.1.2 Titanium--High Purity (Research Grade).	157
	8.1.3 Titanium--Commercially Pure Grades	159
	8.1.4 Zirconium--Reactor Grade	160
	8.2.0 Gas Treatment Atmospheres	161
	8.2.1 Gases	161
	8.2.2 Purification Train	162
	8.3.0 Gas-Treatment: Procedure and Apparatus	165
	8.3.1 Preparation of Titanium Discs	170
	8.3.2 Specimen Gas-Treatment Schedules	171
	8.4.0 Test Specimens	173
	8.5.0 Static Testing	177
	8.5.1 Single-Edge-Notch Tension Test	177
	8.5.2 Rectangular Specimen Tension Test	179
	8.6.0 Dynamic Testing: Instrumented Impact	182
	8.6.1 Use of Impulse-Momentum Principle to Determine the Energy of Fracture	182

Chapter Page

8.6.2.0 Experimental Determination of Dynamic Fracture Energies . . . 183
8.6.2.1 System Calibration 186
8.6.3 Calibration of Impact Tester Tup . . . 189
8.6.4 Calibration of Impact Tester 190
8.6.5 Triggering System 191
8.7.0 Specimen Examination and Chemical Analysis 192

IX. RESULTS AND DISCUSSION 195
Part I.--Nitrogen and Oxygen Treated Titanium and Zirconium 195
9.1.0 Single-Edge-Notch Tensile Fracture Experiments 195
9.2.0 Static Tensile Data for Oxygen and Nitrogen Treatments 201
9.3.0 Impulsive Loading (Impact) Experimental Results 203
9.3.1 Lateral Expansion 203
9.3.2 Absorbed Fracture Energies 205
9.4.0 Post Chemical Analysis of Selected O_2 and N_2 Treated Titanium and Zirconium Samples 208
9.5.0 Discussion of the Effects of Oxygen and Nitrogen Treatments on the Static and Dynamic Failure Tendencies of Titanium and Zirconium 209
9.5.1 Titanium Treated with Nitrogen at 1850°F 209
9.5.2 Zirconium Treated with Nitrogen at 2000°F 214
9.5.3 Titanium Treated with Oxygen at 1725°F 218
9.5.4 Zirconium Treated with Oxygen at 1675°F 221

Part II.--Hydrogen Treated Titanium and Zirconium 222
9.6.0 Static Tensile Results of Hydrogenated High Purity Titanium (HP-BM) 223
9.7.0 Post Hydrogen Treatment Chemical Analysis 223
9.8.0 Impulsive Loading Results of Hydrogenated Titanium and Zirconium 225
9.8.1 Lateral Expansion 225
9.8.2 Absorbed Fracture Energies and Dynamic G_{IC} Values 227
9.9.0 Discussion of the Effects of Hydrogen on the Fracture Properties of Titanium and Zirconium 229

Chapter Page

9.9.1 The Failure of Hydrogenated Pure Titanium (HP-BM) 229
9.9.2 The Failure of Hydrogenated Commercially Pure Titanium (TPC) . . 238
9.9.2.1 Effect of Increasing β Phase. 248
9.9.3 The Failure of Hydrogenated Reactor Grade Zirconium (WCA) 252

X. CONCLUSIONS 255

Appendix

A. CRACK TIP STRESS FIELD 258
A.1 Equilibrium Equations 258
A.2 Compatability Equation 258
A.3 Defining an Airy Stress Function . . . 258
A.4 Harmonic and Biharmonic Functions . . . 259
A.5.1 Analyticity 260
A.5.2 Cauchy-Riemann Conditions 260
A.5.3 Derivative Definitions 263
A.5.4 Cauchy-Riemann Conditions Applied to Functions of the Complex Variable . . 263
A.5.5 Westergaard Stress Function 264
A.6 Determination of the Stresses in Terms of Complex Variable Functions 265
A.6.1 Determination of σ_x 265
A.6.2 Determination of σ_y 265
A.6.3 Determination of σ_{xy} 266
A.7 Analytic Function Representation of a Crack 266
A.8 Polar Coordinate Equivalents of the Real and Imaginary Part of the Analytic Function 268
A.8.1 Polar Equivalents of $\overline{Z}$ 268
A.8.2 Polar Equivalents of Z 270
A.8.3 Polar Equivalents of Z' 270
A.9 Crack Tip Stress Field in Polar Coordinates 271
A.9.1 σ_x in Polar Coordinates 271
A.9.2 σ_y in Polar Coordinates 272
A.9.3 τ_{xy} in Polar Coodinates 273

B. CRACK DISPLACEMENT FIELD 274
B.1 The Strains in Terms of Stresses and Elastic Constants 274
B.2 Displacements in Terms of the Real and Imaginary Parts of the Analytic Function 275

Appendix Page

B.2.1 The Displacement in the x-Direction, u. 275
B.2.2 Displacement in the y-Direction, v . . 276
B.3 Displacement Equations in Terms of K and the Elastic Constants 278
B.3.1 The Displacement in the x-Direction, u. 278
B.3.2 The Displacement in the y-Direction, v. 279

BIBLIOGRAPHY 281

LIST OF TABLES

Table		Page
2.1	Alpha titanium slip system and twinning planes.	40
2.2	Alpha zirconium slip systems and twinning planes.	41
8.1	Typical analysis of U.S. Bureau of Mines electrorefined titanium in parts per million.	158
8.2	Chemistry--per cent by weight of U.S. Bureau of Mines supplied elecrolytic titanium crystals.	158
8.3	Chemistry--per cent by weight of Reactive Metals, Inc., high purity titanium.	158
8.4	Chemistry--per cent by weight of commercially pure titanium (RMI grades).	159
8.5	Chemistry--per cent by weight of commercially pure titanium (ASTM B265-Grade II).	160
8.6	Ingot Chemistry--per cent by weight of reactor grade zirconium plate.	161
8.7	Purity of gases used for thermal treatment.	162
8.8	Designation for metals used in the study.	171
8.9	Soak times for titanium and zirconium specimens treated in nitrogen.	172
8.10	Fracture absorption energies for standard Charpy bars.	190
9.1	Maximum load crack openings of (WCA) treated in nitrogen and oxygen.	199
9.2	The tensile properties of HP-RMI treated in oxygen.	201
9.3	Per cent total strain of several commercially pure titanium grades treated in nitrogen.	202

Table		Page
9.4	Tensile stress (PSI) of several commercially pure titanium grades treated in nitrogen. . .	202
9.5	Instrumented impact fracture energies of nitrogen treated WCA at 2000°F.	208
9.6	Chemical analysis of some oxygen and nitrogen treated titanium and zirconium samples.	210
9.7	Tensile properties of hydrogenated HP-BM titanium treated at various temperatures and times.	223
9.8	Hydrogen analysis of some titanium and zirconium samples treated under various conditions.	224
9.9	Charpy bar lateral expansions of hydrogenated HP-BM and TPC titanium	226
9.10	Charpy bar lateral expansions of hydrogenated commercially pure titanium (RMI) and zirconium (WCA) treated at 1850°F for 2 hours. .	226
9.11	Fracture toughness and fracture energies of hydrogenated HP-BM and TPC titanium.	228
9.12	Fracture toughness and fracture energies of hydrogenated commercially pure titanium (RMI) and reactor grade zirconium (WCA) . . .	228

LIST OF FIGURES

Figure		Page
1.1.0	Octahedral and tetrahedral voids in titanium and zirconium.	8
1.2.0	Partial titanium-nitrogen constitutional diagram.	16
1.2.1	Detail portion of the titanium-nitrogen constitutional diagram.	16
1.3.0	Partial zirconium-nitrogen constitutional diagram.	17
1.3.1	Detail portion of the zirconium-nitrogen constitutional diagram.	17
1.4.0	Isothermal section at 1000°C in the Ti-N-O system.	18
1.4.1	Isothermal section at 14000°C in the Ti-N-O system.	18
1.5.0	Partial titanium-oxygen constitutional diagram.	22
1.5.1	Detail portion of the titanium-oxygen constitutional diagram.	22
1.5.2	Alpha transus determined in commercially pure titanium-oxygen alloys.	22
1.6.0	Partial zirconium-oxygen constitutional diagram.	23
1.6.1	Detail portion of the zirconium-oxygen constitutional diagram	23
1.7.0	Partial zirconium-hydrogen equilibrium diagram.	27
1.8.0	Partial titanium-hydrogen equilibrium diagram.	28

Figure		Page
2.1.0	Mechanical properties of titanium-oxygen alloys, annealed at 850°C.	43
2.2.0	Mechanical properties of titanium-nitrogen alloys, annealed at 850°C.	43
2.3.0	Relationship between vickers hardness and composition by atomic per cent of annealed, high purity, binary, titanium-base alloys, containing N, O, C, and Fe.	43
2.4.0	Effect of oxygen on hardness of iodide zirconium.	48
2.4.1	Effect of oxygen on 0.2% yield strength of iodide zirconium.	48
2.4.2	Effects of oxygen on ultimate tensile strength and elongation of rectangular test specimens of iodide zirconium.	48
3.1.0	Schematic illustrations of fracture viewed at different scales.	59
3.2.0	Normal forces acting on a two-dimensional atomic array.	63
3.3.0	Shear forces acting on a two-dimensional atomic array.	64
3.4.0	Cleavage and shear fracture in polycrystalline metals.	66
4.1.0	Ludwik's triaxial tension theory of brittle fracture.	72
4.2.0	Schematic representation of four possible intersections of flow stress curve with cleavage and shear fracture curves.	74
4.3.0	The periodic lattice potential, and the equivalent value of the shear stress, accompanying the shear of a perfect lattice.	78
4.4.0	Schematic representation of the Griffith problem.	83
4.5.1	Brittle fracture mechanism.	90

Figure		Page
4.5.2	Ductile fracture mechanism.	90
5.1.0	The basic modes of crack surface displacements.	95
5.2.0	Stress required to displace an atom from its neighbor.	98
5.3.0	Fracture under fixed grip conditions. . . .	102
5.4.0	Diagrammatic representation of energy changes involved in crack propagation. . . .	106
5.5.0	A two-dimensional representation of a crack in a plate and the coordinate system. . . .	108
5.6.1	Crack open condition.	111
5.6.2	Crack partially closed condition.	111
5.7.0	Loaded arbitrary section containing a crack.	112
5.8.0	Dependence of G_C on thickness and fracture appearance..	116
5.9.0	Transverse contraction that occur near the tip of a notch in a thick plate.	120
5.10.1	Direction of plane-stress and plane-strain modes of crack propagation in a plate or sheet.	121
5.10.2	Characterization of fracture appearance by percentage of specimen thickness occupied by shear borders (per cent shear).	121
5.11.0	Effective crack length increase due to plastic zone.	123
6.1.0	Typical compliance curves for various metals.	128
7.1.0	Schematic representation of a load-deflection curve obtained by slow three point bending.	145
7.2.0	Typical load-deflection curve shapes for materials ranging from completely brittle to completely ductile.	145

Figure		Page
8.1.0	Sketch of the gas purification train. . . .	163
8.2.0	Sketch of glass specimen-fixture and dome. .	166
8.3.0	Overall picture of heat treatment facility..	169
8.4.0	Dimensional proportions of a single-edge-notch tension specimen.	174
8.5.0	Charpy test bar dimensions.	174
8.6.0	Rectangular tension test specimen dimensions.	174
8.7.0	Specimens machined from single-edge-notch tension bar.	176
8.8(a)	Overall picture of tension fracture test. .	180
8.8(b)	Close-up picture of tension fracture specimen in the loading fixture.	180
8.9.0	Steps to determine the energy of fracture. .	184
8.10.0	Block diagram of dynamic fracture system. .	185
8.11(a)	Overall view of instrumented-impact system..	187
8.11(b)	Close up picture of photo-trigger and hammer.	187
8.12.0	Computer analysis of 1.0 volt calibration pulse.	188
8.13.0	Impact trigger circuit.	192
9.1.0	Single-edge-notch tension specimen crack openings of commercially pure titanium grades (RMI) for various nitrogen treatments.	197
9.2.0	Fracture surfaces of commercially pure titanium (RMI series) for various conditions.	198
9.3.0	Fracture surfaces of reactor grade zirconium for various conditions.	200

Figure		Page
9.4.0	Charpy bar lateral expansions of several commercially pure titanium grades (RMI) after treatment in nitrogen at 1850°F. . . .	204
9.5.0	Total impact fracture energy of various commercially pure titanium grades (RMI) treated in nitrogen at 1850°F.	206
9.6.0	Charpy fracture energies of oxygen and nitrogen treated pure titanium.	207
9.7.0	Oscilloscope load vs. time traces of RMI-50 nitrogen treated at 1850°F for various times.	212
9.8.0	Changes in the α-phase morphology of WCA treated in nitrogen at 2000°F for various times.	217
9.9.0	Oscilloscope load-time traces of WCA nitrogen treated at 2000°F for various times.	217
9.10.0	Oscilloscope load vs. time traces of hydrogenated HP-BM titanium.	231
9.11.0	Photomicrographs of HP-BM titanium treated with hydrogen.	233
9.12.0	Charpy fracture surfaces of hydrogenated HP-BM titanium.	235
9.13.0	SEM fracture morphology pictures of hydrogenated HP-BM titanium	235
9.14.0	Oscilloscope load vs. time traces of hydrogenated TPC titanium.	239
9.15.0	Charpy fracture surfaces of hydrogenated TPC titanium.	239
9.16.0	SEM fracture morphology pictures of hydrogenated TPC titanium.	241
9.17.0	Photomicrographs of commercially pure titanium (TPC) treated with hydrogen.	245
9.18.0	SEM pictures of some commercially pure titanium (RMI-30 and 70) before and after the transition.	251

Figure		Page
9.19.0	SEM pictures of reactor grade zirconium (WCA) before and after the transition. . . .	253
A.1	Region R containing a straight line crack. .	266

CHAPTER I

INTERSTITIALS IN α-TITANIUM AND α-ZIRCONIUM

1.1.0 General Background

Titanium can hardly be considered rare, since it is the ninth most abundant element, and the fourth most abundant metal in the earth's crust, after aluminum, iron and magnesium.

Discovered by William Gregor in 1791, in the form of its oxide at Menaccan, Cornwall, England, he called the substance "Menaccanite." The German chemist, Klaproth, gave the metal its name "titanium" in 1795 when he also discovered it by its oxide in a sample of ilminite.[1,2]

Zirconium, like titanium, was at an earlier time considered in the class of the rare elements. It is plentiful, in fact more so than nickel, copper, lead, zinc and some other familiar metals.[3] J. Berzelius, a Swedish chemist, attempted to produce zirconium metal as early as 1824, from the reduction of potassium zirconium fluoride with sodium.[4]

Since titanium and zirconium are neither new nor rare, one may wonder why it has taken so long for these metals to become useful engineering materials.

The answer lies in the ease with which both react to the interstitial elements: oxygen, nitrogen, hydrogen and carbon. It is this reactivity that completely governs the processing (extraction, melting and fabrication), and which ultimately affects the mechanical properties of the mill product. These problems have only been worked out recently for large scale production, and the materials are now becoming competitive on a cost basis.

1.2.1 Titanium

Titanium's rapid acceptance in the aircraft and areospace industries is not surprising considering that weight savings as high as 60% in aircraft have been reported by the simple substitution of titanium on an equivalent basis with steel.[5]

Many metals retain their structural strengths to about 1/2 their melting temperature on an absolute scale. Aluminum, attractive to aircraft designers because of its low density (ρ = 2.7g/cm^3), is limited to about 200°C with this "rule of thumb." Nickel and its alloys provide good hot strength to about 550°C but have a high density ($\rho \approx$ 8g/cm^3). Titanium was expected to fill the need for an intermediate material with its low density (ρ = 4.5g/cm^3) and high melting temperature (1800°C). It has fulfilled the gap at lower operating temperatures, but not in the range of 600-700°C.[6] Its high reactivity with interstitials

in the temperature range renders the metal brittle and notch sensitive. Alloying has had limited success in helping to inhibit this effect.

Although not having fully lived up to the expectations of the early 1950's, titanium has emerged as an important engineering structural material. This is reflected in the fact that titanium consumption for structural purposes increases year after year. This material has been and continues to be important in the space program. Significant amounts were used in the construction of the Atlas and Titan rockets, and in various structural components of the space crafts of the Mercury and Gemini projects.[7,8]

Titanium is already finding its way into consumer products since it is used in racing cars in all the great racing circuits in the world.[9] Auto designers are trying to capitalize on the high strength-to-weight ratio and/or low elastic modulus compared to steel. Besides the transportation industry, (automotive, marine and aircraft), the huge chemical industry, (process, desalination,[11] etc.) is also starting to use titanium structurally. Titanium is even being used as a surgical implant material. The patient experiences greater comfort due to weight saving, resulting in reduced patient consciousness of the implant.[12]

It would serve little purpose to continue this list of applications since excellent reviews[13,14] on the

subject exist. Considering only this very appended list, one cannot fail to realize titanium's potential as a prime structural material in the not-to-distant future.

1.2.2 Zirconium

Zirconium, like titanium, had interested the United States Air Force as a possible high temperature material. This interest was lost when scientists realized how easily the metal oxidized in air above 500°C. New interest was generated by the government in 1947 for use in the reactors of atomic powered submarines. A thermal reactor's efficiency depends upon the use of neutrons to create more fissionable material, which can be defined as a material, that upon the absorption of neutrons, splits in two, with the liberation of more neutrons. The structural elements of the reactor contribute heavily to the parasitic loss of neutrons. Parasitically absorbed neutrons cause radioactive isotopes and transmuted elements to form within the structural material. These reaction products can cause difficulty in shielding, handling and repair problems.[7,15] A material's ability to absorb particles is given by the absorption cross section, σ_a, with units of $10^{-24}cm^2$ (barn) per nucleus. The desired material properties are structural strength; good hot strength to moderately high temperatures, due to heat released in the reaction; low absorption cross section;

and good corrosion resistance. Reactor grade zirconium best meets these specifications.

Zirconium is slowly finding its way into other applications, mostly where structural strength must be coupled with corrosion resistance. This protection is derived from oxide and monohydride films.[16] Zirconium is used in surgery for implants and also the chemical processing industry.[17] Zirconium has, as yet, not enjoyed the diversity in application that titanium has, but this seems to be due to cost.

1.3.0 History of Brittleness Problems Due to Interstitials

Berzelius is believed to have been the first to prepare metallic titanium by the reduction of potassium fluotitanate with potassium metal. In 1876, Kern reduced titanium tetrachloride vapors with liquid sodium. The metal was highly contaminated with oxygen, which rendered it brittle. At a latter date Nelson and Petersson tried to eliminate the interstitials by carrying out the reaction in an air tight steel bomb. Their product was only 95% pure.[1] At the beginning of the 20th century Hunter claimed that he produced pure titanium by the reduction of pure titanium chloride with sodium metal.[18] All these experiments were laboratory scale chemistry experiments, reducing certain compounds in an effort to

obtain ductile (interstitial free) titanium. The first attempt at winning the metal from its ore on a commercial scale wasn't made until 1938. The product, however, was not very ductile.

Similiar type problems were encountered in attempting to produce ductile zirconium. A malleable product was not possible until 1914, when Lely and Hamburger reacted zirconium tetrachloride with sodium in a sealed pressure bomb. Due to technical difficulties, they never developed this into a commercial process.[19]

By recognizing the importance of eliminating all the air in the reaction vessel, Kroll,[20,21] in 1940, developed a method to make ductile titanium. An argon atmosphere was maintained throughout the reaction of titanium tetrachloride with magnesium.

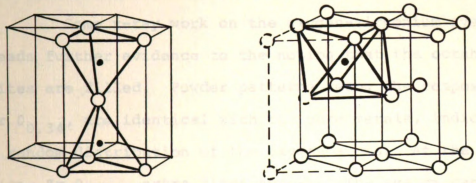
Due to the experience gained from the titanium experiments, Kroll[22,23] reasoned correctly that the complete absence of oxygen, nitrogen and hydrogen during the reduction to zirconium would render it ductile. The process was also similar to the one used for titanium.

Therefore, after their ores were first discovered, the problem of brittleness in titanium and zirconium caused by dissolved interstitials was primarily responsible for about a century's delay of their emergence on the market as engineering materials. Now that the metals are available in the ductile condition, problems do not cease to

exist because the process is reversible. Under the correct conditions these metals will again redissolve interstitials, that is, undergo oxidation to lower the system free energy. Upon doing so, the metal once again becomes brittle. To ensure the proper engineering application of these metals, the conditions under which oxidation will take place must be well understood. The position that the various interstitials take within the metal's lattice helps to explain the degree of solubility, and the effect that each has in rendering the metal brittle. Temperature is known to be important, so binary phase equilibrium and kinetic studies aid in determining the time-temperature solubility relationships. With a knowledge of such relationships, this study seeks to determine the propensity to catastrophic failure due to embrittlement as a function of interstitial content.

1.4.0 Position and Distribution of Interstitials in Titanium and Zirconium

The octahedral and tetrahedral voids or holes in the hexagonal close-packed structure are shown in Figure 1.1.0. Octahedral holes will just contain a sphere of radius 0.41r, and tetrahedral holes a sphere of radius 0.225r in both close-packed atomic arrangements (e.g. HCP and FCC), where r is the radius of the spherical atoms of the close-packed structure.[24]



O Ti or Zr lattice points
• tetrahedral hole position

O Ti or Zr lattice points
• octahedral hole position

Figure 1.1.0--Octahedral & tetrahedral voids in HCP titanium and zirconium. (After Hume-Rothery & Raynor, and used with permission of the publisher.).[24]

Calculations made on pure α-titanium (a = 2.88Å, c/a = 1.58Å), show that the octahedral hole size is 1.24Å, while the tetrahedral holes only 0.68Å. An oxygen atom, with an atomic diameter of 1.32Å, must therefore occupy the octahedral hole.[25] Ehrlich (1941) had made the same suggestion based on solubility limits and lattice parameter changes of oxygen in α-titanium.[26] Size differences led deBoer and Fast[27] to consider that oxygen atoms occupy the octahedral intersticies in zirconium. Although highly suspected, no direct experimental proof exists demonstrating that oxygen and nitrogen occupy the octahedral rather than tetrahedral sites in either titanium or zirconium.

Because the lattice distortions are the same in either case, lattice parameter measurements offer no assistance in determining which is preferred.[28]

Some x-ray work on the oxygen-zirconium system leads further evidence to the notion that the octahedral sites are filled. Powder patterns below the composition, $Zr\ O_{0.34}$, are identical with the pure metals, indicating a random distribution of the oxygen atoms. At the composition, $Zr\ O_{0.35}$, extra lines appear. The system can be indexed hexagonally with a unit cell about three times the size of the parent metal. The metal atoms have the same packing as the pure metal. The oxygen atoms occupy the octahedral positions to form a completely ordered solid zolution, Zr_3O. Beyond the $Zr\ O_{0.35}$ composition to the solid solubility limit ($Zr\ O_{0.40}$, 28.6 atomic percent oxygen), the patterns are analogous to Zr_3O. The excess oxygen atoms evidently start to distribute themselves randomly in the empty interstices. A partly ordered solid solution exists in the composition range.[29] Previously, all compositions of the zirconium rich terminal solid solution were thought to be completely random.[7] Nitrogen is also assumed to occupy octahedral holes.[30] It has been suggested that hydrogen, the smallest interstitial element, occupies the tetrahedral sites in alpha zirconium. These conclusions were drawn from neutron-diffraction studies on zirconium dihydrides.[31]

Considering that the octahedral interstice exceeds 1.00kX units in diameter for all close packed metals except for beryllium, whose octahedral diameter is 0.92kX units, no severe strains would occur by hydrogen's occupation of such sites. The atomic diameter of hydrogen is less than 1.05kX units. In the case of alpha titanium and zirconium the octahedral diameters are 1.2 and 1.3kX units respectively, while the tetrahedral diameters are about 0.66 and 0.72kX units respectively. Obviously considerable amounts of hydrogen could be held in the octahedral as opposed to the tetrahedral voids without creating internal stresses in the lattice. Even in the case of body-centered cubic metals, the hydrogen is held tetrahedrally only because of the severe distortion of the octahedral void. The b.c.c. metals can only accommodate solvent atoms having a radium of not more than 0.154 and 0.291 diameter of the solute in the octahedral and tetrahedral sites respectively. Hydrogen, in tetrahedral sites therefore causes local distortions of the lattice in b.c.c. metals. There is no good evidence at this time that indicates that hydrogen isn't held octahedrally as might be expected from size considerations. The failure mechanism due to hydrogen, to be explained later, also suggests that hydrogen is present in the octahedral voids in titanium and zirconium.[32]

1.5.0 Constitution of Titanium and Zirconium with Interstitials: Theoretical and General Considerations

Some atomic and crystallographic aspects must first be established to interrelate the strenghtening, morphology, and constitution of the systems under consideration. Hume-Rothery[24] postulated that if the solvent atom size differs by more than ± 15% of the solute atom, terminal solid solubility would be very limited. In addition to size factor, crystal structure, valency, and electronegativity factors may also restrict extended solubility. Extended substitutional solid solubility has been shown to exist for elements ± 20% in the case of titanium,[33] while the Hume-Rothery postulation holds (± 14 to 15%) for alpha zirconium. Interstitial solid solution alloying, the subject of this study, generally follows Hägg's rule. Simply stated, interstitial solid solutions can be expected if the ratio of the atomic diameters of the metalloid to the metal is less than 0.59.[34] This condition is met for hydrogen, oxygen, nitrogen and carbon in both titanium and zirconium.

Since both metals are group IV-A (Hubbard classification) elements, they possess the same $d^2 s^2$ outer free electron configuration. Titanium is situated in the first long period, while zirconium in the second. Having incomplete d-shells, both elements are classified as

transition metals. Pauli's exclusion principle dictates a maximum of 2 electrons per quantum level, each having opposite spins. The d-shell can contain a maximum of 10 electrons; thus 5 quantum levels or orbitals exist. The filling requirements of the orbits are that the first 5 electrons be unpaired. Only 1 electron is allowed in each orbit, until each of the 5 orbits contain an electron. These electrons all having the same spin, are considered parallel.

1.5.1 Effect of d-Electron Additions on α-β Transformation

The effect of alloying elements on the α-β transformation can be systematized on the basis of d-electron addition. As d-electrons are added to titanium, the beta or high temperature phase is stabilized, as manifested by the extension of this field, lowering of the β-transus, and usually giving rise to eutectic or eutectoid type of equilibrium. Those transition elements that possess more d-electrons than titanium are those that belong to groups V-A, VI-A, VII-A, VIII-A, B, C. Conversly, if elements of the I-A, II-A, III-A and B, IV-B, V-B, and III-B groups are added, there is a tendency to stabilize the alpha phase, raise the β-transus, and form peritectic or peritectoid reactions. Zirconium, because of its similar free electron configuration, as expected, generally is known

to follow similar alloying tendencies. Zirconium's interatomic distance is approximately 8% larger than titanium's in both the alpha and beta forms. Therefore, some elements too large for titanium will be favorable for zirconium, while elements too small for zirconium would not be for titanium. Recognizing the fact that zirconium's interatomic distance is rather large, it can be expected that more elements would be unfavorable for alloying with zirconium and titanium.

The well known characteristics of carbon in iron seem to be reversed regarding interstitials in zirconium and titanium. In iron, the gamma modification has larger interstices than alpha iron. Carbon is rejected, which if not given time to take place, causes a hardening due to an internally strained system; and a eutectoid reaction which is susceptible to heat treatment. The situation is reversed in titanium and zirconium, the beta modification has smaller interstices than the low temperature alpha phase. An interstitial solution is favored by the HCP phase and results in a peritectoid reaction at elevated temperatures. Oxygen and nitrogen raise the allotropic transformation temperature in titanium and zirconium, but lowers it in iron.[35] The electron density concept discussed in terms of substitutional alloying also seems to hold true for interstitials. The alpha phase dissolves elements of favorable size which decrease or do not

appreciably alter the electron density. Considering only the gaseous interstitials: hydrogen increases the electron density, thus is a beta stabilizer, while nitrogen and oxygen decrease the electron density and hence stabilize the alpha phase.[36]

1.6.0 Constitution of Titanium and Zirconium with Interstitials-Diagrams and Features

The general characteristic features of the individual binary systems and the reaction kinetics help in the understanding of how and why these two metals are so strongly affected by minute amounts of the dissolved reaction products.

1.6.1 Solubility Relationships of Titanium and Zirconium with Nitrogen

As predicted by theory, nitrogen is a stabilizer of alpha-titanium and zirconium as can be seen in Figures 1.2.0 and 1.3.0. In both cases the alpha phase can dissolve more nitrogen than beta. The partial Ti-N, and Zr-N diagrams taken from Hansen[37] are based primarily on the metallographic, incipient melting and x-ray work of A. E. Paltry *et al.*,[38] and R. F. Domagala *et al.*[39] respectively. The important feature of the binary Ti-N diagram is the peritectic alpha formation from the melt (5.1 a.-%N) and the delta phase at 4260°F. The maximum solubility in

alpha is between 6.5 and 7.4 wt.-%N as seen in Figure 1.2.0. The Zr-N diagram (Figure 1.3.0) shows that nitrogen stabilizes its alpha modification too. Similar features can be noted most important of which is peritectic alpha formation from the melt (13.5 a.-%N) and ZrN-solid solution (46 a.-%N) at about 1985°C.

Careful studies have been made of the boundaries of interest in the present study, that is, only up to about 3.0 wt.-%N in both titanium[38] and zirconium.[39] See Figures 1.2.1 and 1.3.1 respectively.

Paltry et al.[38] suggested that the quantity of nitrogen absorbed by the beta phase at any temperature appears to be less for sponge as opposed to iodide titanium. They speculated that this is probably due to the nitrogen impurity already present in the sponge and that the physical form of the metal doesn't alter solubility. The alpha transus for sponge occurs at lower temperatures than iodide titanium with equivalent nitrogen contents apparently because of beta stabilizing impurities in the sponge. Iron is one of the chief beta stabilizing impurities and is present in commercially pure titanium also. These boundary differences are indicated in Figure 1.2.1. There is also the possibility that the shift is due to oxygen present in the sponge. Stone and Margolin[40] investigated the titanium rich corner of the Ti-O-N system. Two isothermal sections at 1000°C and 1400°C (Figure 1.4.0 and 1.4.1) indicate

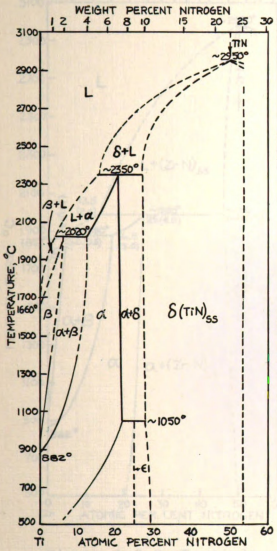


Figure 1.2.0--Partial titanium-nitrogen constitutional diagram (From Constitution of Binary Alloys by Hansen, copyright 1958. Used with permission of McGraw-Hill Book Co.).[37]

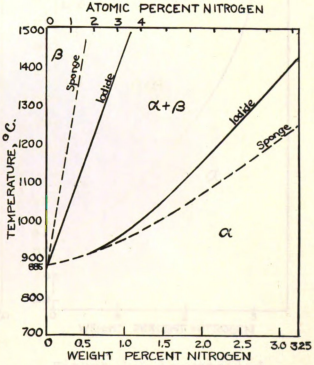


Figure 1.2.1--Detailed portion of the titanium-nitrogen constitutional diagram (After Paltry, et al. used with permission of the publisher).[38]

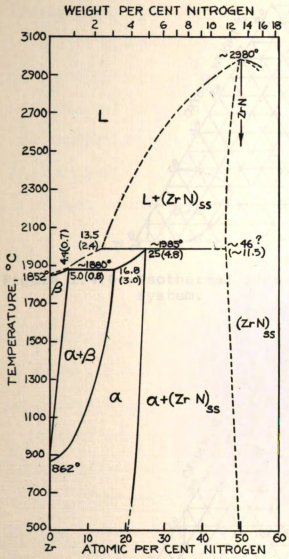


Figure 1.3.0--Partial zirconium-nitrogen constitutional diagram (From Constitution of Binary Alloys by Hansen, copyright 1958. Used with permission of McGraw-Hill Book Co.).[37]

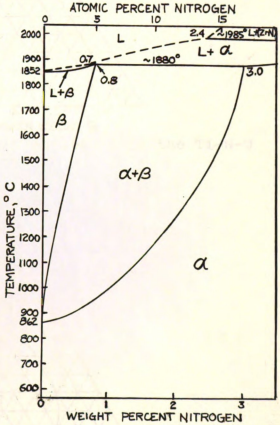


Figure 1.3.1--Detailed portion of the zirconium-nitrogen constitutional diagram (After Domagala et al., used with permission of the publisher).[39]

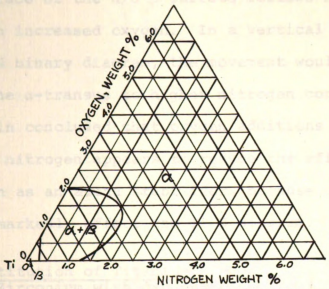


Figure 1.4.0--Isothermal section at 1000°C in the Ti-N-O system.

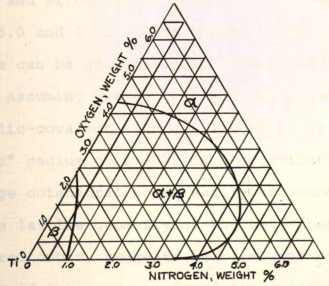


Figure 1.4.1--Isothermal section at 1400°C in the Ti-N-O system. (After Stone and Margolin, used with permission of the publisher).[40]

that the trace of the α/α-β surface follows higher nitrogen levels with increased oxygen. In a vertical section parallel to the Ti-N binary diagram, the movement would appear as a shift of the α-transus to higher nitrogen contents. Stone and Margolin concluded that oxygen additions to titanium containing nitrogen appears to reduce the effectiveness of nitrogen as an alpha stabilizer, because small amounts of oxygen markedly affect the Ti-N diagram.

1.6.2 Constitution of Titanium and Zirconium with Oxygen

Oxygen shows the same extensive solubility for both α-titanium and zirconium as noted for nitrogen as seen in Figures 1.5.0 and 1.6.0. The higher oxygen solubility in both metals can be qualitatively understood by considering titanium. Assuming octrahedral accommodation, the bond is of a metallic-covalent nature. If oxygen is designated by a "metallic" radius of 0.80Å for a coordination number of 6, the large octahedral holes easily accommodate the oxygen atoms. The lattice geometry of the beta phase, being body centered cubic, suggests that serious distortions would occur if the oxygen entered its interstices. Greatly reduced solubility in the beta would be expected, as compared to the alpha modification as is actually observed. This stabilization also results in raising the α-β transformation range.[31]

The Ti-O and Zr-O partial equilibrium diagrams, also taken from Hansen,[37] are due to the work of Bumps et al.[42] and Domagala et al.[43] respectively. Later work on the Zr-O system using reactor grade zirconium with tight control on the reaction with oxygen (isothermally and isobarically loaded), confirmed the shape of the diagram is Figure 1.6.0, but reported a 2 to 4 weight percent increase in the solubility of oxygen in both the alpha and beta phases.[44] A slight shift of the fields to the right in the diagram results.

There are 2 striking differences between these diagrams as compared to the corresponding ones with nitrogen. The alpha solid solution is not formed directly from a peritectic type reaction, but does participate in such reactions. In the Ti-O system,

$$\text{Melt} + \alpha \overset{\substack{1740^\circ C \\ 6a.-\%O}}{\rightleftarrows} \beta \text{ and,}$$

$$\text{Melt} + \alpha \overset{\substack{1770^\circ C \\ 44a.-\%O}}{\rightleftarrows} (TiO)_{SS} \text{ while in the Zr-O system,}$$

$$\text{Melt} + \alpha \overset{\substack{1940^\circ C \\ 10.4a.-\%O}}{\rightleftarrows} \beta.$$

Alpha can, however, form directly in the Zr-O system by a eutectic reaction,

$$\text{Melt} \overset{1900^{\circ}C,\ 41a.-\%O}{\rightleftarrows} \alpha + (ZrO_2)_{SS} \ .$$

The remaining difference is that the alpha phase in the Ti-O and Zr-O systems have open melting points as can be observed in Figure 1.5.0 (1900°C, 25a.-%O.) and Figure 1.6.0 (1995°C, 25a.-%O.) respectively. Greater detail of the phases directly concerned in this study is given in Figures 1.5.1 and 1.6.1.

Commercially pure titanium differs from pure titanium with regard to the alpha and beta transus. The all important alpha transus appears shifted down at least 50°C at any given oxygen content tested by Jenkins and Worner,[41] as seen in Figure 1.5.2. This is important in that commercially the metal rarely is used in the chemically pure form.

1.6.3 Constitution of Titanium and Zirconium with Hydrogen

The hydrogen systems (Figures 1.7.0 and 1.8.0) are included to show the role that hydrogen plays as a beta stabilizer if inadvertently absorbed. The Ti-H diagram, taken from Hansen,[37] is due to the work of A. D. McQuillan.[45] Hydrogen absorption is reversible in both zirconium and titanium; thus the normal usefulness of x-ray, metallographic, and incipient melting techniques is destroyed. The equilibrium relationships of temperature, pressure,

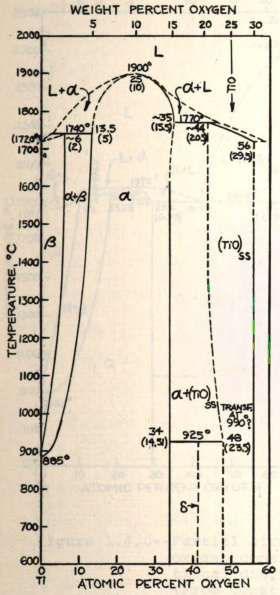


Figure 1.5.0--Partial titanium-oxygen constitutional diagram. (From Constitution of Binary Alloys by Hansen, copyright 1958. Used with permission of McGraw-Hill Book Co.).[37]

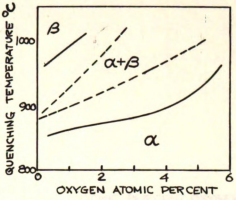


Figure 1.5.2--Alpha transus determined for commercially pure titanium-oxygen alloys. (The broken-line boundaries refer to pure titanium alloys.) (After Jenkins and Warner, used with permission of the publisher.).[41]

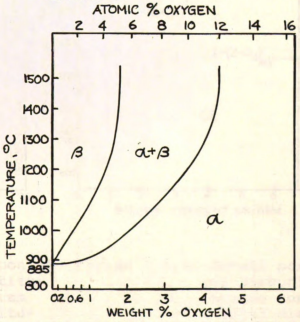
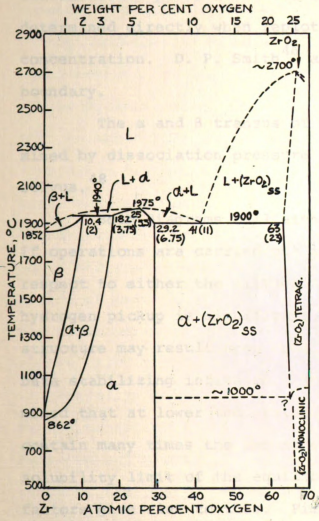


Figure 1.5.1--Detail portion of the titanium-oxygen constitutional diagram. (After Bumps et al., used with permission of the publisher).[42]



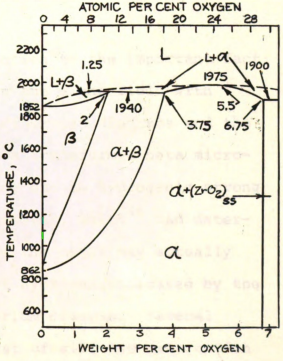


Figure 1.6.0--Partial zirconium-oxygen constitutional diagram (From Constitution of Binary Alloys by Hansen, copyright 1958. Used with permission of McGraw-Hill Book Co.).[37]

Figure 1.6.1--Detail portion of zirconium-oxygen constitutional diagram (After Domagala & McPherson, used with permission of the publisher).[4]

and concentration can be used. Discontinuities in pressure-concentration plots allow the alpha and beta transus to be determined directly when replotted as temperature versus concentration. D. P. Smith[46] added the $\alpha/L + \gamma$ (solvus) boundary.

The α and β transus of the Zr-H system were determined by dissociation pressure techniques[47] as was the solvus.[48]

Both diagrams call attention to the important fact: if operations are carried out in the alpha field with respect to either the nitrogen or oxygen diagrams and the hydrogen pickup is significant, a transformed beta microstructure may result upon cooling due to hydrogen's strong beta stabilizing influence. Moreover, Smith[46] had determined that at lower temperatures the metal may actually contain many times the amount of hydrogen indicated by the solubility limit of the equilibrium diagram. Several factors give rise to this. First of all, the distinction between endothermic and exothermic occluders must be made. An endothermic occluder forms a true solid solution with the gas, and the solubility varies as the square root of the pressure (Sievert's Law). Iron is typical of such an occluder. Titanium and zirconium are exothermic occluders, however, and also form true solid solutions with the initial additions of hydrogen. The difference between the 2 occluders lies in the fact that exothermic occluders

also form hydrides exothermally. Thus one must distinguish between the solubility of hydrogen, which is that content of gas in the metal just before hydride formation starts, and the total amount of hydrogen present. The total content can be increased beyond the solubility limit simply by increasing the hydride formation. The total content in exothermic occluders depends only upon the kinetics of hydride formation. Moreover, the occlusive capacity is based upon a compact metal in equilibrium at a specific temperature and pressure but also differs from equilibrium phase diagram solubility in that it is a function of the degree of prior plastic deformation. Smith has suggested the presence of "gaseous" hydrogen present in rifts and voids, which are repaired during recrystallization. It is generally felt that such hydrogen is present within micro-porosities which are a feature of all metals. Hydrogen solubility in both titanium and zirconium depends on the purity of the metal. For example, the solubility of hydrogen in high purity alpha titanium has a range of about 8a.-% at 325°C to about 0.1a-% at 125°C. There is a large increase of solubility in beta titanium (44a.-% at 325°C, the eutectoid). Commercially pure titanium has been found to dissolve 5.4 to 6.5a.-% hydrogen at 400°C. High purity alpha zirconium's hydrogen terminal solubility falls from a value of 2.8a.-% at 400°C to about 0.9a.-% at room temperature. The commercially

pure metals must be considered multi-component systems. If the solubility of hydrogen in either titanium or zirconium isn't too great, the precipitation of the hydride phase can be prevented, but may precipitate upon room temperature aging depending on the content. There is a critical hydrogen content above which precipitation cannot be suppressed. It also follows that as the hydrogen content is increased, the temperature at which precipitation occurs on slow cooling will be raised. Segregation of beta stabilizers in the commercial purity metals can stabilize the beta phase at sub-eutectoid temperatures. The absence of a hydride phase in some instances, even when the hydrogen content is above the solubility limit for pure alpha-titanium, has caused some concern.[32] Rylski[49] has suggested that the partition function for hydrogen in alpha and beta titanium is such that nearly all the hydrogen is in solution in the retained beta phase. Nitrides and oxides, or at least in the case of zirconium, have a profound effect on reducing the hydrogen absorption into the metal. This protection is lost when the temperature is raised and the films are dissolved into the metal.[50] The early workers failing to realize this, reported hydrogen absorption starting above 500°C.[51] If the surfaces are clean of contamination, the absorption is known to be rapid at 300 to 400°C and measurable at room temperature.

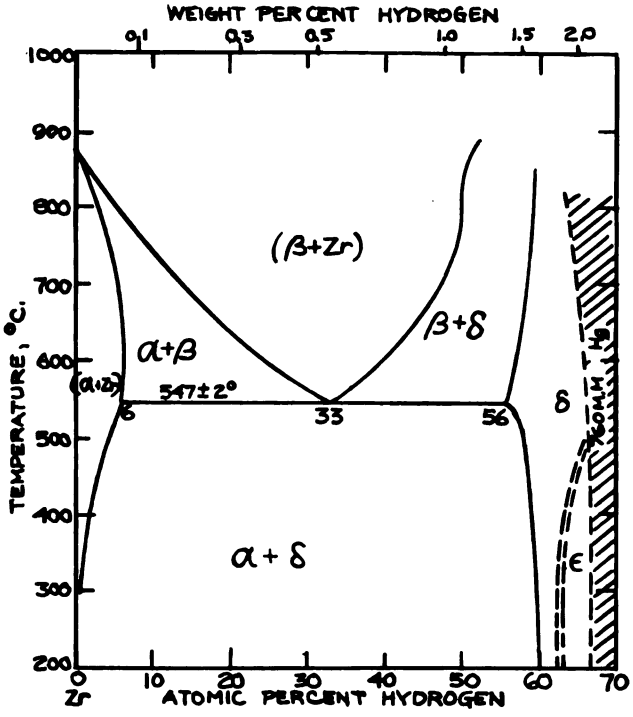


Figure 1.7.0--Partial zirconium-hydrogen equilibrium diagram (From Constitution of Binary Alloys, First Supplement by Elliott, copyright 1965. Used with permission of McGraw-Hill Book Co.).[52]

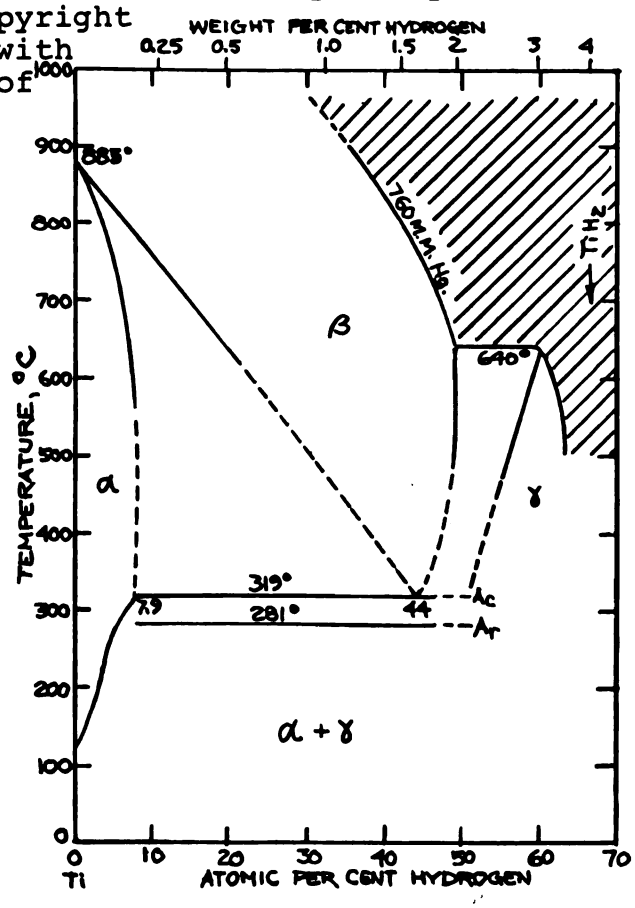


Figure 1.8.0--Partial titanium-hydrogen equilibrium diagram (From Constitution of Binary Alloys by Hansen, copyright 1958. Used with permission of McGraw-Hill Book Co.).[37]

1.7.0 Reaction Kinetics of Interstitial Gases with Titanium and Zirconium

In certain instances the metalloid atoms can diffuse into the solvent metal without displacing the atoms of the latter from their mean lattice positions. The gases hydrogen, oxygen and nitrogen display this type of diffusion due to their size relative to the metal. The gas-metal reaction can be stated in three distinct steps:

1) The condensation of the gas on the metal surface to a thickness of one or two molecules, which is called the process of adsorption.

2) The "gas" may enter the interior of the metal, but only upon prior dissociation. The heat of absorption is sufficient to dissociate the molecules into atoms. The interior movement is called absorption or occlusion.

3) The diffusion of the solute atoms into the interior of the metal.

The kinetics of the gas-metal reaction will depend upon which of the steps is the least rapid. The term sorption is used to describe the dual existence of a gas present in both the adsorbed and absorbed states. It should be pointed out that physical adsorption, resulting in weak bonding between the gas and metal, does not insure that diffusion will necessarily follow. Penetration into the metal is thought to occur from a series of unstable

gas-metal pairs, whereby the gas is transferred from one metal atom to the next in the lattice. The rate of diffusion is expected to increase for a given metalloid as the size of the metal atom increases.[53] This rate has been found to be most appreciable in those metals in which the solubility of the diffusing gas is the greatest.[54] A complete study of the reaction kinetics of both metals with the interstitial gases was done by Gulbransen and Andrew.[55,56]

1.7.1 Metals Reaction with Oxygen

Since at least 5 oxides (TiO, Ti_2O_3, TiO_2, Ti_3O_2 and Ti_4O_3) have been identified, it can be appreciated that the reaction system between the gas and the scale-metal interface is complex. The slowest reaction among the various scale layer interactions and the diffusion rate of oxygen in the metal itself, will be the rate controlling mechanism. This mechanism at steady state conditions is probably different at various temperatures or reaction gas pressures.[57] Jenkins[58] deduced from his x-ray diffraction studies of oxygen content at various locations from the surface to the core, that the rate of oxygen diffusion into the scale is greater than into the metal. Scale build up does not seem to impede the process of titanium oxygenation as might have been hoped.

Zirconium's affinity for oxygen is so strong that the oxygenated metal cannot be reduced with hydrogen, or

carbon monoxide at even extremely high temperatures. The dissolved oxygen will not evolve at temperatures approaching the melting point.[59] Electric field experiments demonstrated that oxygen moves through the metal as a negative ion.[60]

1.7.2 Metals Reaction with Nitrogen

The absorption of nitrogen by titanium is similar to but much less rapid than oxygen.[61] The rate at which nitrogen diffuses through an outer TiN layer is the rate controlling factor for long term reactions. The nitrogen reaction with zirconium is practically insensitive to pressure, so the rate controlling mechanism is the diffusion of nitrogen into the metal.[59]

1.7.3 Metals Reaction with Air

A fundamental knowledge of crack propensity with respect to the interstitials, nitrogen and oxygen, in titanium and zirconium has general application to atmospheric uses of these metals. Understanding the role that air's major constituents individually play in the embrittlement of these materials is a useful step to help discern the more complicated case. It is, after all, an air atmosphere at elevated temperatures that is of practical importance from an engineering point of view.

Realizing that about four-fifths of the normal atmosphere is nitrogen, there is good reason to expect the

Zr-N reaction to be predominant. Nitrogen plays only a minor role in the scaling (and core embrittlement) of titanium heated in air. Nitrogen has a much slower diffusion rate in the metal and its nitride than does oxygen.[62]

The statements made earlier with respect to oxygen generally pertain to air. This is at least true concerning kinetic phenomena which depended on rate of diffusion of oxygen in the metal.

Hayes and Roberson[63] investigated the reaction rates of zirconium with oxygen, nitrogen, and air at various temperatures. Their information along with Phalnikar and Baldwin's[64] data on zirconium scaling studies, shows that between 400 to 1200°C, the rate of reaction of the metal in air is greater than for either pure oxygen or nitrogen. This is explained by assuming that nitrogen dissolves in ZrO_2; since nitrogen is quadrivalent, defects would be created in the oxygen-ion lattice. A higher rate of nitrogen diffusion through the ZrO_2 layer is possible,[65] compared to oxygen alone reacting with the metal. In this case again it is oxygen which is shown to predominate in the air reaction.

CHAPTER II

THE EFFECT OF INTERSTITIALS ON THE MECHANICAL PROPERTIES OF TITANIUM AND ZIRCONIUM

2.1.0 Strengthening Theories of Interstitial Oxygen and Nitrogen in Titanium and Zirconium

The strenghtening effect due solely to solid solution hardening is very pronounced for even small concentrations of either oxygen or nitrogen in solid solution with α-titanium or zirconium. This fact and the lack of interaction between solute atoms make these systems ideal for solid solution hardening studies, and those areas directly related to this phenomena. Feng et al.[1] explained that the increase in strength properties due to oxygen additions to α-titanium occurred from dislocation-solute interactions. Dislocation movement is more difficult to initiate, as the interstitial content increases.[1] Tyson's[2] (1968) initial calculations of the strain fields generated by such interactions indicated that their magnitude was not sufficient to account for the observed strengthening effect. The strengthening was attributed to the obstruction

of atomic motions within the core of a gliding dislocation or to the breaking of bonds between the solute atoms and their neighbors. A recalculation of the elastic interaction energy using anisotropic elasticity suggests that the breaking of chemical bonds in the dislocation core may be a significant source of strengthening in Ti-O alloys.[3] The cohesive energies of some Zr-O alloys have been found to be very large.[4] It seems reasonable to assume that the Ti-O system might respond in an analogous way. Churchman[5] proposed that the oxygen filled interstitial sites obstructed slip on 2 of the possible slip planes in titanium. Interference with the smooth reaction of the atoms at the dislocation core was also given as the reason for solid solution strengthening by Mills and Craig[6] in the Zr-O system. The glide dislocations bypass oxygen atoms in the lattice, either by expansion of the dislocation core, or by the movement of oxygen atoms temporarily from their lattice sites. Arguments along similar lines have been presented to explain the strengthening of nitrogen in zirconium.[7] Conrad[8,9] summarized the work of many previous investigators on the effects of temperature and purity on yield and flow stress of α-titanium. His and their findings indicate that there is an increasing effect of interstitial impurity content on the thermal component of the yield and flow stresses, with a decrease in the temperature from 600 to 0°K in both single and

polycrystalline titanium. Above 600°K, the observed yield stress appeared independent of purity. Furthermore, for the same purity level, the thermal dependence of T* (thermal component of the yield stress at absolute zero), was found to be identical for polycrystalline specimens and for $\{10\bar{1}0\}\langle 11\bar{2}0\rangle$ in single crystals. The rate controlling mechanism for polycrystalline titanium is therefore deduced to be that which controls the dislocation velocity on the first order prism plane, the overcoming of interstitial solute atoms due to assymetrical distortions (Fleischer model).[10] Zirconium probably exhibits similar deformation dynamics.

2.2.0 Effect of Interstitials on Cleavage Fracture and Plastic Deformation to Alpha Titanium and Zirconium

2.2.1.0 Cleavage and the Effect of Interstitials

There are no unique cleavage planes associated with a particular Bravais lattice; FCC metals tend not to cleave at all, while BCC often cleave on {100} or {110} planes. Moreover, cleavage doesn't necessarily occur on the planes of highest packing density (eg. {110} in BCC and {0001} in HCP systems). HCP metals have been reported to cleave on $\{0001\}$, $\{10\bar{1}1\}$, $\{10\bar{1}2\}$, and $\{10\bar{1}0\}$ planes.[11]

Often several factors must be considered simultaneously concerning the brittle nature of metals. Under certain circumstances the metal will deform plastically and under others it will cleave. For example, both the interstitial oxygen content and the temperature were found to influence the type of failure observed in zirconium impact bars. At low interstitial levels twinning accompanies fracture, which decreases with increasing temperature as slip becomes more predominant. At high oxygen contents, fracture occurs by cleavage preceded by twinning. With increasing temperature, the plastic deformation mechanism is mostly twinning.[12] In the present case, brittle fracture occurs due to oxygen's effect on the resistance to deformation at low temperatures.

2.2.1.1 A Theory of Hydrogen Embrittlement in Titanium and Zirconium

The general concept of a ductile-to-brittle transition was originally described by Cottrell.[13] He assumed that thermal fluctuations and stresses aid dislocations to break away from barriers such as impurity atoms which immobilized them. Rapid yielding soon followed due to dislocation multiplication resulting from the initial break away dislocations. The yield strength increases with decreasing temperature due to a corresponding decrease in the thermal fluctuations thus requiring higher stresses to free dislocations from the impurity atoms. When the

temperature is sufficiently high (above the ductile-to-brittle transition temperature), ductile behavior is observed because the dislocations encounter little resistance when moving on the various activated slip planes. When the temperature decreases, higher stresses are required to break away the dislocations or to activate slip planes. There exists a critical temperature, the transition temperature, where the resistance to plastic deformation is so high that the localized stress concentration will exceed the cohesive strength of the metal rather than undergo plastic deformation, hence the brittle fracture.

Impurity atoms are not the only obstacles to dislocation movement. The dislocations can "pile-up" at grain boundaries or precipitates at the end of a slip plane. Such pile-ups will cause high local stress concentrations and ultimately become an embryo of a microcrack. Consider further, the effect of notches which create a triaxial stress-system within the neighboring material causing a severe local stress concentration at the base of the notch. Brittle fracture may again occur if the cohesive strength is exceeded before the various slip systems have been brought into operation.

Both titanium and zirconium are hydride formers, whose morphology is platelets and needles. The sharp edges of such precipitated particles are points of intensive internal stress-concentration capable of initiating

micro-cracks at comparatively low applied stresses. The hydrides will also act as effective barriers to the propagation of dislocations, which will also cause the formation of micro-cracks.[14] A study of 4 different titanium alloys indicates that the precipitation of the hydride occurs on various habit planes depending on the alloy. In all cases, however, these precipitation planes contained the $(10\bar{1}1)$ plane, a principal slip plane of this metal.[15] Like titanium, zirconium precipitates its hydride as a thin plate within the grain.[16] Kunz and Bibb[17] state the habit planes of the hydride in zirconium as $(11\bar{2}2)$, $(10\bar{1}2)$, and $(11\bar{2}1)$. The $(10\bar{1}2)$ is a major twinning plane, but none of the major slip planes (1000) and $(10\bar{1}0)$ were mentioned. Electron microscopy studies of rapidly strained titanium[15] and zirconium[18] have shown that there is little evidence of slip in specimens containing hydride; instead twins were noted to terminate at the precipitate platelets where they sometimes formed micro-cracks at the hydride interface. Especially interesting is the work on zirconium which showed profuse twinning after impact and little slip, but a reverse situation for slowly strained samples. The mechanism of hydrogen embrittlement in these metals is certainly different from steel where the embrittlement is experienced at slow strain rates but insensitive to impact, suggesting a rate controlling mechanism like diffusion. It appears that the exothermic occluders

like titanium and zirconium experience increased embrittlement as the strain rate increases due to the precipitated hydride, especially since considerable ductility exists under those conditions where no hydride exists.

2.2.2.0 Plastic Deformation and the Effect of Interstitials

As opposed to cleavage, a general rule exists that slip in metals occurs most easily on planes of greatest atomic density and largest interplanar spacing. The slip direction is generally the close-packed direction. This rule is followed by many of the common HCP metals such as cadmium, zinc and magnesium, where slip occurs on the basal plane (0001) and in a $<11\bar{2}0>$ direction. The second order pyramidal plane $\{10\bar{1}2\}$ is the usual twinning plane. There are two reasons to expect that both titanium and zirconium would not follow the above rule. The c/a axial ratio is 1.587 for titanium and 1.589 for zirconium, causing a -2.81% and -2.69% deviation respectively from the ideal ratio of 1.633. These metals are compressed along the c-axis, reducing the tendency for basal slip due to a decreased interatomic spacing. A distinct difference between the rolling textures of the ordinary HCP metals and those of titanium and zirconium also exists. A difference in the mechanism of plastic flow is suggested.[19]

2.2.2.1 Plastic Deformation in α-Titanium

The three α-titanium slip systems are given in Table 2.1.0. Churchman[5] determined that $(10\bar{1}0)$ $[11\bar{2}0]$ is the principal slip system in relatively pure α-titanium. A combined oxygen and nitrogen weight percentage ranging from .01 to 0.1 results in an increase in slip on the $(10\bar{1}0)$ $[11\bar{2}0]$ and (0001) $[11\bar{2}0]$ slip systems. Oxygen and nitrogen thus affect the absolute magnitude of the critical-resolved shear stress (CRSS) and also the relative values of CRSS on the 3 systems.

At room temperature twinning takes place on $\{10\bar{1}2\}$ and $\{11\bar{2}x\}$, where x = 1, 2, 3, 4.

2.2.2.2 Plastic Deformation in α-Zirconium

Only 1 slip system has been found for zirconium as Table 2.2.0 indicates. This system even prevailed when Rapperport oriented some samples to favor basal slip over the observed prism slip. These deformation characteristics can be explained by observed dislocation arrangements in commercially pure zirconium (~ 0.1 wt.% O+N) and pure crystal bar zirconium (0.03 wt.% O+N).[25] Straight line arrangements of the type expected for slip on $\{10\bar{1}0\}$ planes were found in the commercially pure metal. Tangled arrangements with loops and dipoles were found in the high purity metal. The latter arrangements are difficult to

Table 2.1.0--Alpha titanium slip systems and twin planes.

Slip Planes and Directions	
Basal {0001}	Churchman [11$\bar{2}$0]
	Anderson et al.[20] [11$\bar{2}$0]
Prismatic {10$\bar{1}$0}	Rosi et al.
	Churchman [11$\bar{2}$0]
	Anderson et al. [11$\bar{2}$0]
Pyramidal {10$\bar{1}$1}	Churchman [11$\bar{2}$0]
	Rosi et al.
Twinning Planes	
{10$\bar{1}$2}	Rosi et al., Liu et al., Anderson et al.
{11$\bar{2}$1}	Rosi et al., Liu et al., Anderson et al.
{11$\bar{2}$2}	Rosi et al., Liu et al., Anderson et al.
{11$\bar{2}$3}	Liu et al.
{11$\bar{2}$4}	Liu et al.

interpret on the basis of {1010} slip alone. In order to explain these observations it was proposed that the stress for dislocation glide on {1010} planes increases less rapidly than that for glide on the basal plane with increasing oxygen and nitrogen content. This infers that basal slip is possible at high purity.

Table 2.2.0 shows that the same twinning planes are operative in zirconium as previously noted for titanium.

Table 2.2.0--Alpha zirconium slip systems and twin planes.

Slip Systems	
$\{10\bar{1}0\}$ Prismatic	Rapperport[22] (1955), Rapperport and Hartley $[\bar{1}2\bar{1}0]$ Rapperport[24] (1959) $[11\bar{2}0]$
Twinning Planes	
$\{10\bar{1}2\}$	Rapperport (1955), Rapperport and Hartley Rapperport (1959)
$\{11\bar{2}1\}$	Rapperport (1955), Rapperport and Hartley Rapperport (1959)
$\{11\bar{2}2\}$	Rapperport (1955), Rapperport and Hartley Rapperport (1959)
$\{11\bar{2}3\}$	Rapperport (1955), Rapperport and Hartley Rapperport (1959)

2.3.0 Effect of Interstitials on Strength and Ductility

Highly pure metal would probably not be suited for engineering structural application due to low strength. Tremendous differences in tensile properties are noted between the sponge metals and the consolidated recrystallized bar. The sponge has an appreciably higher oxygen content. High degree of uniformity and good control of interstitials is possible today, even at the commercial purity level, which is of practical importance. Some of the early work is questionable due to the lack of such control. Commercial titanium's mechanical properties even show considerable differences depending upon the method of reduction: iodide or magnesium. The latter contains higher levels of iron, a beta stabilizer.

The tensile properties of zirconium also vary over a wide range. Iodide zirconium, with the least contamination and most uniformity, shows differences as high as 10,000 PSI in both yield and ultimate strengths.

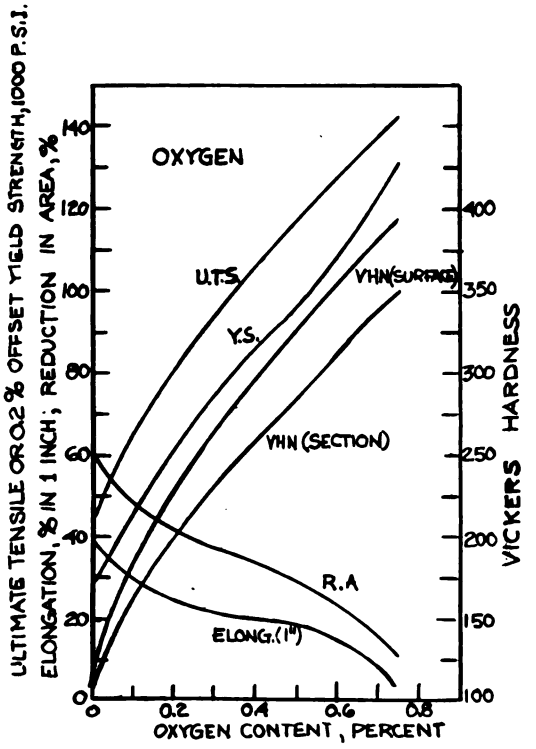


Figure 2.1.0--Mechanical properties of titanium-oxygen alloys, annealed at 850°C. (After Jaffee, Ogden, and Maykuth, used with permission of the publisher).[30]

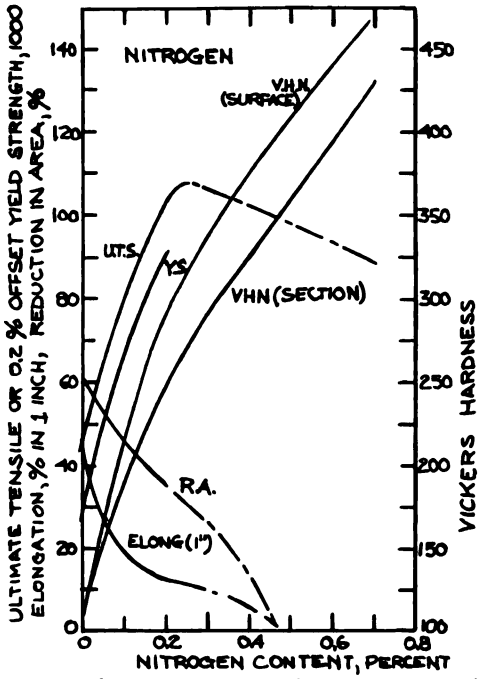


Figure 2.2.0--Mechanical properties of titanium-nitrogen alloys, annealed at 850°C.

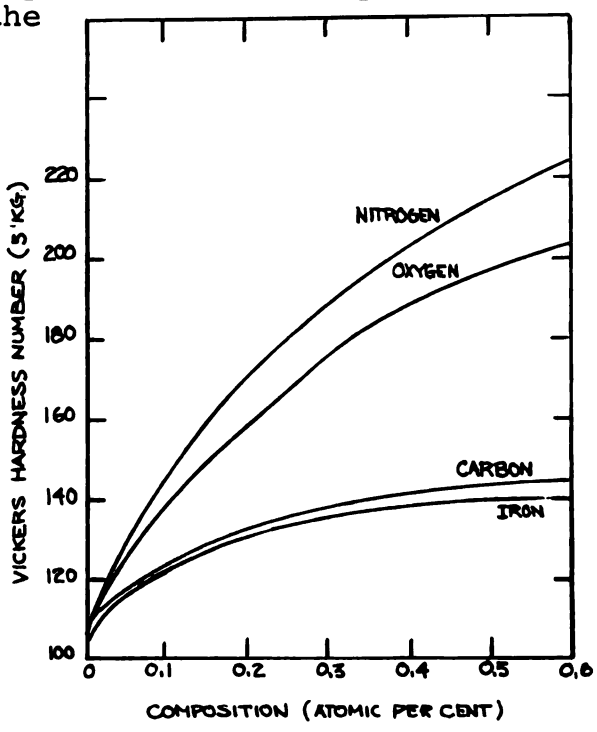


Figure 2.3.0--Relationship between Vickers hardness and composition by atomic percent of annealed, high-purity, binary, titanium-base alloys containing nitrogen, oxygen, carbon and iron. (After Finlay & Snyder, used with permission of the publisher).[29]

Like titanium, magnesium reduced zirconium has higher strengths and lower ductility than the iodide variety.[26]

The strengthening effect of oxygen in titanium is used to good advantage. A whole series of commercially pure grades is available, where oxygen content is varied within prescribed limits, and the other interstitials are held more or less constant. These grades are used in structural applications. Jenkins and Warner[27] suggested that up to 1.5a.-% oxygen could be added to titanium and still have about 30% elongation and a 50% increase over the original proof stress. However, a 2.0a.-% oxygen alloy's ductility drops to less than 3%.

The interstitial effect on strength properties is sometimes quoted in terms of an oxygen equivalent, O_e = 2/3 (pct. C) + pct. 0 + 2 (pct. N). Therefore, knowing how the strength properties vary with oxygen content, one can predict those same properties when one or more of the other interstitials are present in the alloy by use of the indicated formulation.

2.3.1 Effect on Titanium

The effects of oxygen and nitrogen additions on the hardness, tensile strength, and ductility of titanium has been thoroughly investigated.[28-31] Confusion resulted from the early studies. Fast[32] (1938) had concluded that nitrogen was more potent than oxygen, but Wartman[33] (1949) considered oxygen to be the most important impurity in affecting the mechanical properties of titanium. Part of the results of Jaffee et al.[30] (Figures 2.1.0 and 2.2.0) and Finlay et al.[29] (Figure 2.3.0), representative of the more recent work, resolves this question: nitrogen is more potent than oxygen in increasing strength and hardness. Therefore, nitrogen has a greater affect on inducing brittleness. At 0.5 wt.-%N, the room temperature tensile ductility ceases to exist, while this doesn't occur for oxygen until the additions are in excess of about 0.7 wt. %. Jenkins et al.[27] agree with this figure while another study[34] indicated that full brittleness occurred between 0.72 and about 0.76% oxygen depending on the grain size.

The solid solution hardening effect that a substitutional solute has on the solvent is to a varying degree related to size factor, that is, the lower the lattice parameter change per unit addition of the solvent, the lower the hardening effect and correspondingly, the greater the solubility. Lattice parameter measurements,

as a function of nitrogen, oxygen and carbon additions, show that carbon, which is the least soluble in α-titanium, has the smallest hardening effect by far, and exhibits the greatest expansion of the lattice. Nitrogen, the most soluble, has already been shown to have the greatest hardening potency, but the smallest effect on the lattice expansion. The case of carbon can be rationalized by noting that carbon additions have a marked tendency, compared to either nitrogen or oxygen, in changing the c/a ratio towards the theoretical 1.63. Easier slip of the theoretical close packing is assumed to afford lattice expansion compensation. At present, the anamolous behavior of oxygen and nitrogen cannot be explained.[29]

Titanium alloys of oxygen, nitrogen, and carbon combinations show that total content addition of any one of the alloys does not have a combined hardening effect equal to the sum of the individual effects determined from binary alloys. The ternary interstitial alloys correlate with binary interstitial alloys regarding hardness (VPN) versus ultimate strength.[30] The hardness (VPN) steadily increases over the entire alpha solubility range,[35] indicating that even after perceptible tensile ductility has vanished, the metal continues to become harder, and thus more brittle (i.e. more susceptible to fracture). The embrittling effects of nitrogen and oxygen occur at only a small fraction of their total solubility capability in α-titanium.

High purity alpha titanium is not greatly affected by dissolved hydrogen in modest proportions. Below a 1.0a-% concentration the ductility is about 70% elongation, but at increasing concentrations up to about 10.0a-% there is a steady drop to approximately 40% elongation. This ductility level remains constant up to about 25a.-% and at concentrations beyond this leads to catastrophic loss of ductility at room temperature. Commercial purity alpha titanium's tensile ductility is more sensitive to the presence of hydrogen because it is reduced from 70 to 10% elongation by only 12a.-% hydrogen compared to over 30a.-% for the high purity metal. Hydrogen does not seem to affect the hardness in the same way that oxygen and nitrogen does. A 1.0a.-% hydrogen concentration has no perceptible hardening effect at all, that is, does not differ from samples containing no hydrogen after a 70% cold reduction.[28,36]

2.3.2 Effect on Zirconium

Many of the effects noted earlier with respect to titanium also hold true for zirconium, and as such will not be belabored. Figures 2.4.0 to 2.4.2, illustrate the general effects on strength properties as a function of oxygen content.[37] The first small additions have the greatest hardening and embrittling effects, as noted for titanium. Nitrogen is also more potent than oxygen in strengthening and embrittling zirconium. Additions of 0.1 wt.%

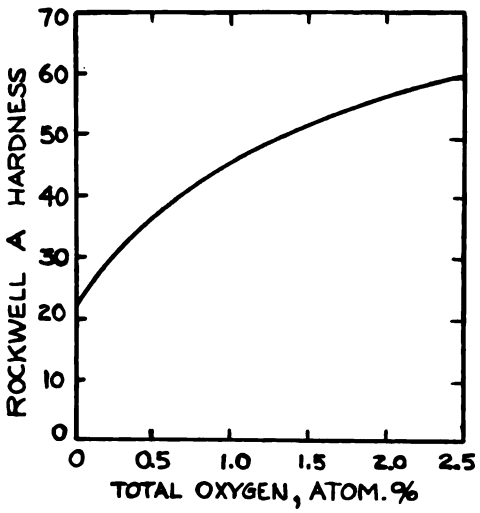


Figure 2.4.0--Effect of oxygen on hardness of iodide zirconium.

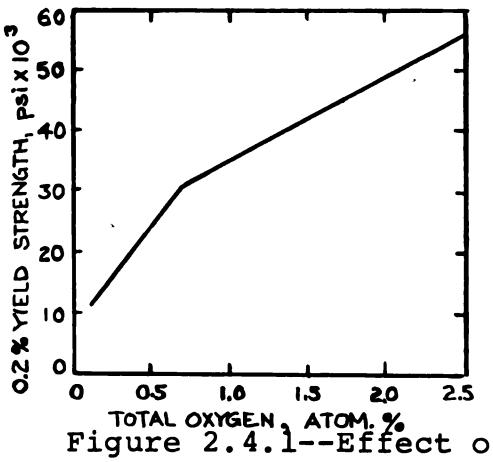


Figure 2.4.1--Effect of oxygen on 0.2% yield strength of iodide zirconium.

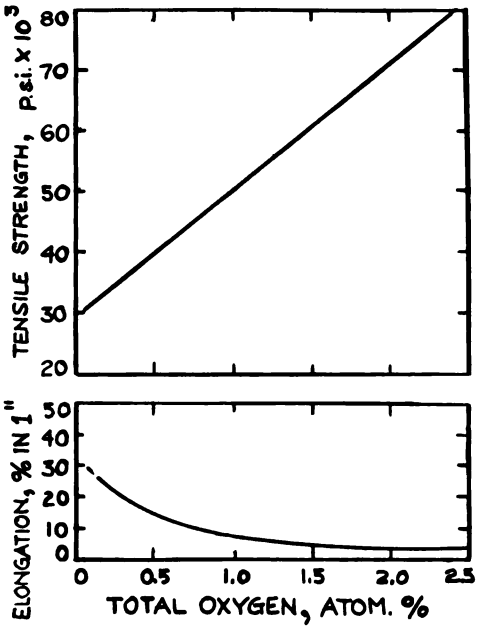


Figure 2.4.2--Effect of oxygen on ultimate tensile strength and elongation of rectangular test specimens of iodide zirconium.

(Figures 2.4.0 to 2.4.2 after R. M. Treco, used with permission of the published).[37]

to zirconium of comparable purity (about 25,000 PSI tensile strength) will increase the ultimate strength to about 100,000 PSI for nitrogen, and 45,000 PSI for oxygen.[38] Other cases include: a 0.14wt.-% N-Zr alloy,[39] and Terco's 1.0wt.-% O-Zr alloy (Figure 2.4.2) with tensile strength's of 98,600 and about 50,000 PSI respectively.

Westlake proposed that the precipitated hydride phase is not responsible for crack nucleation but that the grain boundaries are. The hydride phase merely strengthens the matrix, thus reducing glide at the crack tip, which increases the probability of crack propagation.[40]

2.4.0 Impact Strength of Titanium and Zirconium

Pure iodide titanium does not fracture in a Charpy test at room temperature, but commercially pure grades will. In fact, at room temperature, the absorbed energy can be as low as 10 to 15 foot-pounds. A rapid increase in the absorbed energy is noted at about 200°C.[41] The metal

purity determines the exact temperature at which this increase is observed.[42] This again demonstrates the general role that interstitials play in these materials.

Zirconium behaves in a similar manner. At -195°C, the metal exhibits impact values of about 50 foot-pounds if relatively pure.[43] The fact that interstitials display a collective effect is noted by the correlation between the hardness of titanium sponge and Charpy values of vacumn melted wrought titanium. Independent of the particular interstitials present, any combination resulting in a Brinell hardness between 140 to 150, results in a severe drop in impact strength. This hardness value generally corresponds to yield strengths of about 50,000 PSI.[44]

2.4.1 Effect of Hydrogen on Impact Strength of Titanium and Zirconium

Characteristically, todays iodide and sponge zirconium contains hydrogen in excess of about 30 ppm.not including that introduced during fabrication. Previous to the work of Mudge[45] and Dayton et al.,[46] little precaution was taken in controlling the hydrogen levels in zirconium, nor the cooling rates. Concentrations of about 50 ppm, if quenched in water from at least 315°C to 260°C, yields a fairly tough material. The limit of suppression seems to be about 100 ppm. Slow cooling allows a second phase to precipitate which has been

identified as a hydride of zirconium. Lenning et al.[36] have conclusively shown that in the case of titanium any benefits derived by quenching the hydrogenated metal is later lost upon aging at room temperature. The finely dispersed hydride particles agglomerate with time. For example, a 3-fold decrease in impact strength was noted for a 1.0a.-% hydrogen alloy after aging 1 month at room temperature.

High purity titanium suffers from hydrogen embrittlement on increasing the strain rate, or by the presence of a notch on the surface of a specimen. It has been observed that only 0.25a.-% hydrogen causes a 50% loss in impact strength when compared to similar samples containing no hydrogen. A complete loss of impact strength occurs at 2.0a.-% hydrogen,[47] which has virtually no effect on the tensile elongation. However, commercially pure titanium exhibits an almost complete loss of notch impact strength at about 1.0a.-% hydrogen, which is about half that required for the pure metal.[36] Pure and commercially pure alpha titanium both show an increased sensitivity as the strain rate increases. The latter material even shows this sensitivity in some cases where the solubility limit has not been exceeded (hydride platelets have not formed). In such cases the embrittlement is said to be enhanced by a retained beta phase high in hydrogen located in the grain boundaries of the alpha phase. Like titanium,

arc-melted zirconium bar shows no brittleness when the hydrogen is reduced to less than .01a.-%. A slowly cooled 0.9a.-% hydrogen sample will show about a 60% reduction in impact strength, and a similar material quenched from 550°C, a 30% reduction. The corresponding static tensile properties of the slowly cooled metal do vary but no nearly as drastically, i.e. a 17% reduction in elongation.[48] Ferritic materials do not precipitate a hydride, at least none that has been identified; whereas the metals under consideration definitely do embrittle with the precipitation of a hydride.[49]

2.4.2 Effect of Nitrogen on Impact Strength of Titanium and Zirconium

Nitrogen, normally present in zirconium in concentrations greater than 0.01wt.%, increases the transition temperature and reduces the impact strength at room temperature continuously up to 0.14wt.%.[39]

Using high purity Ti-N alloys, Jaffee et al. showed that independent of the grain size, or if the alloy was quenched from the β or $\alpha + \beta$ field, the first 0.1wt.% N drastically reduces the room temperature absorbed impact energy. Further, nitrogen additions alter the impact absorption only slightly by comparison.[50]

2.4.3 Effect of Oxygen and Oxygen Equivalents on Impact Strength of Titanium and Zirconium

Pure iodide titanium shows no ductile-to-brittle transition, but at an oxygen equivalent (O_e) of 0.36, a definite transition has been noted. The investigators used the same equivalency mentioned earlier for tensile properties. This assumes that the interstitials affect the impact resistance of titanium in the same way as the tensile properties are affected. The transition behavior is a function of the entire interstitial content, rather than on any 1 particular such element. Later, using subsize Charpy V-notch specimens, the transition was fixed at O_e equal to 0.17%.[51] Most recently, by varying the oxygen equivalent from 0.10 to 0.55 in small increments, the ductile-to-brittle transition was accurately placed at 0.13% oxygen equivalent.[12] Superficial oxygen contamination can occur at the notch due to oxygen's reactivity at temperatures obtained during the machining of the test bar if precautions are not taken to use a coolant.[52]

2.4.4 Accumulative Effects of Interstitials on Impact Strength of Titanium and Zirconium

The accumulative effects of interstitials on impact properties can be noted by a direct comparison of the

various binary alloys at a given temperature and composition. No equivalency assumptions need to be made.

At a 0.07% interstitial concentration, the impact absorption energy for nitrogen contaminated titanium[45] is far below that of oxygen[53] between the temperature range from -200 to +100°C. The 0.13% oxygen curve follows fairly closely to the 0.07% nitrogen curve over the indicated temperature range. At least in this case, the aforementioned equivalency is correct. Ogden et al.,[54] using the same high purity titanium as the others,[45,53] demonstrated that 0.38 carbon--0.20 oxygen alloy had a significantly lower impact curve and higher transition temperature, than a 0.47% carbon alloy. The cumulative nature of dissolved interstitials on loss of toughness is thus again demonstrated. Interpolating the family of curves generated by H. R. Ogden et al.[54] for various carbon concentrations, none is found to correspond on an oxygen equivalent basis with the shape of Jenkin's[53] 0.13% oxygen curve. From these comparisons, it is conclusive that the various interstitials do increase notch sensitivity, and nitrogen is most detrimental, while carbon the least.

2.4.5 Combined Factors Affecting Impact Strength

Several factors contribute to the brittleness exhibited by a crystalline material. Strain rate, and the

notch effects are difficult to isolate in the Charpy test due to their interaction. In addition, the notch effect itself is a combination of 2 separate effects: triaxiality and stress gradient. Zirconium seems to be both notch and strain rate sensitive. The general result of both these effects is to shift the transition temperature. Decreasing strain rate and/or eliminating the notch (or decreasing notch acuity) decreases the transition temperature.[55] Titanium and zirconium plate normally show a fair degree of anisotropy. Marked variations in Charpy impact strength have been demonstrated on arc-melted zirconium plane depending on the position of the notch and specimen axis with respect to the rolling direction and plane. Increasing interstitial content or strain rate and the presence of a notch all increased the notch sensitivity of Ti-H alloys.[56] With 50 ppm hydrogen in titanium containing 0.2% oxygen or 0.2% nitrogen, the notch-bend impact strength are significantly decreased in the temperature range -200 to 100°C. The interstitial effect, although related to notch and strain rate effects, can sometimes be shown not to be responsible for the embrittlement in a given situation. This was the case for unnotched tension specimens, whose strength and ductility were relatively unaffected at the same 0.2% oxygen and nitrogen with hydrogen levels up to 200 ppm.[57] These examples should serve to indicate the complexity of notch sensitivity in titanium and zirconium.

CHAPTER III

METAL FRACTURE CHARACTERISTICS

3.1.0 State of Stress

The type of stress which predominates determines the mode of fracture. Normal stresses (σ) tend to separate the material, while shear stresses (τ) tend to produce a translation of 1 part of the material with respect to some other part. In the body, one can choose an infinite number of planes to define the stress system. At any point in the body, regardless of the stress system complexity, there exist 3 mutually perpendicular vectors which represent the directions of the "principle stresses." The stress system is completely defined by stating the direction and magnitude of the 3 principle stresses (σ_1, σ_2, σ_3). No shear stresses operate on the planes normal to these vectors. Except for the special case of total triaxiality ($\sigma_1 = \sigma_2 = \sigma_3$), shear stress will always accompany the principle stresses. The maximum shear stress, τ_{MAX}, acts at 45° to the principle stresses with a magnitude one-half the difference between the greatest and least principle stresses, $\tau_{MAX} = \frac{\sigma_1 - \sigma_3}{2}$. The type of fracture is largely governed by the relationship between tensile and

shear strength for a given loading condition. For example, in tension or bending, $\tau_{MAX} = 1/2\ \sigma_{MAX}$, while in torsion $\tau_{MAX} = \sigma_{MAX}$. Thus, for any value of σ_{MAX}, the corresponding value of τ_{MAX} will be twice as large in torsion as it is in tension. In ductile materials, where the shear strength is less than the cleavage strength, the shear stress in torsion will readily exceed the shear strength of the material. Plastic deformation, once started, will continue till fracture.[1]

3.2.0 State of Strength

This study concerns itself mostly with tension loading. Materials under the influence of a single tension load application exhibit 3 different strength phenomena:

a) a shear yield strength, which implies a shear stress in excess of the stress necessary to initiate plastic flow;

b) a shear ultimate strength, which is the true shear stress at which ductile failure occurs;

c) the cleavage strength, the normal stress above which brittle fracture occurs.

These quantities should not be confused with those determined in a normal uniaxial tensile test. The latter set of quantities are not fundamental due to the nature of the test itself. The qualitative aspects of fracture as they relate to shear and normal stresses are well understood.

In a ductile material the shear stress overcomes the shear yield strength of the metal to cause plastic flow which will continue until the shear ultimate strength is reached, culminating in failure. In those metals where the cohesive strength is lower than the shear strength under identical conditions, catastrophic failure occurs when the principal stress exceeds the cohesive strength.[1]

3.3.0 Levels of Aggregation

A component may fail at a stress well below the yield stress of the material due to a stress concentration. This failure could have involved significant plastic deformation at a stress-raiser, while the remainder of the component experienced only elastic deformation. A failure is generally considered brittle if there is little or no plastic deformation of the entire part or regions surrounding the failure, even though large scale mechnical tests show the bulk material to be ductile. It is therefore necessary to clarify the scale at which a particular failure is described. Several failure scales are shown in Figure 3.1. The choice of how a particular scale is subdivided is quite arbitrary, but these regions may be generalized. The smallest area of description, the atomic or molecular level, the fracture takes place over the dimension of several atomic spaces (10^{-8} in). The material is considered to be discontinuous and comprised of discrete

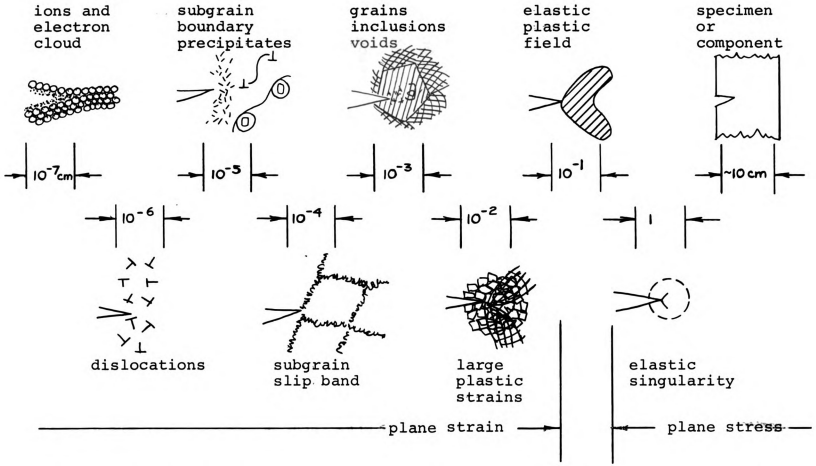


Figure 3.1.0--Schematic illustrations of fracture viewed at difference scales. (For the stress state, it is assumed the specimen or component thickness is one millimeter.) (After McClintock & G. R. Irwin, used with permission of the publisher.)[2]

particles. The next subdivision, the structural level, is that of a fine grain size (10^{-4} to 10^{-3} in), hence of importance in metallurgical studies. The material at this level is continuous but not necessarily homogeneous. Those cracks that are readily visible to the naked eye are on the phenomenological level of aggregation (10^{-1} in), whereby the material is presumed to be both continuous and homogeneous; and composed of identical volume elements of finite dimensions.

The "material body" according to Freudenthal[3] is an aggregation of matter possessing definite shape distinguished by its geometrical and material properties (mass and energy). The material body is made up of structural elements which can be subdivided, as already shown. The purpose of a study dictates the level of structural subdivision to be investigated. The mechanical properties of the material body will be reflected by the geometrical and material properties of the structural element at a particular level of aggregation. The geometrical properties are those which are relevant to the shapes of the elements and their arrangement in space; while the material properties are those related to the mass and converted mass, that is, the binding energy (cohesive strength).

The mechanical responses of a material is generally defined at the phenomenological level of aggregation; expressed in terms of dynamic conditions (forces and stresses)

and also kinematic (displacements, strains). The classical mechanics of deformable bodies, applied at the phenomenological level, assumes a condition of linear elasticity; and also that the material is continuous, homogeneous, and isotropic. Owing to the frequent origin of fractures at discontinuities or flaws, the investigations must often be at either the structural or atomic level. An understanding of the differences in these levels is basic to fracture studies, since an analysis may include any 1 or all of these levels. They can be correlated into a unified theory of mechanical response. The phenomenological level is described in terms of the relations between stresses and strains and their derivatives. On the atomic level the behavior of discrete particles is described by forces of interaction between them, and their relative positions in space. The unifying concept is energy since it has the same meaning at all states of subdivision.[4]

3.4.0 Behavior

In addition to considering the level of fracture (aggregation level), it is necessary to distinguish between behavior, appearance and mode.[5] The behavior of a fracture refers to the amount of permanent deformation that precedes failure. If appreciable, the fracture is classified as ductile; but if little or no preceptable deformation takes place, then it is termed brittle.

3.5.0 Fracture Modes

The mode specifies the specific path that fracture takes. Fracture that follows the grain boundary is referred to as intergranular. Such fractures are either due to segregated alloying elements or elevated temperature. Some metals, in the presence of certain foreign atoms concentrated at the grain boundaries, experience a drastic reduction in cohesion across those boundaries. This loss manifests itself in 2 ways: First, actual precipitates may form in the grain boundaries which are either intrinsically weak or only weakly bonded to the material in the grains; and the other case arises where no actual precipitate can be detected. A well known example of the latter is "temper-brittleness" of low-alloy steels.[6]

Intragranular or transgranular fracture, the interception of the grains themselves, is the most common type of fracture failure. Specific failure locations are: slip planes; or along highly stressed habit planes of precipitates; etc.

3.6.0 Crystallographic Classification

Fracture classification terminology in the literature has been the source of considerable confusion. They are classified by behavior; mode; and appearance.

The mode classification, the most definitive, allows for quantitative analysis within its framework. In the present study, fracture is discussed in terms of cleavage or shear, the components of the crystallographic mode. Cleavage and shear are best described at the atomic and structural levels.

3.6.1 Cleavage

Consider the 2-dimensional atomic array with the interatomic spacing, a_o, in Figure 3.2. A stress distribution, σ_y, acts normal to the plane AA'.

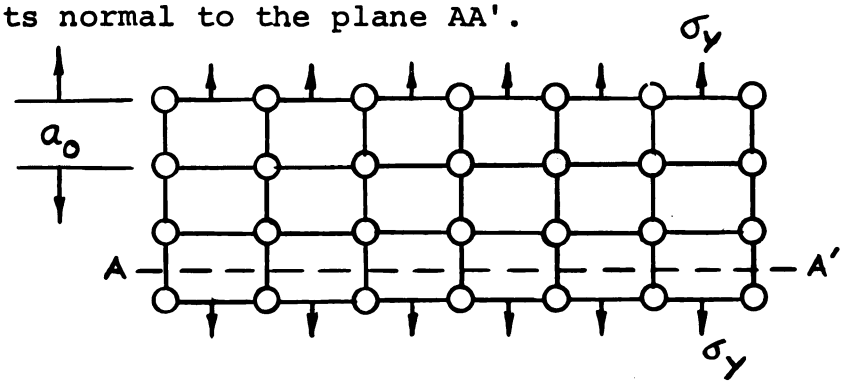


Figure 3.2.0--Normal forces acting on a 2-dimensional atomic array (After Tetelman and McEvily used with permission of the publisher).[8]

If the cohesive strength (the bond strength) between atoms on either side of plane AA' is exceeded, then the metal will fracture or cleave along this plane. A metal's ability to undergo cleavage depends upon the crystallographic system that it belongs to (i.e. BCC, FCC, HCP). The pure FCC metals are not believed to undergo cleavage fracture under any conditions of temperature; therefore, they do

not pose the problem of catastrophic failure. The BCC and HCP materials can fail in a cleavage mode. The cleaveage planes in a given crystallographic system cannot be generalized as discussed earlier in Chapter II.

3.6.2 Shear

If a shear stress, τ, acted along the plane AA', then the top array of atoms would translate with respect to the bottom array as seen in Figure 3.3.0.

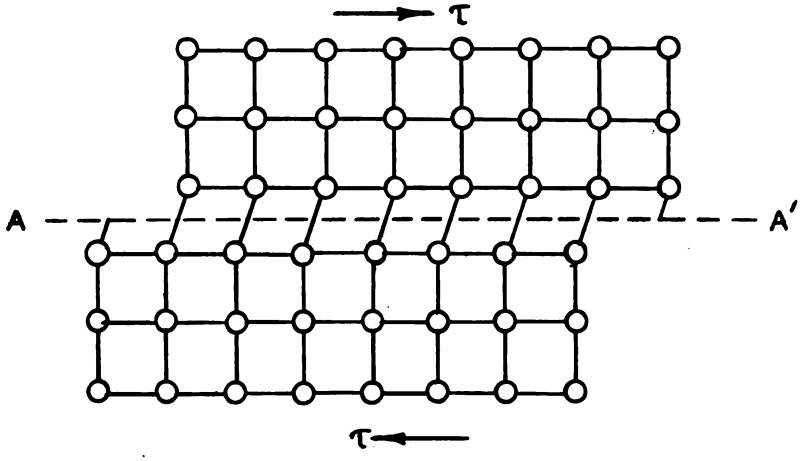


Figure 3.3.0 --Shear forces acting on a 2-dimensional atomic array (After Tetelman and McEvily, used with permission of the publisher).[8]

These translations give rise to plastic flow, generally described as the ductile condition. The phenomena has the following salient features:[7]

1) Regardless of the state of the applied stress, a plastic strain takes place due to the application of a shear stress.

2) There are 2 basic processes. The more common of the 2 is slip, in which the linear crystal defects (dislocations) move on crystallographic planes to cause

the plastic shear to take place in particular crystallographic directions. As a rule, a zone of shear (slip band) consists of parallel planes, fairly close to each other, that have undergone slip. Outside of these bands, no deformation may have taken place at all. Therefore, plastic yielding is an inhomogeneous process. The amount of slip possible is limited. Fracture is nucleated and propogated within a slip band when the metal's resistance is exceeded by the applied resolved shear stress.

During twinning, the other deformation process, a different dislocation event takes place; crystallographic shear is homogeneously distributed within the deformation zone, which is referred to as a twin. The crystallographic orientation of the lattice within the twin bears a mirror image relationship to the surrounding lattice.

3.7.0 Appearance and the Effect of Aggregation

Most engineering materials do not fail exclusively by either the shear or the cleavage crystallographic mode, but rather a combination of both. These materials are also polycrystalline and can generally be expected to have randomly oriented crystallites, but preferred orientation is frequently induced by the material's processing. Individual crystallite orientation, the stress system, and the type of material, determines the gross or macroscopic appearance of the fracture. Appearance of the fracture surface is

yet another means of classifying the fracture. Preceded by plastic deformation, the fracture surface will ordinarily appear gray, silky or fibrous. One revealing little ductility on the fracture surface might appear to be granular, or sparkle when rotated in light.

Under the conditions of uniaxial stress, the fracture surface of a brittle material on the phenomenological level of observation appears bright and is somewhat planar, referred to as "flat" or "square" condition. If inspected at the structural level, the crack is found to follow specific crystillographic planes for each grain that is encountered when traversing the section (as seen in Figure 3.4.0).

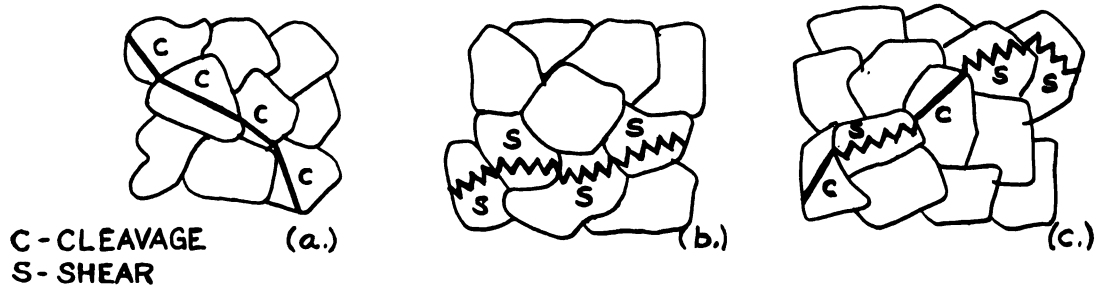


Figure 3.4.0--Cleavage and shear fracture in polycrystalline metals (After Tetelman and McEvily, used with permission of the publisher)[8]

In an aggregation of crystals, the same general principles hold true as discussed for the failure of a single crystal. For example, in the case of a pure cleavage fracture (Figure 3.4.0-a) the specific plane that the crack follows for each crystal, is the one for which the resolved normal stress is greater than the cohesive forces holding the atoms in place. In general,

the preferred cleavage planes for a given crystallographic system will not be oriented normal to the tensile axis. Thus the resolved normal stress component exceeding the critical resistive force for each crystallite. This also explains why the appearance on a structural level will not be flat.

Failure can theoretically be entirely by shear mode (Figure 3.4.0-b), if the maximum resolved shear stress of the primary slip planes is lower in each case than the maximum resolved normal stress required for cleavage. Macroscopic fibrosity is due to slipping on planes oriented to experience the maximum resolved shear stress. This occurs at 45° at the maximum resolved normal stress. The 45° inclined planes intersect each other, thus the jagged or fibrous effect.

There are several varieties of the mixed mode fracture. The fracture section may comprise entire areas that are almost exclusively ductile and others brittle. This will be explained in detail when discussing the fracturing of plates and impact specimens in a later section. A fracture surface may have distributed crystallites that fail by shear and cleavage. The material and conditions are such that shear and cleavage strengths were similar or fairly close.

In summary, the mode in which a particular crystallite fractures depends almost solely upon its orientation and the resulting resolution of stresses.

CHAPTER IV

HISTORICAL DEVELOPMENT OF FRACTURE THEORY

4.1.0 Misconceptions

The bulk toughness is a measure of a material's ability to absorb energy. The absorption occurring during elastic deformation is referred to as strain energy. It is easily determined experimentally as the energy represented by the area under the linear portion of the stress-strain curve, called the modulus of resiliance. When the stress exceeds the elastic limit, the absorbed energy is used to initiate plastic deformation which continues until fracture occurs. The total energy per unit volume of the material as represented by the total area under the stress-strain curve, is a measure of the material's bulk fracture toughness as determined in a uniaxial tension test. Toughness then is a function of both strength properties and ductility, which are themselves of an opposing nature.

Stress raisers often exist such as: voids, discontinuities, such as the interface between phases in a microstructure; cracks; or poor design features. These imperfections must be able to undergo local plastic deformation when a member is loaded in order to preserve its structural

integrity. The stress raisers act as centers for crack initiation and give rise to poor notch toughness.

The historical development of the theory of notch brittleness is very confused. A large portion of the pioneer work was done on steels, since it is the predominant structural material. Impact loads as opposed to notches were thought to be the cause of failures, but at the turn of the century it was recognized that the latter were really responsible.[1] The confusion started by designating a test for notch toughness, "the impact test." This only served to perpetuate the idea that the impact load is responsible for brittle fracture. According to Hoyt, Considere[2] demonstrated that increasing the strain rate raised the temperature of brittle fracture, thus repudiating the impact concept. Another misconception arose from the failure to recognize the effect of triaxiality. The localized stresses in excess of the cohesive strength result in brittle fracture. The use of ductile metals was commonly thought to insure notch toughness by local yielding to relieve stress concentrations. Yet another misconception, generating a good deal of confusion, was the idea that materials possessing the same tensile properties would all perform in like fashion in the presence of a notch. This had not been shown to be a fallacy until as late as 1920.[3] Although the effect of stress raisers was recognized from laboratory

studies, the prevailing opinion held impulsive loads responsible for service failures. This opinion further detracted from the notch's importance.

Orowan[4] noted that notch brittleness had been recognized for sometime, in that bending tests were described as early as 1884 by Tetmajer in Switzerland, and 1885 by Tunner in Austria. The specimens were broken by a hammer and brittleness determined by visual examination of the surface fracture for the degree of crystallinity. Controlled impact testing was introduced at the end of the nineteenth century. Batson and Hyde (1922) investigated the effects of temperature on some mild steels. The transition from a ductile to a brittle failure was observed with a decrease in the temperature.

4.2.0 The Classical Theory of Notch Brittleness

4.2.1 Ludwik's Postulations

P. Ludwik laid the basic ground work for fracture initiation theory by observing that fracture starts at the center of cylindrical tensile test bars. The radial and circumferential stresses tend to create holes or voids. To account for notch brittleness, Ludwik[5] postulated a triaxial state of stress just behind the surface of the notch. Ludwik's concept is easily extended to include fracture in plates. The triaxiality assumed by Ludwik

arises in the following way: The regions surrounding the crack are highly stressed. The stress concentration directly behind the crack tip often exceeds the metal's elastic limit. The stress state at the crack root is biaxial, that is, in the plane of the plate. The highly-stressed, plastically-deformed region is completely surrounded by material only elastically deformed. This large elastic region resists the free yielding required by the plastic region. Lateral contraction, necessary to have plastic flow take place at the crack root, is resisted. The constraint imposed by the "elastic surroundings" causes the stress at the crack root to continuously raise; because the usual relief mechanism, plastic deformation, is not operative. The stress must attain a level which will overcome both the elastic constraint and the material's own resistance to plastic deformation. As stated earlier, the stress state in back of the notch is initially biaxial. The third axial stress, directed perpendicular to the plane of the plate, builds up gradually against the elastic constraint forces in an effort to achieve contraction. The maximum constraint factor is 2.57 assuming a condition of ideal plasticity, i.e. no work hardening or strain rate effects.[6] The constraint factor is defined as the number of times the maximum stress exceeds the uniaxial yield stress of the material.

Ludwik considered the ordinary true-stress versus true strain curve, which is merely the instantaneous values of stress and corresponding strain for a material in uniaxial tension given by A in Figure 4.1. This curve will be referred to as the "flow curve," dictated by convention, although the terminology is poor since it implies flow at a constant stress. This curve continuously rises, adjusting for a reduced area due to necking and work-hardening.[7]

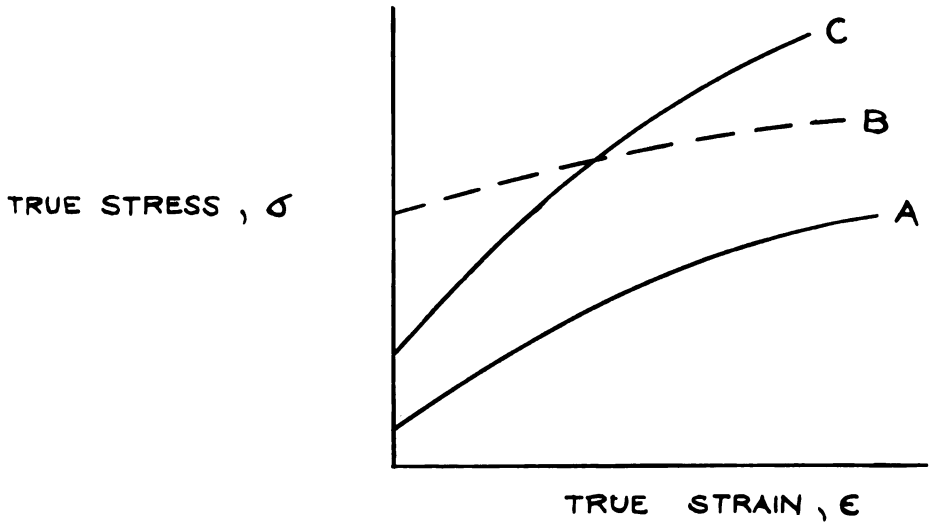


Figure 4.1--Ludwik's triaxial tension theory of brittle fracture

Failure occurs at some critical value of the flow stress. Ludwik also postulated the existence of a "fracture curve," whose relation to the stress-strain curve can be seen on the sketch as curve B. The intersection of the flow and fracture curves determines the fracture stress, for a ductile to brittle failure.

Since the triaxiality at a crack can raise the yield stress about 3 times, it has the effect of raising the flow curve A, shown as curve C. When this occurs, note the reduction in the amount of plastic strain before fracture. Parker suggested that Ludwik's original concept of a brittle fracture curve is oversimplified. He suggested that there should be 2 fracture curves, 1 to represent the shear mode and the other the cleavage mode. The various types of fracture noted in the laboratory and in service are more readily explainable in terms of this modified concept.

Verification of the existence of a fracture curve cannot be made from theory, and only 1 point of the curve can be determined by experiment, the fracture stress itself.

The curves of Figure 4.2 allow some common misconceptions and confusion surrounding farcture to be cleared up. The term "brittle fracture" as previously explained, involves the cleavage mode of failure. Figure 4.2, C and D clearly show a brittle failure may refer to a fracture where failure took place after either a small or a large amount of plastic deformation. A ductile metal in some circumstances may fracture entirely by cleavage, with no evidence of plastic deformation during the fracture.[9] The appearance of such a fracture would be characteristically crystalline and thus termed a "brittle" fracture. Cleavage may follow after significant plastic deformation has taken place.

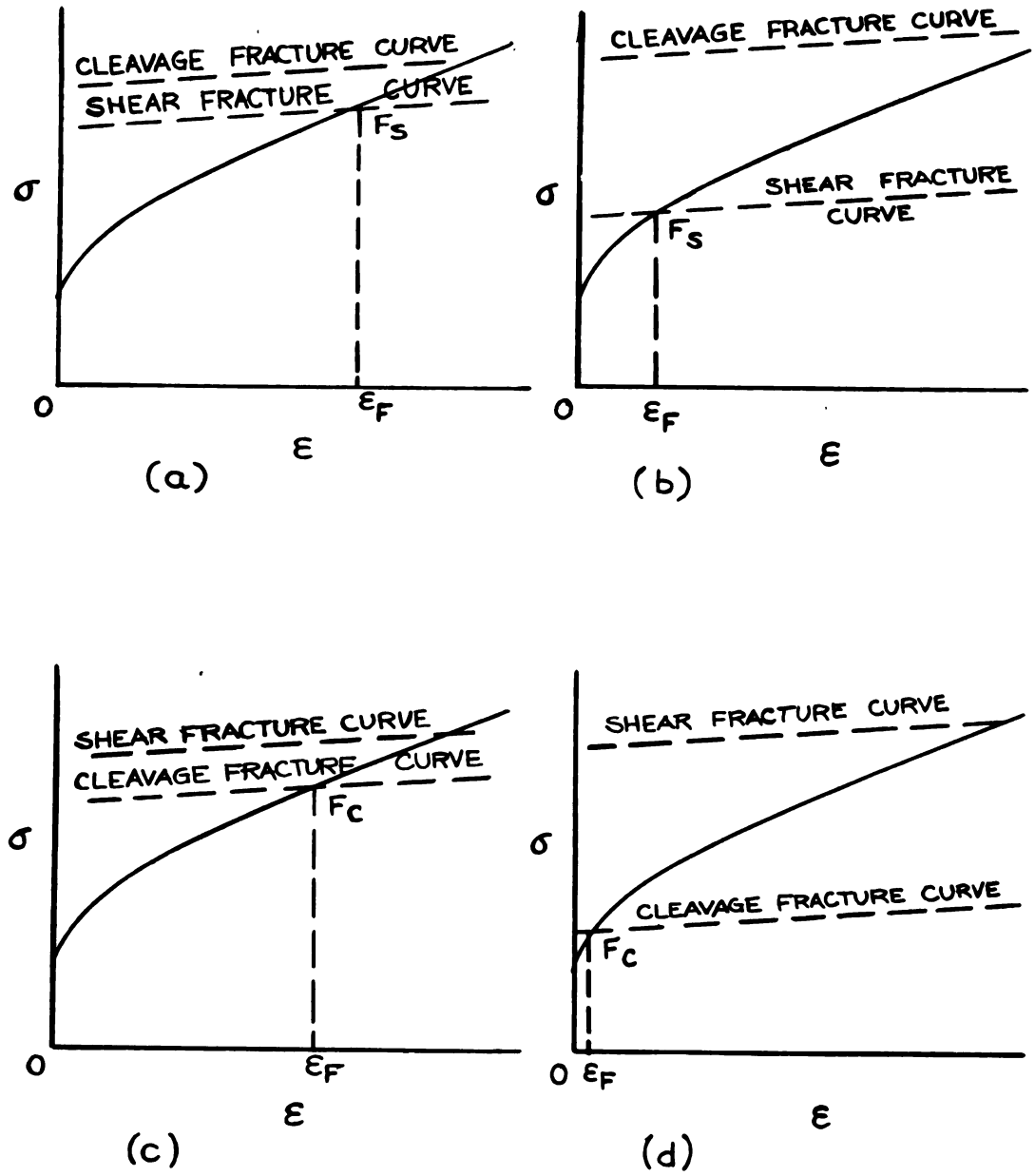


Figure 4.2.0--Schematic representation of four possible intersections of flow stress curve with cleavage and shear fracture curves (F_S indicates a shear fracture, and F_C a cleavage fracture.) (After E. R. Parker, used with permission of the publisher).

The original Ludwik theory was least successful in explaining service type failures. From a theoretical point of view, the theory suffers generally because of the triaxility condition. Significant amounts of plastic deformation must occur to induce the surrounding elastic constraint. Without this plastic deformation, only a small elastic constraint would be realized. Some materials that can be classified as approaching purely elastic undergo only small amounts of plastic deformation confined to the region of the fracture surface during failure. If the Ludwik theory were completely general, that is, all fractures followed accordingly, one must concede that plastic deformation of microscopic proportions is sufficient to cause the required elastic constraint.[10] Calculations to prove the validity of such an assumption have not been made, however.

4.2.2 Velocity Effects

Fractures where the bulk material has not undergone perceptible plastic deformation have been observed. Assuming the possibility of a thin localized plastic layer below the fracture surface, Orowan reasoned that such a region was insufficient to induce the necessary elastic constraint or strain hardening effects.[10] He concluded that brittle fracture in such instances must be due to velocity effects.

As the velocity of the fracture increases, the plastic deformation at the crack tip undergoes extremely high strain rates. Some early work[11] indicated that strain rate effects can raise the yield stress about 30%, although some steels are known to increase by a factor of 2 or 3. The strain rate effect therefore could completely replace the elastic constraint effect. Only the plasticity noted on the surface is necessary.

The triaxial condition at the very onset of fracture is still required because fibrous fracture is maintained until the stress is high enough to promote the propagation of cleavage. This is necessary since the velocity effect (strain rate) cannot start the cleavage propagation as there is no velocity at the initiation of fracture. Once the crack starts, however, the propagation will accelerate. During the acceleration stage, less plastic deformation is required because the velocity effects take over the task of raising the yield stress to the fracture stress value.

4.2.3 Shear Lips

The velocity effects may be used to explain the development of "shear lips" in fractured plate material. The triaxial stress condition cannot exist at the free surfaces of the plate, so cleavage cannot take place there. The ductile shear mode will predominate at the free

surfaces. The plastic deformation itself will cause some constriction which is confined to the region between the already existing crack and the free surface of the plate. Orowan claims that the width of these lips is a measure of the degree to which the velocity effects are able to achieve the cleavage fracture stress. The shear lips are often quite narrow but at some distance from the fracture initiation point they increase in width until merging into a parabolic arc.

4.3.0 Discrepancy Between Theoretical and Observed Strengths

4.3.1 Early Experiments

The period between the realization that materials are effected by flaws and the collection of a body of knowledge which allows prediction of failure due to these flaws, has its origins dating back at least to the experiments of Leonardo di Vinci (1564-1642). An account[12] of the masters sketch book states that he tested a wire till failure and then tested a similar wire of half the original length. He continued to shorten the wire. Lengths equal to one-quarter the original length failed at loads between 15 to 25% higher than that required for the original length. In more recent times, accounts by Todhunter and Pearson[13] describe the work of Lloyd and LeBlanc. Lloyd (1830)

determined that the average strength of short iron bars exceeds that of long ones of the same type, while LeBlanc (1839) essentially repeated the di Vinci experiment with the same results. The interpretation of the results, however, was of the utmost importance. The increased surface area of the long wires increased the probability of a serious inhomogeneity that would give rise to failure. These experiments all suggest that flaws in a material will act to reduce the natural strength of the material while under stress.

4.3.2 Theoretical Strength

The classical work to determine how strong materials would be if no imperfections or flaws existed is due to Frenkel.[14] He considered the periodic potential that exists in a lattice and the corresponding value of the shear stress as shown in Figure 4.3.

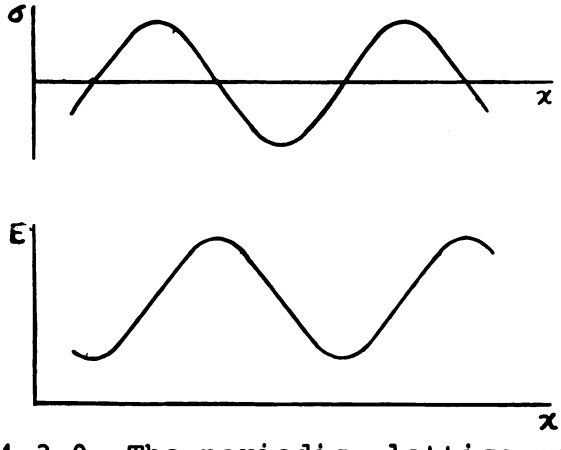


Figure 4.3.0--The periodic lattice potential, and the equivalent value of the shear stress, accompanying the shear of a perfect lattice. (From Theory of Dislocations by J. P. Hirth and J. Lothe, copyright 1968. Used with permission of McGraw-Hill Book Co.)[15]

The case is considered whereby a perfect crystal is shearing on a rational plane; translating through equivalent positions of equal energies. The period, b, is the magnitude of a simple lattice translation vector. Since end effects are small, they are neglected, i.e. disregard the energy requirements in the formation of surface steps. The applied shear stress, τ, required for a translation, x, is proportional to dE_T/dx, where E_T is the energy of translation per unit area of the plane. Frenkel approximated the periodicity of the energy to be sinusoidal so that:

$$\sigma = \sigma_{THEOR.} \sin \frac{2\pi x}{b} \qquad (4.1)$$

In the limit of small shear strain, $\frac{x}{d}$, Hook's law applies in the form

$$\sigma = \mu \frac{x}{d} , \qquad (4.2)$$

where d is the interplaner spacing and μ is the shear modulus. Equations 4.1 and 4.2 are equated and solved for σ_{THEOR}. In the small strain limit the substitution of

$$\sin \left(\frac{2\pi x}{b}\right) \cong 2\pi \, x/b$$

can be made, so

$$\sigma_{THEOR.} = \frac{\mu b}{2\pi d} \simeq \frac{\mu}{5} . \qquad (4.3)$$

There have been refinements made[16] on Equation 4.3 which indicate that σ_{THEOR} could be reduced to $\frac{\mu}{30}$. Subsequently others have even refined this value if melting point corrections are made. If, however, room temperature conditions are imposed, then the theoretical shear strength can be stated as, $\frac{\mu}{5} > \sigma_{THEOR} > \frac{\mu}{30}$. Independent of fine corrections, it is clear considering only orders of magnitude that the maximum resolved shear stress necessary to initiate plastic flow in metals is only 10^{-4} to $10^{-3}\mu$. Recently R. F. Tinder reported plastic deformation in bulk copper[17] and zinc[18] at stress levels as low as $10^{-9}\mu$. A discrepancy of several orders of magnitude exists between how strong a material could be, and how strong it is observed to be. The theoretical calculations have been verified by experimental work on whiskers of several metals presumed to be nearly perfect. The resolved shear stresses for the initiation of plastic flow is about $\frac{\mu}{15}$,--in excellent agreement with calculated values.

4.4.0 Griffith Thermodynamic Crack Propagation Criteria and Fracture Stress Relationship

A. A. Griffith[19] was the first to put forth a quantitative working theory that incorporated all the aspects of fracture to the degree that design criteria could be established. His postulations also account for

the large discrepancy between theoretical and actual strength, on the basis of flaws present. Griffith's work was published on October 21, 1920, and has been the foundation on which a whole new discipline was born--fracture mechanics. His initial investigations indicated that scratches made at 45° to the axis of a soft iron wire caused a permanent twist in the wire at a load ranging from one-quarter to one-third required to cause a permanent set in wires with no scratches. Griffith concluded that the critical fracturing load was obtained in these scratch areas, that is, the scratches reached a stress level in excess of the elastic limit of the material. Therefore, the scratches acted to increase the stress level 3 to 4 times that which the bulk material experienced. Satisfied that flaws cause an intensification of the stress, Griffith went on to formulate the condition for crack propagation. Introducing the use of linear elasticity "on the basis that the crack is assumed to be a traction-free surface," and therefore the stress could be correctly determined at points of the body. The exception to the validity of this concept is at those positions near the ends of the crack where the potential energy is essentially governed by the cohesive forces. Neglecting these molecular forces introduces negligible error for sufficiently large cracks.

Griffith attacked the problem from the "theorem of minimum energy," whereby he stated that the, "criterion

of rupture is obtained by adding to this theorem the statement that the equilibrium position, if equilibrium is possible, must be one in which rupture of the solid has occurred, if the system can pass from the unbroken to the broken condition by a process involving a continuous decrease in potential energy. . . ." The calculation of the potential energy is facilitated by the use of the general theorem which may be stated thus: "In an elastic solid body deformed by specified forces applied at its surface, the sum of the potential energy of the applied forces and the strain energy of the body is diminished or unaltered by the introduction of a crack whose surfaces are traction-free."

Griffith considered the now classical problem of a centrally cracked infinite plate subjected to uniform axial stress, σ. The crack shape was considered elliptical. The plate is loaded by tractions applied at the outer edge of the plate in directions parallel to its surface. These features are sketched in Figure 4.4.0. The stresses and strains were formulated according to the previous work of C. E. Inglis,[20] who solved the general case of this problem by setting forth a theoretical analysis of the stresses around a two-dimensional elliptical opening of arbitrary eccentricity. The method of finding solutions of the equations of elasticity in the elliptical coordinates α,β obtained by the conformal transformation: $x + iy = c \cosh(\alpha + i\beta)$

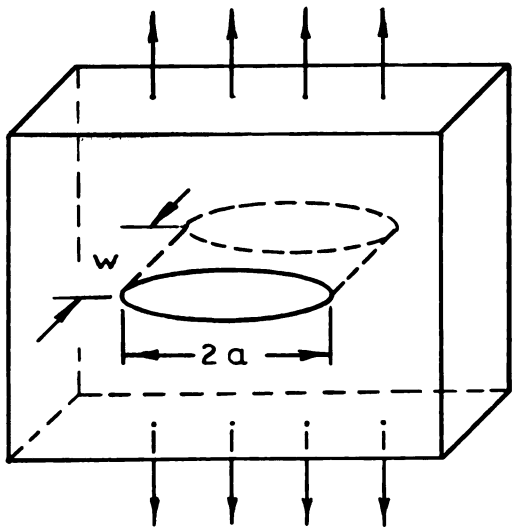


Figure 4.4.0--Schematic representation of the Griffith problem

A balance was determined between the crack surface or potential energy (U) and the strain energy of the system (W). The Griffith criteria for crack propagation can be simply stated: growth will occur without the necessity of additional work if the strain energy of the system is at least as great as the potential or surface energy created by each incremental increase in the crack length (da), that is:

$$\frac{\partial W}{\partial a} \geq \frac{\partial U}{\partial a} \qquad (4.4)$$

The potential or surface energy as a funciton of incremental crack length is given as:

$$\frac{\partial U}{\partial a} = 2\gamma_s w \qquad (4.5)$$

where: γ_s - surface energy/unit area

w - crack width

wa - crack area/surface.

It should be remembered that 2 surfaces are created during fracture, thus the quantity 2 in Equation (4.5). Upon integration of Equation 4.5, the total surface energy becomes

$$U = 2\ \gamma_s\ wa. \qquad (4.6)$$

The corrected form of the Griffith equation[21] for the strain energy, which is the driving force for crack propagation is

$$W = \frac{\pi a^2 \sigma_y^2 w}{8\mu}\ (p + 1), \qquad (4.7)$$

where: $p = 3-4\nu$ (plane strain),

$p = \frac{3-\nu}{1+\nu}$ (plane stress),

$\mu = \frac{E}{2(1+\nu)}$; μ, E, and ν

are the shear modulus, Young's modulus and Poisson's ratio respectively. Griffith's original derivations consisted of quantities U and W in terms of energy per unit thickness of the plate (ft.-#/in.). To make the equation completely general and avoid confusion, this practice will not be followed in the present study, that is, all energy

quantities will have their normal units (ft.-#). Therefore, by letting $R = \pi a^2 \sigma_y w$ and making the proper substitutions,

$$W_{\substack{\text{PLANE}\\\text{STRESS}}} = \frac{4R}{8E} = \frac{\pi a^2 \sigma_y^2 w}{2E} \qquad (4.9.1)$$

and

$$W_{\substack{\text{PLANE}\\\text{STRAIN}}} = \frac{4(1-\nu^2)R}{4E} = \frac{(1-\nu^2)\pi a^2 \sigma_y^2 w}{E} \qquad (4.9.2)$$

the fracture stress, σ_F, can be determined for both the plane stress and plane strain conditions by substituting Equation (4.5) into the left-hand side (LHS) of Equation (4.4) and Equation (4.9.1 and .2) respectively into the right-hand side (RHS). The fracture stress is found to be

$$\sigma_{F_{\substack{\text{(PLANE}\\\text{STRESS)}}}} = \left[\frac{2\gamma E}{\pi a}\right]^{1/2} \qquad \text{and} \qquad (4.10.1)$$

$$\sigma_{F_{\substack{\text{(PLANE}\\\text{STRAIN)}}}} = \left[\frac{\gamma E}{\pi a(1-\nu^2)}\right]^{1/2} . \qquad (4.10.2)$$

The fracture stress equations indicate that the product, $\sigma_F (a)^{-1/2}$, equals a constant. Griffith recognized this as an entirely new way of expressing a material's fracture toughness. The linear dimensions of the flaw itself were never before considered important. Design criteria based upon such a concept allows for comparisons of the fracture

stress with the applied nominal stresses at acceptable or anticipated flaw sizes. In other words, design emphasis is shifted from a critical stress or critical strain idea to considerations of the dimensions of defects likely to exist within the region of a member experiencing the greatest nominal stress. Moreover, it considers those conditions under which these defects will grow to a "critical" size. Upon attaining the critical dimension, the crack will start to propagate rapidly causing catastrophic failure of the whole structure.[22]

Griffith's fracture theory's strongest point is also its most serious drawback: development on the basis of linear elasticity. Its strength lies in its rigor, but apparent weakness lies in limiting its application to truly brittle materials such as glass used in the experimental verification of the theory. The Griffith criteria for crack propagation does make several assumptions, among which are: that the crack tip radius of curvature will be small enough to elevate the local stresses above the cohesive strength of the material. It is also assumed that incremental changes in the crack length are reversible. The closer a material comes to being classified purely elastic, the greater is the likelihood that the assumptions are valid.[23]

4.4.1 Griffith Concept Applied to Metals: Plastic Flow Required

Zener and Holloman[24] extended the Griffith concept to include the brittle fracture of metals. They felt that the presence of microcracks wasn't necessary in the material before deformation, but could be opened or created as a consequence of exceeding the tensile strength of interphases. These interphases may exist between the matrix and intermetallic inclusions or between any ductile and brittle phases, such as ferrite and cementite in steel. The brittle phases themselves may fracture during the plastic deformation of the ductile phase, such as the cementite plates in pearlitic steels. They contended that the critical value of the tensile stress stated by Griffith is still the criterion for stability of a crack independent of its shape under the conditions of pure tension. Considering only fracture resulting from plastic flow, the Zener-Holloman modification was again quite limited in scope.

4.4.2 Plasticity in Brittle Fractures

In the case of mild steel, extensive plastic deformation had been shown to take place on the fracture surfaces independent of their brittle appearance.[10] The depth of the plastic region from the fracture surface was determined by checking the definition of x-ray back

reflection spots after various etchings. The diffuseness of the spots due to plastic deformation eventually becomes clear or well defined after the "worked" region has been removed. From these photographs strains in the order of 1 to 2% were estimated in the worked region of the brittle material.

These findings prompted several more adjustments[10,25] to the Griffith theory which would include the plasticity aspect of fracture. In addition to the system lowering its energy due to the creation of new surfaces during fracture, energy is expended in doing the work of plastic deformation in the crack vicinity. If the dimension of the plastic zone is small in comparison to the crack and plate dimensions then the work of plastic deformation can be considered as part of the surface energy. However, as the plastic zone increases, such an assumption is no longer valid and the surface energy term, γ, must be replaced by an effective surface energy term, $S_{eff.}$. The fracture stress Equations 4.10. and 4.10.2 can be restated as

$$\sigma_{F_{(\text{PLANE STRESS})}} = \left(\frac{2\, S_{eff.}\, E}{\pi a}\right)^{1/2} \quad \text{and,} \tag{4.11.1}$$

$$\sigma_{F_{(\text{PLANE STRAIN})}} = \left(\frac{S_{eff.}\, E}{\pi a(1-\nu^2)}\right)^{1/2} . \tag{4.11.2}$$

The effective surface energy is the summation of the actual surface energy, γ_S and the plastic deformation energy, γ_P. Upon letting

$$\delta = \left(\frac{2E}{\pi}\right) \quad \text{and,} \tag{4.12.1}$$

$$\eta = \left(\frac{E}{\pi(1-\nu^2)}\right) \tag{4.12.2}$$

the fracture stress equations become

$$\sigma_{F_{(\text{PLANE STRESS})}} = \left[\frac{(\gamma_S+\gamma_P)\delta}{a}\right]^{1/2} \quad \text{and,} \tag{4.13.1}$$

$$\sigma_{F_{(\text{PLANE STRAIN})}} = \left[\frac{(\gamma_S+\gamma_P)\eta}{a}\right]^{1/2} . \tag{4.13.2}$$

Orowan's[10] x-ray work indicated that the order of magnitude of the work of plastic deformation in a brittle fracture surface was 10^6 ergs/cm.^{2}, while surface energies are about 10^3 ergs/cm.^{2} . Since plastic surface work, γ_P, is a thousand times greater than the surface energy, γ_S, it is reasonable to neglect the latter. The fracture stress equations are therefore modified to

$$\sigma_{F_{(\text{PLANE STRESS})}} = \left(\frac{\gamma_P\delta}{a}\right)^{1/2} \quad \text{and} \quad \sigma_{F_{(\text{PLANE STRAIN})}} = \left(\frac{\gamma_P\eta}{a}\right)^{1/2} . \tag{4.14.1 \& .2}$$

A statistical theory was modeled to predict the effects of combined stress, temperature, strain rate and metallurgical structures.[26] This model had some limited success.

4.4.3 Ductile Fractures Not Covered by Griffith Equation

Orowan[27] had also shown that the Griffith equation represents a necessary and sufficient condition of tensile fracture, and pointed out that the equation could not be extended to include truly ductile fractures, because the fracture mechanism is different. See Figures 4.5.1 and .2

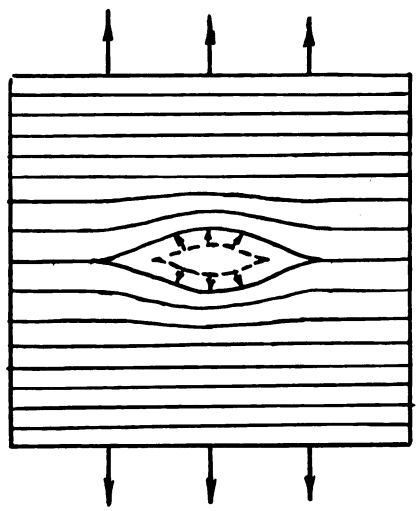


Figure 4.5.1--Brittle Fracture Mechanism

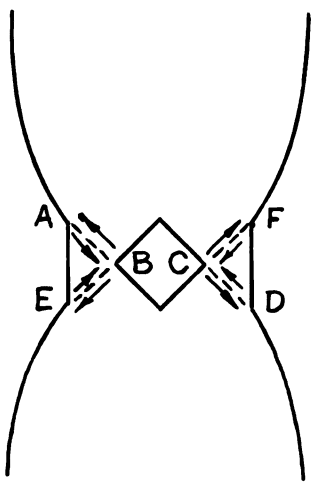


Figure 4.5.2--Ductile Fracture Mechanism

(Figures 4.5.1 and .2 after Orowan, used with premission of the publisher).[27]

Brittle fracture depends on the elastic modulus of the material as noted in Equations 4.10.1 and 4.10.2. The fracture strength would tend towards infinity if the elastic modulus did; however, this is not the case for a ductile material as shown by the sketch of the mechanism of failure. Slip is independent of elastic moduli so Orowan concluded that the force necessary to propagate a ductile crack is simply, $F = \sigma_{YS} A$ where:

σ_{YS} - is the yield stress of the material in tension

A - projection of areas AB and CD on the plane perpendicular to the tension direction.

The fracture equation was derived from the Griffith energy principle, and was shown to depend on the material's elastic modulus. The plastic crack propagation formulation is not dependent upon the elastic modulus, thus indicating that Griffith's equations cannot be applied to ductile failure. When the plastic deformation is confined to a thin layer at the fracture surface as previously indicated, the plastic work energy may be taken as a component of the surface energy and Equations (4.14.1) and 4.14.2) can be used.

CHAPTER V

LINEAR ELASTIC FRACTURE MECHANICS

5.1.0 Introduction

As a material group, metals are by far the most important structural materials in an advanced society. There is, therefore, little wonder as to the reason for the abundance of literature concerning the failure of metals in service. Petch[1] (1954) and Low[2] (1963) have presented comprehensive reviews of these investigations. Of specific interest is the fracture-toughness approach which was ushered in by the Griffith theory. On February 9, 1959, the United States Department of Defense requested the American Society of Testing and Materials (ASTM) to establish a special committee to evaluate the problem of brittle fracture in high-strength alloys. This action was prompted owing to burst test results indicating that Polaris missile cases consistently failed well below the materials rated yield strength (200,000 PSI).[3]

Since that time, the A.S.T.M. Committee on Fracture of High Strength Metallic Materials has reviewed many testing procedures and specimens. Considerable confusion surrounds various aspects of fracture mechanics because

developments have taken place so rapidly in such a short period of time.

5.2.0 Fracture Correlation Poor Between Tension Testing and Service Failures

Fracture toughness in oversimplified terms is simply a measure of the crack length that a material can possess without experiencing failure when loaded to stresses in the vicinity of the yield strength. Past experience has shown that simple mechanical strength tests, such as the uniaxial tension test, don't correlate well with fractures in service. This is probably due to the fact that materials that N. H. Polakowski labels "frangible," perform in a ductile fashion under some conditions and brittle under others. In the uniaxial tension test at room temperature, these materials fail in ductile shear; while in service cleavage mode failures are not uncommon. A simple tension test also fails to distinguish between crack initiation and propagation energy. Real materials already contain the cracks and flaws which ultimately cause failure. The strain energy which accumulates in the region around such flaws is used entirely for propagation purposes.[4] It will be recalled that this was one of Griffith's main points.

5.3.0 Fracture Modes

The displacements due to crack formation can be divided into 3 basic types, which are shown in Figure 5.1. Mode I, the opening mode, displacements are perpendicular to the plane of the crack. Mode II, the edge-sliding or forward mode, is characterized by a displacement of the fracture surfaces over one another in a direction perpendicular to the leading edge of the crack. The tearing mode, mode III, is defined by fracture surface displacements parallel to the leading edge of the crack. The latter 2 are shear modes, and the crack expansion is analogous to edge glide and screw glide dislocation motion through a crystalline material. Mode I fractures are the subject of the present study because empirical evidence invariably shows that the plane of fracturing is usually perpendicular to the direction of the greatest tension load. This is interpreted to mean the opening mode will generally develop more rapidly than the shear modes for the same applied component of crack-extension force.[5]

5.4.0 Arbitrary Parameters to Define Notch Toughness

The role that discontinuities in the form of shoulders, grooves, holes, keyways, threads, etc. play in localizing stress has been known for some time. H. Neuber's charts of stress concentration values in

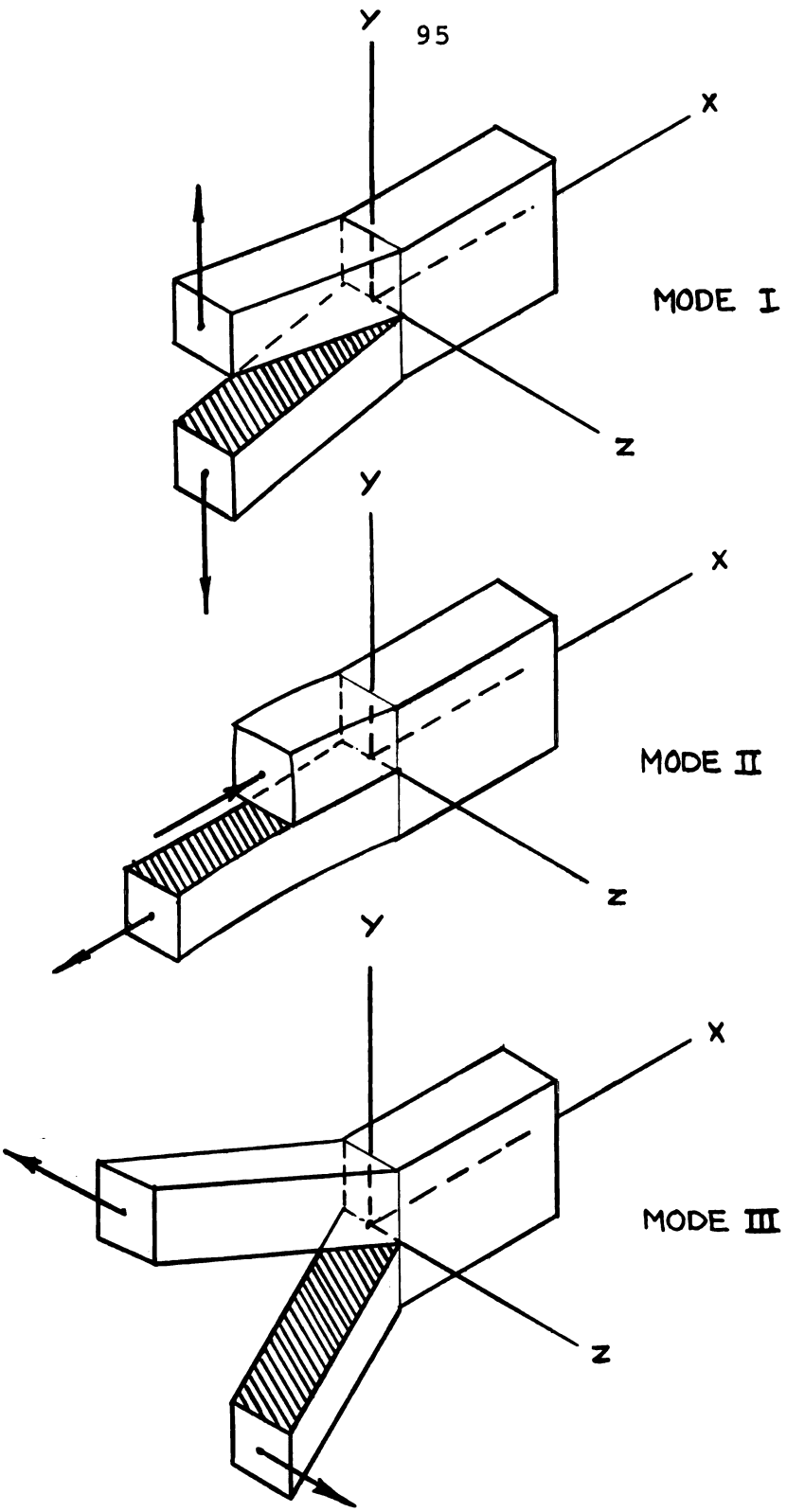


Figure 5.1.0--The basic modes of crack surface displacements.

the vicinity of such discontinuities have been used since 1937. Neuber's work and also photoelastic analysis allowed some design criteria to be formalized which is still used today. These criteria are most often stated in terms of the ratio

$$K_t = \frac{\text{maximum stress of the section}}{\text{average stress of the section}} ,$$

where K_t is the geometrical, or theoretical stress concentration factor and is always larger than unity. There is also an experimental parameter,

$$K_f = \frac{\text{endurance limit of specimens without a notch}}{\text{endurance limit of specimens with a notch}} ,$$

where K_f is the fatigue strength reduction factor or fatigue stress concentration factor. The 2 are related by the quantity

$$K_f = 1 + q\ (K_t - 1),$$

where q is the notch sensitivity factor, which varies from 0 to 1. Notch sensitivity then is dependent upon the geometry of the part and inherent characteristics of the material.[7] For small notch radii K_f may be considerably less than K_t; while for large notches, K_f may approach the value of K_t, but not exceed it. Designs based upon K_t are considered safe since it represents conditions worse than actually experienced in service.[8] Several short comings

of the tensile test for toughness evaluation have already been cited. It has nevertheless been considered as a possibility with some alterations of the test bar. A material's notch toughness is measured by notching the bar and, assuming for analysis purposes, that the groove is hyperbolic. This test, however, yields limited fracture information. Most elementary strength of materials texts have a partial listing of the geometric and experimental stress concentration factors. A complete listing is given by R. E. Peterson[9] and most recently by J. Huckert.[10]

5.5.0 Modern Fracture Mechanics

Arbitrary quantities are frequently used in engineering for evaluation and analysis purposes. The limited success of the aforementioned parameters can be well appreciated from the full realization of the complexity of fracture phenomena. These parameters are arbitrary, and are not described in terms of the quantities that are now known to be of primary importance in governing fracture. Also, since these parameters are not derived from fundamental theories, they yield no information about the mechanism of fracture. Obviously, the most useful type of parameter to a designer would be one that has its origins in linear elasticity. The designer could directly use the fracture quantity in the stress equations.

5.5.1.0 The Strain Energy Release Rate--Simple Elastic Model

An oversimplified, but easily understood, derivation of fracture stress can be made.[11] Consider Figure 5.2, where

d_a = distance between two adjacent atoms,

Δd_a = separation distance between atoms where the stress reaches a maximum, σ_m,

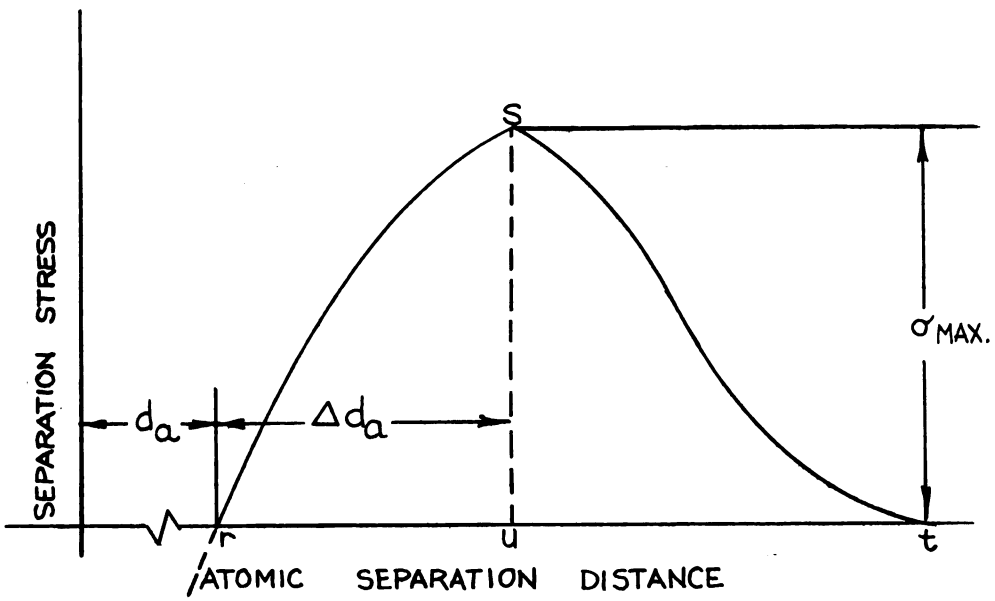


Figure 5.2.0--Stress required to displace an atom from its neighbor (After Polakowski and Ripling, used with permission of the publisher).[4]

Area (rst) = energy of fracture/unit of cross-section and γ = surface energy.

If one assumes that Area $_{(rsu)}$ = Area $_{(stu)}$, and the line rs is straight up to σ_{MAX}, then the sum of the

elastic areas under the two halves of the curve is

$$\text{Area}_{RST} = \Delta d_a \, \sigma_{MAX} \, . \tag{5.1}$$

Using the definition for strain ($\varepsilon = \Delta d_a / d_a$), and Hook's Law, the total energy under the curve is

$$\text{Total Energy} = \frac{(\sigma_{MAX}^2)(d_a)}{E} \, . \tag{5.2}$$

The energy input to cause separation is exactly balanced by the formation of 2 new surfaces, $2W_\alpha$, so

$$2\gamma = \frac{(\sigma_{MAX}^2)(d_a)}{E}$$

or

$$\sigma_{MAX} = \left(\frac{2E\gamma}{d_a}\right)^{1/2} \, . \tag{5.3}$$

The form of the fracture stress equation (Equation 5.3) is exactly like that determined by Griffith (Equation 4.10.1). The Griffith-Orowan modified fracture stress equation is $\sigma = \left(\frac{E\gamma_P}{\pi a}\right)^{1/2}$, which replaced the original Griffith's surface energy term with a plasticity work term. The Griffith-Irwin fracture stress equation is $\sigma = \left(\frac{EG_C}{\pi a}\right)^{1/2}$, where the elasticity parameter G_C is equal to the plasticity term suggested by Orowan.[12] The parameter, G_C, is called the crack extension force, or the strain energy release rate with respect to crack extension.

5.5.1.1 Definition of G From Energy Considerations

There is an incremental increase in absorbed energy, dQ, when new area A, is formed due to crack growth. The available energy in the system, dU, must at least be equal to the absorbed energy. The 2 sources for available energy are the work done, dJ, by the applied load; and the decrease in the stored strain energy (-dV) in the specimen. During a no-growth condition, the stored strain energy increases, supplied by the applied load work (dJ = dV). However, during crack growth, the specimen compliance (extension/unit load), increases. The storage capacity of the specimen can be viewed as reduced, i.e. dV goes negative. The available energy is never negative,

$$dU = dJ - dV.$$

The critical condition for crack extension occurs when $-dV/dA = dQ/dA$, meaning that the energy required for propagation is supplied entirely by the strain energy without any external energy supply such as, dJ The critical condition is considered to take place under "fixed-grip" conditions. Irwin made use of this idea in devising a mechanical test to measure G, which will be explained in the next section. Using these energy quantities, the differences between the original Griffith fracture

concept and the modifications made by Orowan and Irwin are clear. For example: Griffith identified $2\gamma w = \frac{dQ}{dA}$, while Orowan let $\frac{dQ}{dA}$ be the work of plastic deformation. Irwin, however, was interested in dU, because it depends only on elastic properties of the material and the applied load, whereas dQ depends on several unknown parameters. It is interesting to note that $dU = dQ$ only when the kinetic energy approaches 0 since $dU = dQ + KE$. Irwin denoted $\frac{dU}{dA}$ as G, the strain energy release rate or more simply, fracture toughness.[13] These fundamental energy concepts must be generalized into the linear elastic framework.

5.5.2.0 The Relationship Between Strain Energy Release Rate and Elastic Compliance

Irwin and Kies[14] were among the first to point out some of the mechanical concepts surrounding unstable fracture. Referring to Figure 5.3, the unstable crack propagation of a tensile bar may be defined as that in which ℓ = constant, that is, the grip distance does not change. The condition implies that the testing machine and grips are very much stiffer than the test piece, and also that the specimen is purely elastic. It can be shown that these very restrictive conditions can be relaxed in order to make valid experimental measurements on

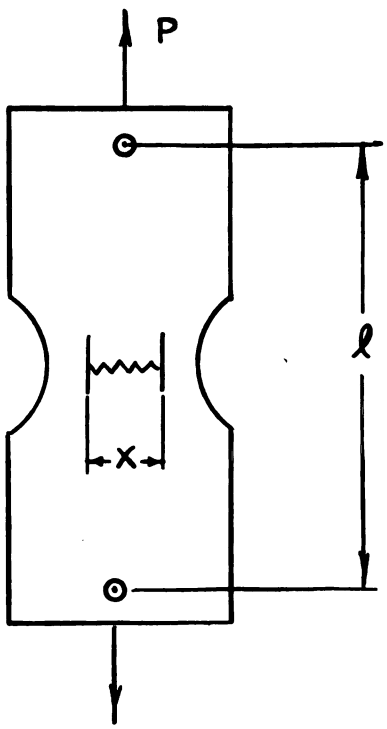


Figure 5.3.0--Fracture under fixed grip conditions (After Irwin and Kies, used with permission of the publisher)[14]

"real" materials. The energy balance with respect to crack length, x, is:

$$P \frac{d\ell}{dx} = \frac{dU}{dx} + \frac{dW}{dx} + \frac{dK}{dx} \qquad (5.4)$$

where: $P \frac{d\ell}{dx} = 0$, for unstable crack propagation, $G = \frac{dU}{dx}$ is the strain energy release rate, $\frac{dW}{dx}$ is the work done by the crack against surroundings, and $\frac{dK}{dx}$ is the kinetic energy of the moving crack. Under unstable conditions

the release energy is spent by doing work (formation of new surfaces) and supplying energy for kinetic effects (crack velocity). Since $dK/dx = 0$ momentarily before fracturing starts,

$$\frac{dU}{dx} = \frac{dW}{dx} . \tag{5.5}$$

The fracture appearance, previously discussed, is a good indication of the extent that Equation 5.5 is satisfied. If $\frac{dW}{dx}$ is significantly less than $\frac{dU}{dx}$, then the difference must be due to the crack velocity. Forking (shattering) of the fracture occurs when there is a sudden change between the release rate and crack work. Large cleavage areas with only occasional branching is an indication that the work rate approximated the release rate.

If the load is partially released, for a given crack length, x, then P and ℓ will decrease, where these parameters are related by

$$dP = M\, d\ell. \tag{5.6}$$

The spring constant of the specimen material is M. If ℓ is a constant, the ratio of $\frac{P}{M}$ should also be constant. Irwin claims that experimental work has shown that this ratio is approximately constant even when extensive plastic deformation takes place, if it is confined to the vicinity of the crack. The reciprocal of the stiffness or spring constant is the compliance ($C = \frac{1}{M}$). The strain

energy is U=1/2 Pe, where e is the displacement of the fracture surfaces. Thus the spring constant and compliance can be defined in terms of the displacement,

$$M = \frac{P}{e} \text{ and } C = \frac{e}{P} \cdot \qquad (5.7.1 \text{ and } 5.7.2)$$

Equation 5.5 may be rewritten

$$\frac{dW}{dx} = \frac{dU}{dx} = \frac{d}{dx} [-1/2\ Pe] . \qquad (5.8)$$

The negative sign in Equation (5.8) arises such that the release rate will always be positive.

Substitution for the displacement yields

$$\frac{dU}{dx} = \frac{d}{dx} [-1/2\ P\ (\frac{P}{M})] = -\ 1/2\ (\frac{P}{M})\ \frac{dP}{dx} . \qquad (5.9)$$

Carrying out the indicated differentiation and remembering that P/M is a constant, Equation 5.9 may be restated as

$$\frac{dP}{dx} = -\ PM\ \frac{d}{dx}\ (\frac{1}{M}) \cdot \qquad (5.10)$$

Finally upon substituting Equation 5.10 into 5.9

$$\frac{dU}{dx} = -\ 1/2\ \frac{P}{M}\ [-PM\frac{d}{dx}\ (\frac{1}{M})] \quad , \text{ or} \qquad (5.11.1)$$

$$G = \frac{dU}{dx} = \frac{P^2}{2}\ \frac{d}{dx}\ (\frac{1}{M}) . \qquad (5.11.2)$$

By similar arguments it has been shown that the same result is obtained if the crack is located at the edge of a plate rather than the center.[15]

Figure 5.4 is a sketch illustrating the changes taking place during crack growth. It also shows that the parallel energy and mechanical compliance approaches are completely complimentary. Energy and compliance concepts are used interchangeably in fracture mechanics for theoretical discussions. Analyses are usually in terms of compliance. Physical toughness measurements can be made on systems so complex that analytical stress solutions would be virtually impossible to calculate. These measurements can be made because G is only a function of the elastic compliance and the applied load (Equation 5.11.2). The usefulness of the compliance relationships will become even more apparent when discussed in more detail in later sections.

5.5.3.0 Strain Energy Release Rate-Compliance Relationship is Completely General

The strain energy release rate equation (Equation 5.11.2) is completely general, and as such is not influenced by the mode of fracture. If compliance measurements are made for a loading perpendicular to fracture, then this tensile load would be the load used in the formula, and the toughness given the designation, G_I. If, however, the compliance measurements are made with respect to a

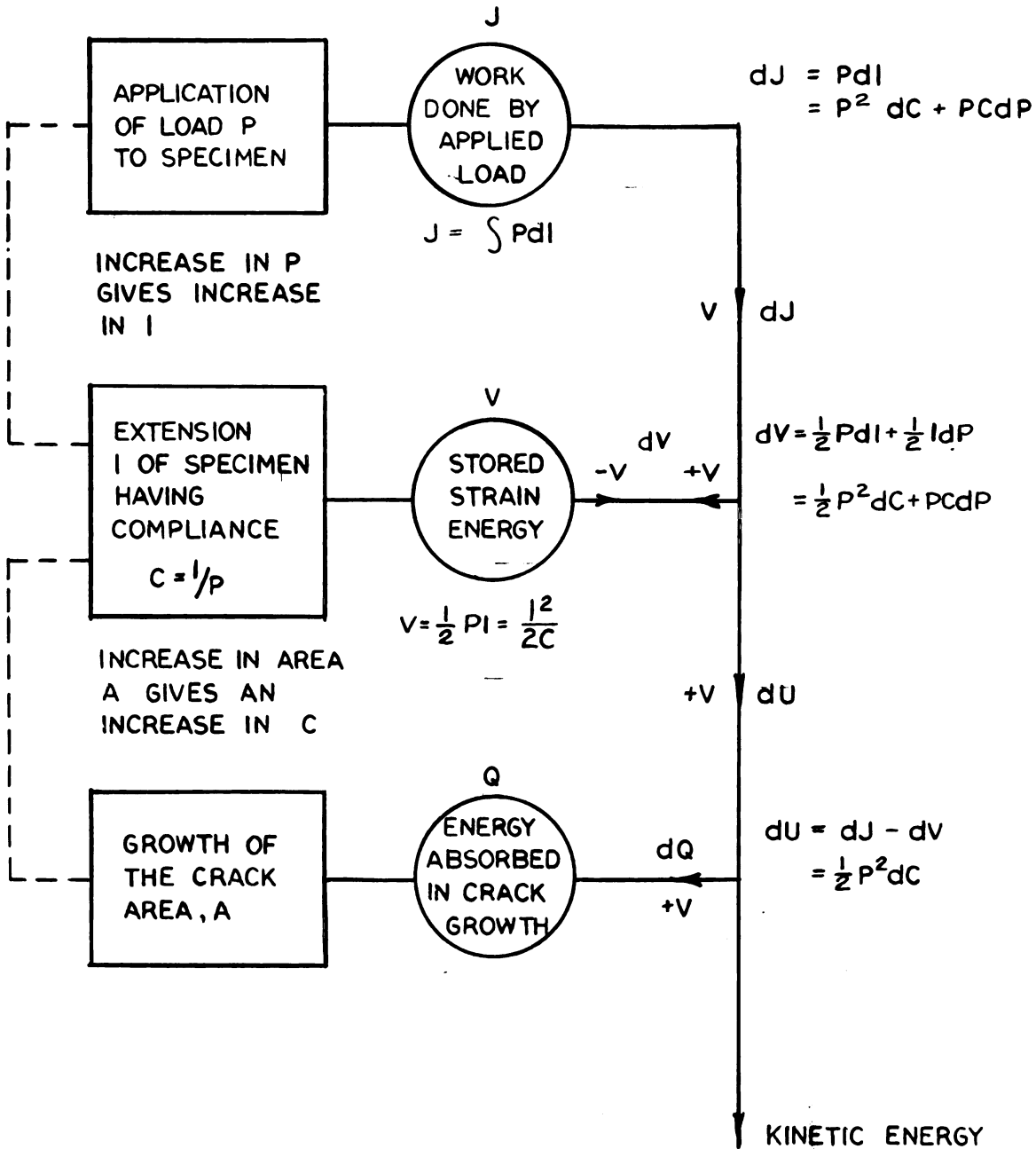


Figure 5.4.0--Diagrammatic representation of energy changes involved in crack growth. (After P. Kenny and J. D. Campbell, used with permission of the publisher).[13]

shear force acting perpendicular or parallel to the leading fracture edge, then these would be the loads used in the equation. In the latter cases the fracture toughness would be designated G_{II} and G_{III} respectively. Using these ideas, the toughness of complex heterogenous systems have been successfully determined where other means would be extremely difficult. The testing of adhesive joints can be cited as an example. A crack in the glue line can propagate by forward shearing. The analysis is simply made from the separate evaluation of compliance measurements of the shearing and tension modes.[16]

5.5.4.0 The Stress Intensity Factor

The stress concentrations near the leading edge of a crack have been investigated.[17] Westergaard's[18] complex variable approach is used, whereby: "A harmonic function of x and y can be obtained, as the real part ReZ and the imaginary part ImZ of an analytic function Z of the complex variable $z = x + i\,y$, with Z being written in the forms $Z = Z(z) = Z(x + iy) = ReZ + iImZ$. The further functions Z', $\overline{Z}$, and $\overline{\overline{Z}}$ are the derivative, first, and second integrals of Z. . . . In a restricted but important group of cases, the normal stresses and the shearing stresses in the directions of x and y can be stated in the form

$$\sigma_x = \text{Re } Z - y \text{ Im } Z'$$

$$\sigma_y = \text{Re } Z + y \text{ Im } Z'$$

$$\tau_{xy} = - y \text{ Re } Z'.^{17}$$

For the present time, it will be considered that no plastic strains are present. A complete analysis of the stress field surrounding the crack using the Westegaard approach is presented in Appendix A. This appendix details an outline presented by Paris and Sih.[19]

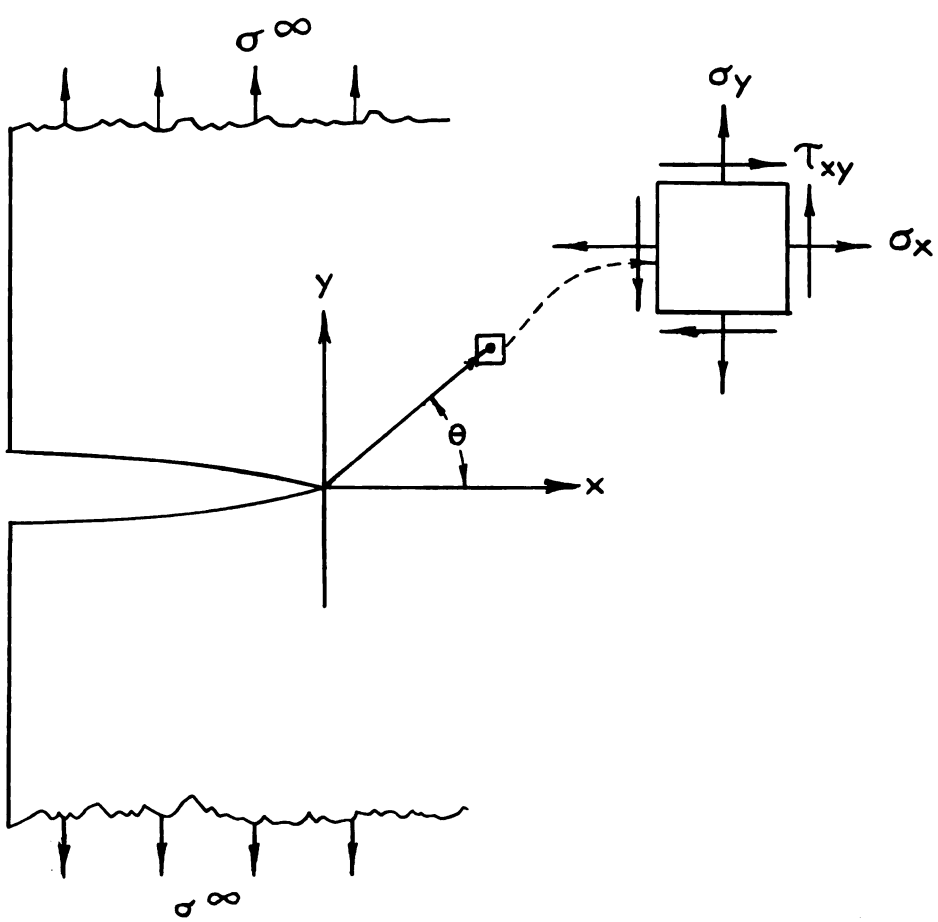


Figure 5.5.0--A two-dimensional representation of a crack in a plate and the coordinate system.

The crack tip stress field equations, as determined by this analysis are summarized as:

$$\sigma_x = \frac{K}{(2\pi r)^{1/2}} \cos\frac{\theta}{2}\left[1-\sin\frac{\theta}{2}\sin\frac{3\theta}{2}\right] \qquad (5.12.1)$$

$$\sigma_y = \frac{K}{(2\pi r)^{1/2}} \cos\frac{\theta}{2}\left[1+\sin\frac{\theta}{2}\sin\frac{3\theta}{2}\right] \qquad (5.12.2)$$

$$\sigma_{xy} = \frac{K}{(2\pi r)^{1/2}} \sin\frac{\theta}{2}\cos\frac{\theta}{2}\cos\frac{3\theta}{2} \quad . \qquad (5.12.3)$$

The usefulness of the above set of equations lies in the fact that all opening mode crack tip problems of isotropic elastic material have an identical form of solution. The equations are therefore independent of the loading or the geometry of the cracked homogeneous member. Therefore, it is concluded that all these factors (i.e. geometry of the member, applied stress, the crack length, etc.) are all grouped into the single parameter, K. Further inspection of these equations also suggests that the terms $r^{-1/2}$ and $f(\theta)$ only pertain to the stress distribution around the crack tip. The actual value of the stresses at any point (r, θ) near the crack tip is directly proportional to K, and thus K is labelled the "stress intensity factor." Another symbol often encountered in the literature is $K = \frac{K}{2\pi}$. One should not confuse the stress intensity factor, K, with the stress concentration factors, K_t and K_f, discussed in section 5.4.

5.5.4.1 The Stress Intensity Parameter is a Measure of Fracture Toughness

When the applied load is increased, then too, K increases because it is a function of the load. As this occurs, slow extension of the crack may or may not take place. At some value of the applied load, and some crack length, if slow extension took place the propagation of the crack will occur without any additional external energy being necessary. At instability, the load is at a maximum, and, correspondingly, the stress intensity factor obtains some critical value, K_c. Therefore, K_c is really a measure of the fracture toughness of a material for a given set of conditions. All the other factors in the stress field equations are distribution terms and can be considered constant. If one has some way of measuring K_c under the same conditions, clearly the material with the highest value of K_c is the toughest. The critical value of the opening mode stress intensity factor is generally designated, K_{IC}. The values of K_{IC} are unique for a given set of conditions, and can be interpreted as fracture toughness because it separates stable from unstable propagation. In such a framework K_{IC} can also be considered a material property. The units of K_{IC} are $(\#/in.^2)(in.)^{1/2}$ which do not convey the normal significance of toughness. Paris and Sih[19] have presented a systematic listing of stress intensity solutions for various stress

conditions. Knowing the value of K_{IC} is useful to a design engineer because the other factors in the equation are familiar to him. The usefulness of K_{IC} is perhaps due mostly to a simple relationship that exists between it and the strain energy release rate.

5.5.5.0 Relationship Between the Strain Energy Release Rate and the Stress Intensity Factor[17, 19]

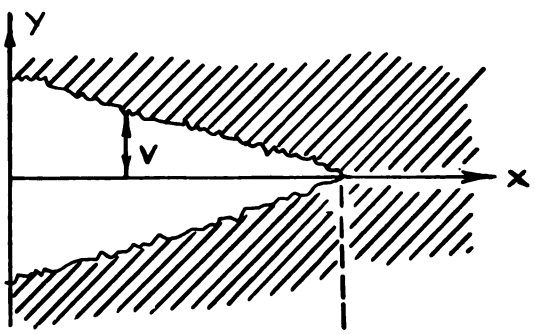


Figure 5.6.1--Crack open condition

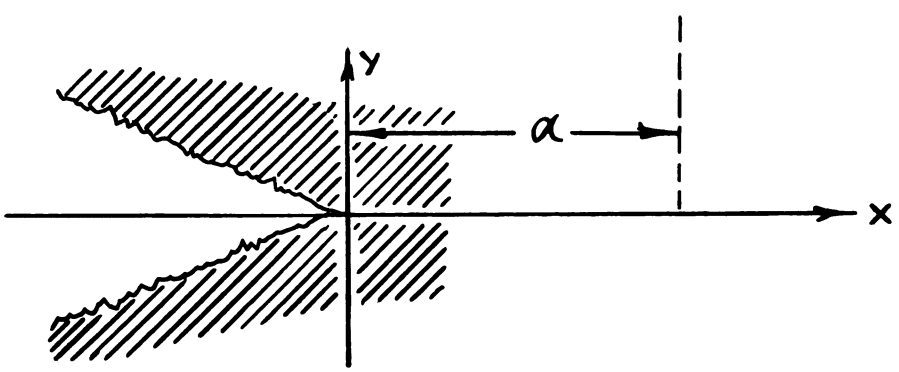


Figure 5.6.2--Crack partially closed condition (After Paris and Sih, used with permission of the publisher).[19]

If the Irwin fixed grip condition is imposed on an elastically loaded body, then the only contribution to G is the strain energy change. G is now considered as the energy per unit of new crack area generated, available for the crack extension process,

$$G = P \frac{de}{da} - \frac{dU}{da} \tag{5.13}$$

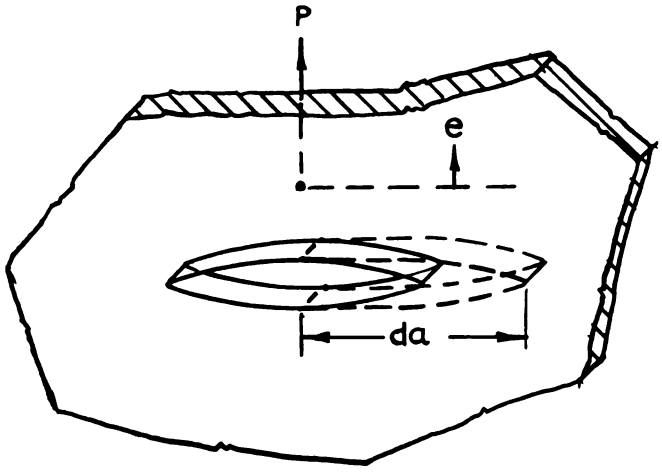


Figure 5.7.0--Loaded arbitrary section containing a crack (After Paris and Sih, used with permission of the publisher).[19]

Following the fracturing process in reverse, the crack is closed by an amount α as shown in Figure 5.6.2. The work required to close this segment of the crack is found by multiplying the traction forces on the surface of the crack by the displacements through which they act.

Then $$G_I^* = \frac{1}{2} \int_o^{\alpha} \sigma_y \, v \, dx, \text{ where} \tag{5.14}$$

G_I^* is the work required to close crack length, α, per unit area for a unit thickness parallel to the crack

front, where v is the y-displacement. The 1/2 factor outside the integral in Equation (5.14) comes about since the displacements are proportional to the tractions (i.e. calculation of work under linear elastic load application). Therefore

$$G_I^* = \left.\frac{dU}{da}\right|_{\substack{\text{FIXED}\\ \text{GRIPS}}} = \lim_{\alpha \to o} \frac{2}{\alpha} \int_o^\alpha \frac{\sigma_y v}{2}\, dx \quad . \tag{5.15}$$

There are 2 crack surfaces, thus the factor 2 before the integral. The crack displacement field equations are developed in Appendix B, where it is shown that,

$$v = \frac{K_I}{\mu} \left(\frac{r}{2\pi}\right)^{1/2} \sin\frac{\theta}{2} \cdot \left[2-2\nu-\cos^2\frac{\theta}{2}\right] \quad . \tag{5.16}$$

Upon closing the crack, the displacements are those with $r = \alpha - x$ and $\theta = \pi$. Remembering that $E = 2\mu(1+\nu)$, then

$$v = \frac{K_I}{\mu} \left(\frac{\alpha-x}{2\pi}\right)^{1/2} (2-2\nu) . \tag{5.17}$$

Upon substituting for the shear modulus, μ, this may be rewritten as

$$v = \frac{4 K_I (1-\nu^2)}{E} \left(\frac{\alpha-x}{2\pi}\right)^{1/2} \quad . \tag{5.18.1}$$

The most suitable form is

$$v = \frac{2 K_I (1-\nu^2)}{E} \left[\frac{2(\alpha-x)}{\pi}\right]^{1/2} \quad . \tag{5.18.2}$$

Appendix A gives the stress σ_y as

$$\sigma_y = \frac{K_I}{(2\pi r)^{1/2}} \cos\frac{\theta}{2}\left[1+\sin\frac{\theta}{2}\sin\frac{3\theta}{2}\right], \qquad (5.19)$$

which is being considered at the opened crack tip, $r = x$ and $\theta = 0$. Substitution of these coordinates simplifies Equation 5.19 to

$$\sigma_y = \frac{K_I}{(2\pi r)^{1/2}} . \qquad (5.20)$$

The further substitution of v and σ_y (Equations 5.18.2 and 5.20), into Equation 5.14 yields

$$G_I^* = \left.\frac{dU}{da}\right|_{\substack{\text{FIXED}\\ \text{GRIPS}}} = \lim \frac{2}{\alpha}\int_0^{\alpha}\frac{\sigma_y v}{2}\,dx$$

$$= \left(\frac{2}{\alpha}\right)\left(\frac{1}{2}\right)\int_0^{\alpha}\left[\left(\frac{2K_I(1-\nu^2)}{E}\right)\left(\frac{2(\alpha-x)}{\pi}\right)^{1/2}\left(\frac{K_I}{(2\pi x)^{1/2}}\right)\right]dx$$

$$= \frac{2}{\alpha}\left(\frac{K_I(1-\nu^2)}{E}\right)\left(\frac{K_I}{(2\pi)^{1/2}}\right)\left(\frac{2}{\pi}\right)^{1/2}\int_0^{\alpha}(\alpha-x)^{1/2}\left(\frac{1}{x^{1/2}}\right)dx$$

$$= \frac{2}{\alpha\pi}\left[\frac{K_I^2(1-\nu^2)}{E}\right]\int_0^{\alpha}\left(\frac{\alpha}{x}-1\right)^{1/2}dx . \qquad (5.21)$$

The integral $\int_0^{\alpha}\left(\frac{\alpha}{x}-1\right)^{1/2}dx$ in Equation 5.21 is evaluated in the following manner:

(a) $$\int_0^{\alpha}\left(\frac{\alpha}{x}-1\right)^{1/2}dx = \int_0^{\alpha}\frac{(\alpha-x)^{1/2}}{x^{1/2}}\,dx$$

(b) Let $y^2 = x$, then $dx = 2y\,dy$

(c) $$\int_0^{\alpha^{1/2}} \frac{(\alpha-y^2)^{1/2}}{y}\ 2y\ dy = 2\int_0^{\alpha^{1/2}} (\alpha-y^2)^{1/2}\ dy$$

(d) Using a Table of Integrals:

$$\int (a^2-x^2)^{1/2}\ dx = \frac{1}{2}\left[x\ (a^2-x^2)^{1/2} + a^2\ \sin^{-1}\left(\frac{x}{a}\right)\right]$$

where $a^2 = \alpha$, $x = y$,

so $$2\int_0^{\alpha^{1/2}} (a^2-x^2)^{1/2}\ dx = 2\int_0^{\alpha^{1/2}} (\alpha-y^2)^{1/2}\ dy$$

$$= (2)\left(\frac{1}{2}\right)\left[y(\alpha-y^2)^{1/2} + \alpha\ \sin^{-1}\left(\frac{y}{\alpha^{1/2}}\right)\right]\Bigg|_0^{\alpha^{1/2}}$$

$$= \frac{\alpha\pi}{2}\ .$$

Therefore

$$\int_0^{\alpha} \left(\frac{\alpha}{x}-1\right)^{1/2}\ dx = \frac{\alpha\pi}{2}\ . \qquad (5.22)$$

Substitute the value of the integral back into Equation 5.21

$$G_I^* = \left(\frac{2}{\alpha\pi}\right)\left[\frac{K_I^2(1-\nu^2)}{E}\right]\left(\frac{\alpha\pi}{2}\right)\ .$$

Thus, the relationship between the strain energy release rate and the stress intensity factor is

$$G_I = \frac{K_I^2\ (1-\nu^2)}{E}\ . \qquad (5.23)$$

5.6.0 Plane Stress-Plane Strain Conditions

5.6.1 Dependence of G or K on Thickness and Fracture Appearance

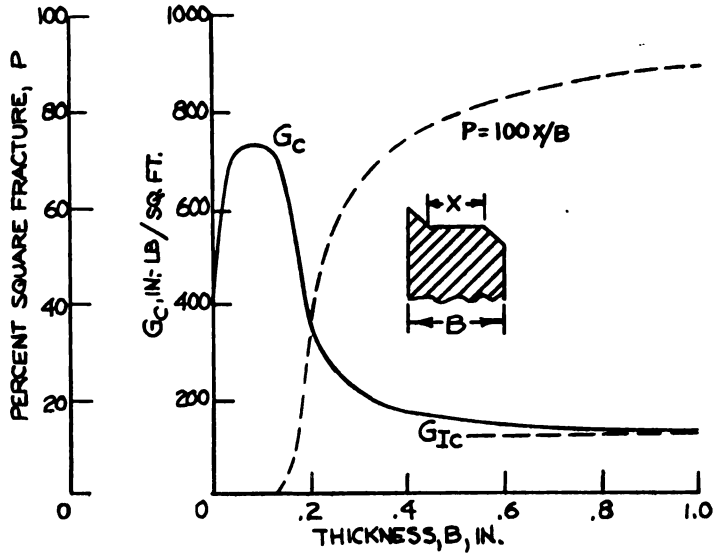


Figure 5.8.0--Dependence of G_C on thickness and fracture appearance (Data determined by Irwin, Kies, and Smith, Proc. A.S.T.M., Vol. 58, 1958 on 7075-T6 aluminum. Figure after Srawley and Brown, used with permission of the publisher).[20]

G_C is shown to be sensitive to the plate thickness in Figure 5.8. Several[21-25] investigators have observed the peaked shape of the G_C curve versus thickness or reciprocal thickness, and therefore believed to be a general characteristic. J. I. Bluhm proposed a bimodal fracture model[26] for sheets. A theoretical curve derived from this model duplicates the observed experimental shape.

Plate material whose thickness has been reduced by machining shows the same thickness effects as one reduced by rolling, hence the effect cannot be attributed entirely to metallurgical process variables.

The ascending portion of the curve is associated with the energy of shear lip fracture and assumed to be proportional to the square of the lip width. Bluhm has assumed that the shear lip occupies the full sheet thickness until a critical sheet thickness t_o is reached, beyond which the total lip width doesn't increase. The decending portion of the curve corresponds to a predominance of "square fracture." Flat fracture is presumed to be a surface phenomenon. The peak notch in the G_C versus reciprocal thickness curve of β-titanium[27] is not in agreement with a volumetric model of shear lip formation. Such a curve can be duplicated by assuming shear lip formation is a surface phenomenon.

Nevertheless, the essential aspect of the curve that all investigators agree upon, is that as the percentage of flat fracture increases, G_C decreases until it attains an approximately constant value. At sufficiently large thickness, the slant fracture occupies only a negligible portion of the total fracture surface. When the thickness is great enough, the stress state at the fracture changes from a condition of plane stress to plane strain.

5.6.2 Plane Stress to Plane Strain Transition

That G_C is a function of plate thickness should not be surprising, from what has been stated earlier concerning the triaxial stress state concept. Thin plates are unable to generate stresses normal to the surface of sufficient degree, so local yielding takes place through the entire section. The plane stress condition is $\sigma_{ZZ} = \tau_{XZ} = \tau_{YZ} = 0$. When the plate is sufficiently thick, contraction normal to the plate does not occur due to the resistance of the surrounding mass of elastic material. This constraint gives rise to large stresses throughout the section. This latter situation gives rise ultimately to plane strain condition, $\tau_{XZ} = \tau_{YZ} = 0$ but $\sigma_{ZZ} \neq 0$. The plane stress-to-strain transition for a given temperature, occurs abruptly as the plate thickness is increased. The G_C versus thickness curve is a measure of this transition. When G_C assumes a constant value, plane strain conditions prevail, and the measured value is G_{IC}. Plane strain crack toughness is especially important since it is a constant for each material for a given set of conditions, and more important, it represents the practical fracture toughness lower limit.

5.6.3 Plasticity Effects

All the discussion thus far has assumed an isotropic, linear elastic condition. The crack tip stress

field equations suggest that as the crack tip is approached (i.e. r approaches zero), the stresses σ_{xx}, σ_{yy}, and σ_{xy} all approach infinity for any finite value of the stress intensity factor, K. Physically, this does not happen, the material close to the crack tip undergoes nonlinear deformation, that is, yields plastically.[28]

The yield exhibits itself in the form of slow crack extension while the load is increasing. A plastic zone precedes the crack front. Plastic deformation, a stress relaxant, reduces the intensification of the local stress field caused by the load and crack length. Both G and K increase at a much greater rate during the slow growth period, than does the plastic region, so failure is imminent with continued loading. If the plate thickness is large enough, it is the plastic region which is constrained by the surrounding elastic material which gives rise to the plane strain condition. It is necessary to emphasize the point that the entire plate is in a state of plane stress, providing the constraint necessary for the establishment of plane strain close to the crack.

The crack plane strain condition is generally confined to the plane of the fracture or regions close to this plane, as the sketch in Figure 5.9 shows. The transition from the normal or tensile mode to a shear texture as the crack front approaches the free surfaces of the sheet corresponds to a relaxation of σ_z, hence the change from

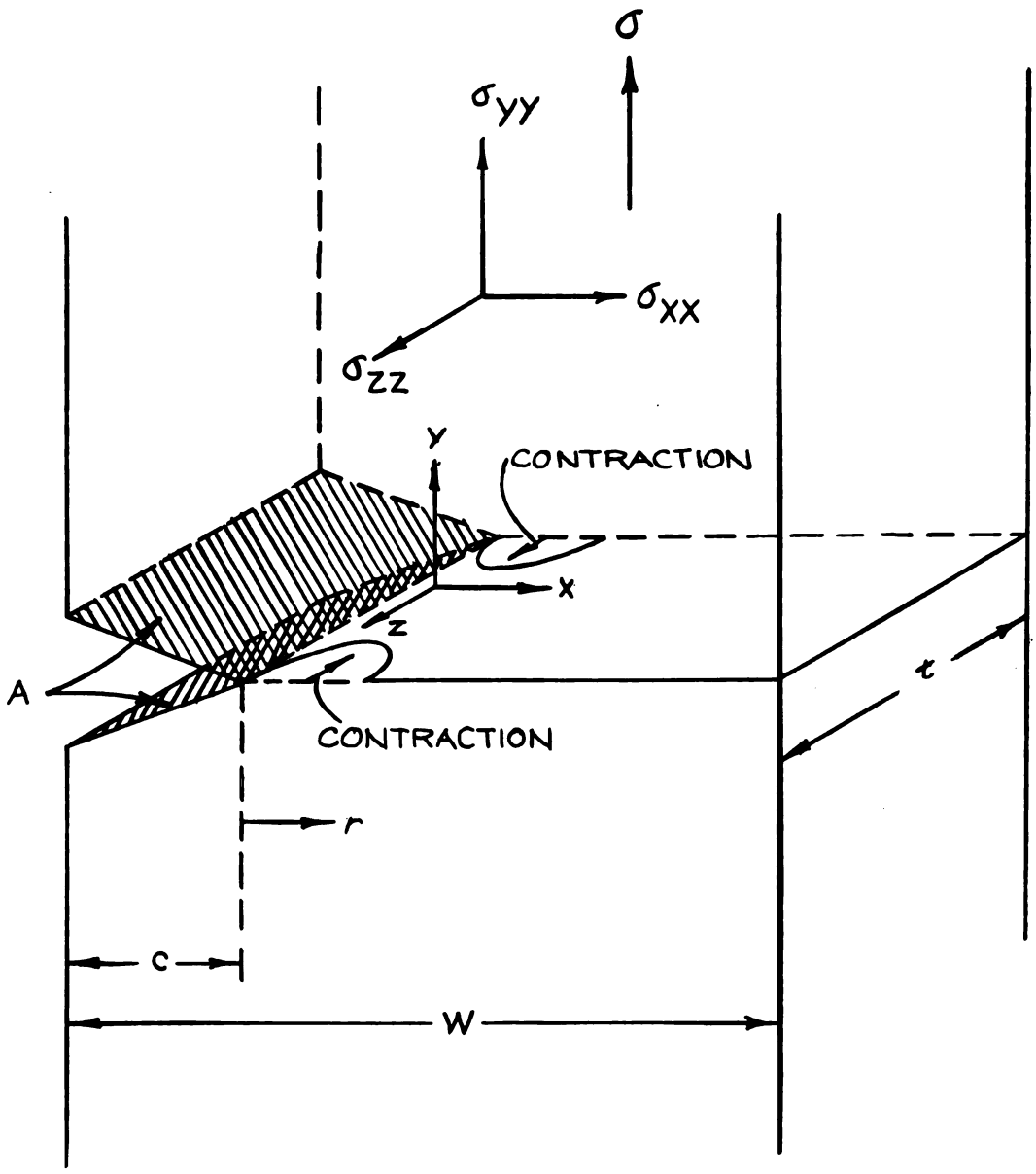


Figure 5.9.0--Transverse contractions that occur near the tip of a notch in a thick plate. (These contractions are opposed by the unyielding faces A of the notch; consequently transverse tensile stresses σ_{zz} and σ_{ss} are set up ahead of the notch tip.) (After A. S. Tetelman & A. J. McEvily, used with permission of the publisher.)[29]

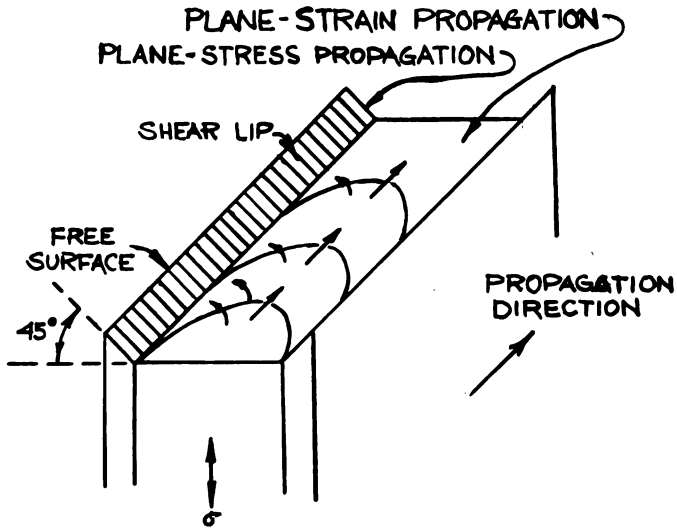


Figure 5.10.1--Direction of plane-stress and plane strain modes of crack propagation in a plate or sheet. (After Tetelman and McEvily, used with permission of the publisher.)[29]

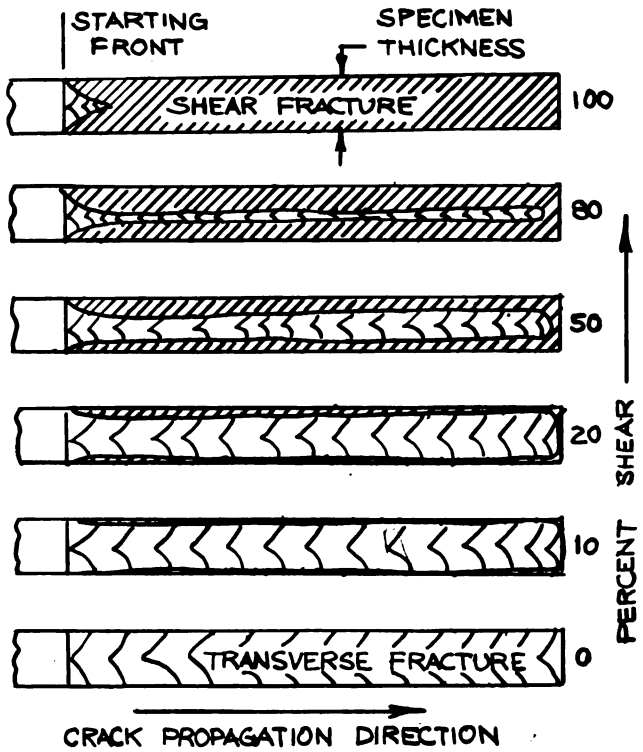


Figure 5.10.2--Characterization of fracture appearance by percentage of specimen thickness occupied by shear borders (per cent shear). (After Special A.S.T.M. Committee Report used with the permission of the publisher.)[31]

plane strain to plane stress[13] (shear lip formation). A relaxation in σ_z causes the plastic zone to increase, which in turn causes further relaxation of σ_z, and so on.[30]

The shear lip formation is sketched in Figure 5.10.1, and the appearance of the fracture surface of a plate as a function of ductility (per cent shear)[31] is sketched in Figure 5.10.2.

5.6.3.1 Size of the Plastic Zone

The size of the plastic zone can be an important consideration when calculating fracture toughness. The relaxation effect at the crack tip, increases the "effective" length of the crack. If the plastic zone size were known, a correction factor could be added to the measured size of the crack at the critical load. An accurate representation of the stress relaxation influence is not possible at the present. Some similarities have been noted between the influence of plastic strains due to cracks in plates and the effect that cylindrical holes have on the nature of the stresses in plates. The stress system near the middle plane of a plate differs very little from one corresponding to a plane strain situation, for a plate in uniaxial tension, if the hole diameter is less than half the plate thickness.[32] It was therefore concluded, that the plane strain situation existing in the central region of the plate isn't disturbed by the relaxing

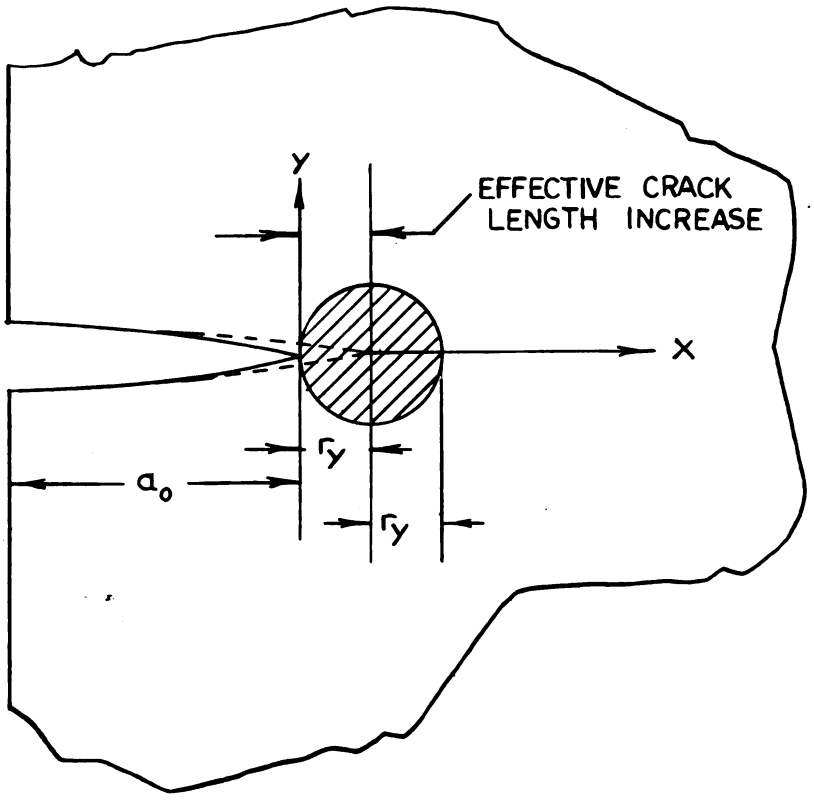


Figure 5.11.0--Effective crack length increase due to plastic zone.

influence of the plastic zone anymore than that exerted by a round hole whose diameter is less than half the plate thickness.[30]

Knowing the stress field equations around the crack tip, the principal extensional stress can be shown to be

$$\sigma_1 = \frac{K}{(2\pi r)^{1/2}} \cos\frac{\theta}{2}\left(1 + \sin\frac{\theta}{2}\right). \qquad (5.24)$$

The elastic-plastic border distance from the crack front is determined by maximizing the principal stress equation

with respect to r. The value of r thus obtained is the distance from the crack edge at which the predicted tensile stress equals the yield stress is greatest at $\theta = 60°$,

$$r_y = 0.84 \frac{K^2}{\sigma_{YS}^2} . \qquad (5.25)$$

The plastic zone can be viewed as a circular region as shown in Figure 5.11, whose radius is r_y. Normally the 0.84 factor on the RHS of Equation (5.25) is taken as unity, so that

$$r_y = \frac{K^2}{\sigma_{YS}^2} = \frac{1}{2\pi} \frac{K^2}{\sigma_{YS}^2} \quad \text{(PLANE STRESS)} . \qquad (5.26)$$

The plane strain plastic region is estimated at about one-third of the plane stress value,[33] so

$$r_{IYS} \approx \frac{1}{6\pi} \frac{K^2}{\sigma_{YS}^2} . \qquad (5.27)$$

5.6.3.2 Effect of Plasticity on G and K Measurements and Calculations

The plastic zone is adequately described by equation (5.27) up to an applied stress of 0.8 σ_{YS}, beyond which it underestimates the value.[34] From Figure 5.11, it can be seen that the effective crack length $a = (a_o + r_y)$ terminates in the center of the "plastic circle" in a 2-dimensional model. The stresses in the elastic material

surrounding this zone undergo a redistribution. The new position and magnitude of these elastic stresses are determined on the basis of considering the plastic zone as being elastic but increasing the crack size from a_o to a. The crack tip stress field equations show that near the tip the stress is high but falls off very rapidly (i.e. as $r^{-1/2}$).

Irwin[17] noted that the assumption should not be made that local stress relaxation and crack-opening distortion by plastic flow change the rate of loss of strain energy with crack extension from that which the linear elastic solution predicts. Moreover, he estimates that if the plastic zone isn't too large as contrasted to the other linear dimensions of the specimen, particularly the crack length, the contribution of the plastic zone to the total strain energy is small by comparison. The fractional contribution to the value of G is approximately $\frac{1}{3}\frac{r_y}{a}$.

5.6.3.3 Constraint Parameter

Having shown that plane stress toughness parameters (G_c or K_c) are strongly dependent on thickness and to some extent on crack length,[35] it becomes apparent that some quantity must be established to indicate when a particular toughness measurement is valid. Several parameters have been proposed to indicate whether a true condition of plane strain has been achieved. A special A.S.T.M.

Committee on fracture testing first proposed,[25] and finally adopted[36] the parameter

$$\beta_{IC} = \frac{K_{IC}^2}{B\sigma_{YS}^2} \tag{5.26}$$

where B is the plate or sheet thickness and the yield strength, σ_{YS}, is determined by the 0.2% offset method. This parameter's significance lies in its relation to the ratio of the plastic zone size to sheet thickness, which determines the degree of constraint. This relation was found to be

$$\frac{B}{2r_y} = \pi \left[\frac{B}{(K_c/\sigma_{YS})^2}\right] = \frac{\pi}{\beta_c} .$$

Experimental data on 7075-T6 aluminum indicated that when $B/(K_c/\sigma_{YS})^2 >> \frac{1}{\pi}, (B>>2r_y)$, the toughness is constant and independent of B. When $B/(K_c/\sigma_{YS})^2 << \frac{1}{\pi}, (B<<2r_y)$, the toughness increases linearly with the plate thickness, B. Between those 2 extremes, there is a decrease in the toughness value to the constant value, K_{IC}.[33] The decrease is termed the "fracture mode transition."

The parameter, β_c, has values extending from plane stress to plane strain. The ASTM Special Committee's first report (1960) stated that a β_c value equal to 2π, corresponds to a 100% shear fracture. The fifth report (1964) set the limits of $\beta_c < 1$, plane strain condition

exists and for $\beta_c > 4$ shear lips normally occupy more than half the fracture surface for many materials.

CHAPTER VI

STATIC FRACTURE MECHANICS PARAMETERS

6.1 Pop-In Method for Determining G_{IC}

In some instances the plate thickness would have to be fairly large to meet the requirements for a valid G_{IC} or K_{IC} measurement. If a large specimen section is tested, then appropiately at instability (G_{IC}) the specimen will fracture completely as skected in Figure 6.1(a).

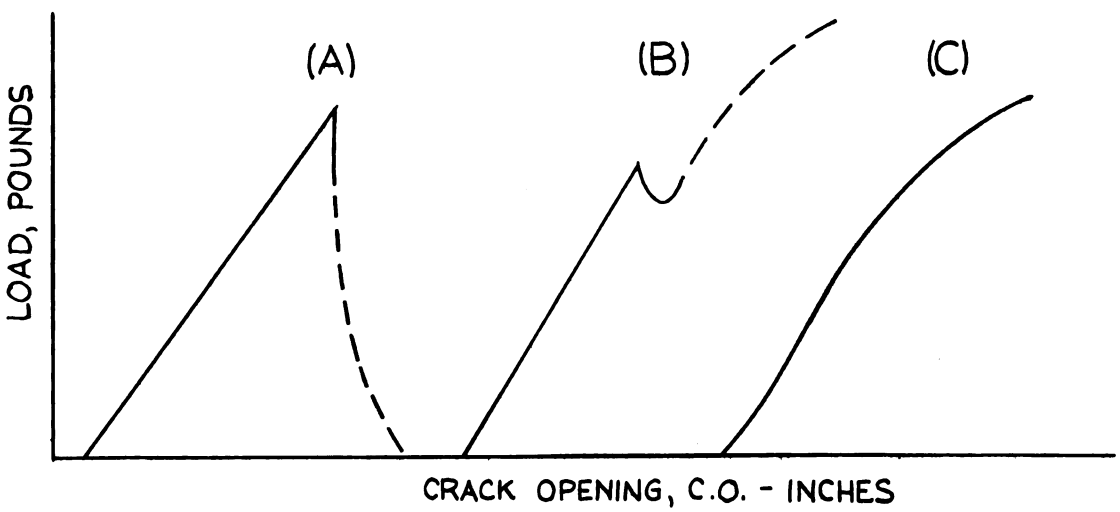


Figure 6.1--Typical compliance curves for various metals.

Boyle et al.[1] made a systematic study of the effect on crack growth resistance prior to rapid fracture by continuously decreasing the plate thickness of edge-notched 7075-T6 aluminum sheet. With the aid of a compliance gauge, specimens of only one-eighth the size of a notched round specimen conventionally used for this purpose yielded good results. The technique that they developed is known as "pop-in." The findings indicate that a plate specimen with a thickness of twice the plastic zone radius, $2r_p$, or more, will leave a break in the load--c.o. curve as indicated in Figure 6.1(b). The maximum applied load before instability is easily discernable from such a plot. Boyle et al. determined that the stress intensity factor determined this way, K_{NC}, is only slightly lower than that found by using conventional samples. Since this equivalency has been determined, the standard designation, K_{IC}, is also applied to pop-in values. As the specimen thickness decreases below the value of $2r_p$ the exact point of instability becomes less distinctive as indicated by the load-c.o. record shown in Figure 6.1(c). Boyle indicates that if the specimen thickness is greater than $4r_p$, it can be expected that most of the section is still elastic; the observed inflection in the curve is accompanied by an audible sound, hence the term "pop-in." It has been pointed out that Boyle's specimens had sharp, machined notches that were not crack tipped which accounted for more distinctive pop-ins than would have been observed if they were fatigue

cracked. Machined notches also result in higher K_{IC} values.

The pop-in characteristic is easily explainable in terms of aforementioned plane stress and strain condition which prevail in the specimen. That is, plane strain prevails near the center portion of the thickness while plane stress conditions exist near the faces. The surface influence extends into the thickness for a distance proportional to $(K_I/\sigma_{YS})^2$. There exists therefore some critical thickness value whereby the constraint-relieving influence of these free surfaces is continuous through the entire section. Under these conditions the stress intensity factor never achieves the value of K_{IC}, and slow crack growth is observed, rather than the abrupt slope change in the load--c.o. record.[2]

The crack arrest situation has been puzzling because a sudden extension of the crack should result in a constant or decreasing load depending on the machine stiffness. It might be logically reasoned that the crack arrest follows from a reduced load which in turn decreases the stress intensity factor below the critical value. The experimental evidence, however, indicates little or no drop in load during pop-in, and that crack arrest even occurs during dead-weight loading. It would seem that a load drop isn't a necessary condition for crack arrest. An engineering model of pop-in indicates that in reality

there is an effective load decrease due to the "relieving" influence of the plastic deformation accompanying fracture.[3] The theoretical aspects surrounding the metastability of pop-in have been fully discussed by Srawley and Brown.[4] The arrest features of pop-in are only discussed to aid in the general understanding of the behavior of fractures. In summary, pop-in behavior can sometimes be useful in obtaining valid K_{IC} values by reducing the section size. Medium strength materials can't possibly be measured by conventional specimens, whereas pop-in techniques offer some hope. Extensive testing of such materials even by pop-in becomes cost prohibitive, inconvenient, and requires a high load capacity universal testing machine.

6.2 Monitoring the Crack Opening

It is essential that the load-displacement conditions be known accurately at instability. Several techniques will be discussed briefly. The experimental method selected should have a high resolution capability of measuring the progress of slow crack growth as well as the point of instability. Changes in resistance due to the decreased current carrying capacity produced by crack extension has been found suitable for this purpose.[5] Similarly potential field distribution diagrams illustrate the potential change with crack growth. The crack growth

is followed by measuring the electric potential across the crack. Errors due to thermal electromotive forces are eliminated by a-c measurements which minimize the current flow in the system.[6] The electric-potential method relies on the fact that the potential distribution in the vicinity of a crack changes during crack growth. A calibration curve is necessary to convert the potential measurements to crack lengths. This calibration was found to be independent of material chemistry, heat treatment, thickness, but is sensitive to the geometry of the crack-starting flaw, as might be suspected.[7] Mechanical-electrical systems have also been used.[8,9] These are extensometers with an attached microformer, whose output is fed to an X-Y recorder to obtain load-displacement curves. Acoustic techniques[10] have also been used successfully. An ordinary phonograph pickup is attached to the specimen. At the onset of cracking (instability) a sound burst is emitted having an intensity well above general background. This method has been found to be sensitive enough to indicate the point of instability even in cases where compliance - gauge records make no clear indication. Fracture toughness, K_{IC}, determined by acoustic methods is always less than that determined by compliance measurements because the first fracture sounds are recorded before abrupt slope changes are noted for the latter. The method is

sensitive to extraneous sounds such as the breaking of surface scale. Another problem is that there is no response to plastic flow. Excessive flow causes notch blunting that in turn raises the pop-in load. Compliance or displacement gauges, such as described in ASTM Designation E 338-68 (Sharp-Notch Tension Testing of High-Strength Sheet Materials), appear to be the most widely used sensors for crack-opening monitoring. A calibration of the gauge output vs. displacement is necessary. The compliance gauge is usually composed of several strain gauges that comprise the various arms of a poteniometric bridge. The outputs from such a bridge and a load transducer are fed to an x-y recorder. The specific sensing techniques used in this study will be explained in greater detail in Chapter VIII.

6.3.0 Static Determination of G and K via Single-Edge-Notch Tension Specimen

Several specimen configurations are used for the determination of fracture-mechanics parameters.[11-14] A closed-form solution for the determination of G from a tension specimen does not exist. It should be mentioned that some analytical work has been done to determine K_{IC} by boundary collocation which is also called point matching.[15-18] A series solution is truncated to the appropriate partial differential equation. The coefficients are evaluated through the use of boundary values at a

finite number of points.[18] The analytical investigations were found to be in good agreement with experimental work.

An approximate solution was developed[19] for the single-edge-notch tension specimen. Equation 5.11.2 can be rewritten as:

$$G = \frac{P_N^2}{2} \frac{dC_N}{da}$$

where C_N and P_N are the normalized compliance and load, that is, per unit plate thickness. In order to non-dimensionalize the equation it is necessary to multiply both sides by the width, w, and the modulus of elasticity, E,

$$\frac{EwG}{P_N^2} = \frac{E}{2} \frac{dC_N}{d(a/w)} \quad . \tag{6.1}$$

6.3.1.1 General Calibration Procedure

In order to determine $dC_N/d(a/w)$ over a wide range, a series of compliance measurements are made for a sufficient number of (a/w) ratios. Equation 6.1 is independent of specimen thickness, since G is in terms of unit length of crack border (ft-#/in). The load and compliance are in terms of unit plate thickness. Moreover, the equation is also independent of the size scale of the specimen dimensions. A calibration performed on 1 single-edge-notch specimen is valid for others so long as their dimensions are in proportion to the originally calibrated

specimen, except for the thickness which can be within certain limits as previously discussed.

6.3.1.2 Development of the Polynomial Form

Srawley, et al. considered various $(\frac{a}{w})$ and the corresponding values of $(\frac{EC}{2})$. These data were fitted to polynomials in $(\frac{a}{w})$ of degrees 3 through 7 by means of a least-squares best-fit digital computer program. The program made allowance for the condition that the coefficient of the first power in $(\frac{a}{w})$ was equal to zero for each of the polynomial groups. This was done to satisfy the physical condition that G = 0 when the crack length equals zero. The 4th-degree polynomial was found to be significantly better than the third-degree, with higher degrees adding little improvement. The best-fit criterion was stated as the smallest index when taking the sum of the squared residuals divided by the number of degrees of freedom, n-k-1, where:

n is the number of data points, and

k is the degree of the polynomial.

The fourth-degree polynomial yielded the lowest index for all cases. The fourth-degree polynomial "best-fit" values for EC/2 compare very favorably with experimental compliance measurements. When the fourth-degree polynomial is differentiated with respect to $(\frac{a}{w})$ an expression $(\frac{E}{2})$

$dC_N/d\left(\frac{a}{w}\right)$ is obtained, which is a third-degree polynomial in $\left(\frac{a}{w}\right)$. The desired expression is

$$\frac{E}{2}\frac{dC_N}{d(a/w)} = \frac{EwG}{P_N^2} = A_1\left(\frac{a}{w}\right) + A_2\left(\frac{a}{w}\right)^2 + A_3\left(\frac{a}{w}\right)^3 + \ldots \quad (6.2)$$

The coefficients determined from the least-squares technique are: $A_1 = 7.586$, $A_2 = -31.90$, and $A_3 = 117.28$; so the working equation is therefore

$$\frac{EwG}{P_N^2} = 7.586\left(\frac{a}{w}\right) - 31.9\left(\frac{a}{w}\right)^2 + 117.28\left(\frac{a}{w}\right)^3 . \quad (6.3)$$

CHAPTER VII

DYNAMIC FRACTURE MECHANICS

7.1.0 Instrumented Impact- Initial Studies

The Charpy impact test does not yield information that can be directly applied in design calculations. At best it is an indication of a material's resistance to brittle fracture, used with good success in the role of quality control. The test is well suited for such work. The Charpy bar is relatively easy to prepare, and the small size helps to conserve material. The test information is only predictive in a broad sense, and therefore only used for screening purposes in materials selection studies. The test results are very repeatable under similar test conditions, which also explains its usefulness in a quality-control role when correlations with service data are available. Although popular, impact testing has never been on a par with the uniaxial tensile test in material studies because-unlike the tensile test-it does not yield material parameters. Only recently have attempts been made to make impact testing quanitative. The impact test, coupled with its simplicity and economy, would be especially desirable for dynamic-

deformation studies if it yielded universally accepted parameters.

To obtain this additional information the impact machine can be instrumented in various ways. All these techniques ultimately yield either force-time, or displacement-time records and in some cases both. These curves are a continuous record of failure, whose shapes, etc. have been analyzed and have given some insight into failure mechanisms. Yamada's photographic plate set up[1] is illustrative of the elaborate optical techniques used in an attempt to monitor the pendulum velocity. Watanabe[2] (1929) introduced a concept that is still used today: directly coupling a force transducer to a loaded member of the assembly. A pair of quartz discs fixed to the anvil supplied the record obtained via the piezo-electric effect. Some of his load-time records did show evidence of brittle failure. In the three decades that followed, little progress was noted due to the lack of good sensors (dynamic load transducers). However, since the invention of the resistance strain gauge, much of this problem seems to have been overcome. S. Ono,[3] among the first to use strain gauges in this type of application, falsely concluded that the test will not allow the absorbed energy to be partitioned into the initiation and propagation stages. It is this feature that makes an instrumented test attractive. Cotterell's[4] (1962) indirectly determined energy absorption data

(calculated from load-time records) were in poor agreement with the directly determined (read from impact tester scale) data. He mounted piezoelectric gauges on the pendulum. Augland[5] (1962), with resistance strain gauges mounted to the anvil, qualitatively obtained the same shape load-time records as did Cotterell. His data, however, did show good agreement between directly and indirectly determined absorption energy. This was a first indication that the records actually would allow the actual energy absorption during fracture to be determined. The assumption of a constant pendulum velocity introduces negligable error when large energy capacity machines are used. Error can, however, be eliminated by the relationship

$$E_{CORR.} = E_{EXP.} - (E^2_{EXP.}/4E_{IN.}), \qquad (7.1)$$

where $E_{CORR.}$ is the energy corrected for a reduced pendulum velocity, $E_{EXP.}$ is the energy derived from the load-time curve, assuming a constant pendulum velocity, and $E_{IN.}$ is the initial energy of the pendulum. In late 1962, G. D. Fearnehough,[6] with the aid of Equation 7.1, confirmed Augland's results: the integration of load-time records results in a direct correspondence between directly and indirectly assessed absorption energy.

7.1.1 Static Calibration of Load Transducers

Independent of the type of force transducer used in instrumented impact studies, the calibration is done

statically. This practice might be questioned since the test is carried out under dynamic conditions. Strain gauges are usually used as transducers because they are cheap, small and easy to mount where desired. Wire gauges have been shown[7] to have a "flat" frequency response up to 20k Hz. with an error not exceeding 5% if sufficient care is taken to insure that only a thin layer of cement is used for bonding.

Study of the response to strain waves with rise times of very short duration have shown that strain gauge rise times are less than 0.5μ-sec. + 0.8 L/C, where L is the gauge length and C is the longitudinal elastic wave velocity of the material on which the gauge is mounted.[8] Wire gauges thus have a response time of about 1 micro-second, and can be considered to be very reliable for transient elastic strain measurements. Tardif and Marquis[9] provided the proof that strain gauges used in the present application yield the correct output records necessary with negligible error. Strain gauges were mounted on the striker to obtain load-time records. They also independently determined dispalcement-time records from the output of a photocell interrupted by the hammer. The total intensity of the light reaching the cell at any instant is proportional to specimen deflection. The photocell calibration was made by pendulum free-fall, where the velocity can be considered constant for the small interval of interest. The displacements obtained from the double

integration of the force-time records were in excellent agreement with the photocell values.[9]

7.2.0 Charpy Impact Test Accuracy and Repeatability: Conventional and Instrumented

It has been shown that the Charpy impact test is highly reproducible if the machine is in good working condition. Ninety percent of the specimens tested with up to 20 ft.-lb. absorption energy can be determined to within an accuracy of $\pm$ 1.0 ft.-lb., and $\pm$ 5 ft.-lb. above 20 ft.-lb. The results would almost always fall within the prescribed limits if 5 specimens are averaged.[10]

The reproducibility of the instrument is of course no guarantee of its accuracy, for it may be consistently high or low. Factors that have been found to seriously affect the accuracy of the readings are related to installation where vibrational losses become important. The alignment must be such as to insure that the center of percussion is at the center of the striking edge. The edge of the freely hanging pendulum must rest uniformly at the back side of the specimen directly behind the notch. Dirty and faulty bearings both give rise to erroneous readings. Sometimes the broken halves of high strength materials do not leave the machine in the direction of the pendulum swing, as most low strength specimens do. Often they have a tendency of leaving in a sidewise direction,

rebounding, and hitting the pendulum before completely clearing the anvil. Such jamming is not unusual and will result in enormously high values. Assuming a previously reported estimated exit velocity of 50 ft./sec. for brittle materials, the kinetic energy for brittle titanium and zirconium Charpy bars would be 2.16 and 3.1 ft.-lbs. respectively. These values are significant becuase brittle materials characteristically have low absorption energies. There are several critical dimensions which must lie within the tolerances stated in the ASTM Standard E23 (Notch Bar Impact Testing of Metallic Materials).[11,12] Machining and positioning of specimens are discussed in E23 and elsewhere.[13,14] If the stiffness of the pendulum arm is decreased, then the peak force that the instrument can develop is also decreased.[15] Many of the sources of error discussed are eliminated with an instrumented impact test. The energy absorbed during impact as indicated by the dial value on the instrument, is not measured directly. The potential energy of the hammer system is fixed by the initial starting position, which is fully converted to kinetic energy at the bottom of the swing. This occurs exactly before the hammer strikes the sample. The position of the upswing of the pendulum, a measure of the energy not required for fracture, is monitored by a mechanical linkage coupled directly to the indicator. It is assumed that the energy absorbed in fracture is the

difference between the initial potential energy and the pendulum energy after fracture. Factors other than fracture may absorb the energy, however. Significant levels of strain energy can be absorbed by the hammer head, hammer arm and anvils; vibrational energy losses can take place in the arm, hammer and anvil; energy absorption takes place in the bolts of the hammer-to-head connection, anvil-to base connection, base-to-floor connection; and the already discussed kinetic energy of the broken pieces, etc. It should be apparent that the indicator reading will only be correct under the best of conditions.

With an instrumented test, the signal is obtained directly from a load transducer. Assuming good electronics, errors introduced by most of the aforementioned factors will be eliminated.

7.3.0 Crack Formation and Progression in Charpy Specimens During Loading

It is useful to have a correlation between crack formation and growth in the sample and the load-deflection curve. This is difficult to determine during an impact test, but relatively simple to do in a slow bend test of a Charpy specimen. The impact test can be thought of as a dynamic 3-point bend test. R. Raring[16] (1952) and J. D. Lubahn[17] (1955) undertook such investigations and note that a linear relationship exists between the load and

the deflection, denoted by OA in Figure 7.1. The departure from linearity at A denotes that plastic deformation commences here. Some plastic deformation takes place before any cracks are noted represented by point B. Such cracks always seem to occur at the root of the notch near the midpoint. If d_i and w_i are the depth and width of the initiating crack respectively, d_i remains about constant up to the maximum load (point c), while the crack width increases laterally to the specimen sides, w_s.[18] Beyond the maximum load, the crack increases in depth, d_p and extends down the sides of the specimens. The crack propagates beyond the maximum load and explains the attendant loss of load carrying capacity with decreasing cross section. Although these observations pertain to static tests there is no obvious reason to believe that fracture initiation and propagation of Charpy specimens is any different in impact, especially since the load-deflection curve characteristics are the same.

7.3.1 Interpretation of Charpy Impact Load-Displacement Curves

Tardif and Marquis[9,19] have described the general shape of load-displacement curves for materials that range from ideally elastic (fully brittle) to ideally plastic (fully ductile). Similar descriptions have also been given by others.[20-22] Curve A (Figure 7.2) is

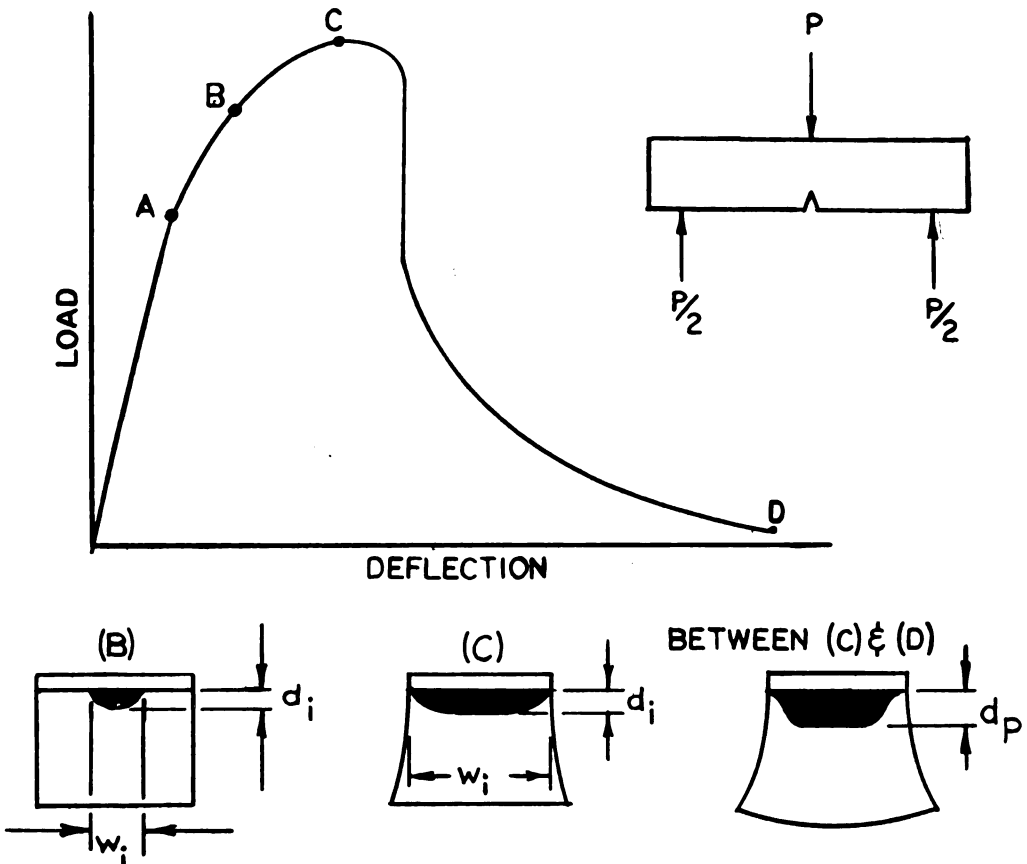


Figure 7.1--Schematic representation of a load-deflection curve obtained by slow three-point bending. (After Hartbower, used with permission of the publisher).[18]

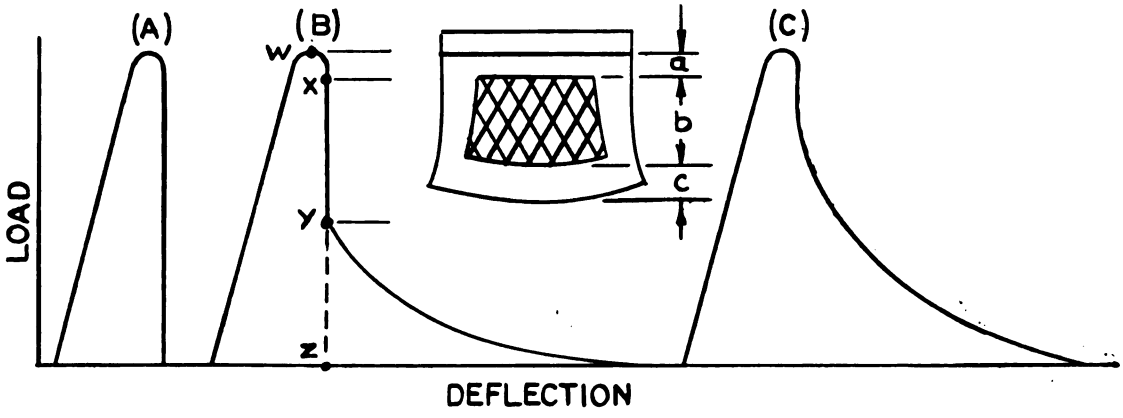


Figure 7.2--Typical load-deflection curve shapes for materials ranging from completely brittle to completely ductile. (After Tardis and Marquis, used with permission of the publisher).[19]

representative of a brittle material. The load rises to a maximum, decreases slightly due to the small plastic deformation that precedes even the most brittle failure. The more brittle a metal is, the less perceptible this slight decrease is. Finally, the load drops abruptly. A very ductile material is represented by curve C, where the load reaches a maximum and decreases very slowly with an ever-changing slope. Most metals are neither entirely brittle nor ductile, and their load-displacement curves are some combination of these 2 extremes, as represented by curve B in Figure 7.2. A sketch of a Charpy bar fracture surface area demonstrates the close correspondence to the load-deflection curve. There is usually a fibrous area (section a) immediately below the notch indicating ductile failure, hence the slow decrease in the load. The hatched area represents predominately cleavage failure, corresponding to the almost vertical drop in load on the curve. The crystalline area is surrounded by fibrous failure which comprise the "shear lips" of the Charpy specimen. Finally fracture resumes in a ductile manner indicated as section C.

These curves are characteristically those noted for the failure of steels; however, their interpretation should be quite general and allow some important conclusions to be made concerning the nature of fracture

initiation and propagation in ideally elastic, ideally plastic, and real materials. For example, the curves confirm the fact that unstable cracks in elastic materials require no extra externally supplied energy for propagation. After the maximum load is attained, propagation is almost instantaneous (catastrophic failure) as evidenced by the almost vertical drop in the load. If the propagation energy isn't supplied externally, then it must be internal (i.e. continuous release of the elastic-strain field energy surrounding the crack). Ductile materials do not fail catastrophically after the maximum load is attained. The slowly decreasing load with time represents the plastic deformation work necessary in order to propagate the crack. Clearly the area beneath the load-displacement curve represents the total energy necessary to cause failure of the Charpy specimen. The instrumented test allows this energy to be partitioned into two fracture stages: initiation, which is given by the area beneath the curve from zero to the maximum load, P_{MAX}; while the propagation energy is represented by the area from P_{MAX} to zero load. The ability to determine a material's crack propagation energy separately is an important development, since most materials already contain flaws. If design is based upon the total fracture energy, the part or structure will be over rated.

Finally, the oscilloscope trace directly allows for a quantitative determination of the per cent crystallinity. This then allows for a more accurate description of the degree of brittleness in the fracture. The brittle component of the failure is easily differentiated from the ductile by the slopes on the load-deflection record. For example, the per cent crystallinity of the failure represented by curve B in Figure 7.2 is

$$\% \text{ crystallinity} = \frac{XY}{WZ} (10^2). \qquad (7.2)$$

Previously the % crystallinity was determinated by a visual approximation, or by planimeter measurements on photographs of fracture surfaces.

7.4.0 Background on Charpy Impact Techniques Used in Dynamic Fracture Mechanics

Dynamic testing to determine fracture parameters has gone through several stages of development, but it is far from being standardized to the extent that the static testing is. Aside from the convenience and economy afforded by a Charpy specimen, it has been hoped that dynamic testing will enable fracture mechanics to be extended to medium strength materials. Statically the plane strain fracture mechanics values can only be obtained if the specimen fails catastrophically with no plastic deformation, or that the plastic deformation conforms to an acceptable "pop-in"

characteristic. Fractures are found always to initiate after gross yielding for materials within the normal transition range when tested by Charpy impact.[23] Therefore, Charpy testing might seem to suffer from the same drawbacks as static testing. Wells[24] recognized the relevance of fracture mechanics to notched specimens which fail after general yield. He determined that: $G_C = \sigma_y \delta$, where σ_y is the yield stress for yielding materials in a state of plane stress and δ is the crack opening displacement (C.O.D.). Well's interpretation of the strain energy release rate is in terms of the local crack tip stress and distance through which the crack has been displaced. There is an analogy between the equations relating the applied stress and crack length to G and also to C.O.D. The early dynamic work is therefore based upon the implication that a critical C.O.D. can be measured although general yielding precedes fracture. Knowing the pendulum velocity, and the time span between the start of impact and initiation of brittle fracture from the load-time record, the bend angle of the specimen can be calculated. The latter in turn is used to determine the C.O.D. from the specimen geometry. For a Charpy specimen both a theoretical slip line analysis[25] and an experimental study[26] indicate that

$$\text{C.O.D.} = 2.4 \times 10^{-3}\ \theta^{o}\ \text{in.} \qquad (7.3)$$

This type of an approach in termed "time-to-brittle fracture" technique.

More refined approaches have been taken using the "time-to-brittle fracture" technique, such as applying 3-point beam bending theory to Charpy bar loading. To adjust these equations for dynamic conditions, the bar's inertia resistance is modeled as a beam on an elastic foundation.[27] Such solutions are well known. Even further refinements have been made by considering the rotational effects caused by the notch in the bar.[25]

7.4.1 Strain Rate Effects on Fracture Mechanics Parameters

The real importance of dynamic fracture testing was brought to light by the work of Eftis and Krafft[29] (1965) who noted that there is a trough (minimum) in K_{IC} versus strain rate, $\dot{\varepsilon}$, curve. The minimum value extended over a wider range of strain rates as the temperature was lowered from +20 to -196°C for the steel tested. This implies that at least some materials possessing low mechanical strength which are sensitive to strain rate or temperature may be expected to exhibit rapid deterioration of their fracture toughness in field applications due to unforseen temperature drops or a quickened loading pace. There is no guarantee that the critical strain rate ($\dot{\varepsilon}$ corresponding to the trough value for K_{IC}) for a

particular metal under test is exactly the same as supplied by an impact tester. In several studies, although all on steel, the impact strain rate did lie in the trough. According to Irwin, the possibilities of determining K_{ID} (dynamic K_{IC}) are very good with a Charpy test. He has found that the load-rise time in such test is controlled by the minimum K_{IC} value in the trough.[30,31] The method has been found to be very effective as a material screening test for dynamic applications.[32]

7.4.2 Problems Due to Oscillations in the Load-Time Record and Inertia Effects

The characteristic "load-time" curve oscillations have been the subject of much concern. Augland[5] felt that they were a general feature of impact testing thus would not allow the exact load record to be determined in the elastic portion of the curve. Cotterell[33] concluded that the oscillations were due to the natural frequency of vibration of the unbroken Charpy specimens by citing some work by T. S. Robertson (1961). The discontinuities are thought not to be a feature of the deformation process in that no significant relationship between them and specimen behavior has been found.[23] The oscillations sometimes occur near the yield point,[4,23] making it difficult to interpret the results of materials that fail close to the yield point. The magnitude of the initial jog in the elastic

portion of the curve is proportional to the impact velocity. These oscillations are gradually damped when appreciable yielding accompanies the fracture. Tardif and Marquis have reported that the Charpy test geometry is the cause of the oscillations. The thickness dimensions have no effect, but the length does (i.e. distance between supports). As the anvil span length increased, the oscillation frequency decreased accordingly, hence identifying the oscillations with the vibrational bending of the specimen during fracture. Other factors such as magnetostriction, specimen alignment, pendulum arm vibration, and stress-wave interaction; do not seem to effect the high frequency load-time oscillations. They concluded that if the impulse curve is assumed to pass through the average of these oscillations, zero error will be introduced into the energy determinations.

A comprehensive study undertaken by the Intra-Group Laboratories of the British Steel Corporation (BISRA) on the vibrational and inertia effects in the Charpy test indicates that the interpretation of a load-time curve is far more complicated than originally thought. Instrumentation of the tup, anvil and specimen for the same impact all yield different curves. In fact, it is possible to register a maximum load on the tup before the specimen comes in contact with the anvil. The load equilibrium is between the inertial load at the center of the specimen and reaction at the tup. Unfortunately no simple relationship seems to exist between the load on the specimen and

on the tup or the anvil. Using the maximum load registered by either the tup or anvil as the fracture load in formulae can cause significant error. The load, P, on the specimen, at any time, t is given by

$$P = \frac{vt}{C_M + C_S}$$

where v, is the velocity of the hammer and assumed a constant throughout the test; and C_M and C_S are the compliances of the test machine and specimen respectively. Beside knowing the actual load at fracture, the time-to-fracture must also be known. The time indicated on the load-time curve is not sufficiently accurate for K_{IC} calculations. The output of post yield strain gauges placed over the notch increases rapidly after fracture initiation and thereby can be used as a time-to-fracture indicator. However, the records from gauges mounted on the side of the specimens can only serve as an indication of the relative toughness among different materials, but again do not yield accurate time-to-fracture information.[34-36]

It has recently been estimated that Charpy dynamic K_{IC} values determined by aforementioned formulations can be inaccurate by as much as 20% due to oscillation and inertia effects.[37]

7.5.0 Controversy Over the Use of the Charpy Impact Test for the Determination of Fracture Mechanics Parameters

Viewing the Charpy specimen from a fracture mechanics point of view, it is merely an undersized 3-point bend specimen. For valid K_{IC} measurements, the crack length and specimen thickness should be greater than some multiple of $(K_{IC}/\sigma_{ys})^2$.[38] Present data suggest that this multiple shouldn't be less than about 2.5. The standard Charpy specimen thus limits the maximum K_{IC} measurement capacity to only 0.28 σ_{ys}. Also the recommended ratio of the span length, L, the width, w, for a 3-point-bend specimen is 8, while only about 4 for the Charpy specimen. Considering all these geometrical factors, it is assumed that G_{IC} values can only be determined if they fall below $\sigma_{ys}^2/10E$. Various techniques have been used to avoid the formation of shear lips and thereby more closely approaching the plane strain condition. In the case of steels, a thin brittle layer on the outside of the sample is easily introduced by nitriding[40,41] or carburizing[21] to suppress the plastic deformation. Also found effective for materials that cannot easily be subjected to such treatments is face grooving and fatigue cracking the notch.[42] Whether such methods are sufficient to supply the constraint in simulating thick section tests is still unanswered.

Perhaps even more important is the uncertainty of the effects of the grooves themselves. If they are too deep, or too sharp, the cracks will initiate from them. Since no systemic study exists to define the various aspects of face grooving, it appears only to add more complexity to an already complex problem. The energy consumed in the Charpy test, $E_{abs.}$, can be equated to the energy necessary for the formation of new surfaces. Orner and Hartbower[43] have stated that the strain energy release rate is equal to the absorbed energy, $E_{abs.}$, divided by the area of the fracture cross section, b(w-a), where b, w, and a are the breadth, width and the crack length dimensions of the Charpy bar respectively. They contend that the energy difference between a Charpy bar tested in slow bending and in impact gives a good measurement of a material's dynamic fracture resistance. A "near-one-to-one relationship" was found for G between a large number of different alloys tested with precracked Charpy bars and various fracture toughness tensile tests. Of particular interest was the fact that some materials demonstrate enhanced fracture toughness under impact, while others, such as an all-beta titanium alloy, the toughness was markedly reduced. Dynamic to static fracture toughness ratios have been suggested as a means of expressing a material's strain rate sensitivity. A comparison of K_{IC} values determined from the same impact tests by evaluating $E_{abs.}/A$ and making a

calculation using the maximum load in a 3-point bend formula, indicate that the latter values compared favorably with those previously determined for the same mild steel using one of the more pedigree static tests.[19] Some excellent correlations between G determined by $E_{abs.}/A$ measurements and the established static techniques exist, but the generality of such a correspondence is yet to be shown. Two gross assumptions exist: that $E_{abs.}$ is only used in the creation of new surfaces, and that the crack extension resistance is constant during the propagation of the crack through the specimen. Both of these assumptions would appear to have some validity when the fractures are predominately square, where G_c approaches G_{IC}. Srawley and Brown[39] feel that Charpy fracture results are good for screening tests but definitely should not be used to calculate critical crack dimensions for structural design work. Other investigators of prominence do not subscribe to this point of view. These differences will continue to exist until future research in these areas point to the proper direction.

CHAPTER VIII

EXPERIMENTAL METHODS

8.1.0 Material

8.1.1 Titanium--High Purity (Electrorefined)

The Bureau of Mines (U.S. Dept. of the Interior) at Boulder City, Nevada, supplied 2 pounds of electrorefined titanium crystals. The material was supplied with a size 8 mesh and 65-70 hardness number. Table 8.1 gives the typical purity of such crystals, and Table 8.2 the chemistry of the supplied material with respect to the elements that are pertinent to this study. The high chloride content is reduced to negligible levels during remelt. Reactive Metals, Inc., Niles, Ohio, remelted the crystals to an ingot which was subsequently forged at 1600°F and rolled from 1300°F to a plate (0.543 x 2.13 x 9.0 inches). This strip was not annealed.

8.1.2 Titanium--High Purity (Research Grade)

Reactive Metals, Inc., supplied 0.4 inch thick plate made from selected portions of the ingot for increased purity with the average chemistry given in Table 8.3.

Table 8.1--Typical analysis of U.S. Bureau of Mines electrorefined titanium in parts per million.

Impurity	PPM	Impurity	PPM
Ag	<5	H	40
Al	25	Mg	15
B	<20	Mn	250
Ba	<160	Mo	3
Be	<80	N	20
C	100	Ni	<15
Ca	<15	O	200
Cl	1600	Pb	<6
Co	<25	Si	<50
Cr	<10	Sn	<25
Cu	50	Sr	<80
Fe	60	V	70

Table 8.2--Chemistry--per cent by weight of U.S. Bureau of Mines supplied electrolytic titanium crystals.

C	N	O	Cl
0.30	0.015	0.03	0.15

Table 8.3--Chemistry--per cent by weight of Reactive Metals, Inc., high purity titanium.

C	N	Fe	O
0.02	0.009	0.04	0.088

The plate was made by hot rolling the ingot to the stated thickness, followed by a 30 minute anneal at 1400°F. The plate was subsequently cleaned by grit blasting and pickling.

8.1.3 Titanium--commercially pure grades

Reactive Metals, Inc., supplied several of their grades of commercially pure titanium. The grade number corresponds to the minimum yield strength, i.e. RMI-30 would yield at stresses no lower than 30,000 PSI. It should be noted in Table 8.4 that interstitial strenghening of commercially pure grades is accomplished by increasing the oxygen content but not the nitrogen.

Table 8.4--Chemistry--per cent by weight of commercially pure titanium (RMI grades).

Heat No.	RMI Grade	C	N	Fe	O_2	H_2
295150	30	0.03	0.009	0.03	0.070	0.0061
294795	40	0.02	0.009	0.17	0.106	0.0042
294595	50	0.02	0.007	0.22	0.187	0.0032
303610	70	0.02	0.008	0.30	0.281	0.0039

These plates were not annealed. The annealing cycle normally suggested is 1350°F for 1 hour followed by air cooling.

In addition, a 3.25 x 10.25 x 0.5 inch plate of commercially pure titanium, ASTM B265 Grade II, was

obtained through Titanium Products Corporation, Detroit, Michigan. The rated tensile and yield strengths are 67,400 and 44,900 PSI respectively, with a 34% elongation. The chemistry of interest is given in Table 8.5.

Table 8.5--Chemistry--per cent by weight of commercially pure titanium, ASTM B265-Grade II.

Fe	C	N	O	H
0.11	.026	.012	.10	.004

8.1.4 Zirconium--Reactor Grade

Reactor grade zirconium plate was supplied by Wah Chang Albany Corp., Albany, Oregon. A 6000 pound ingot was forged to a slab, which was further reduced to the final size (9.0 x 13.5 x 0.4 inches) by hot rolling at about 1000°F. During the rolling operation scale was removed to insure that interstitials could not be picked up. Finally the plate was given an alpha anneal between 1450 and 1550°F. Upon cooling the plate was sand blasted and pickled. Table 8.6 lists the ingot analysis from which the plate was produced. Often the chemistry of the final product changes appreciably from the ingot analysis during the processing of metals. However, in the case of reactor grade zirconium the product has about the same chemistry

Table 8.6--Ingot chemistry--per cent by weight of reactor grade zirconium plate.

Analysis in PPM			For Heat No. 352417
	Top	Bottom	Average
Al	45	40	42
B	0.3	0.3	0.3
C	110	120	115 ←
Cd	<0.3	<0.3	<0.3
Cr	67	59	63
Co	<5	<5	<5
Cu	<25	<25	<25
Fe	376	367	371
H	3.0	14	8 ←
Hf	66	66	66 ←
Mg	<10	<10	<10
Mn	<10	<10	<10
N	36	22	29 ←
Ni	11	13	12
O	1150	970	1060 ←
Si	27	21	24
Sn	25	25	25
Ti	<20	<20	<20
U	1.6	1.9	1.8
W	<25	<25	<25

as the ingot due to the high degree of control required for the product.

8.2.0 Gas Treatment Atmosphere

8.2.1 Gases

The argon, nitrogen, and oxygen used for the thermal treatment of titanium and zirconium were obtained from Liquid Carbonics Division of General Dynamics. Both the argon and nitrogen were high purity while the oxygen was industrial grade. The purity levels are listed in Table 8.7.

Table 8.7--Purity of gases used for thermal treatment.

Gas	Purity Volume Per Cent	Impurities
Hi-Pure Argon	99.999 minimum	oxygen--10 ppm max., 10 ppm typical nitrogen--10 ppm max., 0 ppm typical water vapor--5 ppm
Hi-Pure Nitrogen	99.996 minimum 99.998 typical	oxygen, 10 ppm max. water vapor, 5 ppm max.
Industrial Oxygen	99.5 minimum 99.6 typical	nitrogen and argon maximum of 0.5 volume per cent

8.2.2 Purification Train

In order to have complete control over the diffusion of the various interstitials into both titanium and zirconium, it was found necessary to purify the reaction gases. The purification system or train is sketched in Figure 8.1. A pressure reduction valve on the cylinder allows the pressure, thus the gas flow to be reduced going into the flow meter. The meter with further reduction capability was set to allow a constant flow of 30 $cm.^3$ per minute. The gas was first reacted with shredded pure copper foil 0.005 inches thick to yield a high surface area for reaction per unit weight of copper. The copper was contained in a round 1.0 x 12.0 inch quartz tube with pyrex glass wool on each end for particle

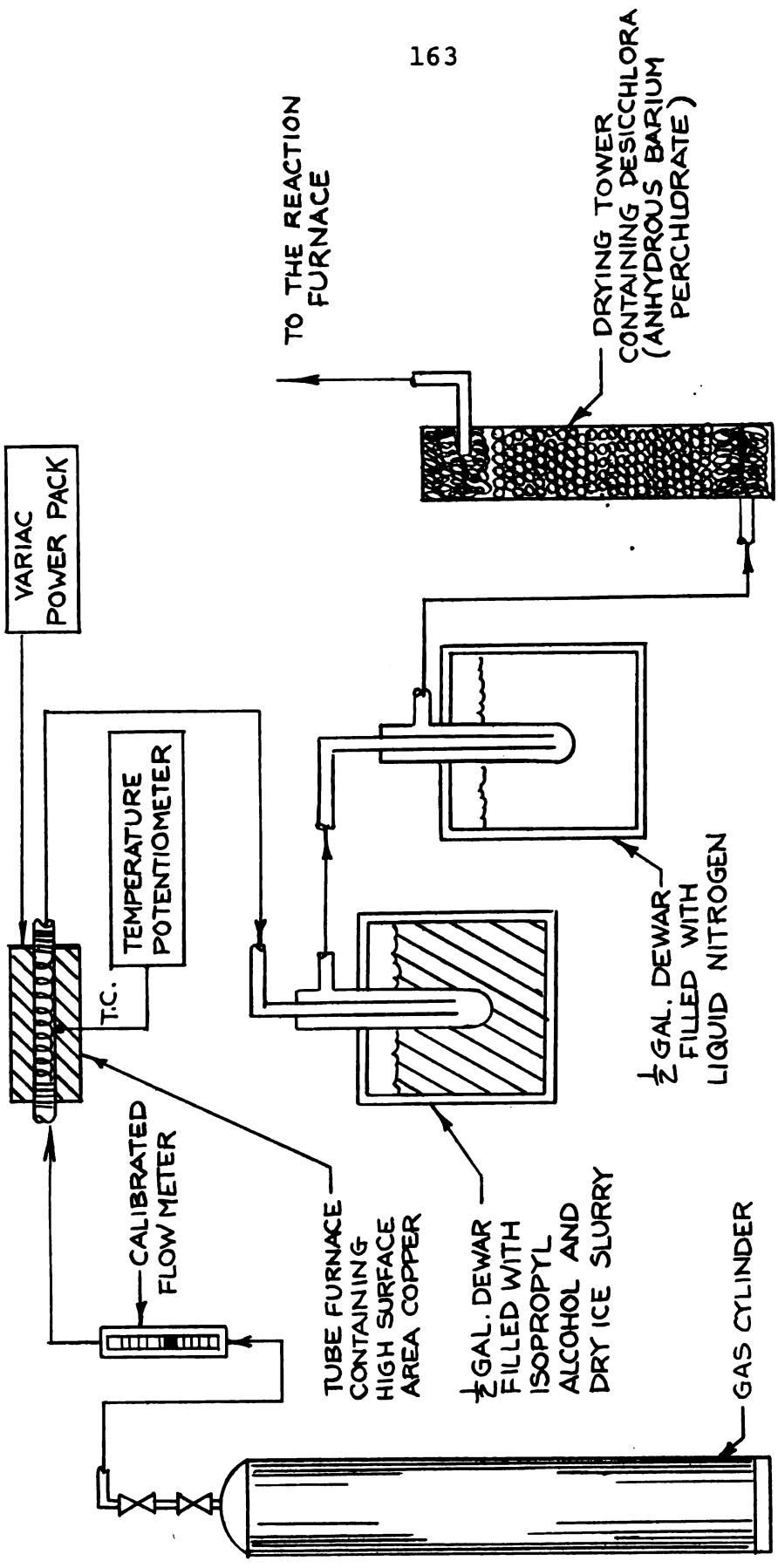


Figure 8.1--Sketch of the gas purification train.

filtering. The tube was maintained at 1300°F in a tube furnace by a Variac power regulator and monitored by a Leeds & Northrup temperature potentiometer. The first stage reduced the oxygen contamination in nitrogen. The next stage of the train, a dry ice (solid CO_2) and isopropyl alcohol cold trap at -60 to -70°C, removed some of the water vapor present in the reaction gases. The trap consisted of a fully self-contained quartz unit that the gas flowed through which was immersed in a cryostat containing a half gallon of the slurry. A six inch immersion depth of the 1.0 inch diameter tube was maintained to allow even minute traces of the vapor to be "frozen out" at the flow rate stated. After the dry ice and alcohol cold trap the gas entered a liquid nitrogen cold trap (-195.8°C) of similar construction. This trap further reduced the water vapor contamination to almost negligible levels and also oxygen contamination because liquid nitrogen will liquify oxygen (-182.6°C). The last stage before the gas entered the reaction furnace was passage through a drying column containing Desicchlora (anhydrous barium perchlorate) to remove any final traces of water vapor that may not have been removed previously. This column also had glass wool packed on top and bottom to prevent particles from being carried in the gas stream. Precaution was taken against possible minute gas leaks in the top and bottom furnace-tube seals which could

give rise to contamination. The glass specimen jig, to be described in detail later, had slotted baskets which contained titanium discs located just above and below the sample, as shown in Figure 8.2. These baskets were used to remove the last traces of oxygen from nitrogen. Titanium is commonly used as a "getter" of oxygen. Although the titanium will react with the nitrogen, it has a much greater affinity for oxygen. These baskets were actually located in the reaction zone yet they are still considered part of the purification train in that they removed the final remnants of oxygen and maintained the purity achieved by the train if there was a minute leak in the seals. All the elements in the train were used for the purification of nitrogen. The main concern in oxygen purification is the removal of water vapor, so only the dry ice-alcohol trap and drying column were used. Argon treatments required no purification in that the gas was used as a carrier of water vapor, which upon dissociation became a source of hydrogen supply. The argon was bubbled through distilled water and directly introduced to the furnace. The particular gas used for thermal treatment determined which elements in the train were used for purification.

8.3.0 Gas-Treatment: Procedure and Apparatus

A Dietert (Model 1977) high temperature, glow-bar type furnace was used for all gas treatments.

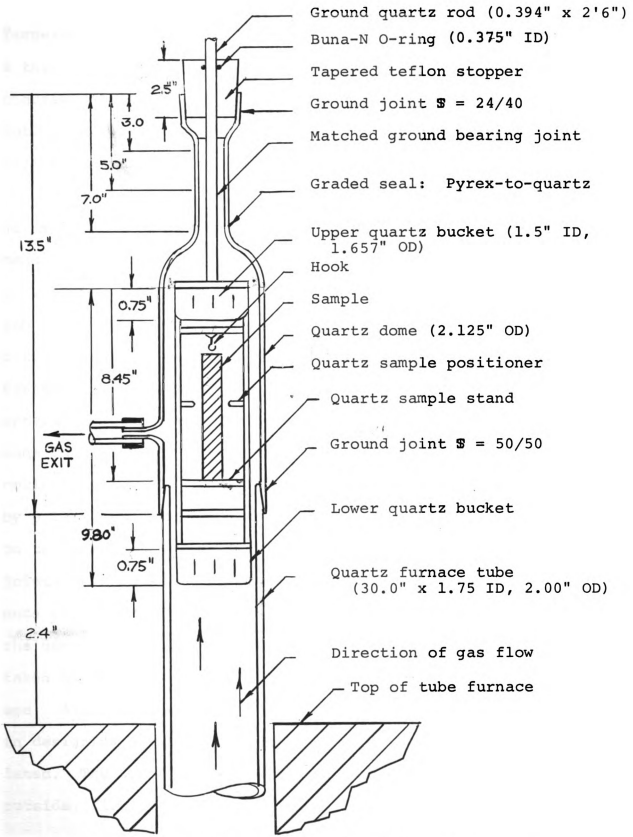


Figure 8.2--Sketch of glass specimen-fixture and dome.

Temperature profiles demonstrated that the furnace possessed a three inch "flat" region at six different temperatures checked ranging from 1500 to 1900°F. Furthermore, it was noted that over the same temperature span a five inch region existed with only a 50°F differential.

A special glass specimen jig was designed for the gas treatments which is sketched in Figure 8.2. The specimens were suspended upright in the furnace by placing them on a support within the glass fixture. By housing the sample fixture completely within the quartz dome located outside and above the furnace before sealing the reaction system, allowed the system to be purged before the sample entered the furnace. The sample was lowered into the hot zone only after at least one hour of purging. The sample could be translated inside the quartz furnace tube simply by pulling or pushing on the ground quartz rod attached to the sample fixture. Standard taper matched ground joints lubricated with silicone grease were used on both ends of the furnace tube to seal the reaction zone to the dome and reduction fixtures. These precautions were taken to minimize the possibility of contamination leakage. Also to avoid contamination, extra care was taken in designing the seal through which the push rod translated. The 0.394" diameter rod upon passing from the outside, first squeezed through a 0.375 inch ID O-ring

seated in a Teflon stopper. The 2.5 inch long stopper itself acted as a partial seal since its inside diameter was only 0.402 inches. The Buna-N rings are rated for usage between -40 to 250°F. Experience has shown that this ring had to be replaced after about ten runs due to degradation. It is not known if this was due to wear caused by the tight fit and/or due to excessive heat when the rod was pulled from the hot zone. The final stage of the push rod seal was a four inch matched ground bearing that the rod had to pass through. After the required soak periods the samples were slowly withdrawn from the hot zone until the sample fixture was again completely housed inside the dome area. The samples remained in this area where they were allowed to cool in the conditioned gas flow for about one hour. Upon their removal from the dome, the samples had usually cooled to nearly room temperature.

The only exception to the heat treatment procedure outlined involved those samples treated with argon bubbled through distilled water. These samples were allowed to furnace cool (requiring about 10 hours) instead of being withdrawn from the heat zone. This was done to avoid any possibility of suppressing hydride formation as discussed earlier by forming a supersaturated solid solution. Figure 8.3 is a picture of the overall heat treatment facility: drying train, furnace, and specimen fixture inside the dome.



Figure 8.3--Overall picture of heat treatment facility.

8.3.1 Preparation of Titanium Discs

Commercially pure titanium discs (0.21" diameter x 0.09") were obtained from Titanium Products Corp. These discs were the product of a punching operation so they required degreasing. This was accomplished by placing about 50 ml. of the discs with 150 ml. of isopropyl alcohol in a 250 ml beaker. The greater part of the grease was removed by successively changing the solvent about three times after ten minute ultrasonic cleaning periods. The sheet from which the discs were punched was lime coated, which had to be removed. This and any remaining grease could be removed by pickling. Several such baths are suggested in the literature, but the most satisfactory for the present purpose was found to be:[1]

Parts (volume)	Reagent
3	HNO_3
9	HCl
2	HF
5	H_2O .

Extreme caution must be exercised when using this pickling bath with titanium because the reaction is violent and copious fuming takes place. A safe way with very satisfactory results of carrying out this pickling step was to spread out about 50 ml. of the degreased discs on the bottom of a high container (1500 ml. beaker) to avoid

splashing and add about 100 ml. of the pickling reagent. The hood window could be closed and the reaction left to go to completion. The discs were thoroughly washed and rinsed with water. For best results the pickling step was repeated. After the proper rinsing and drying, the discs were observed to be bright and smooth.

8.3.2 Specimen Gas-Treatment Schedules

The designations given in Table 8.8 will be used when referring to the various alloys in the gas treatment schedules and throughout the remainder of this paper.

Table 8.8--Designations for metals used in the study.

Designation	Description
RMI-30	Reactive Metals, Inc., Commercially pure Ti, 30,000 PSI. yield strength
RMI-40	Reactive Metals, Inc., Commercially pure Ti, 40,000 PSI. yield strength
RMI-50	Reactive Metals, Inc., Commercially pure Ti, 50,000 PSI. yield strength
RMI-70	Reactive Metals, Inc., Commercially pure Ti, 70,000 PSI. yield strength
TPC	A.S.T.M. (B265) Grade II, Commerically pure Ti
HP-BM	High purity titanium (Bureau of Mines)
HP-RMI	High purity titanium (Reactive Metals, Inc.)
WCA	Wah Chang, reactor grade zirconium

The treatment schedules are as follows:

(a) Nitrogen treatment

Table 8.9--Soak times for titanium and zirconium specimens treated in nitrogen.

Specimen	Nitrogen Soak Treatment Time, hrs. 3	6	9	12	15
HP-RMI	x	x	x	x	
RMI-30	x	x	x	x	x
RMI-40		x	x	x	x
RMI-50		x	x	x	x
RMI-70		x	x	x	
WCA	x	x	x	x	

All the titanium samples were held at 1850°F while all the zirconium samples were treated at 2000°F.

(b) Oxygen treatment

It has been pointed out in Table 8.4 that the oxygen content is varied in the commercially pure titanium series (RMI-30 to RMI-70) while the nitrogen is held approximately constant and the hydrogen only varies between about 3 and 6 ppm. It was therefore not necessary to treat this series in oxygen. However, to ascertain the degree to which titanium is susceptible to oxygen, HP-RMI samples were treated at 1725°F for 3, 6, 9, and 12 hours. Likewise the zirconium samples (WCA) were treated at 1675°F for 2, 4, 5, and 6 hours.

(c) Hydrogen treatment (Argon bubbled through water).

Because some of the previous literature had indicated that the purity of titanium affected the hydrogen levels necessary for embrittlement during impact, both a high purity and commercial purity series of treatments was made. The commercial purity (TPC) treatments were all carried out for 2 hour periods at the following temperatures: 1310, 1415, 1520, 1630, 1730, 1790, and 1850°F. The high purity titanium (HP-BM) samples were treated at 1520, 1630, and 1730°F for 2 hour soak periods, while at 1790°F the time was varied at 2, 4, and 6 hours for the soak period. To get a good comparison of the effect of hydrogen versus the other interstitials, Charpy bars of RMI-30, 40, 50, 70, and WCA were treated in the water bubbled argon for 2 hours at 1850°F. These bars were obtained from the previously nitrogen treated and tested single-edge-notch specimens. The titanium and zirconium samples used in the hydrogen treatments were previously tested with nitrogen for 9 and 12 hours respectively. All the water bubbled argon (hydrogen) treated samples were furnace cooled.

8.4 Test Specimens

The single-edge-notch tension specimen must conform to specific proportions which are given in Figure 8.4. The inside diameter of the furnace tube limited the width and thickness of the tension specimen that could

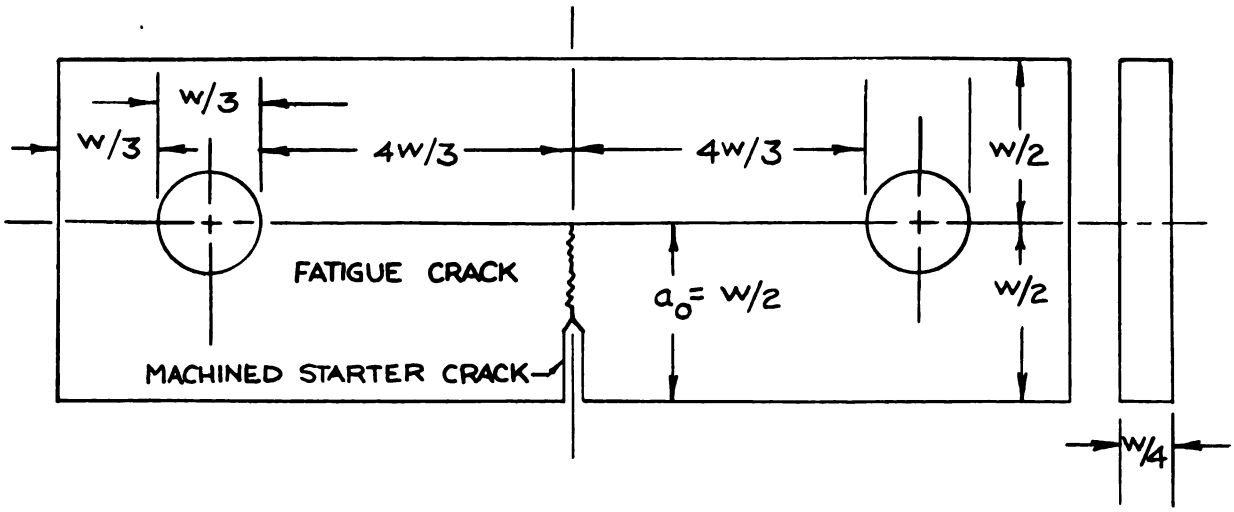


Figure 8.4--Dimensional proportions of a single-edge-notch tension specimen. (Note sketch is not to scale).

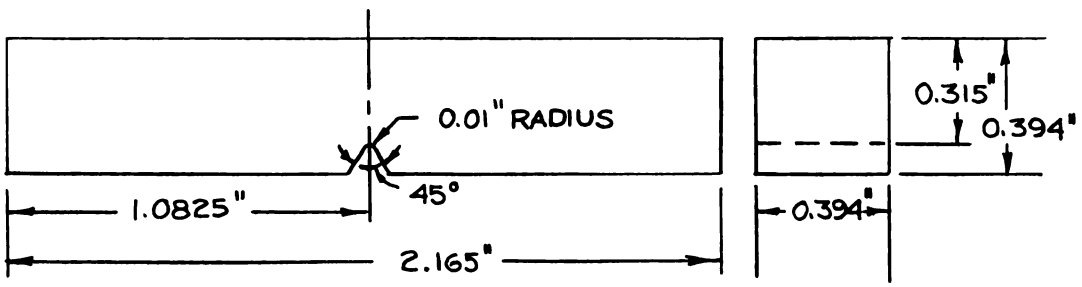


Figure 8.5--Charpy test bar dimensions. (Note sketch is not to scale).

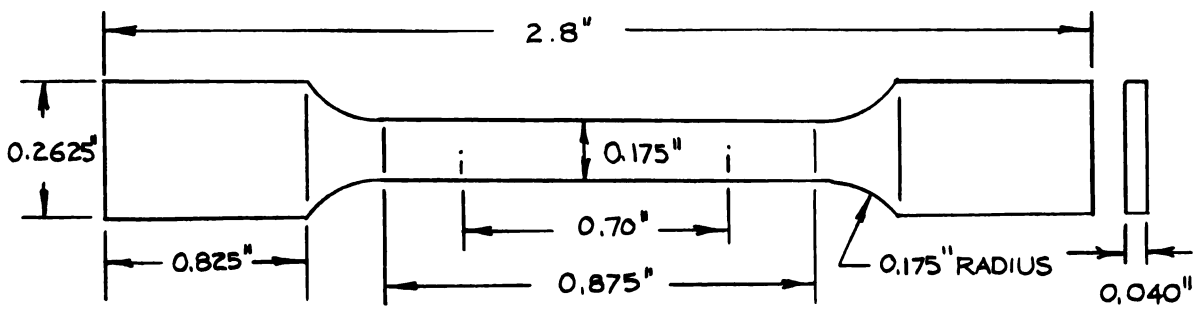


Figure 8.6--Rectangular tension test specimen dimensions. (Note sketch is not to scale).

be used. The tube ID being 1.75 inches therefore set the limit of the specimen width at 1.6 inches. All the other dimensions are in proportion to the width. The preferred specimen thickness was between w/2 and w/4, the lower limit (0.4 inches) did allow the specimen to fit in the furnace tube. The crack starter flaw was machined to a depth of 0.43 inches and terminated at a notch of radius 0.005 inches maximum. The Structural Materials Engineering group at Battelle Memorial Institute (Columbus Laboratories) fatigue cracked the specimens by three point bending. A typical sample required about 30,000 cycles at a maximum load of 3,000 pounds. In all cases the fatigue crack front was observed planar after fracture, and did not veer from the center plane of the sample.

After the single-edge-notch tension bar was tested, a V-notch Charpy impact specimen and a rectangular tension test specimen were machined from the fractured halves according to the scheme shown in Figure 8.7. This was done to reduce the number of experimental variables, that is, for a given heat treatment, the material was a constant for all tests. In a few cases two V-notch Charpy bars were machined, where the additional one was used to demonstrate the effect of hydrogen. The V-notch Charpy bar was machined to the dimensions specified by A.S.T.M. Standard Designation E 23-66 (Notched Bar Impact Testing of Metallic Materials) and is sketched in

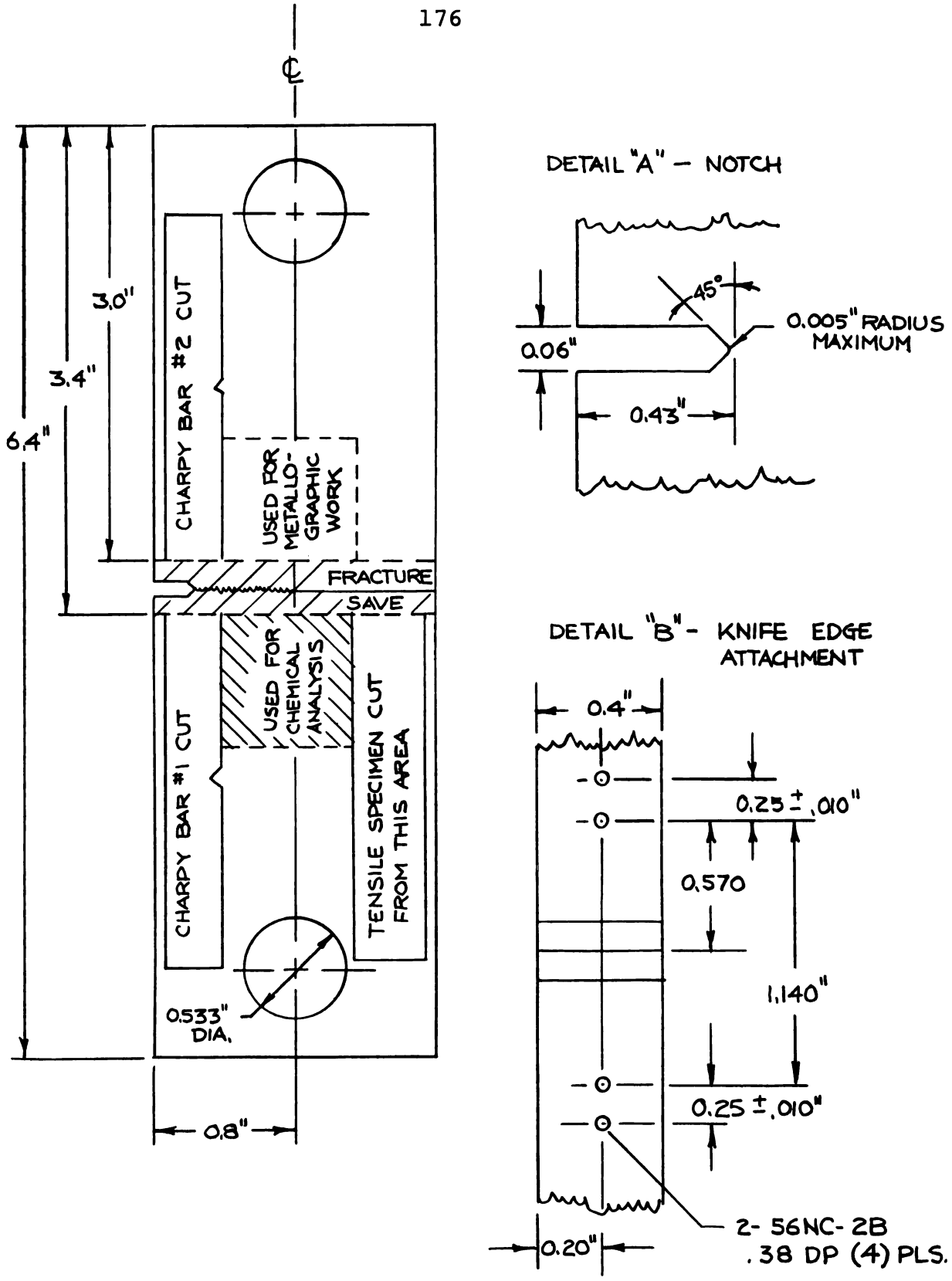


Figure 8.7--Specimens machined from single-edge-notch tension bar.

Figure 8.5. The rectangular tension specimen dimensions have all been uniformly reduced to be 0.7 the value recommended by A.S.T.M. Standard Designation A 370-68. This reduction was necessary to conform with the available size of the broken half of the single-edge-notch tension specimen (about 3.2 inches). The specimen dimensions are given in Figure 8.6.

8.5.0 Static Testing

8.5.1 Single-Edge-Notch Tension Test

Micro-Measurement's foil strain gauges were mounted along the centerline of the longitudinal axis with only a 0.3 inch separation distance from the fatigue crack plane of the specimens. The gauges, EA-05-500 BH-120, and EA-03-500 BL-350, were mounted on titanium and zirconium respectively to compensate the gauges for differences in the thermal coefficient of expansion. Eastman 910 adhesive used with 910 catalyst was satisfactory for mounting the gauges. To protect the gauges from damage, M-Coat, a thirty minute air-drying polyurethane coating, was applied. Lead length and temperature compensation was made with the use of a dummy gauge. The strain gauge mounted directly on the specimen was used as an indicator of the degree of plastic strain that the entire sample experienced. If the fracture

is truly plane strain, the test specimen should not be plastically deformed, that is, if any plastic deformation takes place it should be confined to the region around the fracture plane. Permanent strains would be detected by taking a strain reading on a Baldwin SR-4 strain indicator both before tension testing and after fracture. An MTS Systems Corporation fracture mechanics clip-on gauge (model 632.01) was used to monitor the crack opening displacement. The gauge clips on to knife edges that were directly screwed onto the sample. This compliance gauge was found to be linear up to a calibrated displacement of 0.150 inches. A dc power supply was set and periodically checked with a digital voltmeter to deliver an excitation of 5.935 volts. This was done to keep the displacement-gauge output relationship constant (7.53×10^{-3} inches/mv.). The load on the sample also had to be monitored, which was done with a "tensile link." A Micro-Measurements strain gauge, EA-06-250 BF-350, was mounted along the longitudinal axis of the bottom bar of the loading assembly. The cross-sectional area of this member was accurately machined to be 1.0 $in.^2$ When elastically strained in a universal testing machine corresponding strain readings and output readings from a potentiometric bridge were determined. A constant 6 volts was maintained across the bridge. Thus a linear strain (μ-in./in.) vs. output (mv.) calibration was determined.

Since $\sigma = K\varepsilon$, and the modulus of elasticity is known for the steel rod tensile link, the stress could be calculated for any measured strain. However, since the tensile link was exactly 1.0 $in.^2$, the applied load was known for every measured strain. Finally, the original strain vs. gauge output calibration curve was replotted to be the load or force vs. gauge output calibration curve. Therefore, by feeding the outputs of both the tensile link and the compliance gauge into a Varian F-80 x-y recorder, a continuous record of the load vs. crack opening was made which was necessary to determine if the fracture was of the plane stress or strain variety. If it was plane strain, the load at "pop-in" necessary for K_{IC} calculations could be obtained from this plot. Figure 8.8a shows an overall view of the test, while Figure 8.8b shows a close up of the specimen in the loading fixture.

8.5.2 Rectangular Specimen Tension Test

The rectangular tension test specimen was used to determine several mechanical properties (yield strenth, tensile strength, and % elongation) of each material. A floor model Instron testing machine strained the specimens at a rate of 0.2 cm./minute. The load was recorded from the output of a DM tensile load cell with a full scale range of 500 Kg. By knowing the chart speed

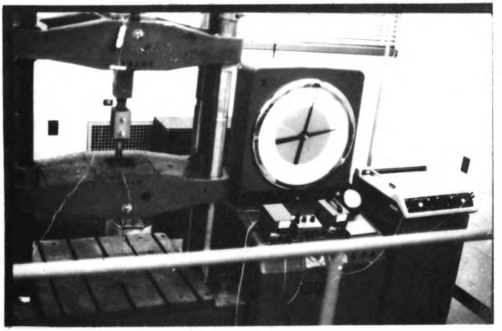


Figure 8.8(a)--Overall view of tension fracture test.

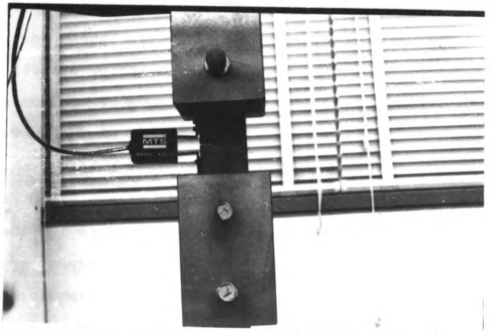


Figure 8.8(b)--Close up picture of tension fracture specimen in the loading fixture.

(3.0 cm./min.) the strain could be calculated from the plot length. Because the strain was of particular importance in this study, a clip gauge was affixed within the 0.7 inch specimen gauge length to eliminate any errors which would arise due to elastic strains generated within the holding fixtures, etc. The clip gauge, with a Micro-Measurements EA-06-062AQ-350 foil strain gauge mounted on it, was calibrated with a special fixture used in MMM-215 laboratory for such a purpose. The clip gauge was held on the sample by mounting a 0.175 inch section of a paper clip on either end of the gauge length with Scotch two part epoxy and curing at room temperature overnight. The clip gauge and a dummy gauge used for lead length and temperature compensation formed two arms of an Ellis Associates BAM-1 (bridge amplifier and meter). With the gain set at 0.1 volts output when the calibration setting was 10, the gauge output-displacement calibration was linear (0.8476 volts/inch) up to a 0.21 inch displacement, the maximum displacement checked. The strain was recorded with a Varian F-80 x-y recorder (where x = time sweep-10 sec./cm., and y = strain signal-10 mv./cm.). Simultaneous recordings of load vs. strain and strain vs. time were made for each tension specimen tested. In addition, the gauge length dimensions of each sample was measured with a micrometer to determine accurately the cross sectional area.

8.6.0 Dynamic Testing: Instrumented Impact

8.6.1 Use of Impulse-Momentum Principle to Determine the Energy of Fracture

The fundamental dynamic relationship between impulse and momentum, derived in standard texts,[3] can be stated as

$$\int_{t_1}^{t_2} F\,dt = m[v_1 - v_2], \text{ where } F, t, m, \qquad (8.1)$$

and v are force, time, mass and velocity respecitvely. The LHS of Equation 8.1 is defined as the impulse and the RHS, the change in linear momentum. This dynamic principle can be used to determine the energy of fracture in an instrumented impact test. The record obtained from the oscilloscope is a load vs. time record, thus an impulse curve. If the load-time curve is integrated and replotted with time as the independent variable, a plot of load-time (lb.-sec.) vs. time is obtained. Since the mass of the striker, however, is a constant, the force-time vs. time curve may be divided by this constant, and thus a velocity vs. time plot results. This plot is then integrated and replotted with time again the independent variable, and one obtains a displacement vs. time curve. Then for any time: t_1, t_2, t_3 --- t_n a value of the load and the corresponding displacement is plotted to yield a load vs. displacement curve. This is the desired

curve for it can be integrated to yield the initiation, propagation, and total energy of fracture. These steps are sketched in Figure 8.9. Note that the division by the constant mass could also have been that of the Charpy sample, in which case the integration would simply have been $\int_{t_1}^{t_2} v(t)\,dt$. Because several series of metals have been used in these experiments, the mass $(\frac{W}{g})$ would have to be determined for each, whereas the pendulum hammer mass remained the same. The velocity of the pendulum hammer just before contact with the Charpy speciman was determined from the fact that the instrument is rated to deliver 264 ft.-lbs. of energy. Therefore, $\frac{1}{2}\,m\,v^2 =$ 264 ft.-lbs., or v = 16.8265 ft./sec. The integration of the velocity vs. time curve was thus done by evaluating $\int_{t_1}^{t_2} [16.8265-v(t)]\,dt$.

8.6.2.0 Experimental Determination of Dynamic Fracture Energies

Figure 8.10 shows a block diagram of the experimental system used to determine the energy of fracturing involved under conditions of impulsive loading. Some of the fracture pulses (load-time records) in the study were expected to be quite short, i.e. about 200 μ-sec. for fairly brittle material. The computer did not have the capability to handle such information "on-line" via one

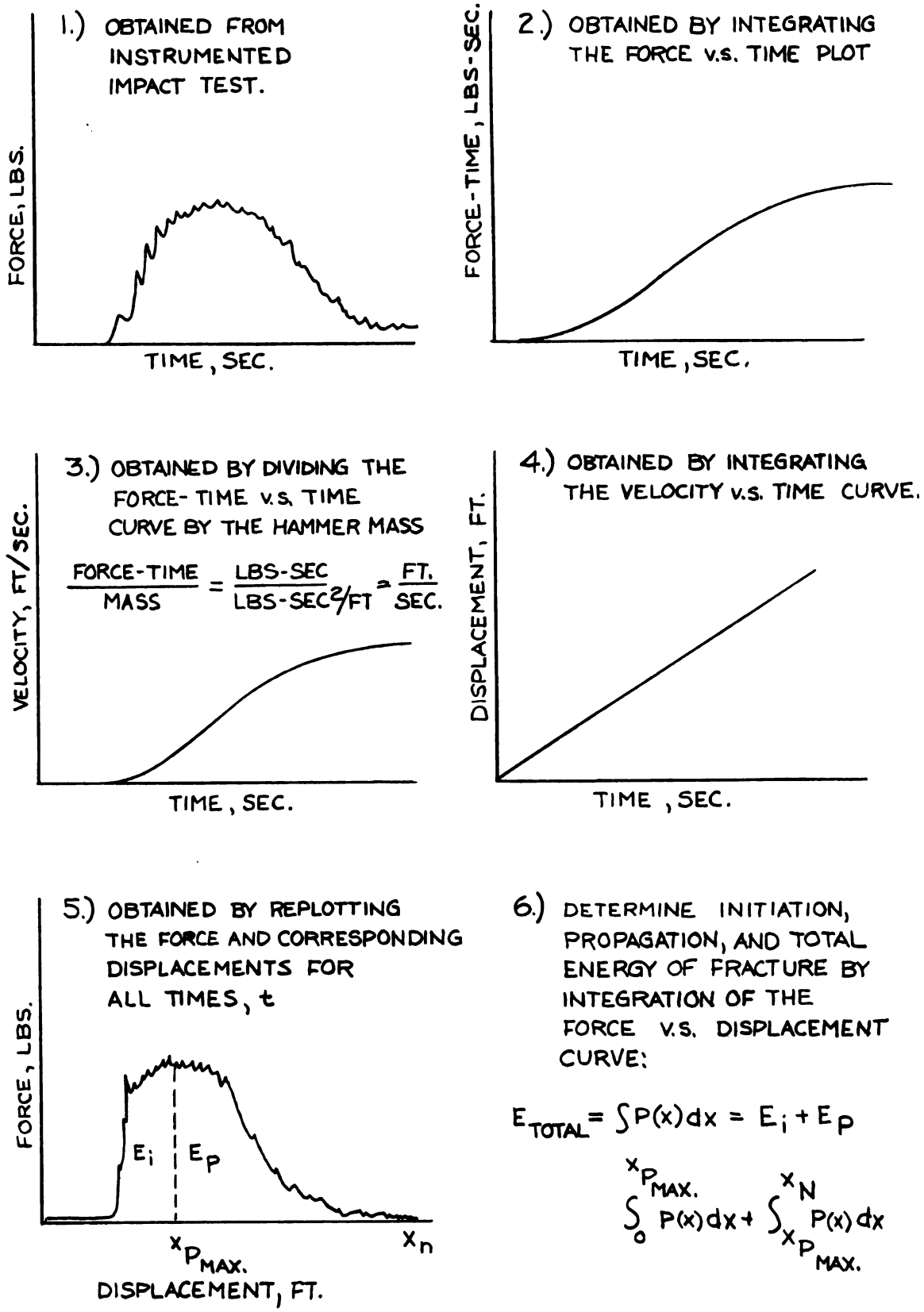


Figure 8.9--Steps to determine the energy of fracture.

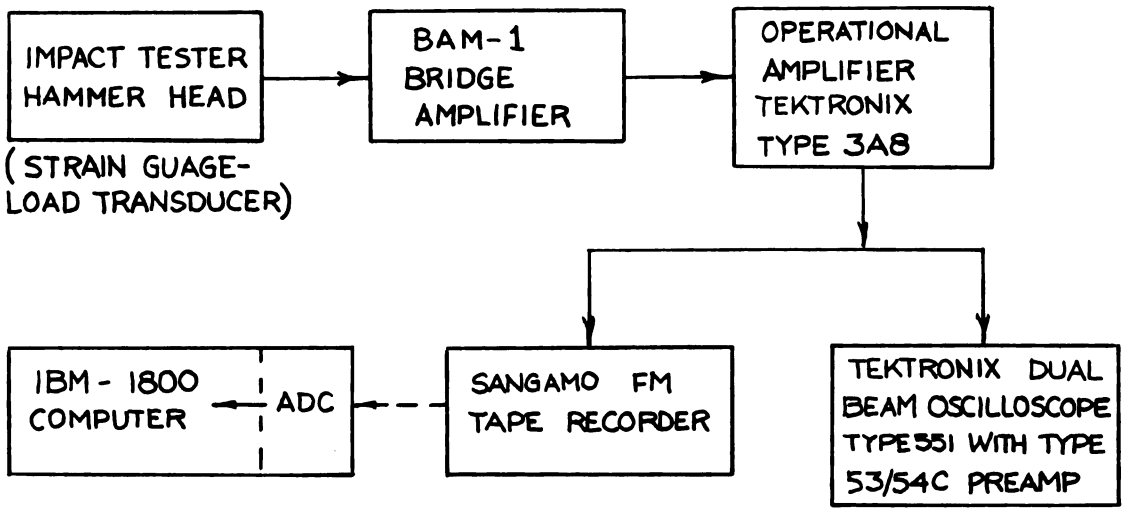


Figure 8.10--Block diagram of dynamic fracture system.

of the analog inputs, that is, it could not sample enough data prints in a 200 μ-sec. time frame to guarantee a significant level of accuracy. Therefore, it became necessary to record the information with a Sangamo 3500 FM-tape recorder at a tape speed of 60 inches per second (ips.). The time required by the IBM-1800 computer to read one data point was 125 μ-sec. which is a read capability of 8,000 data points per second. Most of this time was consumed in the analog-to-digital conversion (ADC). By playing back the tape recorder into the ADC at 3.75 ips., a time spreading factor of 16 was obtained. This allows the computer to sample a data point every 7.8125 μ-sec., thus even a 200 μ-sec. pulse would be represented by 25 data points, however a good portion of the pulse

durations in the experiments were in the range of 800 μ-sec., thereby represented by about 100 data points. The Sangamo tape recorder demonstrated no loss in fidelity when comparing the pulse outputs from playback speeds ranging between 60 to 3.75 ips. with the original input pulse. In order to playback at a slower speed, it was a necessary condition that the reproduce pulse was in no way distorted with respect to the record pulse. The overall computer accuracy is rated at 0.5 per cent. Figure 8.11a and b show an overall and close up view of the instrumented impact system respectively.

8.6.2.1 System Calibration

In order to account for signal gain and attenuation throughout the system, a calibration was made to adjust for such alterations. Before the impact records were recorded, a one volt signal from the BAM, set with a digital voltmeter, was recorded. It should be pointed out that the BAM has a frequency response of 20 k Hz, thus acts as a filter in the system. In addition a 1.0 volt square wave from the oscilloscope calibration was recorded. After the data had been taken, these same calibrations were again recorded to indicate if there was any significant drift. A routine to analyze the data read off of the tape contained the instructions: if the voltage of the calibration square wave is < 0.2 volts,

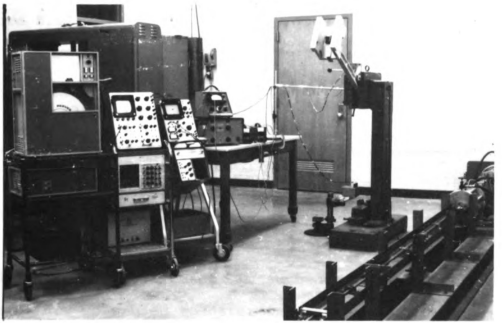


Figure 8.11(a)--Overall view of instrumented impact test system.

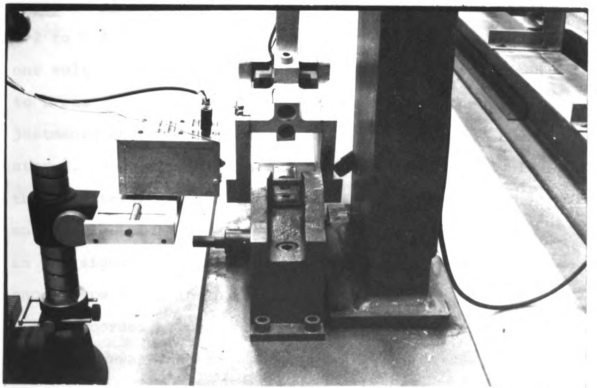


Figure 8.11(b)--Close up picture of photo-trigger and hammer.

then average with the zero-volt reading; but if > 0.8 volts then average with the one-volt readings. See Figure 8.12.

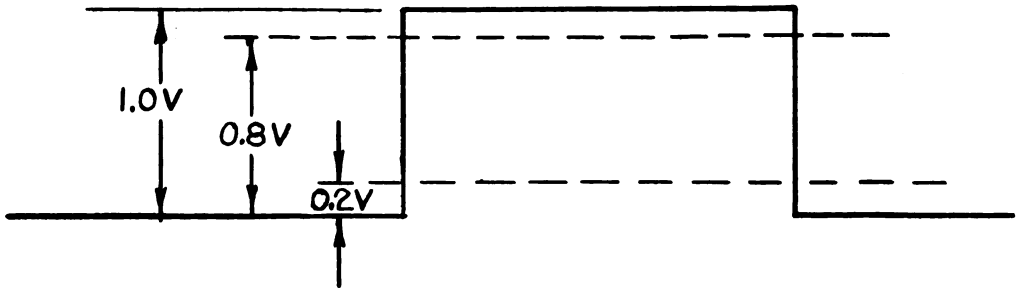


Figure 8.12--Computer analysis of 1.0 volt calibration pulse.

By defining the data points in such a manner about 1000 data points were used to determine the zero voltage reference, and about 500 points for the 1.0 volt reference. The rise and fall parts of the square wave typically contained only about two data points inside the 0.2 to 0.8 volt range. Thus by such a calibration, the one volt originally read in the laboratory is redefined to a one volt level within the computer, and any readjustments necessary to establish the one-volt level are stored. The impulse data are directly adjusted within the computer. The data are thereby calibrated for the entire electrical portion of the system and even changes in the signal caused by the computer itself. No differences were found in the voltage levels of the calibrations recorded before and after the impact testing, so the system was assumed to be electrically stable.

8.6.3 Calibration of Impact Tester Tup

The striking head of a Tinius-Olsen (Model 264) impact tester was removed from the arm such that the instrumented hammer attached to the head could be calibrated directly in place. A Micro-Measurements EA-06-062 AQ-350 foil strain gauge was mounted 0.3 inches above the point where the hammer and specimen made contact during impact. The gauge was coated first with M-Coat, which is a clear and fairly hard durable covering; a layer of Gagekote #1 was added which is a water resistant plastic coating which air dries in 15 minutes. Finally a strip of plastic electrical tape was placed over the gauge area to protect against damage from broken rebounding pieces during the Charpy test. The static calibration of the impact striker was done by placing the entire hammer head in an Instron testing machine and applying a compression load. In order to do this, a special tool was designed to fit the crosshead of the Instron machine on one end, and a hardened tool steel insert with the exact dimensions of a Charpy bar on the other. This insert Charpy bar was brought to rest at the precise position on the hammer that an actual Charpy bar would during a test. The compression loading was done in 250 Kg increments up to 4,500 Kg. The strain gauge was both lead length and temperature compensated

by using a dummy. Both gauges formed two arms of a BAM-1 whose gain was fixed to yield a 1.0 volt output when the calibration position was 10. The BAM-1 output was read with a digital voltmeter. A linear relationship [9.77×10^{-5} volts/lb. (force)] was found to exist between the hammer mounted strain gauge and the applied load up to 4,500 Kg., the limit of the test.

8.6.4 Calibration of the Impact Tester

The impact machine had been checked to comply with the specifications listed in A.S.T.M. Standard E-23. The specimens were positioned with centering tongs as suggested in the standard. It was determined advisable to check the fracture energy results obtained with the system described in this chapter against some standards. The latter Charpy specimens were obtained from the Army Materials and Mechanics Research Center, Watertown, Massachusetts. The results for three absorption energy ranges are listed as rated by the Army, the value read from the machine, and the value determined by instrumented impact. Note the values listed in Table 8.10 are an average of 5 samples per energy range.

Table 8.10--Fracture absorption energies for standard Charpy bars.

Army	Impact Machine	Instrumented Impact System
12.3 ft.-lbs.	16.2 ft.-lbs.	12.72 ft.-lbs.
42.6 ft.-lbs.	45.8 ft.-lbs.	37.82 ft.-lbs.
68.8 ft.-lbs.	70.0 ft.-lbs.	72.34 ft.-lbs.

The instrumented values are in good agreement with the Army standard values. The slight difference that does exist is probably due to the relatively poor control of the Charpy bar temperature as outlined in section 8 of E-23. The values are significant to demonstrate that the instrumented system is accurate at least through the energy ranges tested.

8.6.5 Triggering System

In order to obtain an oscilloscope record (load-time) of the fracture, it is necessary to trigger the oscilloscope at the proper instant before specimen-hammer contact. This was satisfactorily done by attaching an n-p-n planar silicon photo transistor (LS-400) to the upper corner of the striker head that leads during travel towards the sample. This photo transistor is made to intercept a finely collimated beam of light which is emitted from a box that contains the circuitry for the trigger,[2] which is given in Figure 8.13. The rise time which has been measured to be about 50 μ-sec. and the 18 volt output allowed for sharp triggering. If the trigger signal was passed through a Krohn-Hite band bass filter (Model 330M) with a 10 k Hz. high cut off and a 0.2 Hz. low cut off, the trigger system could be used in a lighted room without causing spurious triggering due to shadows, reflections, etc.

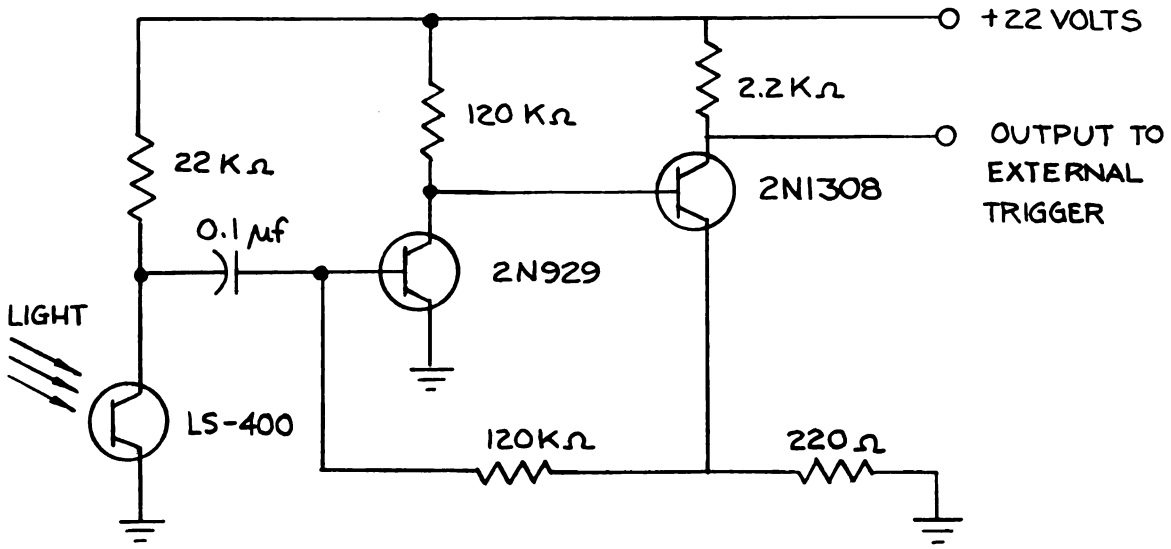


Figure 8.13--Impact trigger circuit.

8.7.0 Specimen Examination and Checmial Analysis

Standard metallographic techniques were used to polish both titanium and zirconium samples. Of the various etchants suggested in the literature, the following[4] was determined to be most effective for titanium:

Parts by volume	Reagent
12	H_2O_2 (30%)
6	H_2O
1	HF (48%) ,

except for the high purity titanium which required 2 to 3 parts of HF in the same solution. From 5 to 60 seconds etching time was required depending if polarized light was to be used in the examination, which required a minimal of etching. The zirconium was etched in a two stage process. The first etchant[4] was designed to be used

immediately after a 600 grit silicon carbide lap. It eliminates the need of fine polishing by rendering the surface smooth. However, it doesn't etch with good definition, thus a second etchant[5] is required. The composition of the solutions are as follows:

(a) Solution I--scratch removal

Parts by volume	Reagent
9	H_2O_2
9	HNO_3
1	HF

(b) Solution II--etchant

Parts by volume	Reagent
92	H_2O
5	HF
3	HNO_3 .

All electron fractographic work was done on an Advanced Metals Research (AMR) Model 900 scanning electron microscope, while some low power fractographic examination was done by photographing the fracture surfaces (static and dynamic) with a Nikon F camera (Micro-Nikkor Auto 1:3.5, f = 55 mm. lens) and Kodak Panatomic-X Film (fine grain) and photographically enlargening.

The chemical analysis of gas treated samples was done by Gallob Analytical Service Corp., New Jersey. The oxygen and nitrogen analysis in both titanium and

zirconium were determined simultaneously by inert fusion. The Leco system is heated by induction to 2500°C for conditioning (outgassing, bakeoff, etc.) and then cooled to about 2000°C. The samples were then introduced to a graphite crucible already containing platinum. A helium carrier gas sweeps the evolved gases into a collection trap. The gases in the trap are then analyzed by gas chromotographic techniques. The lower limit (ND, not dectectable) for nitrogen by such a technique is 100 ppm, while for oxygen 25 ppm.

Hydrogen in both titanium and zirconium was determined by hot extraction. The sample was induction heated under vacuum in a platinum crucible to about 1000°C. The evolved gases in this case are introduced to and analyzed by a gas chromotograph. The results reported are accurate to within $\pm$ 5%.

Element segregation and phase identification studies were carried out on an Applied Research Laboratories EMX-SM electron microprobe.

CHAPTER IX

RESULTS AND DISCUSSIONS

Part I--Nitrogen and Oxygen Treated Titanium and Zirconium

It should be borne in mind that the data of the static properties of the nitrogen and oxygen treated samples presented in the tables below are not intended to be absolute, but rather used as a general indication of trends. Most of the data presented represent a single specimen; thus the emphasis on trends rather than absolute values. The total evaluation of the effect of oxygen and nitrogen on titanium and zirconium under the test conditions, will be the integrated results of several different types of data.

9.1.0 Single-Edge-Notch Tensile Fracture Experiments

Compliance measurements on single-edge-notch tensile specimens indicated that all the titanium and zirconium bars were in a state of plane stress for all conditions of oxygen and nitrogen heat treatments listed in the schedule in Chapter VIII. Plane stress fracture

mechanics parameters were not determined due to their limited value. In addition, a calibration sample would have been necessary for each condition. The crack openings at the maximum recorded load are plotted in Figure 9.1 for the various RMI commercially pure grades that were treated with nitrogen at 1850°F. It is interesting to note that as the soak time progressed, all the grades tended to the same crack opening at the maximum load. The crack opening at maximum load trend can be influenced by several factors thus making interpretation difficult. For example, if all samples had the same crack length, at the same maximum load, then differences in the crack opening would be due to either differences in the material's elasticity, or plasticity. Since we are concerned with plane stress, the differences would be reflected in the plasticity. There are two contributions to the total plasticity: the plasticity near the region about the crack zone and the gross yielding of the bar. Some gross plasticity of the entire bar did take place for all samples, because in each case, the strain gauge mounted 0.3" above the fatigue fracture plane showed some amount of permanent strain after fracture. This might have been due to the fact that the gauges were mounted fairly close to the fracture plane, and perhaps the major part of the bar only underwent minimal plastic strain. Figure 9.2(a) shows that a significant degree

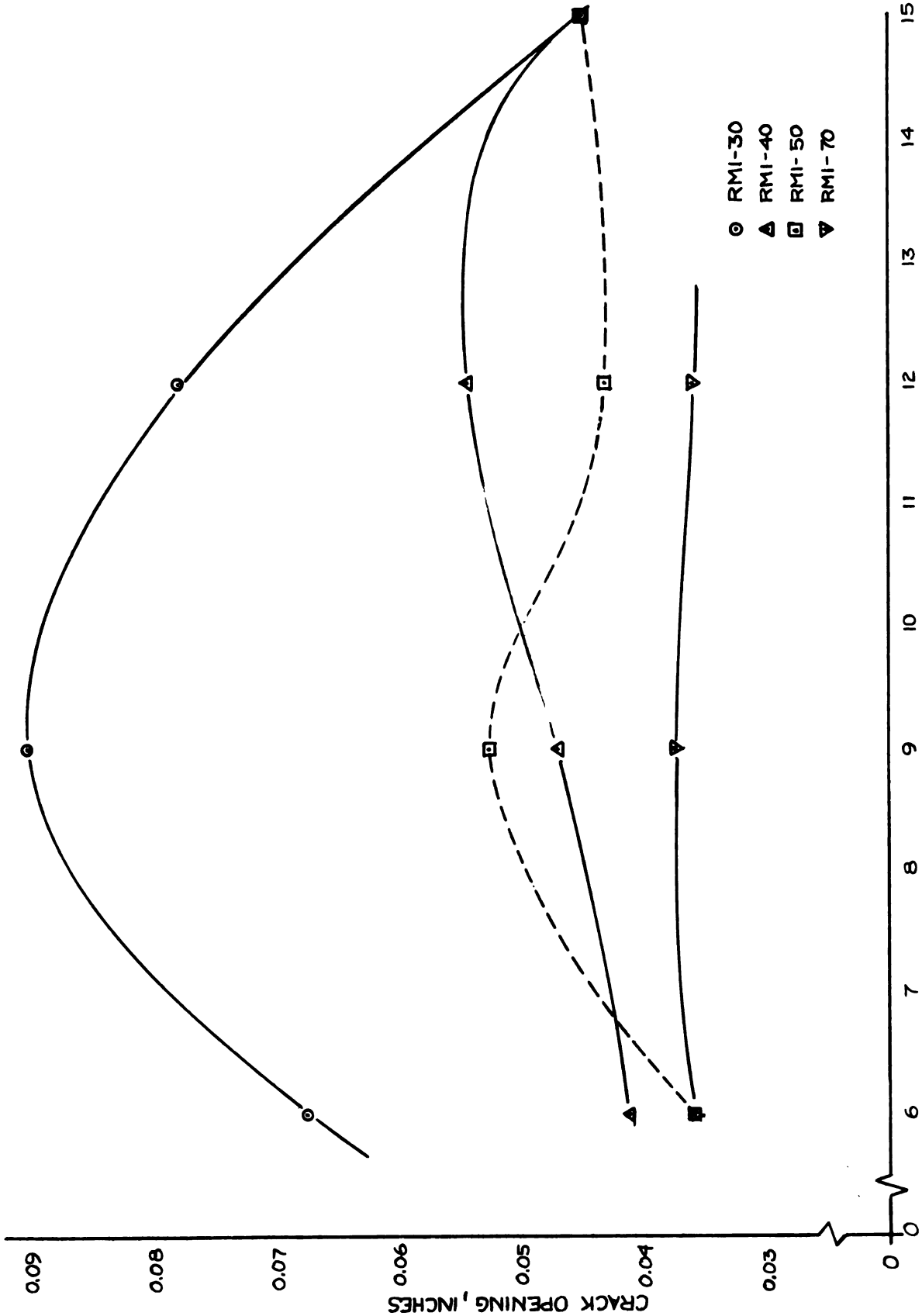
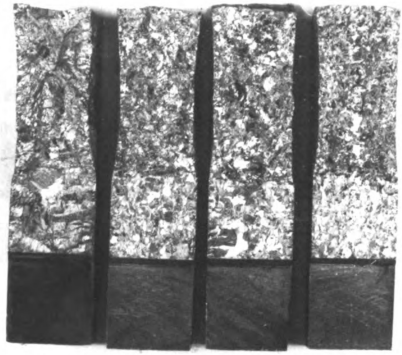
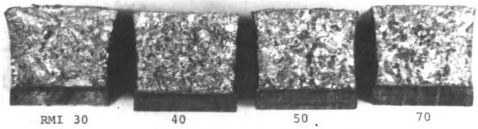


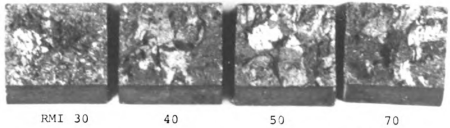
Figure 9.1--Single-edge-notch tension specimen crack openings of commercially pure titanium grades (RMI) for various nitrogen treatments.



(a) Single-edge-notch bars treated at 1850°F, 9 hr., N_2.



(b) Charpy bars treated at 1850°F, 9 hr., N_2.



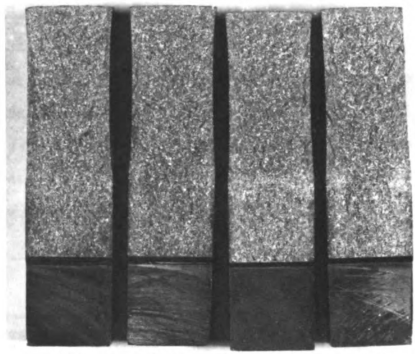
(c) Charpy bars treated as in (b) then at 1850°F, 2 hr., H_2.

Figure 9.2--Fracture surfaces of commercially pure titanium (RMI series) for various conditions.

of contraction took place during the failure of RMI-30, 40, 50, and 70 bars treated in nitrogen for 9 hr. at 1850°F. Note that the Poisson effect becomes less prominent from RMI-30 to 70. The WCA samples demonstrated similar behavior but not as pronounced. Figure 9.3(a) shows that the fracture surfaces and Poisson effect of the reactor grade zirconium samples heated for increasing times (3 to 12 hrs.) at 2000°F in nitrogen differed very little. This is also reflected in the crack opening values of the nitrogen treated zirconium given in Table 9.1. However, the same table shows significant differences for those zirconium bars progressively treated for longer times in oxygen.

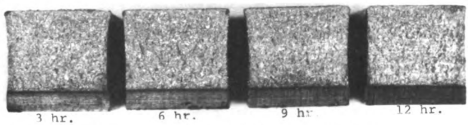
Table 9.1--Maximum load crack openings of (WCA) treated in nitrogen and oxygen.

Material and Condition	Treatment Time, hr.	Crack opening at maximum Load, in.
WCA treated in N_2 at 2000°F	3	.03602
	6	.03200
	9	.03200
	12	.03200
WCA treated in O_2 at 1675°F	2	.03572
	4	.04136
	6	.04700



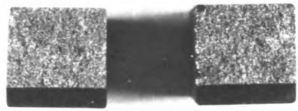
3 hr. 6 hr. 9 hr. 12 hr.

(a) Single-edge-notch bars of WCA treated at 2000°F in N_2.



3 hr. 6 hr. 9 hr 12 hr.

(b) Charpy bars of WCA treated at 2000°F in N_2.



12 hr., 2000°F, N_2 6 hr.,1675°F, O_2

(c) Charpy bars of WCA pretreated as indicated, then treated at 1850°F, 2 hr., H_2.

Figure 9.3--Fracture surfaces of reactor grade zirconium for various conditions.

9.2 Static Tensile Data for Oxygen and Nitrogen Treated Specimens

Data points not supplied in the tables below represent situations where failure occurred less than 0.25" from the gauge length boundary. The results of the tensile properties of pure titanium (HP-RMI) treated with oxygen are given in Table 9.2.

Table 9.2--The tensile properties of HP-RMI treated in oxygen.

1725°F Treatment Time, hr.	Total Strain, %	Tensile Strength, PSI
6	12.64	63,351
9	9.94	69,713
12	11.80	69,598
15	8.43	72,207

As might be expected from the literature cited earlier, there is a general increasing trend in the ultimate strength as the treatment time increases. However, these increases are somewhat modest in that oxygen is known to be a fairly potent strengthening agent in titanium. Correspondingly as the strength increases, the ductility (total strain) decreases. This would indicate that at 1725°F oxygen diffusion into the material is perceptable in terms of the static properties. To superimpose the effect of nitrogen atmosphere on the tensile properties of titanium containing oxygen, the RMI series was tested

in the gas for various times at 1850°F. The results are listed in Tables 9.3 and 9.4.

Table 9.3--Per cent total strain of several commercially pure titanium grades treated in nitrogen.

Material	Condition: 1850°F Soak Periods, hr. 6	9	12	15
RMI-40	3.37	----	8.76	10.95
RMI-50	----	8.26	10.62	6.57
RMI-70	8.09	9.61	10.11	----

Table 9.4--Tensile stress (PSI) of several commercially pure titanium grades treated in nitrogen.

Material	1850°F Soak Periods, hr. 6	9	12	15
RMI-40	62,631	------	89,759	75,587
RMI-50	------	71,270	71,986	61,806
RMI-70	78,957	80,415	85,485	------

The general trend of the commercially pure titanium grades (RMI) was to increase in ductility as the soak time increased, although there was a noticeable trend toward increased tensile strength over these same periods. The strength increase became less pronounced as the material increased in grade number, i.e., increased in oxygen content. Although there appears to be a slight increase in strength, note that there is no corresponding decrease in ductility, but rather an increase the greater the

nitrogen soak time. The reason for this will become apparent later in this chapter.

9.3.0 Impulsive Loading (Impact) Experimental Results

9.3.1 Lateral Expansion

The rectangular tension specimen and Charpy bars both having been machined from the single-edge-notch tension specimens, duplicate the general chemistry and thermal treatment condition of the latter. Figures 9.2(b) and 9.3(b) are pictures of the Charpy fracture surfaces of RMI-30 to 70 treated in nitrogen for 9 hr. at 1850°F, and WCA also heated in nitrogen but for times ranging from 3 to 12 hr. at 2000°F. The fracture morphology of the RMI grades and WCA samples treated in nitrogen appear similar when comparing the static and dynamic conditions. The lateral expansion, measured as specified by A.S.T.M. Standard A-370-68, provides a means of judging the dynamic ductility. Such measurements made on 1850°F, N_2 treated RMI alloys for various times indicate in Figure 9.4 that little or no change in the plasticity occurs with time at temperature. Thus at 1850°F nitrogen could not have diffused into the metal, for if it had the expectation would be a decreased expansion with a progressively increased soak time. The effect of oxygen is also quite clear since the expansions generally decreased as more oxygen was present in the

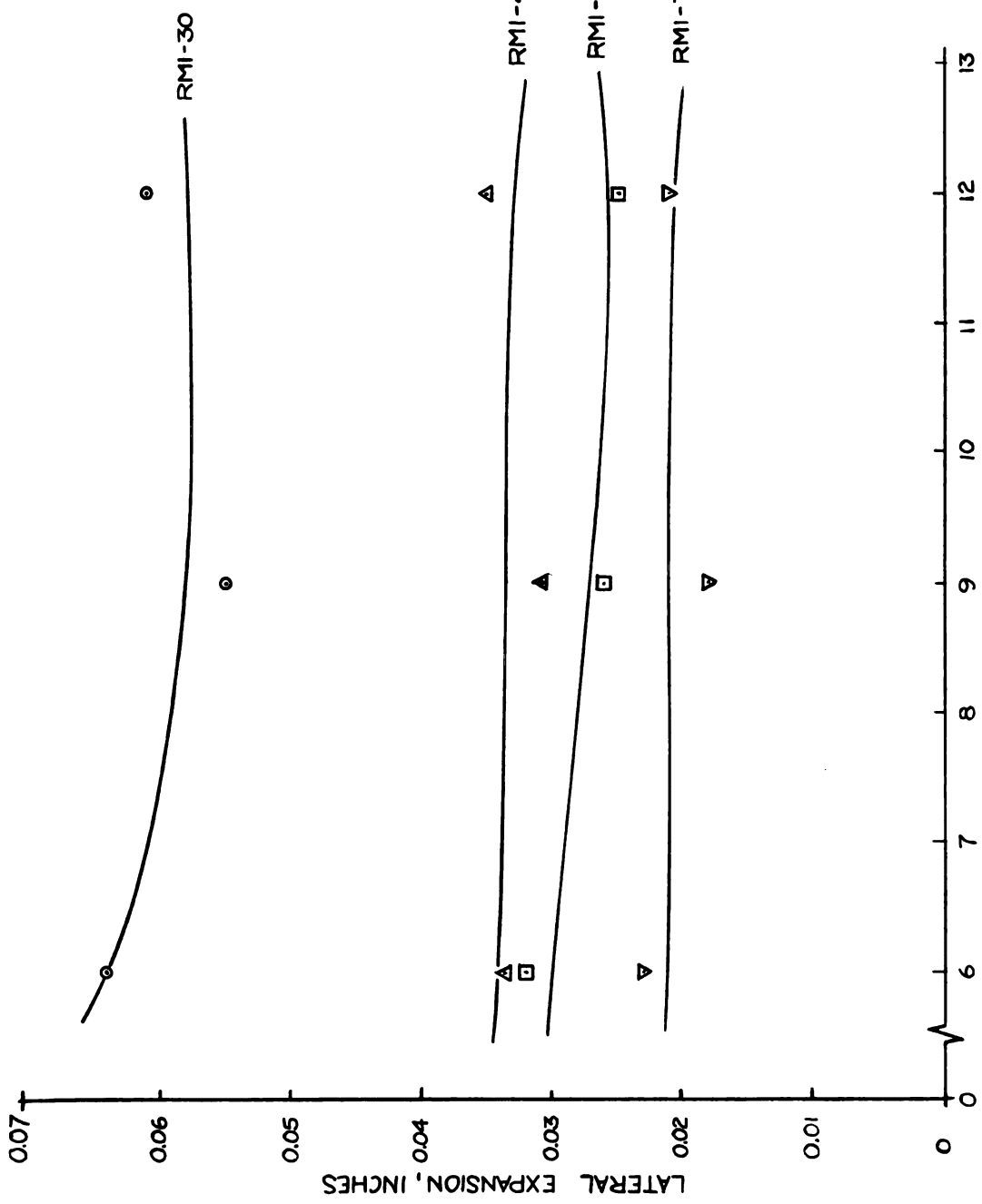


Figure 9.4--Charpy bar lateral expansions of several commercially pure titanium grades (RMI) after treatment in nitrogen at 1850°F.

system, that is, at any constant treatment time, the expansion decreased as the RMI grade number increased. This is only to be expected since oxygen's strenghthening effects are well documented in the literature.

9.3.2 Absorbed Fracture Energies

To be consistent with the foregoing data presented on RMI grades of commercially pure titanium treated with nitrogen at 1850°F, it would be expected that the impact data reflect a constant total fracture energy for any particular grade as a function of time at temperature; and that the higher the grade number (greater oxygen content), the lower the energy of failure. The impact data does indeed fulfill these expectations as shown in Figure 9.5. The individual fracture toughness effects of oxygen and nitrogen treated pure titanium (HP-BM) at 1725°F and 1850°F respectively are shown in Figure 9.6. The total fracture energy increases slightly with nitrogen treatment time, while decreasing considerably with oxygen treatment time. From the trends of the static data presented, oxygen gives every indication of having diffused into the material at 1725°F. The initiation energy decreases and seems to assume an approximately constant value; however the propagation energy decreases continuously with oxygen treatment time. The impact data (Table 9.5) of nitrogen treated WCA shows that little change occurred

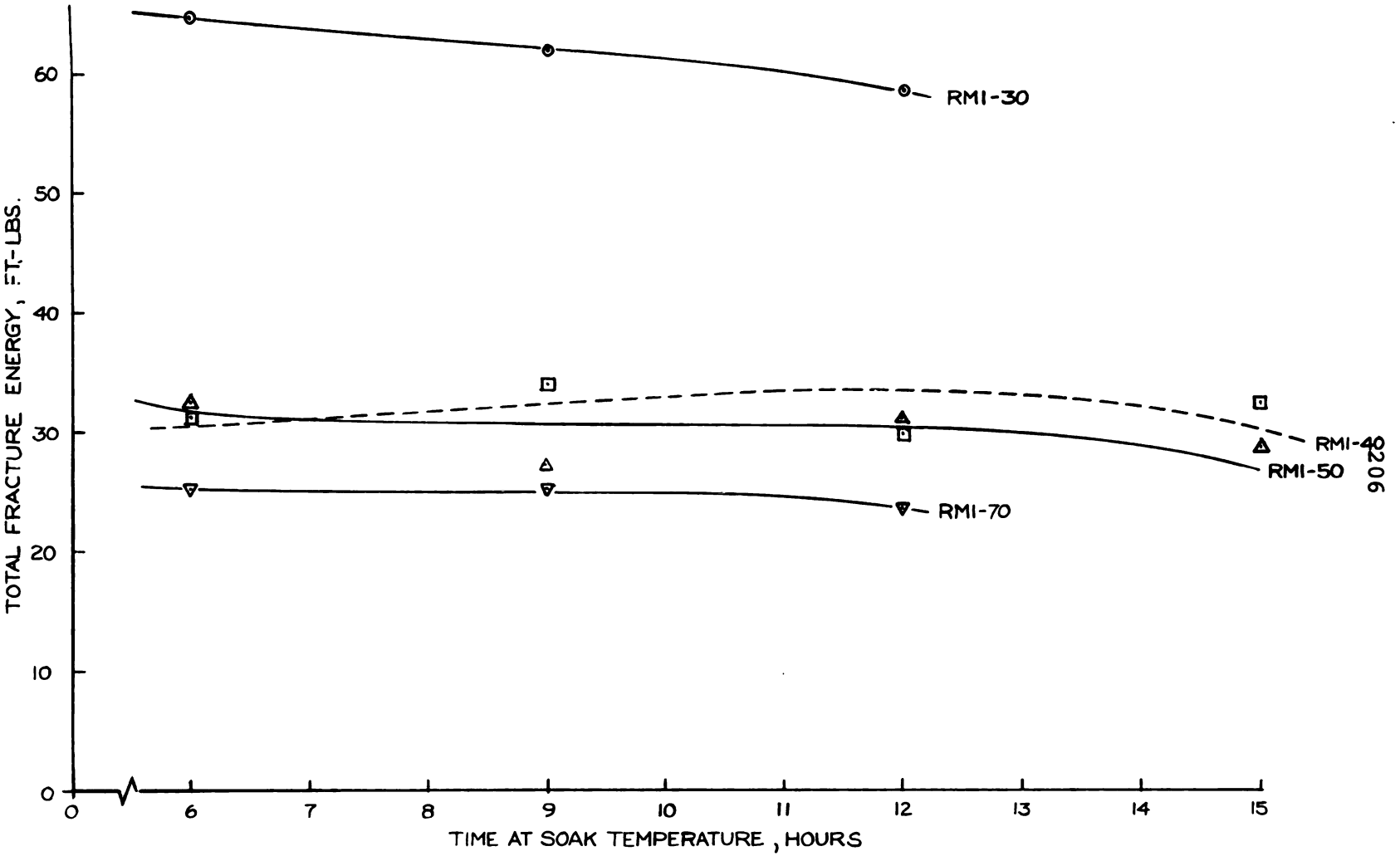


Figure 9.5--Total impact fracture energy of various commercially pure titanium grades (RMI) treated in Nitrogen at 1850°F.

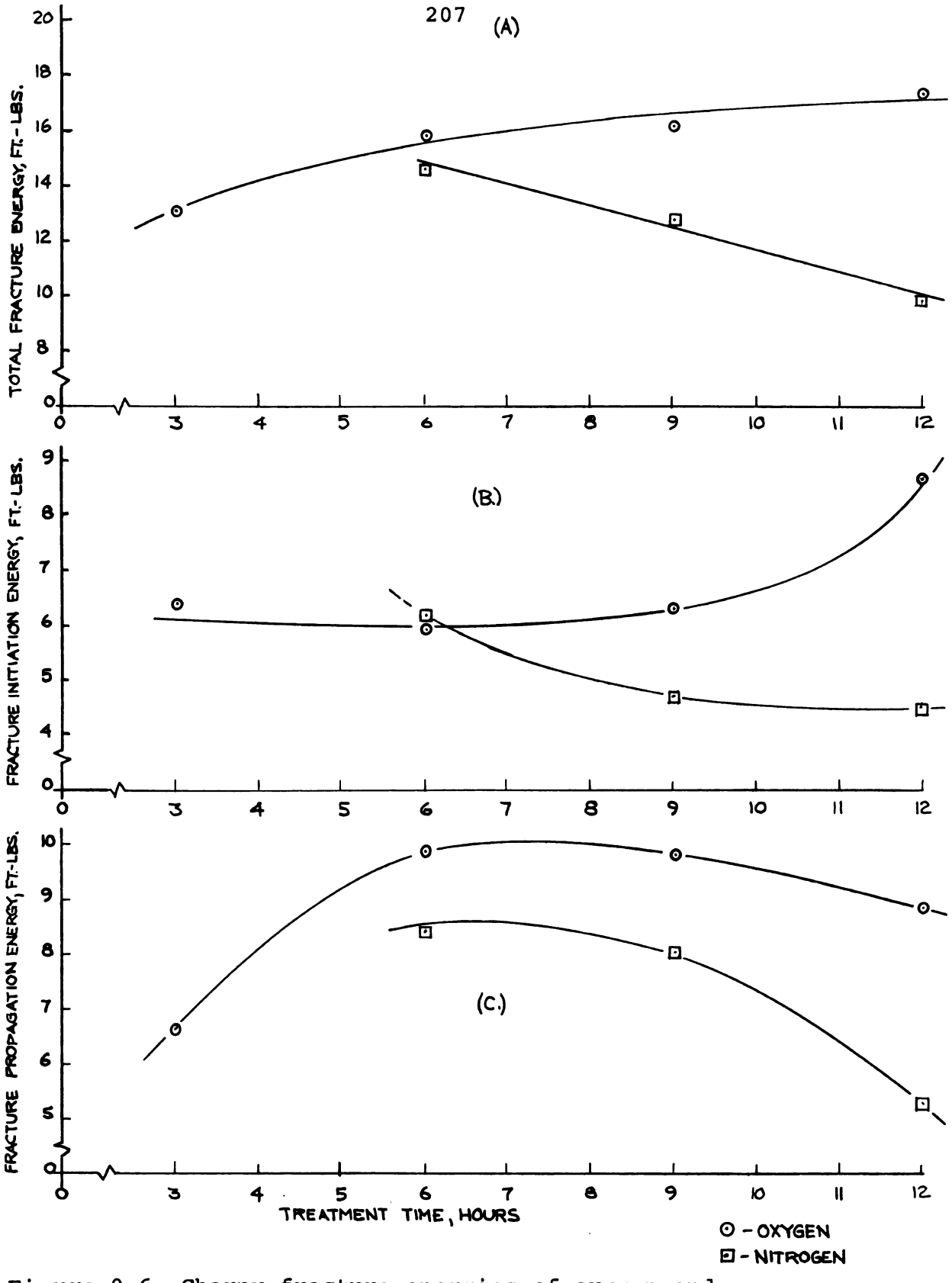


Figure 9.6--Charpy fracture energies of oxygen and nitrogen treated pure titanium (HP-RMI).

as a function of treatment time, that is, at least up to 12 hours at 2000°F.

Table 9.5--Instumented impact fracture energies of nitrogen treated WCA at 2000°F.

Treatment Time hr.	Total Fracture Energy, ft.-lbs.	Initiation Energy, ft.-lbs.	Propagation Energy, ft.-lbs.
3	13.10	5.28	7.83
6	10.90	5.67	5.23
9	12.18	5.64	6.54
12	11.93	7.50	4.43

9.4 Chemical Analysis of Selected Oxygen and Nitrogen Treated Titanium and Zirconium Samples

A chemical analysis was made on some samples to determine their interstitial content after treatment. Usually only the first and last sample in the series was analyzed. This indicated the extent to which a particular interstitial was diffusing into the metal over the time span of the treatment at the test temperatures. The reader should be mindful of the fact that the symbol ND listed several times for nitrogen content means that the sample contains less than 100 parts per million of that particular interstitial. It should not be interpreted as the sample containing no nitrogen.

9.5.0 Discussion of the Effects of Oxygen and Nitrogen Treatments on the Static and Dynamic Failure Tendencies of Titanium and Zirconium

A composite analysis of the effects of oxygen and nitrogen on titanium and zirconium under the test conditions is now possible from the observations reported.

9.5.1 Titanium Treated With Nitrogen at 1850°F

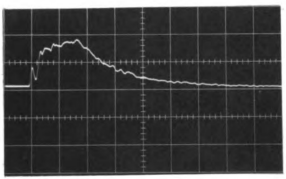
The results of the lateral expansion data (Figure 9.4) and the Charpy fracture energy (Figure 9.5) indicate that little or no significant difference occurred in those properties with time as the various grades of commercially pure titanium where heated in nitrogen at 1850°F. Furthermore it was shown that pure titanium (HP-BM) demonstrated the very same characteristics as shown in Figure 9.6(a). The static properties, however, do show some mechanical property sensitivity with increasing nitrogen soak time. For example, Tables 9.3 and 9.4, show a slight increase in ductility but a corresponding increase in strength with increasing nitrogen soak time. These factors can be explained by referring to the chemical analysis of nitrogen treated specimens (Figure 9.7). The commercially pure grades in all cases dissolved some nitrogen in the time tested, but this solution was very modest (100 ppm representing the most severe case). These slight

Table 9.6--Chemical analysis of some oxygen and nitrogen treated titanium and zirconium samples.

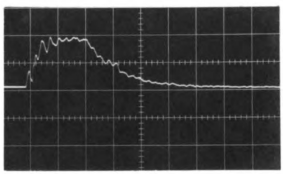
Sample Material	Gas Treatment and Temperature, °F	Soak Time hrs.	Interstitial Content, ppm. N	O	H
WCA	N_2, 2000	3	ND	620	0.5
WCA	N_2, 2000	9	--	---	0.1
WCA	N_2, 2000	12	ND	760	0.5
WCA	O_2, 1675	6	ND	700	---
HP-RMI	N_2, 1850	3	ND	880	---
HP-RMI	N_2, 1850	12	ND	1000	---
HP-RMI	O_2, 1725	6	ND	950	---
HP-RMI	O_2, 1725	12	100	1100	---
RMI-40	N_2, 1850	6	250	900	15
RMI-40	N_2, 1850	15	300	1000	11
RMI-50	N_2, 1850	6	100	1500	11
RMI-50	N_2, 1850	15	200	1400	9
RMI-70	N_2, 1850	6	ND	1600	9
RMI-70	N_2, 1850	12	ND	2000	10

increases might be interpreted as causing the corresponding increases in static strength properties; however, photomicrographs showed that the alpha plate distance between retained beta stringers increased with treatment time. These plates and stringers will be more fully discussed later. But presently suffice it to say that the industry has recognized a significant increase in both strength and ductility (static) as the microstructure changes from this "pearlite-like" structure, which

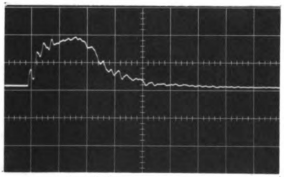
will be referred to as "the plate structure," to an equiaxed alpha structure. The annealing of the plate-like structure results in the widening of the plates with time. The equilibrium stage of this process is an equiaxed alpha morphology.[1] Although static strength properties were noted to increase with nitrogen soak time, it appears that such increases were not entirely due to the slight increases in that interstitial alone, but were also aided by morphology chnages. This also accounts for the fact that there was an increase in ductility with soak time. If the effects noted were entirely due to an increasing interstitial content, a corresponding decrease in ductility should have followed. The dynamic data seem to indicate that the very slight nitrogen increases and the morphology changes do not affect the total fracture energy very much under the conditions of the test. The instrumented impact test did, however, show an interesting feature develop in each of the commercially pure titanium series (RMI). Figure 9.7 is a series of load vs. time oscilloscope traces of RMI-50 heated in nitrogen for times ranging from 6 to 15 hours at 1850°F. With increasing nitrogen soak time a brittle component of failure is seen to develop. That is, a vertical drop develops after the maximum dynamic load. This development of an increasing normal type failure



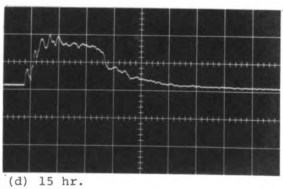
(a) 6 hr.



(b) 9 hr.



(c) 12 hr.



(d) 15 hr.

Figure 9.7--Oscilloscope load vs. time traces of RMI-50 nitrogen treated at 1850°F for various times. (Vertical = 0.2 v/cm and Horizontal = 200 μ-sec./cm for all traces).

is again presumed to be due to morphology changes as opposed to the slight nitrogen increases. It is further postulated that in general this is why lower impact values are noted for an equiaxed structure as opposed to the plate like structure. The reason why little or no change was noted in the total fracture energy of the test range can be seen by comparing the plastic range at maximum load of the 6 hr. sample with that of the 15 hr. sample. The latter pulse definitely exists for a longer duration. The increased dynamic ductility and drop off seem to compensate for each other. However, at some more advanced stage in the morphology change, these factors would not compensate, i.e., the drop off would almost be entirely to the base line. This is one of those rare cases whereby the material exhibits a fair degree of plasticity but fails in a brittle manner. The proposition that the drop off is due to morphology rather than small nitrogen increases is further supported by the chemical analysis. The 6 hr. RMI-40 sample contained 250 ppm. nitrogen and showed no drop off; but this material did exhibit such a drop off after the 15 hour treatment. In that interval the metal only increased by 50 ppm. nitrogen. By comparison, the 6 hr. RMI-70 sample contained less than 100 ppm. N_2. After 12 hours of treatment it still contained less than 100 ppm. N_2 but did show the drop off. It must

be concluded that the nitrogen level does not cause this drop off. The only factor that was common to all samples was the increase in plate distance noted with treatment time.

9.5.2 Zirconium Treated With Nitrogen at 2000°F

The chemical analysis indicates that the nitrogen content was below 100 ppm. before treatment and remained this way after treatment for 12 hours at 2000°F. The results of nitrogen treated zirconium has many similarities to titanium just discussed. For example, static testing shows very little difference in the static properties as a function of treatment time. The single-edge-notch fracture bars nearly all had identical crack openings at the maximum loads (Table 9.1). The static tensile data were 54,993; 50,341; 56,690; and 56,368 PSI for treatments of 3, 6, 9, and 12 hours respectively. Some definite and significant trends where exhibited by the dynamic testing, however. Table 9.6 shows that the fracture energy decreased with increased treatment time. A decrease in the dynamic fracture toughness due to morphology changes seems to follow a similar type pattern as discussed for titanium. The as-received metal was both fine grained and equiaxed. Annealing studies on this alloy had indicated that heating

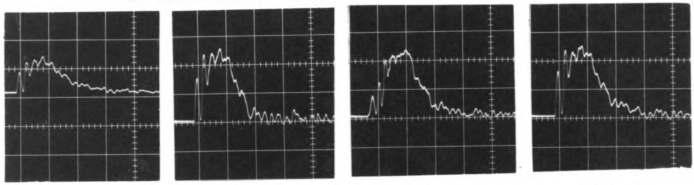
somewhere between 1800 and 1900°F for 1/2 hour caused rapid grain growth. Treating at 2000°F virtually insured entry into the beta field. Among the alpha stabilizers are the impurities: carbon, nitrogen, oxygen, aluminum, and hafnium; while the beta stabilizers are iron and chromium. There are of course others but these are among the most important due to their quantity. Oxygen is by far the single most important element and thus determines the alpha transus. The iron and chromium content determine the beta transus. The alloy under consideration had an average 1060 ppm. oxygen content alone to a combined average of 434 ppm. Fe and Cr. If the alloy is quenched from the β field, an all-alpha "Widmanstätten-like" microstructure results. Under somewhat slower cooling conditions the ends of the needles become rounded. Upon even slower cooling an elongated grain results, that is, it's several times larger than it is wide. This type of behavior is also commonly experienced in the industry.[2] What is of importance in this process is that these elongated grains show a preferred alignment with respect to their major axis. This alignment isn't necessarily in the direction of roll, but probably related to it. This aligned structure approximates the plate-like structure of titanium. Although there is no retained β in the case of zirconium (its eutectoid formers are not sluggish as is iron in titanium),

the impurities are known to show a high degree of segregation in the grain boundaries after a beta treatment. So instead of having a morphology of long stringers of retained β, the morphology of zirconium consists of short plates (adjacent elongated grains) of alpha, separated by highly segregated boundaries present in more or less straight discontinuous lines along the alignment direction. It is proposed that this condition gives rise to weakness especially evident under dynamic conditions in the same way proposed for the plate-like structure of titanium. These microstructural changes can be seen in Figure 9.8, which shows the equiaxed "as-received" microstructure, the elongated grains rather randomly oriented after a 3 hour soak, and finally some definite signs of preferred orientation after a 12 hour soak preiod. An oscilloscope trace of the 3 hour nitrogen treated zirconium sample has the same shape as the 6 hour nitrogen treated titanium sample of Figure 9.7. The other nitrogen treated zirconium samples heated for 6, 9, and 12 hours all had quick drop offs after their maximum loads were obtained (Figure 9.9). The reason why the fracture energy was noted to decrease very slightly can be answered from the fact that the force-time traces didn't alter much after the first three hour treatment. Apparently this is due to the fact that after the initial treatment not



(a) As Received 100X (b) 2000°F, 3 hr. 100X (c) 2000°F, 12 hr. 100X

Figure 9.8--Changes in the α-phase morphology of WCA treated in nitrogen at 2000°F for various times.



(a) 3 hr. (b) 6 hr. (c) 9 hr. (d) 12 hr.

Figure 9.9--Oscilloscope load-time traces of WCA nitrogen treated at 2000°F for various times. (Vertical = 0.2 v/cm. for (a) and 0.1 v/cm. for (b), (c), and (d). Horizontal = 200 μ-sec./cm. for all traces).

much additional grain growth takes place as evidenced by comparing the 3 and 12 hour treatment grain sizes. In the model presented, this means that little or no difference in plate sizes take place. The only real difference in the microstructure is the general alignment of the long axis of the grains. After this alignment is achieved, only small changes in the load vs. time records (total impact energy) can be expected. It should be mentioned that the drop off here is of little practical value since the 3 hour condition only corresponds to a 13.10 ft.-lb. level, while the 12 hour sample had a fracture energy of 11.93 ft.-lbs. What is important is to understand that the failure mechanism is linked to the phase morphology and that both titanium and zirconium fail in quite the same manner when these phase morphologies are similar. Because of the small differences in magnitude that are involved, the samples of all the treatment conditions in both static and dynamic load application appear similar in their fracture appearance as seen in Figure 9.3(a) and (b).

9.5.3 Titanium Treated With Oxygen at 1725°F

The oxygen treated titanium data definitely indicates that sufficient quantities of the interstitial did diffuse into the metal causing very marked changes

in the properties. The static tensile data indicates (Table 9.2) that between the 6 and 15 hour oxygen treatments the ultimate strength increased from 63,351 to 72,207 with a corresponding decrease in the total strain from 12.64 to 8.43 per cent. This was still ductile enough to cause the 0.4 inch plate to fail in plane stress when tested for static fracture toughness. The chemical analysis indicates that 150 ppm. oxygen was picked up in a 6 hour period at 1725°F. The reactivity and the diffusion of oxygen occurs at a much greater rate than nitrogen, since the adsorption levels for oxygen were found to be greater in a shorter period of time and at a temperature 125°F lower than the nitrogen reactions were run. Note should be made of the fact that the third important interstitial, hydrogen, is not entering as a possibility in causing the noted effects reported here. The analysis shows that the scrubbing system was quite effective. Only 0.5 ppm. hydrogen dissolved during the nitrogen-zirconium reaction which was carried out at the highest test temperature. Even in the RMI series reactions, the hydrogen remained at the same level as reported for the "as received" material, thus no hydrogen was added during these experiments. Figure 9.6 shows that even the progressive adsorption of 150 ppm. will continuously decrease the impact resistance. After the material becomes sufficiently brittle (about 10 ft.-lbs.

total fracture energy), the energy to initiate the crack levels out at about 5 ft.-lbs.; while the energy necessary to drive the crack continuously decreases with increasing oxygen content. This is typical of materials that become increasingly more brittle. The deleterious effect that oxygen has regarding the static and dynamic ductility was illustrated also by the RMI series. Figure 9.1 definitely shows that the greater the oxygen content (higher RMI number) the smaller the crack opening at the maximum load during static fracture toughness testing. As already noted the static tensile strength increased due to interstitial strengthening with increased oxygen. This is a desired condition, but correspondingly causes ductility reductions. Visually the Poisson effect of the single-edge-notch fracture test bars was noted to decrease [Figure 9.2(a)] as a function of increased oxygen content, as was the lateral expansion [Figure 9.2(b) and 9.4] under dynamic conditions. Figure 9.5 shows with little doubt that the metal's fracture toughness is markedly reduced in dynamic testing with increased oxygen levels. These data are therefore offered as a verification of oxygen's effect on titanium since the literature amply documents these same general effects. It is, however, the primary purpose of this investigation to show that the effects of oxygen treatments at 1725°F are readily detectable via mechanical property changes

over the entire treatment time of 12 hours. It must therefore be concluded that the use of the material at this temperature and above in oxygen-containing atmospheres should be discouraged.

9.5.4 Zirconium Treated With Oxygen at 1675°F

Although the experimental information is not as voluminous as in the other studies, both the available static and dynamic data do indicate that little or no oxygen seems to be diffusing into the metal at 1675°F. The crack openings recorded at the maximum loads (Figure 9.1) indicated that the metal was generally exhibiting increased static fracture toughness as a function of soak time. Moreover, the oxygen content of a 6 hour soak sample (Table 9.6) was only 700 ppm. The ingot analysis for WCA was 1150 and 970 ppm. oxygen at the top and bottom of the ingot respectively. That no embrittlement had taken place over a 6 hour soak period is further evidenced by the fact that 12.99 ft.-lbs. of energy were required for total dynamic fracture. This should be compared with the 13.1 ft.-lbs. of the 3 hour, 2000°F nitrogen treated WCA sample. The former had a .017 inch lateral expansion, while the latter .019 inches. It will be recalled that the 3 hour, 2000°F nitrogen treated WCA sample exhibited a ductile load vs. time pulse [Figure 9.9(a)],

thereafter the pulses showed a brittle component (drop off). The 6 hour, 1675°F oxygen load vs. time trace also was of the characteristically ductile type, that is, a continuously changing shape after the maximum load is attained (no sudden drop off). From the results of these data it is suggested that reactor grade zirconium heated at 1675°F in an oxygen atmosphere does not experience appreciable diffusion of that interstitial into the metal to the extent that there is a perceptible decrease in the static and dynamic fracture toughness.

Part II--Hydrogen Treated Titanium and Zirconium

It will be the purpose of this section to detail the effects of hydrogen on the strength properties of titanium and zirconium, especially under conditions of impulsive loading. In the case of titanium both pure metal (HP-BM) and the commercially pure RMI grades have been investigated. The commercially pure Charpy specimens were cut from the single-edge-notch fracture bars previously heated in nitrogen for 9 hours at 1850°F. The WCA Charpy bars used were also cut from the static fracture test specimens that were previously heated in nitrogen for 12 hours at 2000°F.

9.6 Static Tensile Results of Hydrogenated High Purity Titanium (HP-BM)

The results of the static tensile data obtained from hydrogenated HP-BM are given in Table 9.7.

Table 9.7--Tensile properties of hydrogenated HP-BM titanium treated at various temperatures and times.

Treatment Temperature, °F	Time at Temp., hr.	Total Strain %	Yield Stress PSI	Tensile Stress PSI
1520	2	59.62	26,618	40,710
1630	2	30.37	35,436	42,524
1730	2	40.83	35,135	47,355
1790	2	48.71	26,674	38,344
1790	4	41.96	26,618	39,144
1790	6	29.53	37,083	44,809

The effect of hydrogenation temperature between 1520 and 1790°F at a constant 2 hour soak was investigated, as was the effect of a constant 1790°F temperature with an increasing soak time from 2 to 6 hours.

9.7 Post Hydrogen Treatment Chemical Analysis

Table 9.8 lists the hydrogen content in ppm. for pure (HP-BM) and commercially pure titanium (RMI series and TPC). A WCA sample is also included. The initial decrease in hydrogen content from 39 to 26 ppm. and then an increase to 38 ppm. in the high purity titanium (HP-BM) is due to the phase transition of the metal from alpha to

Table 9.8--Hydrogen analysis of some titanium and zirconium samples treated under various conditions.

Treated Material	Treatment Temp., °F	Treatment Time, hr.	Hydrogen Content, ppm.
HP-BM	1520	2	39
HP-BM	1630	2	36
HP-BM	1730	2	26
HP-BM	1790	2	38
HP-BM	1790	4	48
HP-BM	1790	6	46
TPC	"As Received"		25
TPC	1310	2	32
TPC	1415	2	42
TPC	1520	2	48
TPC	1630	2	40
TPC	1730	2	41
TPC	1790	2	39
TPC	1850	2	39
RMI-30	1850	2	36
RMI-40	1850	2	40
RMI-50	1850	2	40
RMI-70	1850	2	46
WCA	1850	2	21

beta. That hydrogen absorption did take place is quite evident when comparing the "as received" TPC hydrogen level of 25 ppm. with any other sample in the sequence. Table 9.4 showed that after the nitrogen treatments the highest hydrogen content of an RMI commercially pure sample was 15 ppm. The lowest after hydrogenation is 36 ppm. Similarly the 9 hour, 2000°F nitrogen treated WCA sample contained 0.1 ppm. before hydrogenation and 21 ppm. hydrogen after treatment. Moreover, both the RMI and WCA samples were also analyzed for nitrogen and

oxygen after hydrogenation. Neither interstitial's content level increased during the hydrogenation. All future conclusions regarding changes in mechanical properties will be based upon the fact that hydrogen is the sole interstitial variable and that the argon-H_2O system is truly a hydrogen generator. The water dissociates into its component gases. Hydrogen is absorbed into the metal because of its rapid diffusion compared to that of oxygen. The metal becomes charged with hydrogen while little or no oxygen charging occurs. The argon through water technique generates only small amounts of the two gases, a requirement for these experiments because the data and analysis to be presented will demonstrate that rather large property changes occur over the range of 0-50 ppm. hydrogen.

9.8.0 Impulsive Loading Experiments of Hydrogenated Titanium and Zirconium

9.8.1 Lateral Expansion

The Charpy bar lateral expansions of hydrogenated titanium and zirconium are given in Tables 9.9.0 and 9.10.0.

The dynamic ductility decreased considerably for the high purity titanium after the 1790°F, 2 hour treatment and passed through the brittle transition upon being treated for 4 hours at the same temperature. The commercially pure titanium's (TPC) expansion was very small at

Table 9.9.0--Charpy bar lateral expansion of hydrogenated HP-BM and TPC titanium.

Material	Treatment Temp., °F	Treatment Time, hr.	Lateral Expansion in.
HP-BM	1520	2	.065
HP-BM	1630	2	.065
HP-BM	1730	2	.068
HP-BM	1790	2	.045
HP-BM	1790	4	.008
HP-BM	1790	6	.008
TPC	1310	2	.001
TPC	1415	2	.006
TPC	1520	2	.000
TPC	1630	2	.001
TPC	1730	2	.000
TPC	1790	2	.001
TPC	1850	2	.009

Table 9.10.0--Charpy bar lateral expansions of hydrogenated commercially pure titanium (RMI series) and WCA treated at 1850°F for 2 hours.

Material	Lateral Expansion, in. After N_2 Treatment	After H_2 Treatment
RMI-30	.055	.005
RMI-40	.031	.001
RMI-50	.026	.002
RMI-70	.018	.005
WCA	.004	.001

even low treatment temperatures. Finally, the commercially pure titanium (RMI series) samples all experienced drastic changes in their dynamic plasticity after hydrogen treatment as compared to the values recorded after the

9 hour nitrogen treatments. Likewise the WCA also decreased in lateral expansion after the hydrogenation.

9.8.2 Absorbed Fracture Energies and Dynamic G_{IC} Values

The fracture energies are given in Tables 9.11 and 9.12 as determined via the instrumented impact test. Note that G_{IC} values are only given for the 1790°F, 4 and 6 hour hydrogen treatments in the HP-BM series because all the other samples exhibited significant plasticity, thus a G_{IC} calculation would not be valid. Furthermore, Table 9.12 gives a comparison between the total, initiation, and propagation energies after the 9 hour nitrogen treatment at 1850°F, and after the 2 hour hydrogenation at 1850°F. Similar information is presented for the WCA sample previously treated at 2000°F in nitrogen for 12 hours. It will be recalled that the Charpy bars used for this hydrogenation were machined from the single-edge-notch tension specimens previously treated under the stated conditions. Such a comparison will serve to demonstrate that hydrogen is much more important in terms of promoting failure under impulsive loading conditions. A significant reduction in the total absorbed energy of fracture for the HP-BM titanium is noted to occur at the 1790°F, 2 hour treatment and drastically falls off at the same temperature upon treating for 4 hours. A similar

Table 9.11--Fracture toughness and fracture energies of hydrogenated HP-BM and TPC titanium.

Material	Treatment Temp., °F	Treatment Time, hr.	Total Fracture Energy, ft.-lbs.	Initiation Energy, ft.-lbs.	Propagation Energy ft.-lbs.	$G_{IC} = \frac{\text{Total Energy}}{(b)(w-a)}$ ft.-lbs./in.^{2}
HP-BM	1520	2	68.64	49.13	19.51	-----
HP-BM	1630	2	63.47	39.15	24.31	-----
HP-BM	1730	2	72.44	41.89	30.54	-----
HP-BM	1790	2	41.46	27.56	13.89	-----
HP-BM	1790	4	4.53	2.10	2.43	36.50
HP-BM	1790	6	3.41	2.00	1.40	27.45
TPC	1310	2	7.79	6.37	1.42	62.73
TPC	1415	2	6.12	5.82	0.30	49.29
TPC	1520	2	1.23	1.03	0.20	9.89
TPC	1630	2	1.18	0.98	0.20	9.49
TPC	1730	2	1.69	1.23	0.46	13.59
TPC	1790	2	1.38	1.11	0.27	11.13
TPC	1850	2	1.00	0.84	0.17	8.09

Table 9.12--Fracture toughness and fracture energies of hydrogenated commercially pure titanium (RMI) and reactor grade zirconium (WCA).

Material	Total Fracture Energy, ft.-lbs.		Initiation Energy ft.-lbs.		Propagation Energy ft.-lbs.		G_{IC} after Hydrogenation ft.lbs./in.^{2}
	before	after	before	after	before	after	
RMI-30	62.13	2.10	27.26	0.89	34.87	1.21	16.89
RMI-40	27.28	2.82	10.37	0.92	16.91	1.90	22.72
RMI-50	34.20	2.87	17.39	1.37	16.81	1.50	23.15
RMI-70	25.48	3.83	7.14	1.51	18.33	2.30	30.83
WCA(a)	11.93	2.66	7.50	1.88	4.43	0.78	21.47
WCA(b)	12.99	2.58	5.01	1.62	7.98	0.96	20.80

Note: RMI series previously treated in nitrogen at 1850°F for 9 hours. WCA(a) previously treated in nitrogen at 2000°F for 12 hours. WCA(b) previously treated in oxygen at 1675°F for 6 hours.

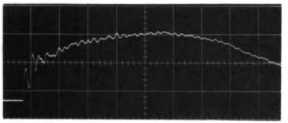
type of drop off in the total fracture energy is noted for the commercially pure titanium (TPC). This material demonstrated considerable brittleness in that only 7.79 ft.-lbs. were absorbed after treatment at the lowest test temperature (1310°F). Even with an initial brittleness, a definite drop off occurred after the 2 hour treatment at 1520°F. These reductions are even more apparent when comparing the fracture toughness values, G_{IC}. The recorded impact values indicated that catastrophic failure had occurred in each case of the RMI series after the hydrogenation treatment. Likewise the zirconium (WCA) samples pretreated with either oxygen or nitrogen also behaved in a brittle manner in impact after the hydrogen treatments.

9.9.0 Discussion of the Effects of Hydrogen on the Fracture Properties of Titanium and Zirconium

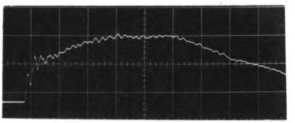
9.9.1 The Failure of Hydrogenated Pure Titanium (HP-BM)

From the data already presented, the evidence seems to overwhelmingly support the notion that hydrogen, at least under impulsive conditions, presents a far more serious threat to titanium's fracture toughness than do either oxygen or nitrogen under the test conditions imposed by this study. A comprehensive analysis of the effect of hydrogen in titanium is presented, which will

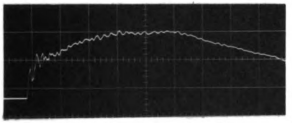
allow a fracture model to be delineated. The literature cited, concerning the mechanical properties of hydrogenated titanium, indicated that the interstitial had little effect as a strengthening agent compared to oxygen and nitrogen. This study supports this conclusion because Table 9.7 shows that the variation in strength does not follow the progressive increase in hydrogen content given in the analysis. The observed changes are due to other factors. Likewise the ductility is little affected by the hydrogen content. Marked embrittlement under impulsive loading conditions was manifested in several ways, however. The lateral expansion of the HP-BM titanium dropped off initially at the 1790°F, 2 hour treatment condition, and then catastrophically at the 4 hour condition with the same treatment temperature (Table 9.9). The total energy of fracture (Table 9.11), as determined by the instrumented impact test, indicated identical type reductions at the same treatment temperature and times, i.e. 1790°F at 2 and 4 hours. Figure 9.10, the load-time oscilloscope traces of the various treatment conditions, shows that the pulse shape is shorter for the 1790°F, 2 hour condition than previous traces in the series. In fact, the trailing edge of these other pulses had not reached the base line at the end of the trace, whereas the 1790°F, 2 hour sample had. The pulse shape of the 1790°F, 4 hour treatment sample is much shorter in length



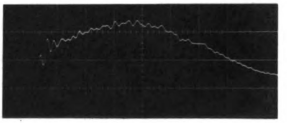
(a) 1520°F, 2 hr.



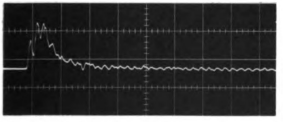
(b) 1630°F, 2 hr.



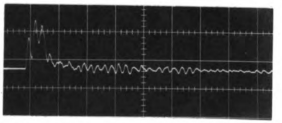
(c) 1730°F, 2 hr.



(d) 1790°F, 2 hr.



(e) 1790°F, 4 hr.



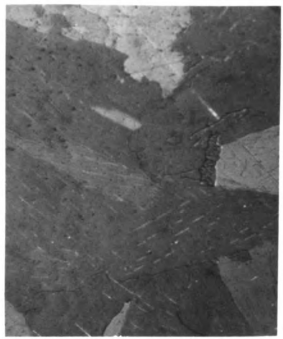
(f) 1790°F, 6 hr.

Figure 9.10--Oscilloscope load vs. times traces of hydrogenated HP-BM titanium (Vertical = 0.1 v/cm, horizontal = 200 μ-sec./cm for all traces).

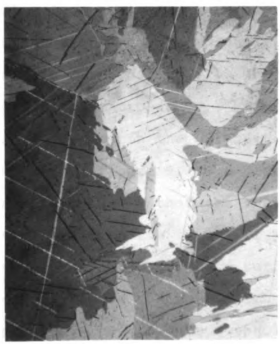
and has a lower maximum load magnitude than obtained from the previous treatments in the series. That such drastic changes have taken place at the 1790°F, 4 hour treatment condition under impulsive loading conditions is important, but even more important is why and how it came about. Figure 9.11 shows the microstructural changes which took place in the material. The 1630°F, 2 hour microstructure of heavily twinned large alpha grains is representative of the material for all the conditions up to 1790°F, 2 hours. The twinning must have occurred during the mechanical polishing, for the pure metal is known to twin easily. The photomicrograph of the 1790°F, 2 hour condition shows white streaks which are aligned in definite directions in each grain. These stringers were subsequently identified as being the initial stages of hydride formation. These hydrides are seen to increase in size and development on passing to the 1790°F, 4 hour condition photomicrograph. In several instances these stringers are seen to cross grain boundaries which might cause some concern. Hydrides, as any precipitate, have a habit plane which is identified in the literature. Two adjacent grains would not have identical orientations, thus the stringer should change direction upon passing a grain boundary. One must remember, however, that these samples were furnace cooled. As such, there was sufficient time for grain growth and hydride development. Consider a grain containing a hydride



(a) 1630°F, 2 hr. 100X



(b) 1790°F, 2 hr. 100X



(c) 1790°F, 4 hr. 100X



(d) 1790°F, 6 hr. 100X

Figure 9.11--Photomicrographs of HP-BM titanium treated with hydrogen.

being consumed by an adjacent grain. The consuming grain can't reorient the existing hydride, and thus must accommodate it. Having done so, the hydride can thus continue to grow into that consuming grain. These stringers often are stretched out the full dimension of the grain. Consider further the situation shown in the photomicrograph of the 1790°F, 6 hour condition, whereby twins are noted to fracture the brittle hydrides as they intercept them. This is at least one way that microcracks are created along the path of the hydride. Twinning is known to be of increasing importance in the deformation of titanium as the strain rate becomes rapid. From the conditions referred to, one might well expect that the fracture be flat from grain to grain as it follows the path of the hydride stringers completely across the grain. Under such conditions the fracture path would not veer a great deal on a macro-scale. On a micro-scale the fracture path would depend on the orientation of the precipitated hydride. Figure 9.12, a picture of the Charpy fracture surfaces, shows that the typical fibrous appearance vanishes with the 1790°F, 2 hour sample replaced by a very granulated fracture surface starting with the 1790°F, 4 hour sample. Note also the difference in the lateral expansion. The fracture morphology pictures obtained from these Charpy surfaces by scanning electron microscopy (SEM) as shown in Figure 9.13 lend further evidence to the fracture

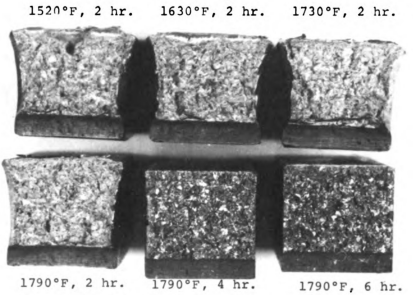
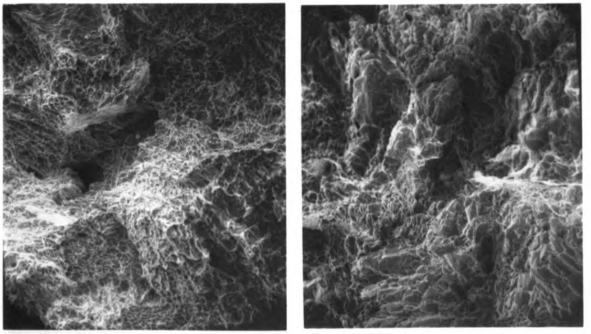
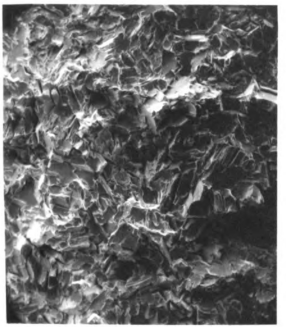


Figure 9.12--Charpy fracture surfaces of hydrogenated HP-BM titanium.



(a) 1630°F, 2 hr. 100X (b) 1790°F, 2 hr. 100X

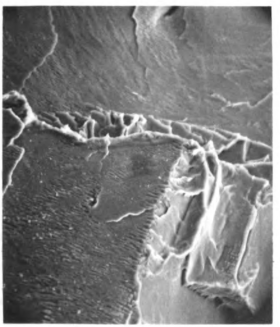
Figure 9.13--SEM fracture morphology pictures of hydrogenated HP-BM titanium.



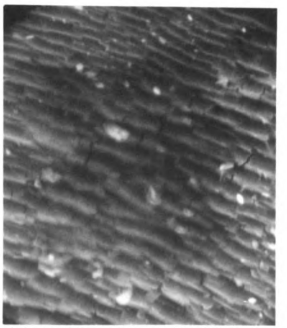
(c) 1790°F, 4 hr. 20X



(d) 1790°F, 6 hr. 20X



(e) 1790°F, 4 hr. 1000X



(f) 1790°F, 4 hr. 10,000X

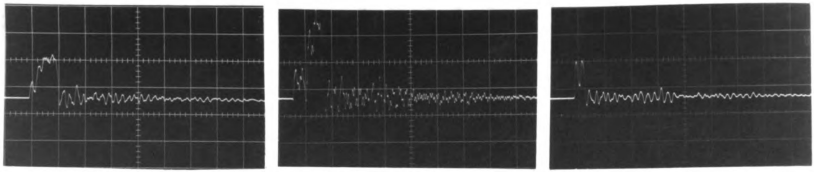
Figure 9.13--continued.

model suggested. Figure 9.13(a) is representative of the fracture surface for all the conditions from 1520 to 1790°F, 2 hour. The only difference being a general decrease in the fine deformation structure (decrease in ductility) of the morphology as shown in Figure 9.13(b). Incidentally, it is this fine detail which gives the fracture the dull gray appearance. The type of fracture which was predicted to occur at 1710°F, 4 hour does indeed take place. The small degree of ductility that exists is due to the type of fine ductile deformation structure noted in earlier pictures which is present on some of the ridges of the fracture surface. The ductility decreases continuously by increasing the hydrogenation time. This aids in increasing the length and development of the hydride. It can be seen from the 1790°F, 6 hour sample that the detail on the ridges decreases and the individual flat areas increase in size (apparently due to grain growth) as hydrogenation time is increased at a constant treatment temperature. The flat and smooth appearing surfaces of the brittle morphology, which will be referred to as "blocky structure," are not really smooth at all on a fine scale as seen by Figure 9.13(e). The fine detail (ductile component of the morphology) can also be seen between the ridges in this picture. The true surface is composed of parallel outcroppings which are felt to be due to fine less-developed hydride

precipitates which were found to exist on this scale in copious quantities. These flat shale-like outcroppings are badly broken up. Numerous microcracks are in evidence as is the fracture debris.

9.9.2.0 Failure of Hydrogenated Commercially Pure Titanium (TPC)

The commercially pure titanium (TPC) demonstrated largely the same type of failure behavior already discussed in reference to the high purity titanium (HP-BM). There are some microstructural differences. Since the TPC type of titanium represents a series of dilute interstitially strengthened alloys available on the market, a complete analysis is presented for this material. Table 9.11 shows that the fracture energy drops off sharply at the 1520°F treatment condition, which is more dramatically indicated by the fracture toughness values, G_{IC}. The oscilloscope impact traces show the transition through the drop off in Figure 9.14. Pictures of the Charpy fracture surfaces would lead one to believe that the transition to complete brittleness occurs at the 1730°F condition due to the obvious change in appearance (Figure 9.15). The impact properties suggest, however, that the transition is complete at the 1520°F condition. SEM fracture morphology studies do indeed indicate that the transition actually occurs at the 1520°F condition.



(a) 1310°F, 2 hr. (b) 1415°F, 2 hr. (c) 1520°F, 2 hr.

Figure 9.14--Oscilloscope load vs. time traces of hydrogenated TPC titanium.
Note: Vertical = 0.2 v/cm for (a) and 0.1 v/cm for (b) and (c).
Horizontal = 200 μ-sec/cm for (a), (b), and (c).

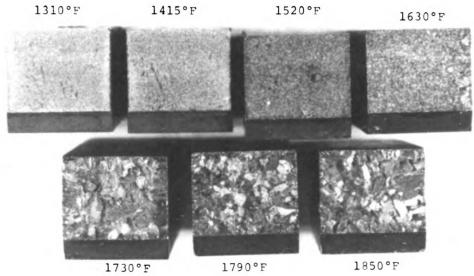


Figure 9.15--Charpy fracture surfaces of hydrogenated TPC titanium.

The deformation structure is on a very fine scale thus causing the confusion. The morphology was generally similar for the 1310 and 1415°F treatments. The latter pictured in Figure 9.16 is representative of the deformation structure. The 1520°F series of photographs do in fact show the transition in the morphology. For example, upon comparing the 20x photographs, more detailed outlines of the existence of a granular structure is noted. This is even in more evidence at the 100x level of magnification. Finally at 500x it is clear that the 1415°F failure sample contained a good deal of the fine detail noted earlier in the ductile type failure of HP-BM titanium, while the 1520°F sample shows a prominance of the blocky type structure. The fracture granularity became even more pronounced at the 1630°F condition as evidenced by the 20x photograph. An increase in prominance of the blocky condition with an increase in area of the discrete flat areas are easily distinguished at 100x when progressing from the 1520°F to 1630°F treatment condition. The amount of fine detail had appreciably decreased. A different fracture morphology had developed in the 1730°F sample. Note that at magnifications as low as 20x the fracture surface is seen to consist of large flat areas resembling broken up shale. This gross structure is the one which gave the Charpy samples the appearance of the transition occurring at that condition.

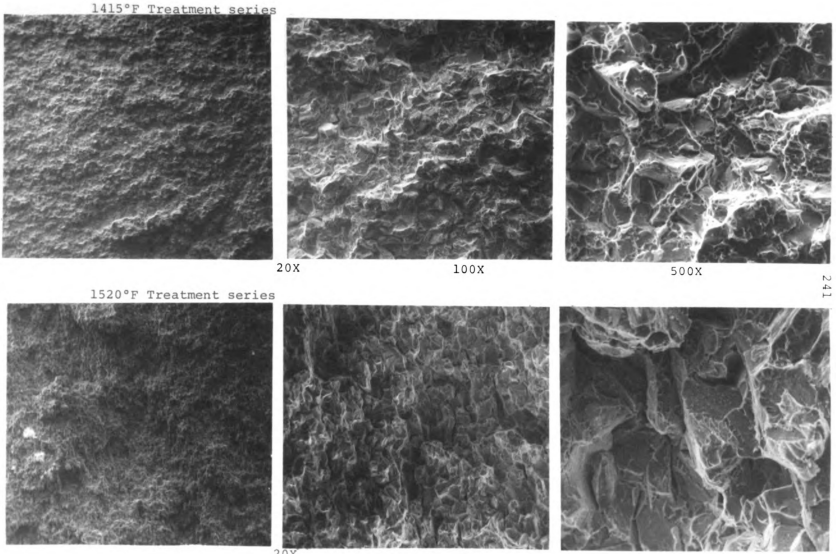
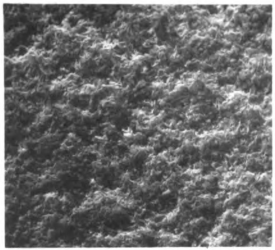
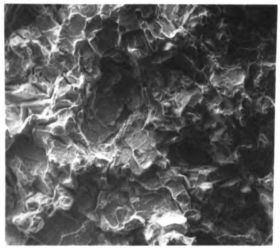


Figure 9.16--SEM fracture morphology pictures of hydrogenated TPC titanium.

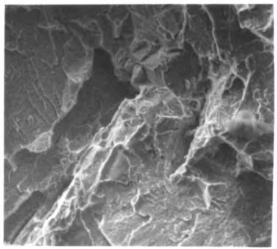
1630°F Treatment series



20X

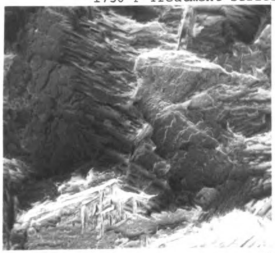


100X

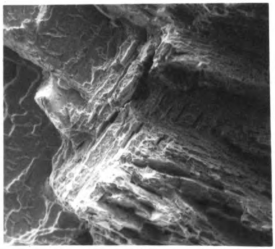


500X

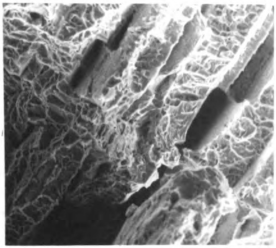
1730°F Treatment series



20X



100X

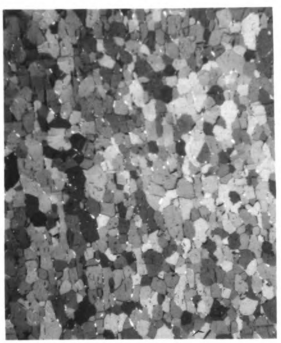


500X

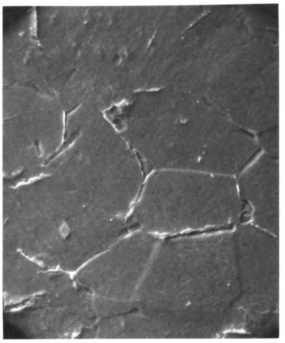
Figure 9.16--continued.

This structure was noted to exist for the remaining test conditions, except that the fine detailed deformation structure which was seen to exist at the broken ends of the shale-like outcropping in the 500x picture of the 1730°F treatment series progressively become less in evidence at the higher temperature treatments. This feature of the fracture morphology allows a sensible explanation to be given for the recorded fracture toughness and energies of Table 9.11. The increase in G_{IC} from 9.49 to 13.59 ft.-lbs./in.^{2} corresponds to the change in fracture morphology between the 1630°F and 1730°F treatments. Further decreases in G_{IC} at higher treatment temperatures follows the increasing absence of the fine deformation structure (ductile component of failure) at the ends of the fracture outcroppings. The phase morphology determined by metallographic techniques greatly aids in helping to explain the fracture morphology. In addition it yields good evidence as to why there were some fracture morphology differences noted between the pure and commercially pure titanium metals. The (TCP) metal was fine grained for all conditions up to and including the 1520°F treatment as the section indicates in Figure 9.17(a). However, at 1520°F, a precipitate is seen in Figure 9.17(b) to be present in the grain boundary. The selective etching is seen to have been very rapid at these sites. This same precipitate was also noted in the 1415°F sample. Electron microprobe analysis showed that the

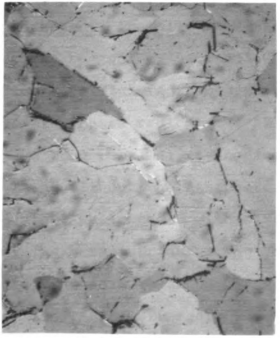
precipitate was iron stabilized and thus considered to be the retained β in the structure. This stabilization likely occurred during the fabrication. The increased treatment temperatures seems to aid in the agglomention of beta in the alpha grain boundaries. It follows, therefore, that the observed embrittlement starting with the 1415°F sample is due to the initial embrittlement of beta. The catastrophic failure of the 1520°F sample is just due to the increased solution of hydrogen. The total hydrogen content in the two samples was 42 and 48 ppm. respectively. For a proper understanding of the remaining microstructures of Figure 9.17 it is necessary to investigate the effects that the impurities have upon the stabilization and kinetics of the titanium alpha-to-beta transformation. Commercially pure titanium alloys contain the interstitials: oxygen, nitrogen, and carbon which all have the tendency to stabilize the alpha phase. Oxygen is especially important simply because it is purposely added as a strengthening agent and therefore present in the largest quantity. Thus a high strength (≈ 70,000 PSI yield strength) commercially pure titanium alloy could contain about 0.3 wt. % (3000 ppm.) oxygen. However, equally important is the fact that the industry uses iron, a very potent beta stabilizer, as a grain refiner. Therefore, when both are present one may think of the oxygen as raising the alpha transus and the iron



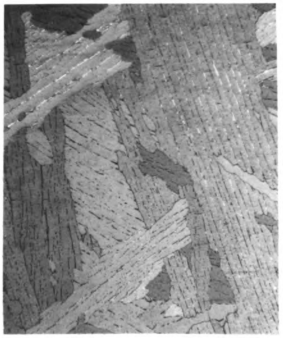
1520°F, 2 hr. 100X



1520°F, 2 hr. 100X



1630°F, 2 hr. 400X



1730°F, 2 hr. 100X

Figure 9.17--Photomicrographs of commercially pure titanium (TPC) treated with hydrogen.

lowering the beta transus. Regarding the kinetics, the partial Fe-FeTi equilibrium phase diagram is a beta eutectoid system, that is $\beta \overset{1094°F}{\rightleftarrows} \alpha + FeTi$. However, iron is a sluggish eutectoid former and as such the reaction does not take place as stated. Instead some of the β transforms to its α allotrope, but little or none of the intermetallic compound is formed. The remaining beta is stabilized at room temperature due to the segregation of the iron. The iron content in the alpha (transformed β) is generally uniform, while greatly increased concentrations exist at the sites where the beta is precipitated. With these things in mind it is now possible to explain the observed microstructures and how they gave rise to the fracture morphologies already presented. The alloy under consideration had an iron and oxygen content of 0.11 and 0.10 wt.-% respectively. Figure 9.17(c) indicates that the sample was heated into the two phase region ($\alpha + \beta$) because some of the grains have long parallel stringers, while others do not. The grains without the stringers are the original alpha grains, while those with stringers are the original β grains before transforming to alpha. Upon cooling they did transform to alpha but not completely as suggested earlier. The stringers are therefore retained β phase. This fact was verified via electron probe analysis which indicated very steep peaks in iron content each time a

stringer was scanned. Such an analysis allows a β stringer to be differentiated from a hydride stringer since their general appearances are very similar. Finally at the 1730°F treatment the photomicrograph suggests the soak took place entirely in the β field since no original alpha grains are present. All the alpha (transformed β) is present as alternate plates with the retained β. This structure is very similar to pearlite in steel. Note that appreciable grain growth took place. Since hydrogen is many times more soluble in beta phase than alpha, it seems reasonable that the partition of this interstitial would be favored by the beta. The commercially pure titanium having retained beta in its microstructure explains why the long stretched out hydrides observed in the pure material are not present the commercially pure grades. After the alpha phase in the pure metal attains its limit of solid solubility for hydrogen it precipitates the hydride, but the commercially pure material's beta phase dissolves the extra hydrogen that would have gone into hydride formation. The impact values presented, however, reflect that little appears to be gained from a practical point of view in enhancing the fracture toughness, due to the beta dissolving the excess hydrogen. Instead of the failure being promoted by the presence of the long brittle hydrides as in the mode of failure of the pure material; it follows the long beta stringers containing the hydrogen.

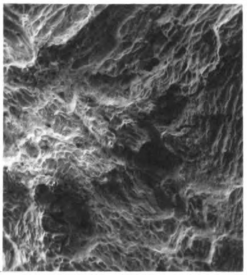
The beta is also present in the grain boundaries, so the fracture path can follow either the boundaries or the stringers. The plate like structure of the commercially pure metal yields more of a broken shale type fracture appearance than the pure metal. Presumably this is due to the fact that there are more β-stringers present in the structure of the former than there are hydride stringers in the latter per unit volume of metal. Therefore, there are more fracture paths available in the commercially pure metal giving rise to a higher degree of surface fragmentation and irregularity on a gross scale.

9.9.2.1 Effect of Increasing Beta Phase

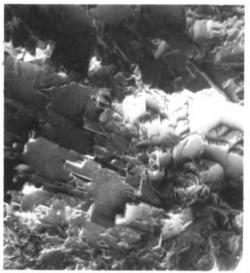
A final comparison of interest between the pure metal and the commercially pure concerns the level of hydrogen necessary to promote the brittle condition under impulsive loading. The transition in the pure material occurred at 1790°F after four hours of treatment. The hydrogen level was determined to be 48 ppm., but no beta was retained due to the absence of such stabilizers. Therefore all the hydrogen after the solid solubility limit of alpha had been attained went into hydride production. It was abundantly clear that the failure was due to the hydrides and not to the hydrogen in solution. The transition of the commercially pure titanium (TPC),

represents a case of an embrittled beta phase. Again a 48 ppm. hydrogen concentration existed. Obviously it was partitioned between the alpha and beta phases since no hydrides were noted to have formed. Because the embrittled beta concentrated in the grain boundaries, and the metal was fine grained, the fracture had a highly granular appearance corresponding to the intergranular failure path. The failures of the samples treated between 1730 and 1850°F, the transformed beta structures, had hydrogen levels as low as 39 ppm. which was still enough to cause the transition under impulsive loading. Little or no advantage in the dynamic performance of the metal seems to have been realized by transferring the excess hydrogen from the hydride to a state of dissolution within the beta. One might well wonder if failure would still occur if more beta phase were present in the structure, and thus lowering the average hydrogen content per unit volume of that phase. To get an indication of beta's embrittlement characteristics as a function of hydrogen content the RMI series previously treated in nitrogen at 1850°F for 9 hours, were all treated in hydrogen at 1850°F for 2 hours. This was done because the iron content is seen to vary from 300 to 3000 ppm. in the series. An 1850°F treatment is high enough to insure complete entry into the beta field. Increasing the amount of β in the structure by increasing the Fe content had the effect of maintaining a

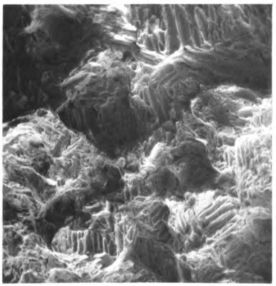
complete beta structure upon cooling to a lower temperature. Consequently, a constant hydrogen content was not obtained (varied from 36 to 46 ppm.) even through the heating and cooling conditions were the same. Oxygen, an alpha stabilizer, also increased from 700 to 2810 ppm. Exactly what its effect was is unknown. By comparing the fracture energy values before and after hydrogenation in Table 9.12, the material in all cases is seen to have passed through the brittle transition. These results generally indicate that increasing amounts of a beta stabilizer such as iron to the level normally used in commercially pure titanium alloys does little to improve the alloy with respect to hydrogen embrittlement under impulsive conditions. This would be an area for further fruitful research, for all the experimental variables were not under close control. Table 9.12 does show some encouraging trends to warrant such studies. Before hydrogenation there was a general trend of decreased ductility (decreasing fracture energy) with increasing RMI sequence number. After hydrogenation this trend was reversed. In fact, the fracture toughness, G_{IC}, for RMI-70 with 46 ppm. hydrogen was almost double that of RMI-30 with only 36 ppm. hydrogen. The photomicrographs of these materials showed that the RMI-30 contained no perceptible retained β, while the long hydride stringers were dispersed throughout. The other



(a) RMI-30, 1850°F, 9 hr., N_2 20X



(b) RMI-30, 1850°F, 2 hr., H_2 20X



(c) RMI-70, 1850°F, 9 hr., N_2 20X



(d) RMI-70, 1850°F, 2 hr., H_2 20X

Figure 9.18--SEM pictures of some commercially pure titanium (RMI-30 and 70) before and after the transition.

RMI commercially pure alloys all were plate structures (alternate alpha and retained β). Figure 9.18 shows the difference in the fracture morphology at the same 20x magnification of RMI-30 and RMI-70 before and after the transition.

9.9.3 The Failure of Hydrogenated Reactor Grade Zirconium (WCA)

The effects of hydrogen in zirconium were also found to be bad. The pretreated 2000°F, 12 hour nitrogen sample with 0.5 ppm. hydrogen, absorbed an additional 20.5 ppm. upon hydrogen treatment at 1850°F for 2 hours. This sample did undergo the brittle transformation as the fracture energy data in Table 9.12 shows. The fracture morphology of the pre and post hydrogen treatment sample originally treated in nitrogen for 12 hours at 2000°F is shown in Figure 9.19. The pre-treatment SEM pictures (a, b, and c) show that the ductile mode of failure is much like what was noted for the commercially pure RMI series, Figure 9.18. That is a "dished out" deformation structure which coincides with the grain size and shape. The RMI series, however, contained a mixed ductile deformation morphology: the dished out and fine structure seen in the fractures of the pure metal. Zirconium does not contain any of the fine deformation structure at all. The reactor grade zirconium has a different transition fracture morphology

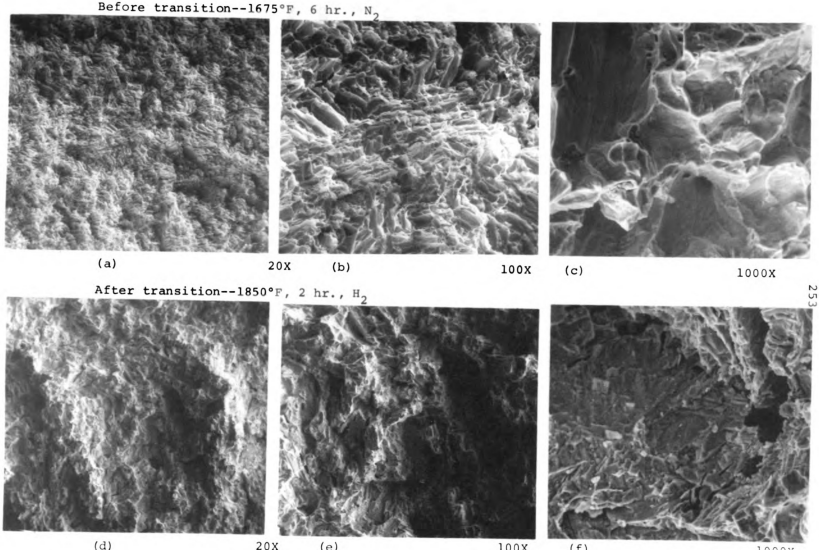


Figure 9.19--SEM pictures of reactor grade zirconium (WCA) before and after the transition.

than titanium, as might be expected if the failure mechanisms proposed for the hydrogen embrittled titanium are correct. Note (pictures d, e, and f of Figure 9.19) that there is a general appearnace of granularity, but it is not developed to the degree that was noted earlier in the commercially pure (TPC) titanium. In the latter case failure occurred via an embrittled beta phase in the alpha grain boundaries, thus the high degree of granularity. The zirconium does not have any retained beta in its structure, however. The hydrogenated zirconium fracture morphology still contains a good deal of tearing. The tearing (ductility component) is caused when the main fracture path is made continuous upon joining together existing microcracks. Picture (d) shows the high degree of fragmentation and micro-cracks present. That some granularity exists has been demonstrated, but the ductile tearing on the fine scale gives the dull gray macro-appearance generally indicative of a ductile failure which is seen in Figure 9.3(c). That figure also shows that there is little difference in the appearance with an additional oxygen content.

CHAPTER X

CONCLUSIONS

1. Pure and commercially pure titanium with as much as 0.281 weight per cent initial oxygen fractures in a state of plane stress under near static loading conditions in sections at least as large as 0.4 inches when heated in nitrogen for as long as 15 hours at 1850°F.

2. Similarly, pure titanium heated in oxygen at 1725°F for 12 hours; and reactor grade zirconium treated in nitrogen for 12 hours at 2000°F, and in oxygen for 6 hours at 1675°F all failed in a state of plane stress in the static fracture testing with 0.4 inch plate sections. This occurred in each case although the surfaces consisted of brittle oxides or nitrides. The cores thus exhibited good fracture toughness.

3. The increasing tendency of a brittle failure component with increased treatment time at 1850°F was attributed to morphology changes within the microstructure of the RMI commercially pure titanium grades, rather than embrittlement due to nitrogen. The diffusion of this interstitial is felt to be negligible in terms of affecting the fracture properties. These differences were only noted under dynamic loading conditions.

4. It appears that little or no nitrogen diffuses into zirconium at 2000°F to cause embrittlement of the plate material, but morphology changes do cause some loss of impact strength. The mechanism of failure is modeled after that proposed for titanium.

5. Titanium absorbs oxygen at a sufficient rate at 1725°F to cause significant strengthening of the material with a corresponding loss of ductility, even over a period between 3 to 15 hours at temperature. These mechanical property changes were recorded under both static and dynamic loading conditions.

6. Zirconium gave little indication of any differences in the material's response to static fracture and impulsive testing suggesting a minimal diffusion of oxygen at 1675°F over a 6 hour period.

7. This study verified the fact that hydrogen embrittlement in titanium occurs under the conditions of dynamic loading as opposed to static.

8. Hydrogenated titanium, containing insufficient amounts of beta phase in the microstructure to absorb the excess hydrogen after the alpha phase has reached its solid solubility limit, will form hydrides which are dispersed within the grain in preferred directions. A model of how the hydrides give rise to a reduced dynamic fracture toughness has been presented.

9. In those titanium microstructures containing retained β phase, evidence has been presented to suggest that the dynamic fracture toughness is reduced due to an embrittlement of this phase in that hydride formation is not in evidence. A fracture model has also been presented for this situation.

10. Increasing the amount of β phase shows some indication of increasing the total fracture energy. Whether the brittle transformation can be avoided entirely by the increased presence of this phase has not been ascertained. If the alloy is to be primarily alpha, the indications are it cannot.

11. Hydrogenated reactor grade zirconium also undergoes the ductile-to-brittle transition upon hydrogenation. It has no retained β phase since the eutectoid former impurities are not sluggish as is the case with titanium. The transition fracture appearance was one typically associated with a ductile failure, due to the ductile tearing on a fine scale.

APPENDICES

APPENDIX A

CRACK TIP STRESS FIELD[1]

A.1 Equilibrium Equations

From the theory of elasticity, the equilibrium equations for plane extention are

$$\frac{\partial \sigma_x}{\partial x} + \frac{\partial \tau_{xy}}{\partial y} = 0 \tag{1a}$$

$$\frac{\partial \tau_{xy}}{\partial x} + \frac{\partial \sigma_y}{\partial y} = 0 \tag{1b}$$

$$\tau_{xy} = \tau_{yx} \, . \tag{1c}$$

A.2 Compatability Equation

The compatability equation is obtained from the strain-displacement relationship and Hooke's Law

$$\nabla^2 (\sigma_x+\sigma_y) = [\frac{\partial^2}{\partial x^2} + \frac{\partial^2}{\partial y^2}](\sigma_x+\sigma_y) = 0 \, . \tag{2}$$

A.3 Defining an Airy Stress Function

The equilibrium equations are satisfied by defining an Airy stress function, ϕ, in terms of its relationship to the stresses

$$\sigma_x = \frac{\partial^2 \phi}{\partial y^2}$$

$$\sigma_y = \frac{\partial^2 \phi}{\partial x^2} \qquad (3\ a,b,c)$$

$$\tau_{xy} = \frac{-\partial^2 \phi}{\partial x \partial y} \ .$$

Substitute Equations (3) into Equation (2)

$$\nabla^2 \ (\sigma_x + \sigma_y) = \nabla^2 \ (\frac{\partial^2 \phi}{\partial y^2} + \frac{\partial^2 \phi}{\partial x^2}) = 0$$

where $$\nabla^2 = \frac{\partial^2}{\partial x^2} + \frac{\partial^2}{\partial y^2}$$

so $$\nabla^2 \ (\sigma_x + \sigma_y) = \nabla^2 \ (\nabla^2 \phi) = \nabla^4 \phi = 0 \ . \qquad (4)$$

The stress function and the boundary conditions of the problem must be such to satisfy the biharmonic equation (Equation 4). The stress function is chosen,

$$\phi = \psi_1 + x\psi_2 + y\,\psi_3 + \text{---} \qquad (5)$$

which will satisfy the biharmonic equation if the individual ψ_i are themselves harmonic, that is,

$$\nabla^2 \ \psi_i = 0 \ . \qquad (6)$$

A.4 Harmonic and Biharmonic Functions

A function is harmonic if it satisfies the Laplace equation (Equation 6) at all points within the body.

When there are no body forces present, it can be shown that each displacement u, v, w satisfies the equation

$$\nabla^4 \phi = 0 \qquad (7)$$

at all points within the body. All the components of stress and strain also satisfy this equation.[2] The importance of the form and solution of this equation is obvious. In rectangular Cartesian coorindates

$$\nabla^4 = \frac{\partial^4}{\partial x^4} + \frac{\partial^4}{\partial y^4} + \frac{\partial^4}{\partial z^4} + 2\,\frac{\partial^4}{\partial x^2 \partial y^2} + 2\,\frac{\partial^4}{\partial y^2 \partial z^2} + 2\,\frac{\partial^4}{\partial z^2 \partial x^2} .$$

Equation 4 is called the biharmonic equation, and its solution called a biharmonic function. The Airy stress function $\Phi(x,y)$ generates the stresses which will satisfy the equations of equilibrium. It can generate only those stress fields which satisfy the compatability conditions and therefore Φ is not entirely arbitrary.

A.5.1 Analyticity

"A function f(Z) is said to be analytic at a point $Z = Z_o$ if it is defined, and has a derivative, at every point in some neighborhood of Z. It is said to be analytic in a domain D if it is analytic at every point in D"[3]

A.5.2 Cauchy-Riemann Conditions

"If the derivative f'(Z) of a function f = u + iv exists at a point Z, then the partial derivatives of the

first order, with respect to x and y, of each of the components u and v must exist at that point and satisfy the Cauchy-Riemann conditions,

$$\frac{\partial u}{\partial x} = \frac{\partial v}{\partial y} \quad \text{and} \quad \frac{\partial u}{\partial y} = - \frac{\partial v}{\partial x} \quad . \tag{8 a,b}$$

Also, f'(Z) is given in terms of those partial derivatives by

$$f'(Z) = \frac{\partial u}{\partial x} + i \frac{\partial v}{\partial x} = \frac{\partial v}{\partial y} - i \frac{\partial u}{\partial y} \tag{9}$$

then one can define the complex variable

$$z = x + iy, \text{ where } i = \sqrt{-1} \quad .$$

Moreover, the real and imaginary part of any analytic function of a complex variable is harmonic. Also the derivative of an analytic function

$f(Z) = u(x,y) + i\, v(x,y)$ is itself analytic. From this important fact it follows that u(x,y) and v(x,y) will have continuous partial derivatives of all orders. The mixed second derivatives of these functions will be equal:

$$\frac{\partial^2 u}{\partial x \partial y} = \frac{\partial^2 u}{\partial y \partial x} \quad , \quad \frac{\partial^2 v}{\partial x \partial y} = \frac{\partial^2 v}{\partial y \partial x} \tag{10}$$

Differentiate the Cauchy-Riemann equations (Equations 8 a,b)

$$\frac{\partial}{\partial x}\left[\frac{\partial u}{\partial x}\right] = \frac{\partial}{\partial x}\left[\frac{\partial v}{\partial y}\right]$$

$$\frac{\partial^2 u}{\partial x^2} = \frac{\partial^2 v}{\partial x \partial y} \tag{11a}$$

$$\frac{\partial}{\partial y}\left[\frac{\partial u}{\partial x}\right] = \frac{\partial}{\partial y}\left[\frac{\partial v}{\partial y}\right]$$

$$\frac{\partial^2 u}{\partial y \partial x} = \frac{\partial^2 v}{\partial y^2} \tag{11b}$$

$$\frac{\partial}{\partial x}\left[\frac{\partial u}{\partial y}\right] = \frac{\partial}{\partial x}\left[-\frac{\partial v}{\partial x}\right]$$

$$\frac{\partial^2 u}{\partial x \partial y} = -\frac{\partial^2 v}{\partial x^2} \tag{11c}$$

$$\frac{\partial}{\partial y}\left[\frac{\partial u}{\partial y}\right] = \frac{\partial}{\partial y}\left[-\frac{\partial v}{\partial x}\right]$$

$$\frac{\partial^2 u}{\partial y^2} = -\frac{\partial^2 v}{\partial y \partial x} \quad . \tag{11d}$$

This set of equations will be used later in determining the stresses, and can be used to show that the real and imaginary part of a complex function

$$f(Z) = u(x,y) + i\, v(x,y)$$

that is analytic in a domain D are solutions of Laplace's equation in D, and have continuous partial derivatives in D.[5] That is,

$$\nabla^2 u = \frac{\partial^2 u}{\partial x^2} + \frac{\partial^2 u}{\partial y^2} = \frac{\partial^2 v}{\partial x \partial y} - \frac{\partial^2 v}{\partial x \partial y} = 0, \tag{12a}$$

$$\nabla^2 v = \frac{\partial^2 v}{\partial x^2} + \frac{\partial^2 v}{\partial y^2} = - \frac{\partial^2 u}{\partial x \partial y} + \frac{\partial^2 u}{\partial x \partial y} = 0. \qquad (12b)$$

A.5.3 Derivative Definitions

Once the complex variable has been defined (i.e. $Z = x + iy$), then the derivatives of functions of that complex variable may be defined. Consider the function, $\overline{\overline{Z}}\ (z)$, the derivatives will be

$$\overline{Z} = \frac{d}{dz}\ (\overline{\overline{Z}}), \qquad Z = \frac{d}{dz}\ (\overline{Z}), \qquad Z' = \frac{d}{dz}\ (Z) \qquad (13a,b,c)$$

From the foregoing discussion it is understood that these functions all have harmonic and real parts if they are analytic (that they are continuous and well behaved and thus will not blow up due to a singularity). For example: $\overline{Z} = \text{Re}\ \overline{Z} + i\ \text{Im}\ \overline{Z}$.

A.5.4 Cauchy-Riemann Conditions Applied to Functions of the Complex Variable

The function, $\overline{\overline{Z}}$, and its derivatives may be expressed in terms of the Cauchy-Riemann conditions, by letting u and v be the real and imaginary parts respectively.

Since $\frac{\partial u}{\partial x} = \frac{\partial v}{\partial y}$ and $\frac{\partial u}{\partial y} = - \frac{\partial v}{\partial x}$,

then $\frac{\partial \text{Re}\overline{\overline{Z}}}{\partial x} = \frac{\partial \text{Im}\overline{\overline{Z}}}{\partial y} = \text{Re}\overline{Z}$ and $\qquad (14a)$

$$\frac{\partial \mathrm{Im}\overline{\overline{Z}}}{\partial x} = -\frac{\partial \mathrm{Re}\overline{\overline{Z}}}{\partial y} = \mathrm{Im}\ \overline{Z} \tag{14b}$$

Similarly,

$$\frac{\partial \mathrm{Re}\overline{Z}}{\partial x} = \frac{\partial \mathrm{Im}\overline{Z}}{\partial y} = \mathrm{Re}\ Z, \tag{15a}$$

$$\frac{\partial \mathrm{Im}\overline{Z}}{\partial x} = -\frac{\partial \mathrm{Re}\overline{Z}}{\partial y} = \mathrm{Im}\ Z, \tag{15b}$$

$$\frac{\partial \mathrm{Re}Z}{\partial x} = \frac{\partial \mathrm{Im}Z}{\partial y} = \mathrm{Re}\ Z', \text{ and} \tag{16a}$$

$$\frac{\partial \mathrm{Im}Z}{x} = -\frac{\partial \mathrm{Re}Z}{y} = \mathrm{Im}\ Z'. \tag{16b}$$

These relationships will be useful in differentiating the functions $\overline{\overline{Z}}$ through Z.

A.5.5 Westergaard Stress Function

Westergaard[6] introduced the stress function

$$\Phi_1 = \mathrm{Re}\ \overline{\overline{Z}}_1 + y\ \mathrm{Im}\ \overline{Z}_1 \tag{17}$$

where both parts are harmonic. This is just Equation (5) where

$$\psi_1 = \mathrm{Re}\ \overline{\overline{Z}}_1,\ \psi_2 = 0, \text{ and } \psi_3 = \mathrm{Im}\ \overline{Z}_1.$$

Since ψ_1, ψ_2, and ψ_3 are harmonic, then Φ, is biharmonic and satisfies both compatability and equilibrium.

A.6.0 Determination of the Stresses in Terms of Complex Variable Functions

A.6.1 Determination of σ_x

Substitute the Westergaard stress function (Equation 17) into Equation 3a,

$$\sigma_x = \frac{\partial^2 \Phi}{\partial y^2} = \frac{\partial^2}{\partial y^2} [\text{Re } \overline{Z} + y \text{ Im } Z] \ .$$

The partial differentiation is carried out by using the appropriate Cauchy-Riemann Equations (14 through 16) for substitution.

$$\text{Therefore } \sigma_x = \frac{\partial}{\partial y} [-\text{Im } \overline{Z} + y \text{ Re } Z + \text{Im } \overline{Z}]$$

$$= [-\text{Re } Z + y \ (-\text{Im } Z') + \text{Re } Z + \text{Re } Z]$$

$$= \text{Re } Z - y \text{ Im } Z' \qquad (18)$$

A.6.2 Determination of σ_y

Substitute the Westergaard stress function (Equation 17) into Equation 3b, and proceed as in section A.6.1.

$$\sigma_y = \frac{\partial^2 \Phi}{\partial x^2} = \frac{\partial^2}{\partial x^2} [\text{Re } \overline{Z} + y \text{ Im } \overline{Z}]$$

$$= \frac{\partial}{\partial x} [\text{Re } \overline{Z} + y \text{ Im } Z]$$

$$= \text{Re } Z + y \text{ Im } Z'. \qquad (19)$$

A.6.3 Determination to σ_{xy}

Substitute the Westergaard stress funciton (Equation 17) into Equation 3c and proceed as in sections 1.6.1 and 1.6.2.

$$\tau_{xy} = \frac{-\partial^2}{\partial x \partial y} = \frac{-\partial^2}{\partial x \partial y} [\text{Re } \bar{\bar{Z}} + y \text{ Im } \bar{Z}]$$

$$= \frac{\partial}{\partial y} [\text{Re } Z + y \text{ Im } Z]$$

$$= [\text{Im } Z - y \text{ Re } Z' - \text{Im } Z]$$

$$= -y \text{ Re } Z' \, . \qquad (20)$$

A.7 Analytic Function Representation of a Crack

Consider Figure A.1, which is a straight line crack inside the region, R.

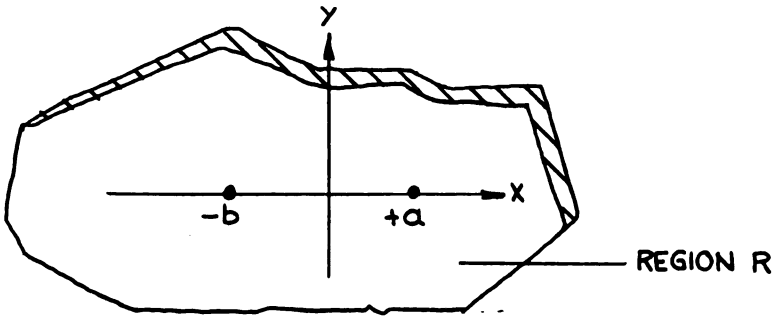


Figure A.1--Region R containing a straight line crack.

The analytic function in the region R except for the branch cut along the portion of the x-axis that represents the crack (i.e. from -b to +a) has the general form

$$Z = \frac{g(z)}{[(z+b)(z-a)]^{1/n}} \cdot \qquad (21)$$

In this case n = 2, to conincide with the physical problem. The crack is assumed a straight line, and n = 2 will yield a straight line branch along the x-axis.

For a case like a cracked single-edge-notch specimen, the crack only runs from zero to +a. Equation (21) then takes the form

$$Z = \frac{g(z)}{(z-a)^{1/2}} \cdot \qquad (22)$$

Let $\xi = (z-a)$, so that $g(z) = f(\xi)$. Substitute these values into Equation (22)

$$Z = \frac{f(\xi)}{\xi^{1/2}} \cdot \qquad (23)$$

The function $f(\xi)$ is well behaved and is subject to all the conditions placed upon $g(z)$. It will solve crack problems for cracks along x-axis from -b to +a at y = 0, became $\sigma_y = \tau_{xy} = 0$ if Im $g(x) = 0$, for that interval. Remembering that

$$z = x + i\,y \quad \text{and at } y = 0,$$

the function $f(\xi)$ will be well behaved near the crack tip where x = a. At the tip $|\xi|$ approaches zero, so that the function, $f(\xi)$ in Equation (23) may be replaced by a real constant

$$f(\xi) = \frac{K}{(2\pi)^{1/2}} = k \text{ (constant)} . \tag{24}$$

Substitute Equation (24) back into Equation (23)

$$Z\Big|_{|\xi|\to 0} = \frac{K}{(2\pi\xi)^{1/2}} = \frac{k}{\xi^{1/2}} . \tag{25}$$

Paris and Sih have shown that other stress functions for the opening mode have the same form as Equation (25).

A.8 Polar Coordinate Equivalents of the Real and Imaginary Part of the Analytic Function

$$\xi = r\, e^{i\theta} \quad \text{and} \tag{26}$$

$$e^{i\alpha} = \cos\alpha + i \sin\alpha \tag{27a}$$

A.8.1 Polar Equivalents of $\overline{Z}$

Remembering that $Z = \frac{f(\xi)}{\xi^{1/2}}$

then

$$\overline{Z} = \int Z\, dz = \int \frac{f(\xi)}{\xi^{1/2}}\, dz .$$

But $f(\xi)$ can be replaced by a real constant, k, (Equation 24) so

$$\overline{Z} = k \int \xi^{-1/2}\, dz = 2\, k\, \xi^{1/2} = 2\, \left(\frac{K}{(2\pi)^{1/2}}\right) \xi^{1/2}. \quad (27b)$$

Substitute Equation (26) into (27b)

$$\overline{Z} = 2\, \left(\frac{K}{(2\pi)^{1/2}}\right)\, r^{1/2}\, e^{i\theta/2}\ . \quad (27c)$$

Substitute the identity for $e^{i\alpha}$, where $\alpha = \frac{\theta}{2}$, into Equation 27c

$$\overline{Z} = 2\, \frac{K\, r^{1/2}}{(2\pi)^{1/2}} \left(\cos \frac{\theta}{2} + i \sin \frac{\theta}{2}\right)$$

so

$$\text{Re } \overline{Z} = 2K\, \left(\frac{r}{2\pi}\right) \cos \frac{\theta}{2} \quad (27d)$$

$$\text{Im } \overline{Z} = 2K\, \left(\frac{r}{2\pi}\right) \sin \frac{\theta}{2}\ . \quad (27e)$$

A.8.2 Polar Equivalents of Z

Substitute the identities given by Equations 26 and 27 into Equation 25

$$Z\Big|_{|\xi|\to 0} = \frac{K}{(2\pi\xi)^{1/2}} = \frac{K}{(2\pi)^{1/2}(re^{i\theta})^{1/2}}$$

$$= \frac{K}{(2\pi r)^{1/2}} e^{-i\theta/2}$$

where $\alpha = \frac{\theta}{2}$.

Therefore

$$Z\Big|_{|\xi|\to 0} = \frac{K}{(2\pi r)^{1/2}} \left(\cos \frac{\theta}{2} - i \sin \frac{\theta}{2}\right)$$

so $$\text{Re } Z = \frac{K}{(2\pi r)^{1/2}} \cos \frac{\theta}{2} \qquad (28)$$

$$\text{Im } Z = - \frac{K}{(2\pi r)^{1/2}} \sin \frac{\theta}{2} \cdot \qquad (29)$$

A.8.3 Polar Equivalents of Z'

If $\xi = z - a$, then

$\frac{d}{d\xi} = \frac{d}{dz}$, where "a" is a constant. Differentiate Equation (23)

$$\frac{dZ}{d\xi} = \frac{d}{d\xi} \left[\frac{f(\xi)}{\xi^{1/2}}\right]$$

$$= [f'(\xi)]\ \xi^{1/2} - \frac{1}{2}\ \xi^{-1/2}\ [f(\xi)] \ .$$

The first term on the RHS goes to zero,

so
$$Z' = -\frac{f(\xi)}{2\xi^{3/2}} \cdot \tag{30}$$

Substitute Equation (24) into the numerator, and Equation (26) into the denominator of Equation (30)

$$Z' = -\frac{K}{2(2\pi)^{1/2}(re^{i\theta})^{3/2}} = -\frac{K}{2r(2\pi r)^{1/2}} e^{-i3\theta/2}.$$

Using the identity for $e^{i\alpha}$, where $\alpha = -3\theta/2$,

$$Z' = -\frac{K}{2r(2\pi r)^{1/2}} \left[\cos\frac{3\theta}{2} - i \sin\frac{3\theta}{2}\right]$$

so
$$\text{Re } Z' = -\frac{K}{2r(2\pi r)^{1/2}} \cos\frac{3\theta}{2} \tag{31}$$

$$\text{Im } Z' = \frac{K}{2r(2\pi r)^{1/2}} \sin\frac{3\theta}{2} \cdot \tag{32}$$

A.9.0 Crack Tip Stress Field in Polar Coordinates

A.9.1 σ_x in Polar Coordinates

Substitute Equations (28) and (32) into Equation (18)

$$\sigma_x = \text{Re } Z - y \text{ Im } Z'$$

$$= \left[\frac{K}{(2\pi r)^{1/2}} \cos\frac{\theta}{2}\right] - \left[(r \sin\theta)\left(\frac{K}{2r(2\pi r)^{1/2}} \sin\frac{3\theta}{2}\right)\right]$$

$$= \frac{K}{(2\pi r)^{1/2}} \left[\cos \frac{\theta}{2} - \frac{\sin \theta}{2} \sin \frac{3\theta}{2}\right] .$$

The identity exists that,

$$\sin \theta = 2 \sin \frac{\theta}{2} \cos \frac{\theta}{2} \text{ , then}$$

$$\frac{\sin \theta}{2} = \sin \frac{\theta}{2} \cos \frac{\theta}{2} \quad . \tag{33}$$

Therefore

$$\sigma_x = \frac{K}{(2\pi r)^{1/2}} \left[\cos \frac{\theta}{2} - \left(\sin \frac{\theta}{2} \cos \frac{\theta}{2}\right) \sin \frac{3\theta}{2}\right]$$

and rearranging,

$$\sigma_x = \frac{K}{(2\pi r)^{1/2}} \cos \frac{\theta}{2} \left[1 - \sin \frac{\theta}{2} \sin \frac{3\theta}{2}\right] . \tag{34}$$

A.9.2 σ_y in Polar Coordinates

Substitute Equation (28) and (32) into Equation (19).

$$\sigma_y = \text{Re } Z + y \text{ Im } Z'$$

$$= \left[\frac{K}{(2\pi r)^{1/2}} \cos \frac{\theta}{2}\right]$$

$$+ \left[(r \sin \theta) \left(\frac{K}{2r(2\pi r)^{1/2}} \sin \frac{3\theta}{2}\right)\right]$$

$$= \frac{K}{(2\pi r)^{1/2}} \left[\cos \frac{\theta}{2} + \frac{\sin \theta}{2} \sin \frac{3\theta}{2}\right] .$$

Substitute the identity for $\frac{\sin \theta}{2}$ (Equation 33)

$$\sigma_y = \frac{K}{(2\pi r)^{1/2}} \left]\cos \frac{\theta}{2} + (\sin \frac{\theta}{2} \cos \frac{\theta}{2}) \sin \frac{3\theta}{2}\right]$$

and rearrange

$$\sigma_y = \frac{K}{(2\pi r)^{1/2}} \cos \frac{\theta}{2} \left[1 + \sin \frac{\theta}{2} \sin \frac{3\theta}{2}\right] . \qquad (35)$$

A.9.3 τ_{xy} in Polar Coordinates

Substitute Equation (31) into Equation (20)

$$\tau_{xy} = - y \text{ Re } Z'$$

$$= - (r \sin \theta) \left[\frac{-K}{2r(2\pi r)^{1/2}} \cos \frac{3\theta}{2}\right]$$

$$= \frac{K}{(2\pi r)^{1/2}} \frac{\sin \theta}{2} \cos \frac{3\theta}{2} .$$

Substitute the identity for $\frac{\sin \theta}{2}$ (Equation 33)

$$\tau_{xy} = \frac{K}{(2\pi r)^{1/2}} \sin \frac{\theta}{2} \cos \frac{\theta}{2} \cos \frac{3\theta}{2} . \qquad (36)$$

APPENDIX B

CRACK DISPLACEMENT FIELD[1]

B.1 The Strains in Terms of Stresses and Elastic Constants

These relationships will not be derived here but only summarized since any elementary mechanics text[2,3] will present a full development,

$$\frac{\partial u}{\partial x} = \varepsilon_{xx} = \frac{1}{E}\left[\sigma_{xx} - \nu(\sigma_{yy} + \sigma_{zz})\right] \tag{1a}$$

$$\frac{\partial v}{\partial y} = \varepsilon_{yy} = \frac{1}{E}\left[\sigma_{yy} - \nu(\sigma_{xx} + \sigma_{zz})\right] \tag{1b}$$

$$\frac{\partial w}{\partial z} = \varepsilon_{zz} = \frac{1}{E}\left[\sigma_{zz} - \nu(\sigma_{yy} + \sigma_{xx})\right] , \tag{1c}$$

where E and ν are Young's modulus of elasticity and Poisson's ratio respectively. When plane strain conditions exist, it is understood that $\varepsilon_{zz} = 0$, however, σ_{zz} is not zero.

Since $\frac{\partial w}{\partial z} = \varepsilon_{zz} = 0 = \frac{1}{E}\left[\sigma_{zz} - \nu(\sigma_{yy} + \sigma_{xx})\right]$,

then $-\frac{\sigma_{zz}}{E} = -\frac{\nu}{E}(\sigma_{yy} + \sigma_{xx})$.

Multiply both sides by E

$$\sigma_{zz} = \nu\ (\sigma_{yy} + \sigma_{xx}) \cdot \qquad (2)$$

B.2 Displacements in Terms of the Real and Imaginary Parts of the Analytic Function

B.2.1 The Displacement in the x-Direction, u

Substitute Equation (2) into Equation (1a)

$$\frac{\partial u}{\partial x} = \frac{1}{E}\ \{\sigma_{xx} - \nu[\sigma_{yy} + \nu\ (\sigma_{xx} + \sigma_{yy})]\}$$

and upon rearranging

$$\frac{\partial u}{\partial x} = \frac{1}{E}\ \{\sigma_{xx} - \nu^2\ [\frac{\sigma_{yy}}{\nu} + \sigma_{xx} + \sigma_{yy}]\}\ .$$

Substitute the complex variable equivalents for σ_{xx} and σ_{yy} (Equations 18 and 19, Appendix A)

$$\frac{\partial u}{\partial x} = \frac{1}{E}\{(\text{Re } Z - y \text{ Im } Z') - \nu^2\ [\frac{(\text{Re } Z + y \text{ Im } Z')}{\nu}$$

$$+ (\text{Re } Z - y \text{ Im } Z') + (\text{Re } Z + y \text{ Im } Z')]\}$$

which reduces to

$$\frac{\partial u}{\partial x} = \frac{1}{E}\ \{(\text{Re } Z - y \text{ Im } Z') - \nu(\text{Re } Z + y \text{ Im } Z')$$

$$- 2\ \nu^2 \text{ Re } Z\}\ .$$

Collect similar terms

$$\frac{\partial u}{\partial x} = \frac{1}{E} \{\text{Re } Z \ (1-\nu-2\nu^2) - y \text{ Im } Z' \ (1+\nu)\}$$

and since $(1-\nu-2\nu^2) = (1+\nu) \ (1-2\nu)$

then

$$\frac{\partial u}{\partial x} = \frac{(1+\nu)}{E} \ \{(1-2\nu) \text{ Re } Z - y \text{ Im } Z'\}.$$

Finally

$$u = \int \frac{\partial u}{\partial x} dx = \frac{1+\nu}{E} \int \{(1-2\nu) \text{ Re } Z - y \text{ Im } Z'\} dx$$

and the integration of Re Z and Im Z' can be obtained directly from the Cauchy-Riemann conditions (Equations 15a and 16b, Appendix A).

Therefore,

$$u = \frac{1+\nu}{E} \{(1-2\nu) \text{ Re } \overline{Z} - y \text{ Im } Z\}. \qquad (3)$$

B.2.2 Displacement in the y-Direction, v

Substitute the complex variable equivalents for σ_{xx} and σ_{yy} (Equations 18 and 19, Appendix A)

$$\frac{\partial v}{\partial y} = \frac{1}{E} \{(\text{Re } Z + y \text{ Im } Z') - \nu^2 \left[\frac{(\text{Re } Z - y \text{ Im } Z')}{\nu}\right.$$

$$\left. + (\text{Re } Z - y \text{ Im } Z') + (\text{Re } Z + y \text{ Im } Z')\right]\}$$

which reduces to

$$\frac{\partial v}{\partial y} = \frac{1}{E}\{(\text{Re } Z + y \text{ Im } Z') - \nu(\text{Re } Z - y \text{ Im } Z') - 2\nu^2 \text{ Re } Z\} .$$

Expand and collect similar terms

$$\frac{\partial v}{\partial y} = \frac{1}{E}\{\text{Re } Z\ (1-\nu-2\nu^2) + y \text{ Im } Z'\ (1+\nu)\}$$

and substitute $(1+\nu)(1-2\nu)$ for $(1-\nu-2\nu^2)$

$$\frac{\partial v}{\partial y} = \frac{(1+\nu)}{E}\{(1-2\nu) \text{ Re } Z + y \text{ Im } Z'\} .$$

Finally,

$$v = \int \frac{\partial v}{\partial y}\, dy = \frac{(1+\nu)}{E}\int\{(1-2\nu) \text{ Re } Z + y \text{ Im } Z'\}\, dy \quad (4)$$

where Re Z can be integrated directly from the Cauchy-Riemann condition (Equation 15a, Appendix A). The term y Im Z' can be integrated by parts. The parts formula will be given in terms of r and s instead of the customary u and v to avoid confusion with the same symbols used for displacement in this section.

Let: $r = y$, $ds = \text{Im } Z'\, dy$

then $dr = dy$, $s = -\text{Re } Z$ (by the Cauchy-Riemann condition, Equation 16b, Appendix A). Substitute into the integration by parts formula

$$\int r\, ds = rs - \int s\, dr$$

$$\int y \, \mathrm{Im}\, Z' \, dy = - y \, \mathrm{Re}\, \bar{Z} + \int \mathrm{Re}\, Z \, dy$$

$$= - y \, \mathrm{Re}\, Z + \mathrm{Im}\, \bar{Z} \, . \qquad (5)$$

Substitute Equation (5) back into (4)

$$v = \frac{(1+\nu)}{E} \{(1-2\nu) \, \mathrm{Im}\, \bar{Z} + (- y \, \mathrm{Re}\, Z + \mathrm{Im}\, \bar{Z})\}$$

and rearrange

$$v = \frac{(1+\nu)}{E} \{2(1-\nu) \, \mathrm{Im}\, \bar{Z} - y \, \mathrm{Re}\, Z\}. \qquad (6)$$

B.3 Displacement Equations in Terms of K and the Elastic Constants

B.3.1 The Displacement in the x-Direction, u

There exists the elastic constants identity

$$E = 2 \mu (1+\nu) \qquad (7)$$

where μ is the shear modulus. Substitute Equations (27d and 29, Appendix A) and (7) for Re $\bar{Z}$, Im Z, and E respectively in Equation (3)

$$u = \frac{1+\nu}{2\mu(1+\nu)} \{(1-2\nu) \, 2K\left(\frac{r}{2\pi}\right)^{1/2} \cos\frac{\theta}{2}$$

$$- [(r \sin\theta) \{\left(\frac{-K}{(2\pi r)^{1/2}}\right) \sin\frac{\theta}{2}\}]\} \, .$$

Using the identity,

$$\sin\theta = 2 \sin\frac{\theta}{2} \cos\frac{\theta}{2} ,$$

$$u = \left(\frac{K}{2\mu}\right) \cos\frac{\theta}{2} \{(1-2\nu)\ 2\ \left(\frac{r}{2\pi}\right)^{1/2}$$

$$+ 2r\ (2\pi r)^{-1/2} \sin^2\frac{\theta}{2}\}$$

rearranging

$$u = \left(\frac{K}{\mu}\right)\ \left(\frac{r}{2\pi}\right)^{1/2} \cos\frac{\theta}{2}\ [1-2\nu + \sin^2\frac{\theta}{2}] \ . \qquad (8)$$

B.3.2 The Displacement in the y-Direction, v

Substitute Equations (27e and 28, Appendix A) and (7) for Im $\overline{Z}$, Re Z, and E respectively in Equation (6),

$$v = \frac{(1+\nu)}{2\mu(1+\nu)} \{2(1-\nu)\ 2K\ \left(\frac{r}{2\pi}\right)^{1/2} \sin\frac{\theta}{2}$$

$$-[(r \sin\theta)\ \{\left(\frac{K}{(2\pi r)^{1/2}}\right) \sin\frac{\theta}{2}\ \}]\}.$$

Using the identity,

$$\sin\theta = 2 \sin\frac{\theta}{2}\ \cos\frac{\theta}{2} ,$$

$$v = \left(\frac{K}{2\mu}\right)\ \sin\frac{\theta}{2}\ \{2(1-\nu)\ 2\left(\frac{r}{2\pi}\right)^{1/2}$$

$$- 2\ r\ (2\pi r)^{-1/2} \cos^2\frac{\theta}{2}\}$$

rearranging

$$v = \left(\frac{K}{\mu}\right) \left(\frac{r}{2\pi}\right)^{1/2} \sin\frac{\theta}{2} \left[2-2\nu-\cos^2\frac{\theta}{2}\right] . \qquad (9)$$

BIBLIOGRAPHY

BIBLIOGRAPHY

CHAPTER I

1. Higbie, K. B., and Stamper, J. W. "The Production of Primary Titanium Metal," D.M.I.C. Memorandum No. 234 ("Titanium for the Chemical Engineer,") April 1, 1968, 8-12.

2. Monagham, J. "Development and Application of Titanium," Engineering, CXCIV, (Nov. 23, 1962), 676-678.

3. Kline, M. H. "Occurrence of Zirconium," The Metallurgy of Zirconium. (Lustman, B., and Keize, F. (eds.) New York: McGraw-Hill Book Co., Inc., 1955, 50.

4. Kauffman, A. J., and Dilling, E. D. "Zirconium Production Methods," The Metallurgy of Zirconium. Lustman, B., and Keize, F. (eds.) New York: McGraw-Hill Book Co., Inc., 1955, 66.

5. Monagham, J. loc. cit.

6. Kay, V. B. "Titanium and Its Alloys-Part I: Equipment for the Chemical Industry, No. 2," The Engineer, CCXXV, (March 8, 1968), 404-405.

7. Higgins, G. T. "Metals for the Space Age," Advances in Materials Science. (Loftas, A. A., and Gwynne, P. (eds.)) London: U. of London Press, Ltd., 1966, 16-26.

8. Obryut, J. J. "Titanium Holds the Key to New Programs," Iron Age, CXCVII, No. 2, (Jan. 13, 1966), 49-54.

9. Rakowski, L. R. "Aluminium, Magnesium, Titanium Star in the Sport of Speed," Modern Metals, XXV, No. 6, (July, 1969) 27-28, 32, 35-36.

10. "Titanium Exchangers Defy Chlorine," Chemical Engineering, LXVII (July 24, 1961), 170-174.

11. Maykuth, D. J., and Wood, R. A. "Nonaerospace Uses of Titanium," D.M.I.C. Memorandum No. 242, March 1, 1969.

12. Hille, G. H. "Titanium for Surgical Implants," J. of Materials, I, No. 2, (June, 1966), 373-383.

13. Minkler, W. M. "The Future of Titanium in Everyday Uses," Metal Progress. LXXXVI, No. 4 (Oct., 1964), 170, 172, 174, 179, 182.

14. Preece, Robert L., and Gowen, K. W. J. "Application and Uses of Titanium and Its Alloys," Metallurgical Reviews, VI, (Institute of Metals) London: W. Clowes and Sons, Ltd., 1961.

15. Miller, Edward C. "The Metal Zirconium and Its Place in Nuclear Power Plants," Metal Progress, LXIII, (May, 1953), 67-74.

16. "Corrosion of Zirconium," Metal Progress, LXXVIII, No. 1, (July, 1960), 198.

17. "Zirconium Siphon for Pickle Liquors," Metal Progress, LXXXI, No. 1, (Jan., 1962), 8.

18. Hunter, M. A. "Metallic Titanium," Journal American Chemical Society, XXXII, 1910, 330-336.

19. Kauffman, A. J., and Dilling, E. D. loc. cit., 66-68.

20. Kroll, W. J. "Production of Ductile Titanium," Trans. Electrochem. Soc., LXXVII, 1940, 35-47.

21. Kroll, W. J. "Method for the Manufacture of Titanium and Alloys Thereof," U.S. Patent, No. 2, 205, 854, June 25, 1940.

22. Kroll, W. J., Schlecten, A. W., and Yerkers, L. A. "Ductile Zirconium from Zircon Sand," Trans. Electrochem. Soc., LXXXIX, 1946, 263-276.

23. Kroll, W. J., Schlechten, A. W., Carrmody, W. P., and Gilbert, H. L., "Recent Progress in the Metallurgy of Malleable Zirconium," Trans. Electrochem. Soc. XCII, 1947, 99-113.

24. Hume-Rothery, William, and Raynor, G. V. The Structure of Metals and Alloys. London: Institute of Metals, 1962.

25. Gupta, D., and Weining, S. "Interactions Between Interstitial and Substitutional Solutes in an HCP Lattice," Acta Metallurgica, X (April, 1962), 292-298.

26. Ehrlich, Paul. "Lösungen von Sauerstoff in Metallischem Titan," Zeitschrift für Anorganische und Allgemeine Chemie, CCXLVII, 1941, 53-64.

27. deBoer, J. H., and Fast, J. D. "Influence of Oxygen and Nitrogen on the α-β Transition of Zirconium," LV, 1936, 459-467. Recueil des Travaux Chimiques de Pays-Bas (Amsterdam).

28. Tyson, W. R. "Strengthening of HCP Zr, Ti, and Hf by Interstitials Solutes--a Review" Canadian Metallurgical Quart., VI, No. 4, 1968, 301-332.

29. Holmberg, Bo, and Dagerhamm, Tore. "X-ray Studies on Solid Solutions of Oxygen in Alpha Zirconium," Acta Chemica Scandinavica, XV, No. 4, 1961, 919-925.

30. Fast, J. D. "Extremely High Solubility of Nitrogen and Oxygen in Several Metals; Studies on Zirconium and Titanium," Metallwirtschaft, XVII, 1938, 641.

31. Rundle, R. E., Shull, C. G., and Woolan, E.O. "The Crystal Structure of Thorium and Zirconium Dehydrides by X-ray and Neutron Diffraction," Acta Crystallographia, V, 1952, 22-26.

32. Cotterill, P. "The Hydrogen Embrittlement of Metals," Progress in Materials Science, IX, No. 4, 1961, 205-301.

33. Jaffee, R. I. "Physical Metallurgy of Titanium Alloys," Progress in Metal Physics, VII, No. 2, New York: Pergamon Press, 1958, 65-163.

34. Hume-Rothery, William, and Raynor, G. V. loc. cit., 217-222.

35. Schwope, A. D. "A General Comparison of the Metallurgy of Zirconium With That of Better Known Commercial Metals," Zirconium and Zirconium Alloys. Cleveland: A.S.M., 1953, 292-304.

36. Hayes, E. T. "Zirconium Alloy Systems," The Metallurgy of Zirconium. (Lustman, B., and Kerze, F. (eds.) New York: McGraw-Hill Book Co., Inc., 1955, 432-489.

37. Hansen, Max. Constitution of Binary Alloys. New York: McGraw-Hill Book Co., Inc., 1958.

38. Palty, A. E., Margolin, H., and Nielson, J. P. "Titanium-Nitrogen and Titanium-Boron Systems," Trans. Am. Soc. Metals, XLVI, 1954, 312-328.

39. Domagala, R. F., McPherson, D. J., and Hansen, M. "System Zirconium-Nitrogen," Trans. A.I.M.E. (Metals Branch), CCVI, (Feb., 1956), 98-105.

40. Stone, L., and Margolin, H. "Titanium Rich Regions of the Ti-C-N, Ti-C-O, and Ti-N-O Phase Diagrams," Trans. A.I.M.E. (J. of Metals, V, Nov., 1953), 1498-1502.

41. Jenkins, A. E., and Worner, H. W. "The Structure and Some Properties of Titanium-Oxygen Alloys Containing 0-5 Atomic Percent Oxygen," J. of the Institute of Metals (London), LXXX, 1951-52, 157-166.

42. Bumps, E. S., Kessler, H. D., and Hansen, M. "The Titanium-Oxygen System," Trans. Am. Soc. Metals, XLV, 1953, 1008-1025.

43. Domagala, R. F., and McPherson, D. J. "System Zirconium-Oxygen," Trans. A.I.M.E. (J. of Metals, VI, Feb., 1954), 238-246.

44. Gebhardt, Erich, Sighizzi, H., and Durrschnabel, W. "Untersuchungen in System Zirkonium-Sauerstoff, Part 2" J. of Nuclear Materials, IV, No. 3, 1961, 255-268.

45. McQuillan, A. D. "An Experimental and Thermodynamic Investigation of the Hydrogen-Titanium System," Proc. Royal Soc. (London), CCIV, Sec A., 1950, 309-333.

46. Smith, D. P. Hydrogen in Metals. Chicago: U. of Chicago Press, 1948.

47. LaGrange, Lee D., Dykstra, L. J., Dixon, John M., and Merter, Ulrich. "A Study of the Zirconium Hydrogen and the Zirconium-Hydrogen-Uranium Systems Between 600 and 800°," J. of Physical Chemistry, LXIII, (Dec., 1954), 2035-2041.

48. Gulbransen, E. A., and Andrew, K. R. "Solubility and Decomposition Pressures of Hydrogen in α-Zr.," Trans. A.I.M.E., CCIII, 1955, 136-144.

49. Rylski, O. Z. Department of Mines and Technical Surveys, Mines Branch, Ottawa, Canada. PM. 203 [CAN].

50 Hall, M. N. A., Martin, S. L. M., and Rees, A. L. G. "The Solubility of Hydrogen in Zirconium and Zirconium-Oxygen Solid Solutions," Trans. Faraday Soc., XLI, 1945, 306-316.

51. Fitzwilliam, J., Kaufman, A., and Squire, C. "Magnetic and X-ray Studies on Ti and Zr with Dissolved Hydrogen," J. Chemical Physics, IX (Sept., 1941), 678-682.

52. Elliott, Rodney P. Constitution of Binary Alloys, First Supplement. New York: McGraw-Hill Book Co., Inc., 1965.

53. Smithells, C. J., and Ransley, C. R. "The Diffusion of Gases Through Metals," Proceedings of the Royal Society (London), Series A, Cl, (May, 1953), 172-197.

54. Rhines, F. N. "Atom Movements," Trans. A.S.M., XLIII, 1951, 174-191.

55. Gulbransen, Earl A., and Andrew, Kenneth F. "Kinetics of the Reactions of Zirconium with Oxygen, Nitrogen, and Hydrogen," Trans. A.I.M.E. (Metals Branch), CLXXXV (Aug., 1949), 515-525.

56. Gulbransen, Earl A., and Andrew, Kenneth F. "Kinetics of the Reactions of Titanium with Oxygen, Nitrogen, and Hydrogen," Trans. A.I.M.E. (Metals Branch), CLXXXV (Oct., 1949), 741-748.

57. McQuillan, A. D., and McQuillan, M. K. Metallurgy of the Rarer Metals-4: Titanium. London: Butterworths Scientific Publications, 1956, 402.

58. Jenkins, A. E. "The Oxidation of Titanium at High Temperatures in an Atmosphere of Pure Oxygen," J. of the Institute of Metals (London), LXXXII, 1953-54.

59. Gulbransen, E. A. "Gas,-Metal Reactions of Zirconium," The Metallurgy of Zirconium. (Lustman, B., and Keize, F. (eds.)) New York: McGraw-Hill Book Co., Inc., 1955, 557, 559.

60. deBoer, J. H., and Fast, J. D. "Electrolysis of Solid Solutions of Oxygen in Metallic Zirconium," Rucueil des Travaux Chimiques des Pays-Bas (Amsterdam), LIX, 1949, 161-167.

61. Richardson, L. S., and Grant, N. J. "Reaction of Oxygen and Nitrogen with Titanium From 700° to 1050°C," Trans. A.I.M.E., CC, 1954, 69-70.

62. McQuillan, A. D., and McQuillan, M. K. loc.cit., 417.

63. Hayes, E. T., and Roberson. "Some Effects of Heating Zirconium in Air, Oxygen, and Nitrogen," Trans. Electrochem. Soc., LXLVI, 1949, 142-151.

64. Phalnikar, C. A., and Baldwin, W. M. "Scaling of Zirconium in Air," Proc. A.S.T.M., LI, 1951, 1038-1059.

65. Gulbransen, E. A. loc. cit., 594-95.

CHAPTER II

1. Fing, C., Elbaum, C., and Winegard, W. C. "The Effect of Oxygen on the Tensile Properties of α-Titanium," Trans. T.M.S.-A.I.M.E., CCXV (Aug., 1959), 632-635.

2. Tyson, W. R. "Strengthening of the HCP: Zr, Ti, and Hf by Interstitial Solutes--A Review," Canadian Metallurgical Quart., VI, No. 4, 1968, 300-332.

3. Tyson, W. R. "Solution Hardening of Titanium by Oxygen," Scripta Metallurgica, III, 1969, 917-922.

4. Roos, B. "A Liquid Field Treatment of the Zirconium-Oxygen Crystal," Arkiv För Pysik (Stockholm), XXV,

5. Churchman, A. T. "The Slip Modes of Titanium and the Effect of Purity on Their Occurrence During Tensile Deformation of Single Crystals," Proc. Royal Soc. (London), Sec. A, CCXXVI, (Dec., 1954), 216-226.

6. Mills, D., and Craig, G. B. "The Plastic Deformation of Zr-O Alloy Single Crystals in the Range 77 to 950°K," Trans. T.M.S.-A.I.M.E., CCXLII (Sept., 1968), 1881-1890.

7. Tyson, W. R., and Craig, G. B. "Deformation of Zr-N Alloys," Canadian Metallurgical Quart., VII, No. 3, (July-Sept., 1968), 119-126.

8. Conrad, H. "The Rate Controlling Mechanism During Yielding and Flow of α-Titanium at Temperatures Below 0.4 Tm," Acta Metallurgica, XIV, 1966, 1631-1633.

9. Conrad, H. "Thermally Activated Deformation of α-Titanium Below 0.4 Tm," Canadian J. of Physics, XLV, 1967, 581-590.

10. Fleischer, Robert L. "Solution Hardening of Tetragonal Distortions: Application to Irradiation Hardening in F.C.C. Crystals."

11. Richman, M. H. "Calculation of Cleavage Characteristics of Hexagonal-Close-Packed Crystals," Trans. A.S.M., LIX, 1966, 374-383.

12. Rennhack, E. H., and Libach, J. F. "Influence of Tin and Aluminum on the Transition Behavior of Oxygenated Titanium," Trans. T.M.S.-A.I.M.E., CCXV (Dec., 1959), 942-946.

13. Cotterill, A. H. Dislocations and Plastic Flow in Metals. Oxford: Clarendon Press, 1953.

14. Cotterill, P. "The Hydrogen Embrittlement of Metals," Progress in Materials Science, IX, No. 4, 1961, 205-301.

15. Liu, T. S., and Steinberg, M. A. "The Mode of Hydride Precipitation in Alpha Titanium and Alpha Titanium Alloys," Trans. A.S.M., L, 1958, 455-477.

16. Schwartz, C. M., and Mallett, M. W. "Observations on the Behavior of Hydrogen in Zirconium," Trans. A.S.M. XLVI, 1954, 640-654.

17. Kunz, F. W., and Bibb, A. E. Habit Plane for Hydride Precipitation in Zirconium and Uranium-Zirconium, U.S.A.E.C. Report No. K.A.P.L.-2002, (Jan. 22, 1959), 10 pp.

18. Young, A. P., and Schwartz, C. M. "Observations on Microcrack Formation in Hydrogen-Embrittled Zirconium," Trans. A.I.M.E. (Met. Soc.), CCXII (June, 1958), 309-310.

19. Rosi, F. D., Dube, C. A., and Alexander, B. H. "Mechanism of Plastic Flow in Titanium--Determination of Slip and Twinning Elements," J. of Metals, III (Feb., 1953), 257-265.

20. Anderson, E. A., Jillson, D. C., and Dunbar, S. R. "Deformation Mechanism in Alpha Titanium," Trans. A.I.M.E., CXCVII (Sept., 1953), 1191-1197.

21. Lui, T. S., and Steinberg, M. A. "Twinning in Single Crystals of Titanium," J. of Metals, IV (Oct., 1952), 1043.

22. Rapperport E. J. "Deformation Processes in Zirconium," Acta Metallurgica, III, No. 2, 1955, 208.

23. Rapperport, E. J., and Hartley, C. S. "Deformation Modes of Zirconium at 77°, 575°, and 1075°K," Trans. T.M.S.-A.I.M.E., CCXVIII (Oct., 1960), 869-876.

24. Rapperport, E. J. "Room Temperature Deformation Processes in Zirconium," Acta Metallurgica, VII (April, 1959), 254-260.

25. Barley, J. E. "Electron Microscope Studies of Dislocations in Deformed Zirconium," J. of Nuclear Materials, VII, No. 3, 1962, 300-310.

26. Rogers, B. A. "The Properties of Eleven Less Common Metals," Metals for Supersonic Aircraft and Missiles. (Granbecker, T. W. (ed.)). Cleveland: A.S.M. Publication, 1958, 267.

27. Jenkins A. E., and Warner, H. W. "The Structure and Some Properties of Titanium-Oxygen Alloys Containing 0.5 Atomic Percent Oxygen," J. of the Institute of Metals (London), LXXX, 1951-52, 157-166.

28. Jaffee, Robert I., and Campbell, I. E. "The Effect of Oxygen, Nitrogen, and Hydrogen on Iodide Refined Titanium," J. of Metals, I (Sept., 1949), 646-654.

29. Finlay, Walter L., and Snyder, John A. "Effects of Three Interstitial Solutes on the Mechanical Properties of High-purity Alpha Titanium," J. of Metals, 11 (Feb., 1950), 277-286.

30 Jaffee, R. I., Ogden, H. R., and MayKuth, D. J. "Alloys of Titanium with Carbon, Oxygen and Nitrogen," Trans. A.I.M.E. (Metals Branch), CLXXXVIII (Oct., 1950), 1261-1266.

31. Abkowitz, Stanley, Burke, John J., and Hiltz, Ralph H. Titanium in Industry. New York: D. VanNostrand Co., Inc., 1955, 52.53

32. Fast, J. D. "Ductile Shaping of Zirconium and Titanium," Metallwiss, XVII, 1938, 459-462.

33. Wantman, F. S. "Production of Titanium Powder by the Bureau of Mines," Metal Progress, LV, 1949, 188-190.

34. Feng, C., Elbaum, C., and Winegard, W. C. "The Effect of Oxygen on the Tensile Properties of Titanium," Trans. T.M.S.-A.I.M.E., CCXV (Aug., 1959), 632-635.

35. Bumps, E. S. Kessler, H. D., and Hansen, M. "The Titanium--Oxygen System," Trans. A.S.M., XLV, 1008-1025.

36. Lenning, G. A., Craighead, C. M., and Jaffee, R. I. "Constitution and Mechanical Properties of Titanium-Hydrogen Alloys," J. of Metals, VI, No. 3, (March, 1954), 367-376.

37. Treco, R. M. "Some Properties of High Purity Zirconium and Dilute Alloys with Nitrogen," Trans. A.S.M., XLV, 1953, 872-890.

38. Chubb, W., and Others. "Mechanical Properties of Zirconium and Its Alloys," The Metallurgy of Zirconium. (Lustman, B., and Keize, F. [eds.]) 1st ed. New York: McGraw-Hill, 1955, 510.

39. Schwope, A. D., and Chubb, W. Mechanical Properties of Iodide Zirconium Alloys. Report BMI-780, Nov., 1952.

40. Westlake, D. G. "The Combined Effects of Oxygen and Hydrogen on the Mechanical Properties of Zirconium," Trans. T.M.S.-A.I.M.E., CCXXXIII (Feb., 1965), 368-372.

41. Hanink, H. H. "A Realistic Approach to the Use of Titanium," Product Engineering, XXII, No. 11 (Nov., 1951), 164-171.

42. Ditler, R. K., and Jaffe, L. D. "Toughness of Titanium," Metal Progress, LVII, 1950, 776-778.

43. Chubb, W., and Others, loc. cit., 520.

44. Brown, C. M., Folkman, R. L., and Schussler, M. Preliminary Report on: The Properties of Sodium-Reduced Titanium. Regional Reactive Metals Conference of the A.I.M.E., Buffalo, New York, March 19, 1956.

45. Mudge, M. L. "Effect of Hydrogen on the Embrittlement of Zirconium and Zirconium-Tin Alloys," Zirconium and Zirconium Alloys. Cleveland: A.S.M., 1953, 146.

46. Dayton, R. W., and Others. Hydrogen Embrittlement of Zirconium. Report BMI-767, Aug. 22, 1952.

47. Rylski, O. Z. Dept. of Mines and Techanical Surveys, Mines Branch, Ottawa, Canada, Report PM 203 (CAN).

48. Young, A. P., and Schwartz, C. M. A Fundamental Investigation of Hydrogen Embrittlement in Zirconium, U.S.A.E.C. Report No. B.M.I.-1100, (June 27, 1956), 24 pp.

49. Chubb, W. loc. cit., 523.

50. Jaffee, R. I., Holden, F. C., and Ogden, H. R. "Mechanical Properties of Alpha Titanium as Affected by Structure and Composition," J. of Metals, VI (Nov., 1954), 1282-1290.

51. Rennhack, E. H. "The Effect of Oxygen on the Impact Transition of Iodide Titanium," Trans. T.M.S.-A.I.M.E., CCXII (Aug., 1958), 487-489.

52. McQuillan, A. D., and McQuillan, M. K. The Metallurgy of the Rarer Metals--4: Titanium. London: Butterworths Scientific Publications, 1956, 356.

53. Jenkins, A. E. "A Further Study of the Oxidation of Titanium and Its Alloys at High Temperature," J. of the Institute of Metals (London), LXXXIV, 1955-56, 1-9.

54. Ogden, H. R., Maykuth, D. J., Finlay, W., L., and Jaffee, R. I. "Mechanical Properties of High Purity Ti-Al Alloys," J. of Metals, V, No. 2, (Feb., 1953), 267-272.

55. Chubb, W. loc. cit., 522-523.

56. Jaffee, R. I., Lenning, G. A., and Craighead, C. M. "Effect of Testing Variables on the Hydrogen Embrittlement of Titanium and a Ti-8 Pct. Mn Alloy," J. of Metals, VIII (Aug., 1956), 907-913.

57. Lenning, G. A., Spretnak, J. W., and Jaffee, R. I. "Effect of Hydrogen on Alpha Titanium Alloys," Trans. A.I.M.E. (Metals Branch), CCVI, (Oct., 1956), 1235-1240.

CHAPTER III

1. Wulpi, D. J. "How Components Fail I: Modes of Fracture," Metal Progress, LXXXVIII, No. 3, (Sept., 1965), 72-77.

2. McClintock, F. A., and Irwin, G. R. "Plasticity Aspects of Fracture Mechanics," Fracture Toughness Testing and Its Applications. (A.S.T.M.-S.T.P. No. 381). Philadelphia: A.S.T.M. 1965.

3. Freudenthal, A. M. The Inelastic Behavior of Engineering Materials and Structures. New York: John Wiley and Sons, Inc., 1950, 74.

4. Spretnak, J. W. A Summary of the Theory of Fracture in Metals. Battelle Memorial Institute D.M.I.C. Report No. 157 (Columbus: Aug. 7, 1961).

5. Parker E. R. Brittle Behavior of Engineering Structures. New York: John Wiley & Sons, Inc., 1957, 25-28.

6. Knott, J. F. "Brittle Fracture Mechanisms," Metal Industry (Sept. 10, 1964), 341-343.

7. Johnson, T. L. "Fracture of Polycrystals," Fundamental Phenomena in the Material Sciences-Vol. 4: Fracture of Metals, Polymers, and Glasses. (Borius, L. J., Duga, J. J., and Gilinaw, J. J. (eds.)) New York: Plenum Press, 1957, 1-2.

8. Tetelman, A. S., and McEvily, A. J. Fracture of Structural Materials. New York: John Wiley & Sons, Inc., 1967.

CHAPTER IV

1. Hoyt, S. L. "Notch-Bar Testing--Theory and Practice," Symposium on Impact Testing, (A.S.T.M.-S.T.P. No. 176). Philadelphia: A.S.T.M., 1955, 3-4.

2. Considere. "Contribution a ℓ' Etude de la Fragilite' dans les Fers et les Aciers," 1904.

3. Hoyt, S. L. Principles of Metallography. New York: McGraw-Hill Book Co., Inc., 1920, 226.

4. Orowan, E. Proc. Conf. Brittle Fracture in Mild Steel Plates, B.I.S.R.A., 1945, p. 70.

5. Ludwick, P, and Schew, R. Stahl und Eisen, XLIII, 1923, 999.

6. Hill, R. The Mathematical Theory of Plasticity. Oxford: University Press, 1950.

7. Tipper, C. F. "The Brittle Fracture of Metals at Atmospheric and Sub-Zero Temperatures," Metallurgical Reviews, 11, 1957, 195-259.

8. Parker, E. R. Brittle Behavior of Engineering Structures. New York: John Wiley and Sons, Inc., 1957, 36-37.

9. McAdam, D. J., Geil, G. W., and Mebs, R. W. Influence of Plastic Deformation, Combined Stresses, and Low Temperatures on the Breaking Stress of Ferritic Steels," Trans. A.I.M.E., CLXXII, 1947, 323-362.

10. Felbeck, D. K., and Orowan, E. "Experiments on Brittle Fracture of Steel Plates," Welding J. (Research Supplement), XXXIV, 1955, 570s-575s.

11. Clark D. S., and Datwyler, G. "Stress-strain Relations Under Tension Impact Loading," Proc. A.S.T.M., XXXVIII, 1938, 98-111.

12. Uccelli, Arturo. Leonardo da Vinci. New York: Reynal and Co., 1956.

13. Todhunter, I., and Pearson, K. History of the Theory and of the Strength of Materials. Cambridge Univ. Press, 1886, Sections 1503 and 936.

14. Frenkel, J. "Zur theorie der Elastizitätsgrenze und der Festigkeit kristallinischer Körper," Zietschrift Für Physik, XXXVII, 1926, 572-609.

15. Hirth, John P., and Lothe, Jens. Theory of Dislocations. New York: McGraw-Hill Book Co., Inc., 1968, 6-7.

16. Mackenzie, J. K. Doctoral Dissertation. Bristol: Univ. of Bristol, 1949.

17. Tinder, R. F., and Washburn, J. "The Initiation of Plastic Flow in Copper," Acta Metallurgica, XII, No. 2, (Feb., 1964), 129-137.

18. Tinder, R. F. "Initial Plastic Behavior of Zinc," J. of Metals, XVI, No. 1, (Jan., 1964), 94.

19. Griffith A. A. "The Phenomena of Rupture and Flow in Solids," Philosophical Trans. of the Royal Society (London), CCXXI, Series A, 1921, 163-198.

20. Inglis, C. E. "Stresses in a Plate Due to the Presence of Cracks and Sharp Corners," Trans. Inst. Naval Architects (London), LV, (March 14, 1913), 219-230.

21. Griffith, A. A. "The Theory of Rupture," International Congress of Applied Mechanics, Delft, 1924. (Biezeno, B., and Burgen, J. M. [eds.]), Delft, Netherlands: J. Waltman, Jr., 1924, 55-63.

22. Freudenthal, Alfred M. Introduction to the Mechanics of Solids. New York: John Wiley and Sons, Inc., 1966, 243.

23. Gilman, John J. "Metallurgical Classics (Commentary)," Trans. A.S.M., LXI, 1968, 861-906.

24. Zener, C., and Holloman, J. H. "Plastic Flow and Rupture of Metals," Trans. A.S.M., XXXIII, 1944, 163-212.

25. Orowan, E. Proc. of the Symposium on Fatigue and Fracture of Metals. New York: John Wiley and Sons, 1950, 139-167.

26. Fisher, J. C., and Holloman, J. H. "A Statistical Theory of Fracture," Trans. A.I.M.E., CLXXI, 1947, 546-561.

27. Orowan, E. "Energy Criteria of Fracture," Welding J. (Research Supplement), XXXIV, (March, 1955), 157s-160s.

CHAPTER V

1. Petch, N. J. "The Fracture of Metals," Progress in Metal Physics, V, 1954, 1-52.

2. Low, J. R. "The Fracture of Metals," Progress in Materials Science, XII, No. 1, 1963, 1-96.

3. Campbell, J. E. "Current Methods of Fracture-Toughness Testing of High-Strength Alloys with Emphasis on Plain Strain," Defense Materials Information Center Report No. 207. Columbus, Ohio: Battelle Memorial Institute, Aug. 31, 1964.

4. Polakowski, N. H., and Ripling, E. J. Strength and Structure of Engineering Materials. New Jersey: Prentice-Hall, Inc., 1966, 390.

5. Irwin, G. R. "Fracture Mechanics," Structural Mechanics--Proceedings of the 1st Symposium on Naval Structural Mechanics. (Goodier, J. Norman, and Hoff, J. Nicholas [eds.]), New York: Pergamon Press, Inc., 1960, 561.

6. Neuber, H. "Theory of Notch Stresses," A.E.C.-tr-4547 (1961), OTS, Dept. of Commerce, Wash., D.C. Translated from: Kerbspannungslehre, Springer-Verlag, 1937, revised in 1958.

7. Horger, Oscar J. (ed.). A.S.M.E. Handbook: Metals Engineering Design. 1st ed. New York: McGraw-Hill Book Co., Inc., 1953, 298-299.

8. Phelan, Richard M. Fundamentals of Mechanical Design. New York: McGraw-Hill Book Co., Inc., 1957, 82-83.

9. Peterson, R. E. Stress Concentration Design Factors. New York: John Wiley and Sons, Inc., 1953.

10. Lipson, Charles, and Juvinall, Robert C. Handbook of Stress and Strength. New York: Macmillan Co., 1963.

11. Polakowski, N. H. and Ripling, E. J. loc. cit., 243-244.

12. Davis, R. A., and Quist, W. E. "Fracture Toughness," Materials in Engineering Design (Nov., 1965), 91-97.

13. Kenny, P., and Campbell, J. D. "Fracture Toughness," Progress in Materials Science, XIII, No. 3, 1967.

14. Irwin, G. R. and Kies, J. A. "Critical Energy Rate Analysis of Fracture Strength," Welding J. (Research Supplement), (April, 1954), 193s-198s.

15. Universal Technology Corp. and Del Research Corp. Workshop in Fracture Mechanics. 5th ed., 1968.

16. Ripling, E. J., Mostovoy, S., and Patrick, R. L. "Measuring Fracture Toughness of Adhesvie Joints," Materials Research and Standards, IV (March, 1964), 129-134.

17. Irwin, G. R. "Analysis of Stresses and Strains Near the End of a Crack Traversing a Plate," J. of Applied Mechanics (Sept., 1957), 361-364.

18. Westergaard, H. M. "Bearing Pressures and Cracks," J. of Applied Mechanics (June, 1939), A49-A53.

19. Paris, Paul C., and Sih, George C. "Stress Analysis of Cracks," Fracture Toughness Testing and its Applications. (A.S.T.M.-S.T.P. No. 381) Philadelphia: A.S.T.M., 1965, 30-83.

20. Srawley, John E., and Brown, William E. "Fracture Toughness Testing Methods," Fracture Toughness Testing and Its Applications. (A.S.T.M.-S.T.P. No. 381) Philadelphia: A.S.T.M., 1965, 144.

21. Tiffany, C. F., and Masters, J. N. "Applied Fracture Mechanics," Fracture Toughness Testing and Its Applications. (A.S.T.M.-S.T.P. No. 381) Philadelphia: A.S.T.M., 1965, 253.

22. Srawley, J. E., and Beachem, C. D. "Crack Propagation Tests on High Strength Sheet Materials, Part IV: The Effect of Warm Prestraining," Naval Research Laboratory Report No. 5400, April 18, 1960.

23. Srawley, J. E., and Beachem, C. D. "Crack Propagation on High-Strength Sheet Steels Using Small Specimens," Naval Research Laboratory Report No. 5127, April 9, 1958.

24. Arnold, S. V. "Toughness of Sheet Steel: The Advantage of Laminating," Watertown Arsenal Laboratory Report, W.A.L.-T.R. 834.21/2, Oct., 1960.

25. A.S.T.M. Special Committee. "Fracture Toughness Testing of High-Strength Sheet Materials: A Report of a Special A.S.T.M. Committee," A.S.T.M. Bulletin No. 243, Jan., 1960, 29-40.

26. Bluhm, Joseph I. "A Model for the Effect of Thickness on Fracture Toughness," Proc. A.S.T.M., LXI, 1961, 1324-1331.

27. Repko, A. J., Jones, M. H., and Brown, W. F. "Influence of Sheet Thickness on Sharp-Edge-Notch Properties of a β-titanium Alloy at Room and Lower Temperatures," Symposium on Evaluation of Metallic Materials in Design for Low Temperature Service. (A.S.T.M.-S.T.P. No. 302) Philadelphia: A.S.T.M. and N.A.S.A., 1962, 213-229.

28. Corten, H. T. "Toughness of Materials," Ocean Engineering, I, 1969, 261-284.

29. Tetelman, A. S., and McEvily, A. J. Fracture of Structural Materials. New York: John Wiley and Sons, Inc., 1967.

30. Irwin, G. R. "Fracture Mode Transition for a Crack Traversing a Plate," J. of Basic Engineering, LXXXII (June, 1960), 417-425.

31. A.S.T.M. Special Committee. "Fracture Testing of High-Strength Sheet Materials: A Report of a Special A.S.T.M. Committee," A.S.T.M. Bulletin No. 244, Feb., 1960, 18-28.

32. Sternberg, E., and Sadowsky, M. A. "Three Dimensional Solution for the Stress Concentration Around a Circular Hole in a Plate of Arbitrary Thickness," J. of Applied Mechanics, XVI, 1949, 27-38.

33. Irwin, G. R. "Plastic Zone Near a Crack, and Fracture Toughness," Proceedings of the 7th Sagamore Ordnance Materials Conf. Syracuse: Syracuse Univ., 1960, IV 63-78.

CHAPTER VI

1. Boyle, R. W., Sullivan, A. M., and Krafft, J. M. Determination of Plain Strain Fracture Toughness with Sharply Notched Sheets," Welding Journal (Research Supplement), (Sept., 1962), 428s-432s.

2. Brown, William F., and Srawley, John E. Plain Strain Crack Toughness Testing of High Strength Metallic Materials, (A.S.T.M. Special Technical Publication No. 410), Baltimore: A.S.T.M., 1966, 6-7.

3. Gerberich, W. W., Key, P. L., and Parker, E. R. "A Semi-Qualitative Model of Pop-In Behavior," Engineering Fracture Mechanics, 11, No. 1, (July, 1970), 47-59.

4. Srawley, John E., and Brown, W. F. "Fracture Toughness Testing Methods," Fracture Toughness Testing and Its Applications (A.S.T.M. Special Technical Publication No. 381), Baltimore: A.S.T.M., 1965, 133-198.

5. Steigerwald, E. A., and Hanna, G. L. "Initiation of Slow Crack Propagation in High Strength Materials," Proccedings A.S.T.M., LXII, 1962, 885-905.

6. Anctile, A. A., Kula, E. B., and Di Cesare, E. "Electric Potential Technique for Determining Slow Crack Growth," Proceedings A.S.T.M., LXIII, 1963, 799-808.

7. Johnson, H. H. "Calibrating the Electrical Potential Method for Studying Slow Crack Growth," Materials Research and Standards, (Sept., 1965), 442-445.

8. Boyle, R. W. "A Method for Determining Crack Growth in Notched Sheet Specimens," Materials Research and Standards, II (Aug., 1962), 646-651.

9. Van Der Sluys, W. A. "Effects of Repeated Loading and Moisture on the Fracture Toughness of S.A.E. 4340 Steel," Transactions A.S.M.E. (J. of Basic Engineering), LXXXVII (June, 1965), 363-373.

10. Jones M. H. and Brown, W. F. "Acoustic Detection of Crack Initiation in Sharply Notched Specimens," Materials Research and Standards, IV (March, 1964), 120-127.

11. Brown, W. F., and Srawley, John E. op. cit., 60-63.

12. Srawley, John E., and Brown, William F. op. cit., 188-191.

13. Campbell, J. E. "Current Methods of Fracture Toughness Testing of High Strength Alloys with Emphasis on Plane Strain," D.M.I.C. Report No. 207. Columbus: Battelle Memorial Institute, August 31, 1964, 10-13.

14. Sullivan, A. M. "New Specimen Design for Plane-Strain Fracture Toughness Tests," Materials Research and Standards, IV (Jan., 1964), 20-24.

15. Gross, Benard, Srawley, J. E., and Brown, W. F. Stress Intensity Factors for a Single-Edge-Notch Tension Specimen by Boundary Collocation of a Stress Function, N.A.S.A. Technical Note, TN D-2395, 1964, 11 pp.

16. Srawley, J. E., and Gross, B. Stress Intensity Factors for Crackline-Loaded Edge-Crack Specimens, N.A.S.A. Technical Note, TN D-3820 (November 8, 1966), 19 pp.

17. Gross, B., and Srawley, J. E. Stress Intensity Factors by Boundary Collocation for Single-Edge-Notch Specimens Subject to Splitting Forces, N.A.S.A. Technical Note, TN D-3295 (Dec., 1965), 10 pp.

18. Gross, Benard, Roberts, E., and Srawley, J. E. Elastic Displacements for Various Edge-Cracked Plate Specimens, N.A.S.A. Technical Note, TN D-4232 (July, 1967), 12 pp.

19. Srawley, J. E., Jones, and Gross, B. Experimental Determination of the Dependency of Crack Extension Force on Crack Length for a Single-Edge-Notch Tension Specimen, N.A.S.A. Technical Note, TN D-2396.

CHAPTER VII

1. Yamada, Ryonosuke. "On the Relation Between Stress and Strain in the Impact Test," Journal of the Japan Society of Mechanical Engineers, XXXI, No. 136, (Aug., 1928), 420-446.

2. Watanable, Shumpei. "Study on Impact Test by Means of Piezo-Electricity and Cathode Ray Oscillograph," Scientific Papers of the Institute of Physical and Chemical Research, (Tokyo), XII, No. 213, 1929, 99-112.

3. Ono, Shuichi. "Micro-Time Structure of Impact Fracture Concerning Charpy Test," Proceedings of the 1st Japan Congress for Testing Materials. Kyoto: Japan Soc. for Testing Materials, 1958, 98-100.

4. Cotterell, B. "Fracture Toughness and the Charpy V-Notch Impact Test," British Welding Journal, IX, (Feb., 1962), 83-89.

5. Augland, B. "Fracture Toughness and the Charpy V-Notch Test," British Welding Journal, IX, No. 7 (July, 1962), 434-435.

6. Fearnebough, G. D. "Correspondence," British Welding Journal, IX, No. 11, 1962, 621.

7. Nisbet, J. S., Brennan, J. N., and Tarpley, H. I. "High Frequency Strain Gauge and Accelerometer Calibration," J. of the Acoustical Soc. of America, XXXII, No. 1, (Jan., 1960), 71-75.

8. Oi, Koshiro. "Transient Response of Bonded Strain Gauge," Experimental Mechanics, VI, No. 9, 1966, 463-469.

9. Tardif, H. P., and Marquis, H. "Force Measurements in the Charpy Impact Test," Canadian Metallurgical Quarterly, 11, No. 4, (oct.-Dec., 1963), 373-398.

10. Driscoll, David E. "Reproducibility of Charpy Impact Test," Symposium on Impact Testing, A.S.T.M. Special Technical Publication No. 176. Philadelphia: A.S.T.M., 1955.

11. Fahey, Norbert H. "Effects of Variables in Charpy Impact Testing," Materials Research and Standards, I, (Nov., 1961), 872-876.

12. Fahey, Norbert H. "The Charpy Impact Test: Its Accuracy and Factors Affecting Test Results," Impact Testing of Metals, A.S.T.M. Special Technical Publication No. 466. Philadelphia: A.S.T.M., 1970, 76-92.

13. Sieman, S. E. "Method of Notching Impact Test Specimens," A.S.T.M. Bulletin (March, 1946), 45-46.

14. Speer, J. R. "Improved Guides for Positioning of Impact Specimens," A.S.T.M. Bulletin (March, 1946), 46-47.

15. Bluhm, Joseph I. "The Influence of Pendulum Flexabilities on Impact Energy Measurements," Symposium on Impact Testing, A.S.T.M. Special Technical Publication No. 176. Philadelphia: A.S.T.M., 1956, 84-93.

16. Raring, R. "Load-Deflection Relationships in Slow Bend Tests of Charpy V-Notch Specimens," Proceedings A.S.T.M., LII, 1952, 1034-1053.

17. Lubahn, J. D. "Room Temperature Crack Propagation and Size Effect on Mild Steel," Welding Journal (Research Supplement), XXXIV (Oct., 1955), 518s-528s.

18. Hartbower. Carl E. "Transition Behavior in V-Notch Charpy Slow-Bend Tests," Symposium on Impact Testing, A.S.T.M. Special Technical Publication No. 176. Philadelphia: A.S.T.M., 1956, 10-24.

19. Tardif, H. P., and Marquis, H. "Impact Testing with an Instrumented Machine," Metal Progress (Feb., 1964), 79-82, 132, 134, 136.

20. Tanaka, Minoru, and Sokichi, U. "On the Breaking Behavior in Charpy Impact Bending Tests," Proceedings of the 1st Japan Congress on Testing Materials. Kyoto: Japan Society for Testing Materials, 1958, 95-98.

21. Koboyshi, Toshiro, Takai, K., and Maniwa, H. "Transition Behavior and Evaluation of Fracture Toughness in Charpy Impact Testing, Transactions of the Iron and Steel Institute of Japan (Tokyo), VII, 1967, 115-125.

22. Ayama, Shigetsune, and Saruki, K. "Correlations Between Crack Propagation Energy, Fracture Appearance and Temperature in Charpy Impact Tests," Proceedings of the 9th Japan Congress on Testing Materials. Kyoto: Japan Society of Materials Science, 1966, 54-57.

23. Fearnehough, G. D., and Hoy, C. J. "Mechanism of Deformation and Fracture in the Charpy Test as Revealed by Dynamic Recording of Impact Loads," J. of the Iron and Steel Institute, CCII (Nov., 1964), 912-920.

24. Wells, A. A. "Application of Fracture Mechanics At and Beyond General Yielding," British Welding J., X, No. 11, (Nov., 1963), 563-569.

25. Wells, A. A. "Unstable Crack Propagation in Metals," presented at Crack Propagation Symposium on Sept., 1961, at College of Aero. and the Royal Aero. Soc., Canfield, England.

26. Wilshaw, T. R. "Deformation and Fracture of Mild Steel Charpy Specimens," J. of the Iron and Steel Institute, CCIV (Sept., 1966), 936.

27. Radon, J. C., and Turner, C. E. "Fracture Toughness Measurements by Instrumented Impact Tests," Engineering Fracture Mechanics, I, No. 3 (April, 1969), 411-428.

28. Turner, C. E. "Measurement of Fracture Toughness by Instrumented Impact Test," Impact Testing of Metals, A.S.T.M. Special Technical Publication No. 466. Philadelphia: A.S.T.M., 1970, 93-114.

29. Eftis, J., and Krafft, J. M. "A Comparison of the Initiation with Rapid Propagation of a Crack in a Mild Steel," Transactions A.S.M.E. (J. of Basic Engineering), March, 1965, 257-263.

30. Irwin, G. R. "Structural Aspects of Brittle Fracture," Applied Materials Research, III, 1964, 65-81.

31. Irwin, G. R. "Crack Toughness Testing of Strain-Rate Sensitive Materials," A.S.M.E. Paper No. 63-WA-217, 1963.

32. Bothers, A. J., and Martens, H. E. "Dynamic Notched Screening Tests," Proceedings 7th Sagamore Ordnance Materials Conference. Syracuse: Syracuse Univ. Research Institute, 1960, V79-V82.

33. Cotterell, B. "Correspondence," British Welding Journal, IX, No. 11, 1962, 621.

34. May, M. J., and Priest, A. H. K_{IC} Measurement at Different Loading Rates. B.I.S.R.A.: The Intra-Group Laboratories of the British Steel Corporation (London), Jan., 1968.

35. Venzi, S., Priest, A. H., and May, M. J. Influence of Inertial Load in Instrumented Impact Tests. B.I.S.R.A.: The Intra-Group Laboratories of the British Steel Corporation (London), Report No. MG/C/85/68.

36. Priest, A. H., and May, M. J. Fracture Toughness Testing in Impact. B.I.S.R.A.: The Intra-Group Laboratories of the British Steel Corporation (London), Report No. MG/C/46/69.

37. Turner C. E. Personal communication.

38. Brown, William F., and Srawley, J. E. Plain Strain Crack Toughness Testing of High Strength Metallic Materials, A.S.T.M. Special Technical Publication No. 410. Philadelphia: A.S.T.M., Dec., 1967, 25.

39. Srawley, John E., and Brown, W. F. "Fracture Toughness Testing Methods," A.S.T.M. Special Technical Publication No. 381. Philadelphia: A.S.T.M., April, 1965, 167, 190.

40. Newhouse, D. L., and Wundt, B. M. "A New Fracture Test for Alloy Steels," Metal Progress, LXXVIII, No. 7, 1960, 81-82.

41. Wundt, B. M., and Newhouse, D. L. "Slow Bend and Impact Testing of Nitrided Charpy V-Notch Specimens," Welding Journal (Research Supplement), XLII, (July, 1963), 325s-336s.

42. Radon, J. C., and Turner, C. E. "Note on the Relevance of Linear Fracture Mechanics to Mild Steel," Journal of the Iron and Steel Institute, XX (Aug., 1966), 842-845.

43. Orner, George M., and Hartbower, C. E. "Sheet Fracture Toughness Evaluated by Charpy Impact and Slow Bend," Welding Journal (Research Supplement), XL (Sept., 1961), 405s-416s.

CHAPTER VIII

1. McQuillan, A. D., and McQuillan, M. K. Metallurgy of the Rarer Metals--Vol. 4. London: Butterworths Scientific Publications, 1956, 97-99.

2. Texas Instruments, Inc. Bulletin No. DL-S 6911291, December, 1969. Typical Applications Data.

3. Goodman, Lawrence E., and Warner, William H. Dynamics. Belmont, California: Wadsworth Publishing Co., 1963, 88-89.

4. Cuhn, F. M. "Simplified Procedure for Metallography of Zr and Hf and Their Alloys," Zirconium and Zirconium Alloys. Cleveland, Ohio: A.S.M. Publication, 1953.

5. Soller, H. A. and Dickerson, R. F. Notes From the Second Metallographic Congress. Battelle Memorial Institute, January, 1950, 12 pps.

CHAPTER IX

1. Baumberger, H. Director of Research, Reactive Metals Corp. Personal communication.

2. Kaufmann, P. Wah Chang Albany Corporation. Personal communication.

APPENDIX A

1. Paris, Paul C., and Sih, George C. "Stress Analysis of Cracks," Fracture Toughness Testing and Its Applications. American Society for Testing and Materials S.T.P. No. 381 (Philadelphia: A.S.T.M.), 1965, 30-38.

2. Love, A. E. H. A Treatise on the Mathematical Theory of Elasticity. 4th ed. New York: Dover Publications, 1944, 135.

3. Kreyszig, Erwin. Advanced Engineering Mathematics. 2nd ed. New York: John Wiley & Sons, Inc., 1967, 542.

4. Churchill, Ruel V. Complex Variables and Applications, 2nd ed. New York: McGraw-Hill Cook Co., 1960, 35.

5. Kreyszig, Erwin. op. cit., p. 546.

6. Westergaard, H. M. "Bearing Pressures and Cracks," Trans. A.S.M.E., J. of Appl. Mechanics, (June, 1939), A-49 to A-53.

APPENDIX B

1. Paris, Paul C., and Sih, George C. "Stress Analysis of Cracks," Fracture Toughness Testing and Its Applications. American Society for Testing and Materials S.T.P. No. 381 (Philadelphia: A.S.T.M.), 1965, 30-83.

2. Shames, Irving H. Mechanics of Deformable Solids. New Jersey: Prentice-Hall, Inc., 1965, 99.

3. Timoshenko, S. Strength of Materials--Part I. New York: D. Van Nostrand Co., Inc., 1966, 66.

MICHIGAN STATE UNIVERSITY LIBRARIES
3 1293 03175 6715